DEVELOPMENT, TESTING, AND EVALUATION OF SHAPE MEMORY ALLOY-BASED STRUCTURAL CONTROL DEVICES FOR SEISMIC RESILIENCE

BY

Amedebrhan M. Asfaw

A DISSERTATION

Presented to:

The School of Engineering and Applied Science of the

University of Virginia

in partial fuilfillment of the requirments for the degree of

DOCTOR OF PHILOSOPHY

Major: Civil Engineering

December 2021

DEVELOPMENT, TESTING, AND EVALUATION OF SHAPE MEMORY ALLOY-BASED STRUCTURAL CONTROL DEVICES FOR SEISMIC RESILIENCE

BY

Amedebrhan M. Asfaw

A DISSERTATION

Presented to the School of Engineering and Applied Science of

the University of Virginia

in partial fuilfillment of the requirments for the degree of

DOCTOR OF PHILOSOPHY

Major: Civil Engineering

Approved by:

Chair of Advisory Committee	Jose P. Gomez
Committee Members	Osman E. Ozbulut (Advisor)
	Arsalan Heydarian
	Devin K. Harris
	Kirk Martini

December 2021

ABSTRACT

Improving community resilience to natural hazards such as earthquakes is one of the central challenges in the 21st century. Among others, the performance of individual buildings is a critical factor that dictates how soon societies impacted by seismic hazards could recover. Recent earthquakes have demonstrated that many buildings designed based on modern code requirements were not occupiable due to substantial structural damages, taking months or years to repair or reconstruct. Mitigating the devastating socio-economic impacts of earthquakes requires an urgent need for expanding performance goals beyond life safety to achieve rapid re-occupation and functional recovery. In that perspective, residual drifts play a significant role in determining the post-event functionality of buildings. The necessity to limit residual deformations within an acceptable threshold has urged researchers to develop self-centering structural systems that can return to their original plumb position after a seismic event. While self-centering capability in a structure can be realized in several ways, superelastic shape memory alloys (SMAs) that possess inherent re-centering and energy dissipation capabilities are promising materials to develop self-centering devices.

This research proposes innovative SMA-based structural control devices that can enable re-occupancy or functional recovery of buildings after a major earthquake within a reasonable amount of time. This dissertation follows a thorough investigation starting from material-level characterization, then moving to a component-level investigation, and finally to a system-level evaluation. First, the buckling and post-buckling behavior of large-diameter superelastic SMA bars were explored. A digital image correlation measurement system and an infrared thermal imaging camera were implemented to monitor full-field strain and surface temperature fields. The interaction between material nonlinearity (due to phase transformation) and geometric nonlinearity was explored. Furthermore, the effects of strain rate on the buckling and post-buckling responses were examined. Second, the studied SMA bars were employed to develop a new damping device named Confined Superelastic Dissipater (CSD). The proposed dissipater consists of a fused superelastic SMA bar as the functional kernel component encased in grout filled steel tube. The bar carries axial loads and dissipates energy through axial deformation, while the steel tube and infill grout restrain the bar and preclude buckling in compression. Quasi-static cyclic tests were conducted to characterize the hysteretic behavior and failure modes of CSDs. Next, a novel SMA-based hybrid damper that leverages the high tensile resistance and excellent self-cantering capability of SMA cables and non-sacrificial energy dissipation of a frictional damping mechanism was developed. The proposed damper, named Superelastic Friction Damper (SFD), employs judicious design features, manifested by additional advantages such as scalability for real-world application, reusability, ease of fabrication, and adaptability of its hysteretic response. A large-scale prototype damper was fabricated, and its mechanical behavior under repeated cyclic loading at different loading rates and ambient temperatures was characterized. Finally, the efficacy of the SFD in controlling the seismic responses of special steel moment-resisting frame was evaluated through nonlinear response history analyses. Engineering demand parameters of the frame with and without the damper were compared. Overall, the experimental and numerical results demonstrate that the SMA-based control devices can be implemented to meet higher performance objectives and achieve functional recovery of structures after a major earthquake, paving the way for designing resilient built environment.

ACKNOWLEDGEMENTS

First and foremost, I would like to express my deepest gratitude to my supervisor and mentor, Professor Osman Ozbulut, for his guidance, invaluable advice, continuous support, and encouragement during my Ph.D. study. Being a well-known expert in the field of shape memory alloy and earthquake engineering, Prof. Osman Ozbulut enriched the area of research addressed by this work. I feel privileged to have worked under his supervision. I thank the members of my doctoral advisory committee, Professors Jose Gomez, Devin Harris, Arsalan Haydarian, and Kirk Martini for their time, interest in my work, thoughtful comments, and feedback.

I would also like to thank the current and former RAIL research group members and visiting scholars who have contributed, in one way or the other, to the successful completion of my research. A special thanks to Assistant Professor Muhammad Sherif for his technical support related to Digital Image Correlation system as well as for his encouragement and many inspiring discussions. I am indebted to Mr. William Ordel from the Virginia Transportation Research Council and Mr. Sebring Smith from the Lacy Student Experimental Center at the University of Virginia, who helped me with the experimental tests. Their assistance is acknowledged with thanks. I also extend grateful appreciation to Lehigh University researchers, Professor James Ricles and Dr. Liang Cao, for their collaboration and assistance on the superelastic friction damper experimental work.

Last but not least, many thanks to my family; this dissertation would not have been possible without their unconditional support.

TABLE OF CONTENTS

LIST OF TABLES

LIST OF FIGURES

LIST OF ABBREVIATIONS AND ACRONYMS

ABC	Accelerated Bridge Construction
ACI	American Concrete Institute
AD	Added Damping
AQ	Articulated Quadrilateral
ASCE/SEI	American Society of Civil Engineers/Structural Engineering Institute
ASTM	American Society of Testing Materials
BRB	Buckling Restrained Brace
BRP	Buckling Restraining Plate
CFR	Clamping Force Ratio
CLT	Cross Laminated Timber
CSD	Confined Superelastic Dissipator
CSS	Curved Surface Slider
DAD	Damage Avoidance Design
DASMAFD	Deformation-Amplified Shape Memory Alloy -Friction Damper
DBD	Displacement-Based Design
DBE	Design Basis Earthquake
DCR	Dissipated Controlled Rocking
DIC	Digital Image Correlation

EDR	Energy Dissipation Ratio
EVD	Equivalent Viscous Damping
FEMA	Federal Emergency Management Agency
FRP	Fiber Reinforced Polymer
HDRB	High-Damping Rubber Bearing
IDA	Incremental Dynamic Analysis
IMK	Ibarra Medina Krawinkler
LCC	Life Cycle Cost
LRB	Lead Rubber Bearing
LVDT	Linear Variable Displacement Transducer
MCE	Maximum Considered Brace
ML-SLRB	Multi-Level SMA Lead Rubber Bearing
MSM	Martensite-Superelastic-Martensite
NiTi	Nickel Titanium
NRB	Natural Rubber Bearing
OpenSees	Open System for Earthquake Engineering Simulation
PBEE	Performance Based Earthquake Engineering
PFA	Peak Floor Acceleration
PGA	Peak Ground Acceleration

PID	Peak Interstory Drift
PTFE	Polytetrafluoroethylene
PZ	Panel Zone
RBD	Resilient Based Design
RBS	Reduced Beam Section
RC	Reinforced Concrete
RDASD	Re-centering Deformation Amplified SMA Damper
RID	Residual Interstory Drift
RSE	Relative Self-centering Efficiency
RSLD	Re-centering SMA-Lead Damper
RSMAD	Re-centering Shape Memory Alloy Damper
SC	Self-Centering
SCBF	Steel Concentrically Braced Frame
SC-BRB	Self-Centering Buckling Restrained Brace
SCNSD	Self-Centering Negative Stiffness Damper
SDC	Seismic Design Category
SDOF	Single Degree of Freedom
SE	Superelastic Effect
SFB	Spring-Friction Bearing

SFD	Superelastic Friction Damper
SIMT	Stress Induced Martensite Transformation
SMA	Shape Memory Alloy
SMA+VD	Shape Memory Alloy Visco-Recentring Damper
SMAB	Shape Memory Alloy Brace
SMA-BF	Shape Memory Alloy Braced Frame
SMAGD	Shape Memory Alloy Gap Damper
SMA-LRB	Shape Memory Alloy Lead Rubber Bearing
SMARB	Shape Memory Alloy Rubber Bearing
SMA-SCEB	Shape Memory Alloy Self-Centering Energy Dissipative Brace
SMA-UD	Shape Memory Alloy U-Shaped Damper
SME	Shape Memory Effect
SMM	Shape Memory Materials
SMRF	Steel Moment Resisting Frame
SMS	Superelastic-Martensite-Superelastic
SRB	Shape Memory Alloy Rubber-Based
SSMAFD	Superelastic Shape Memory Alloy Friction Damper
SVD	Superelastic Viscous Damper
VF-SCEB	Variable Friction Self-Centering Energy Dissipation Brace

1 INTRODUCTION

1.1 Background and Problem Statement

Although predicting earthquakes' occurrence, magnitude, and epicenter is challenging and beyond our scientific knowledge, earthquakes are sure to happen. They have caused disastrous impacts in the past and are expected to cause more in the future. Nearly half of the United States population (150 million people) reside in different states prone to occurrence of a highly damaging earthquakes within the next five decades [1]. In regions of high seismic risk such as San Francisco, California where a major earthquake has not happened for some time, scenario studies have predicted deaths in the thousands, injuries in the tens of thousands, and direct economic losses in hundreds of billions of dollars apart from long-term destabilizing impacts to community services [2–5]. In all cases, whether historic or scenario-based, the societal and economic losses are direct consequences of the inability of the built environment to resist the effects of earthquakes.

Over the last century, modern seismic design and construction technologies have undergone significant developments. The state-of-practice in seismic design allows structures to undergo plastic deformations to dissipate input earthquake energy. The most commonly used seismic force-resisting systems, such as steel moment-resisting frames (SMRFs), steel concentrically braced frames (SCBFs), and concrete shear walls, are designed to dissipate energy through substantial yielding near the beam ends, inelastic buckling and yielding of the braces, and through yielding of reinforcing steel and crushing of concrete, respectively. While this design method satisfactorily protects human lives by preventing collapse, it does not fully account for the aftermath of public life. People may be unable to return to their damaged houses and may be forced to stay inconveniently in evacuation shelters for a long recovery term. They may not have access to jobs and other essential community services. The central problem of conventional seismic load resisting systems has been clearly demonstrated during the 2011 Christchurch earthquake in New Zealand. While less than 1% of damaged structures collapsed during the Christchurch earthquake, more than 70% of the structures that remained intact and survived the strong shaking were declared unusable [6,7]. They were subsequently demolished since they sustained significant damage. Similar damage was observed during the 2010 Maule earthquake in Chile, the 2011 Tohoku earthquake in Japan, and the 2020 Van earthquake in Turkey. In addition, statistics from a recent study conducted by the US Federal Emergency Management (FEMA) show that 20% to 40% of modern code-compliant buildings in an earthquake-prone area would be unfit for re-use following an earthquake, taking months or years to recover complete serviceability [8]. Apart from that, 15% to 20% of buildings would be economically unrepairable, taking several years to replace. Note that older buildings that do not conform to modern design requirements would perform even worse than code-compliant buildings. Given the facts described above, it is evident that there is room to improve the current seismic design practice.

Some drawbacks of traditional seismic force-resisting systems can be effectively mitigated by making structural components play separate roles. This means that the primary structural systems will support the gravity load while the seismic members mainly resist earthquake loads. A similar concept can be found in nature and industrial products. For example, fuses in computers and expensive equipment are buffers to protect the central system against excessive electric currents. Similarly, collarbones are broken to ease forces in the human body. By the same logic, control devices that act like “fuses” can be installed in civil structures to protect the primary gravity load-carrying members against earthquake damage. Repairing damaged structures is expensive and time-consuming because the damage is typically distributed throughout the structure in many non-replaceable elements. Thus, it is paramount important to contain damage through control devices. In general, structural control devices can be grouped into four main types: passive, active, semi-active, or hybrid, depending on whether an external power source is required or not for their operation.

Passive control devices are the most desirable devices due to their stability, reliability, and simplicity without needing a power supply and feedback algorithm. They can be broadly categorized as displacement-dependent (e.g., friction dampers) and rate-dependent (e.g., viscous fluid dampers and viscoelastic dampers) devices. Various passive dampers have been successfully implemented worldwide and are deemed to provide satisfactory performance [9–14]. Among those, metallic yielding dampers are one of them which dissipate energy through yielding and inelastic deformation. The yielding mechanism can be flexural, shear, torsion, axial deformation, or a combination. They offer unique features such as high energy dissipation capacity and economic efficiency while requiring neither special expertise for fabrication nor maintenance for service life. Although the structural fuse design concept has proved to be a significant step forward in seismic hazard mitigation, structures equipped with passive dampers are inevitably left with permanent deformations and excessive damages in these fuses. In addition, most of these passive dampers lack a self-centering capability.

One of the critical parameters used to quantify the performance level of buildings is the lean that remains after a seismic event. This lean is generally expressed as a ratio of the horizontal deformation of a story to the story height at the end of ground shaking, and it is called permanent or residual drift. The formation of residual drifts in buildings have received increased attention in recent years as its extent determines the post-event functionality [15,16]. The guidelines in FEMA P-58 [17] present helpful information on the relation between the residual story drift and the damage state. Accordingly, repairing a structure is economical if the residual drift is limited to 0.5%. When the residual drifts are above this threshold for economical repair, buildings may be demolished. Figure 1-1 shows two example buildings with excessive residual drifts but without significant dame. Both buildings were demolished since economical repair was not warranted due to substantial residual drifts. On the other hand, if the drift is limited by 0.2%, the repair work will be further narrowed to non-structural members. However, it is challenging to meet these stringent requirements when using traditional seismic load resisting systems or even some of the relatively new technologies such as buckling restrained braces (BRBs). Nonlinear time-history analyses of a four-story BRB frame conducted by Fahnestock et al. [18] indicated that the maximum residual drifts averaged 0.5% and 1.2% under design basis earthquakes (DBE) and maximum considered earthquakes (MCE), respectively. Similarly, Trembly et al. [19] concluded that the median residual drifts of 2-story to 16-story BRB frames ranged from 0.84% to 1.38% under DBE and between 1.41% to 4% under MCE level ground motions.

Apartment building with 2% residual drift after the 2011 Tohoku earthquake in Japan [20]

Plaza del Rio towers with 1.5% residual drift after the 2010 Maule earthquake in Chile [21]

Figure 1-1. Representative examples that show buildings demolished after an earthquake event due to excessive residual drift.

Self-centering structural systems have emerged as a viable option to minimize or eliminate system-level residual drifts, thus enabling enhanced performance levels [22]. Self-centering refers to the ability of a structure to return to its original plumb position after a seismic event. A typical self-centering system consists of two main components: (1) a mechanism that provides a restoring force, usually using unbonded post-tensioned tendons or bars, (2) an energy-dissipating component. Combining these two behaviors produces a “flag-shaped” hysteretic behavior, which means the restoring force brings the displacement of the self-centering system back to zero after every cycle. Several different configurations have been devised to produce the desired self-centering characteristics [23–27]. These include rocking systems [28,29], self-centering moment-resisting frames [30], and different types of self-centering braces or damping devices [31–40]. The studies mentioned above have demonstrated that systems with self-centering capabilities have about the same maximum drift as comparably designed conventional systems but with substantially less residual drift. Nevertheless, self-centering systems are rarely used in practice because of cost and construction difficulties associated with post-tensioning procedures. Most of the existing self-centering braces have complex configurations characterized by many moving parts, a large number of tendons, numerous connection details, and are very large in size.

Shape memory alloys (SMAs) are a smart class of metallic alloys that have been exploited for the development of self-centering devices [41–46]. Their superelastic effect, which is the ability of the material to recover large nonlinear deformations upon the removal of applied loads accompanied by hysteretic energy dissipation, has made them appealing materials for earthquake engineering applications. Unlike conventional self-centering devices that rely on post-tensioning, the inherent material behavior of SMAs can be utilized for both self-centering capability and energy dissipation capacity. This could alleviate some of the complexity issues discussed above. To date, many SMA-based seismic protection technologies have been developed. A more thorough literature review of recent developments, trends, and challenges of SMA-based structural control devices is presented in Chapter 2. Despite their promising performances in seismic hazard mitigation, most of the devices developed so far have been laboratory-scale prototypes in which SMA wires with a diameter of 1 mm or 2 mm were used. Thus, damping devices with relatively high force capacities and stroke that can accommodate demands in real-world applications are needed.

As the awareness of the significance of individual buildings’ performance to community resilience to earthquakes increases among policymakers and other stakeholders, the performance goals continue to expand beyond life safety and collapse prevention. In 2016, the United States Congress mandated federal agencies, specifically, the National Institute of Standards and Technology (NIST) and FEMA, to identify research needs towards achieving rapid re-occupation and functional recovery not only in critical buildings such as hospitals and emergency response centers but also in other buildings after natural disasters such as large earthquakes [47]. The report underscores the necessity of inventing innovative materials and new building systems to ensure structural integrity and provide higher levels of post-event functionality. As illustrated in Figure 1-2, there are three milestones in the post-earthquake timeline: re-occupancy, functional recovery, and full recovery. These post-earthquake performance states are collectively called recovery-based objectives. Re-occupancy occurs when the re-entry to buildings is deemed safe, while functional recovery marks the restoration of the primary functions of the building and indicates the building is operational. On the other hand, functional recovery indicates that the building is restored to its pre-event use within a reasonable time. To this end, new design philosophies, such as performance-based earthquake engineering (PBEE) [48–51], resilient-based design (RBD) [52,53], and damage avoidance design (DAD) [54,55] have been developed. Recovery-based design philosophy can be considered as the next generation of PBEE, DAD, and RBD.

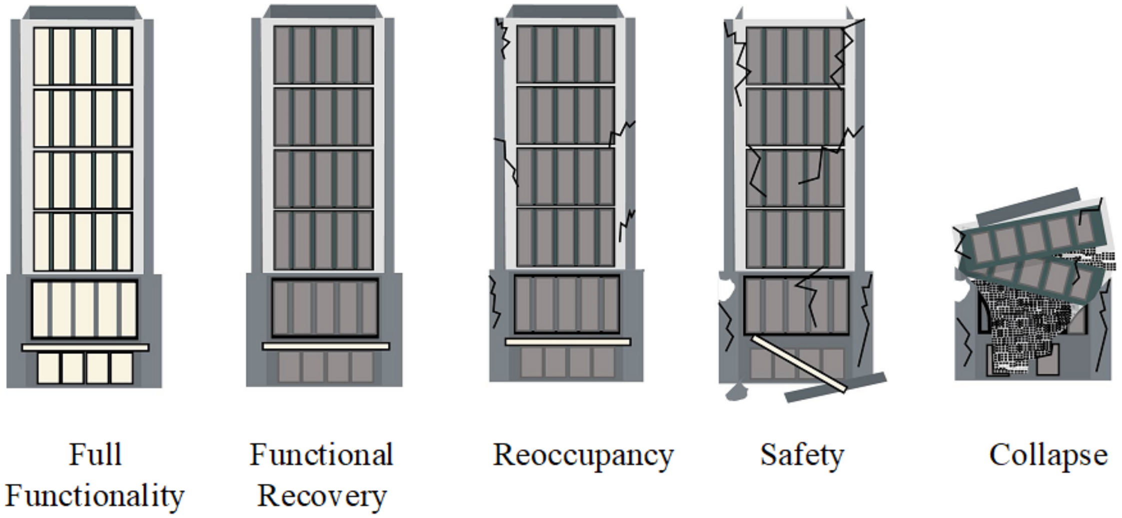

Figure 1-2. Schematic representation of post-earthquake performance states

In light of the push for a paradigm shift towards recovery-based design objectives, there remains a need for resilient lateral load resisting systems for both new construction and retrofit of existing. As noted previously, higher residual deformations will lead to substantial socio-economic losses in terms of downtime of building occupation and post-disaster reconstruction. Therefore, an ideal lateral force resisting structural system must include, the following essential design features:

- Capability to control peak story drifts, residual drifts, and peak floor accelerations simultaneously
- Ability to minimize damage at design level earthquake and protect structural and non-structural components
- Usability with no or minimal repair after large earthquakes

The main goal of this dissertation is to develop, characterize, and evaluate innovative SMA-based structural control devices that can be used to achieve recovery-based design objectives. The specific aims and objectives of the research are detailed in Section 1.2.

1.2 Research Objectives

The specific research goals of this dissertation include: (1) understand the buckling and post-buckling behavior of superelastic NiTi SMA bars to foster their practical application and provide an improved understanding of their complex thermomechanical behavior in compression; (2) develop a new type of SMA-based energy dissipaters that can be used for various applications, notably for seismic retrofitting of existing substandard structures; (3) develop an innovative SMA-based damper that can be implemented to achieve functional recovery performance targets, and (4) evaluate the efficacy of the new SMA-based damper in seismic response control through numerical simulations. These goals are achieved by fulfilling the following tasks:

- Conduct a state-of-the-art review and analysis as well as critical examination, including advantages and challenges of existing SMA-based structural control devices.
- Investigate NiTi SMA bars' buckling and post-buckling behavior by testing specimens that cover a wide range of slenderness ratios.
- Design and fabricate a damping device called confined superelastic dissipater (CSD), and characterize its hysteretic behavior and failure modes under cyclic tension-compression loading.
- Design and fabricate a new SMA-hybrid damper called superelastic friction damper (SFD) and evaluate its hysteretic properties through cyclic loading tests under various ambient temperature and loading rates.

- Examine the influence of key design parameters such as the quantity of SMA cables, length of the cables, frictional force, and pretentioning of SMA cables on the mechanical behavior of the damper.
- Perform nonlinear time history analysis of a steel moment-resisting frame with and without SFD and evaluate the efficacy of the damper in mitigating the response of the structure.

1.3 Organization of the Dissertation

This dissertation is organized as follows:

Chapter 1 provides background information and the motivations of this research. It also elaborates the research objectives and scope of the work.

Chapter 2 presents a state-of-the-art review and analysis of SMA-based structural control devices. Since early 2000s, SMAs have been explored for various applications in civil engineering. Notably, SMAs have been heavily researched for earthquake engineering to devise various technologies to protect civil structures against earthquake damages. However, the decades of studies over SMA-based devices are highly scattered throughout the academic community. This chapter provides a comprehensive review of advancement (development and application) in the field of SMA-based passive control devices, which primarily include dampers, braces, and isolation bearings. Moreover, the critical review summarizes the advantages and limitations of each device and highlights the research gap for the ease of further studies and generating future research directions. This chapter lays a foundation for the remaining chapters.

Chapter 3 examines the buckling and post-buckling responses of large diameter SMA bars experimentally. One of the factors hindering the use of SMA bars is the lack of experimental data on their compression behavior compared to the tensile behavior. This is vital for the development and implementation of various types of SMA-based control devices. The experimental program is carefully designed to cover a wide range of slenderness ratios. A digital image correlation (DIC) technique is implemented to monitor full-field surface displacements and strains along with the specimens. The temperature field on the surface of the specimens is also recorded by an and Infrared camera. The cyclic properties of the bars are systematically compared with respect to hysteresis characteristics, loading rate effect, strain amplitude effect, and slenderness ratio.

Chapter 4 proposes a new SMA-based energy dissipater and characterizes its hysteretic behavior through comprehensive cyclic tests. The proposed dissipator consists of a fused superelastic NiTi SMA bar as the functional kernel component encased in grout filled steel tube. The bar carries the axial load and dissipates energy through axial deformation, while the steel tube and infill grout restrain the bar and preclude buckling in compression. Global and local stability criteria are derived for the design of the buckling restraining system. Response quantities of prime interest for earthquake engineering, such as energy dissipation, equivalent viscous damping, and self-cantering capability, are evaluated. The effect of geometric parameters such as fuse diameter and bar length on the hysteretic parameters as well as failure mechanisms of CSDs are explored. Based on the experimental results and visual observations of failed specimens, specific recommendations are made to improve the performance of the CSDs. At the end of the chapter, a numerical case study is presented to demonstrate the application of CSDs for seismic retrofitting of substandard reinforced concrete beam-column joints.

Chapter 5 develops an innovative SMA-based hybrid damper that leverages the high tensile resistance and excellent self-cantering capability of SMA cables and non-sacrificial energy dissipation of a frictional damping mechanism. The components and basic working principle of the proposed damper are first described, and the advantages of the proposed damper compared to the existing SMA-based hybrid dampers are highlighted. The analytical expressions for the prediction of the load-displacement relationship of the damper are then derived. A large-scale prototype damper was fabricated, and its mechanical response under repeated cyclic loading at different loading rates and at different ambient temperatures are characterized. Following the experimental work, a simple yet effective numerical model of the damper specimen was developed and validated. A parametric analysis is conducted to investigate the influence of key design parameters on the damper performance.

Chapter 6 evaluates the efficacy of the damper developed in Chapter 5 in controlling the seismic responses of steel frame building through nonlinear response history analyses. First, a four-story frame is designed as a conventional moment resisting frame to meet current seismic design requirements. A numerical model that accounted for strength and stiffness degradation of the frame elements is created using the OpenSees finite element framework. Next, a reduced strength version of the fully code-compliant frame, which satisfied strength requirements but violet story drift limits, is developed. SFDs are designed and installed in all bays of each floor to satisfy code drift requirements. Then, the seismic performance of the uncontrolled and controlled frames is evaluated under a suite of 14 far-field strong ground motion records in terms of peak interstory drift (PID), residual interstory drift (RID), and peak floor acceleration (PFA). Lastly, a sensitivity analysis study is carried out to evaluate the effect of SFD design parameters, namely the frictional force, on the overall performance of the steel frame with SFDs.

Chapter 7 finishes the dissertation by summarizing the work done in the presented study, highlighting the main conclusions and contributions of the research. Finally, limitations of the research and some future research directions are suggested.

2 A STATE-OF-THE-ART REVIEW ON SMA-BASED STRUCTURAL CONTROL DEVICES

2.1 Overview

One of the promising strategies for a resilient design of civil structures is the using shape memory alloy (SMA)-based seismic protection systems. SMAs are often the key component in smart devices that can be incorporated into structures to enable functions such as self-sensing, energy dissipation, actuation, monitoring, self-adapting, and self-healing of structures. The use of SMAs as emerging materials for civil engineering applications dates back to the 1990s. Since then, extensive research advancement has been made, and SMAs have been considered for various civil engineering applications. Specifically, their use in seismic response control has been the most widely studied area.

This chapter critically synthesizes the vast body of literature related to the application of SMAs in passive seismic control systems. Among other compositions of SMAs, nickel-titanium (NiTi) is the most widely exploited owing to its outstanding properties, such as excellent superelasticity, modest energy dissipation capacity, and high corrosion resistance. This chapter emphasizes superelastic SMA dampers or energy dissipating devices, bracing systems, and isolation bearings proposed during the past decade (2010-2020). In the following sections, a review of each control device is provided. First, the fundamental material properties of SMAs are introduced, followed by descriptions of common SMA products and a summary of basic experimental tests to characterize their mechanical behavior. Next, SMA-based dampers and energy-dissipators are described, followed by different types of SMA-based bracing systems. Then, a review of representative smart isolators is presented. A concise summary of the working principles, experimental testing (if applicable), and performance assessment for each seismic control device are discussed. Finally, current challenges, opportunities, and future research needs are highlighted and discussed.

2.2 Fundamentals of Shape Memory Alloys (SMAs)

2.2.1 A brief history

The first discovery of SMAs can be traced back to 1932, when Arne Olander identified a phase transformation phenomenon in cadmium-gold (*CdAu*) alloy [56]. However, Vernon [57] introduced the term “shape memory” almost ten years later for his polymetric dental material. In the 1950s, many other alloys such as *CuZn* and *CuAl* were found exhibited the shape memory effect. From then on, researchers verified that the phenomenon of shape memory was associated with reversible martensitic transformation. This metallurgical characteristic generated considerable attention within the community of material scientists. Extensive experiments on SMAs pointed out that the deformation of the material could be recovered at room temperature, a characteristic called superelasticity (also known as pseudoelasticity), which was discovered by Rachinger [58] in 1958. It refers to the ability of SMA to regain its original shape upon removal of the applied load.

The significance of shape memory materials (SMMs) was not recognized until Buehler et al. [59] at the US Naval Ordnance Laboratory discovered a new class of nickel-titanium (*NiTi*) alloy in 1963. It is also commonly referred to as “Nitinol,” derived from a unique coupling of the material composition (NiTi) and the initials of the invention place (Naval Ordnance Laboratory). Numerous investigations on potential applications of SMAs have been perused since its discovery. In 1965, Wang et al. [60] demonstrated that the phase transformation temperature of *NiTi* SMA could be altered by adding alloy elements such as *Co* or *Fe,* and this observation advanced the commercialization of SMA in many industries. In 1969, Melton et al. [61] and Raychem Corporation implemented one of the earliest practical applications of *NiTi* SMA in the F-14 fighter project. Couplings made of NiTi were used for combining aircraft hydraulic air tubes. The popularity of NiTi SMA began to evolve in the biomedical field in the 1970s. Nevertheless, the actual commercial breakthrough was made in the 1990s when *NiTi* SMA stents were made and widely recognized by the public. Continued research led to the use of *NiTi* SMA in the military and civil engineering disciplines. Concurrently, SMAs gained further use in the electrical, automotive, aerospace, robotics, and oil industries.

Since the twenty-first century, there has been a dramatic increase in the application of SMAs in different sectors, as revealed from a vast number of publications. A survey conducted using Elsevier’s Scopus database indicates that more than 30,000 articles related to SMAs have been published from 1990 to 2020. Figure 2-1 illustrates the distribution of publications between different disciplines and by publication type. With searching keywords limited to “civil engineering” and “shape memory alloy” or “Nitinol”, greater than 900 pertinent journal and conference papers have been published over the same period.

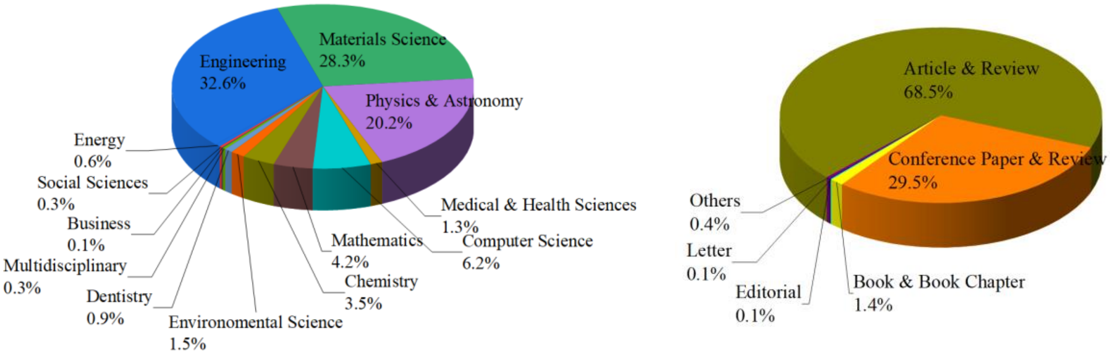

Figure 2-1.The number of SMA-related publications by subject area and type between 1990 to 2020. (Source: Elsevier Scopus)

2.2.2 Basic properties of SMAs

SMAs have two predominant phases: martensite and austenite, with three distinct crystal structures, i.e., twinned martensite, detwinned martensite, and austenite. The austenite (also known as the parent phase) is stable at high temperatures and low stress with a body-centric atomic structure, while the martensite phase is stable at low temperatures and high stress with a parallelogram structure. The existence of the two distinct martensite crystal structures is associated with the different orientation directions (variants) of the martensitic crystal. The martensite can change its position by moving twin boundaries, while the austenite deforms by the generation of dislocation. As a result, the martensite phase is weaker and provides lower yield strength than the austenite phase. The unique strain recovery property of SMAs is due to reversible phase transformations between austenite and martensite. It is a phenomenon associated with shear lattice distortion instead of dislocation-based plasticity exhibited by other construction materials such as carbon steel.

The phase transformation can be either thermally induced, which results in shape memory effect (SME), or stress-induced, in which case the material exhibits superelastic effect (SE). If there is no external load (stress), four characteristic temperatures define the transformation processes. As illustrated in Figure 2-2, the martensite start (M_s) and finish (M_f) temperatures define the start and finish of the transformation from austenite to martensite, respectively. On the other hand, the temperatures at which the transformation from martensite to austenite begins and is complete are defined by A_s and A_f, respectively. The involvement of stress makes the transformation process more complicated. The inner plot in Figure 2-2 highlights the relationship between transformation temperatures and applied stress.

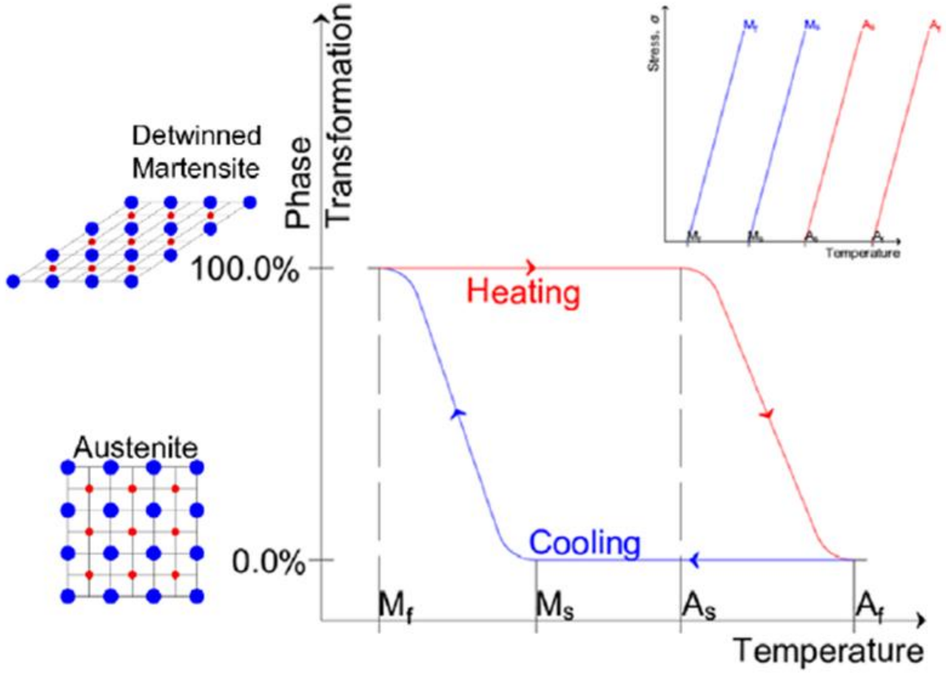

Figure 2-2. The schematic diagram of phase transformations with respect to change in temperature and the relationship between transformation temperatures and applied stress

When SMA is loaded at a temperature below M_f, a transformation from the twinned martensite to the detwinned martensite occurs. This process begins when the stress reaches a critical level σ_s^{cr} and ends at the end of the loading plateau at σ_f^{cr}. With a continued increase in stress, the elastic behavior of the detwinned martensite is displayed until the permanent yield stress of the martensite is achieved. If the load is removed at a stress level below the permanent yield stress, transformation-induced residual strain (ε_r) remains, but heating the deformed SMA above A_f can foster strain recovery, i.e., SME.

On the other hand, when the SMA is loaded at its austenite phase (i.e., at a temperature above A_f), the material holds the strain by transforming from austenite into detwinned martensite. Upon unloading, a reverse transformation to the austenite phase occurs, which leads to full shape recovery and a substantial hysteresis loop. This phenomenon is called SE. The maximum recoverable strain due to phase transformation can be up to 8% to 10%, depending on the metallic composition. As indicated in Figure 2-3, four characteristic stresses define a complete stress-strain cycle of SE, namely forward transformation start (σ_s^{AM}) and finish (σ_f^{AM}) stresses and reverse transformation start (σ_s^{MA}) and finish (σ_f^{MA}) stresses.

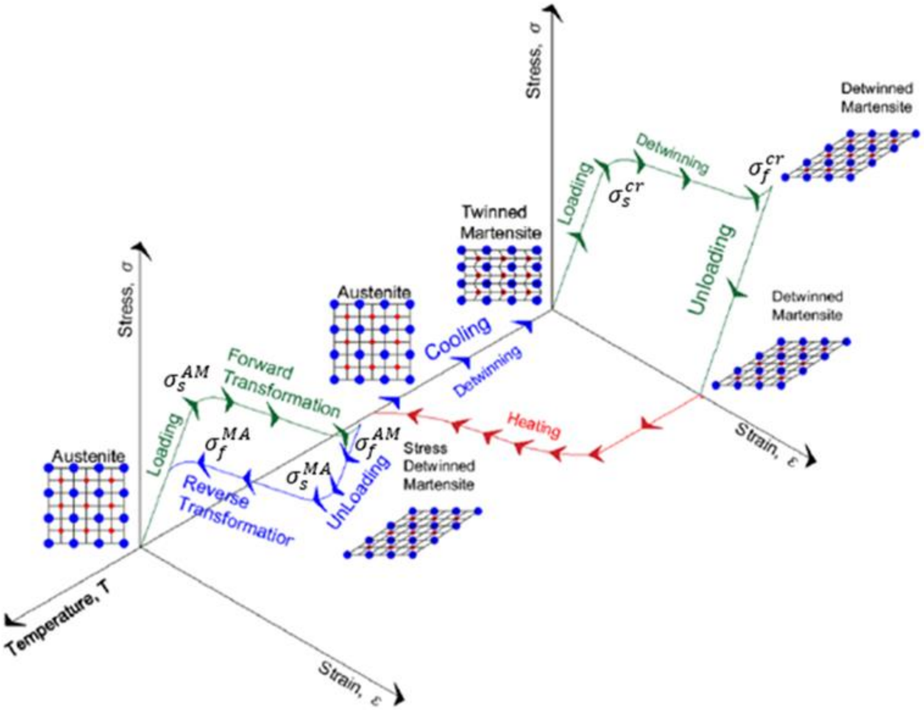

Figure 2-3. Typical stress, strain, and temperature interactions of shape memory effect (SME) and superelastic effect (SE) in SMAs [62]

2.2.3 Compositions and mechanical properties

Many types of SMA compositions have been developed and investigated. The three major types that have been explored the most are nickel-titanium (*NiTi)-based*, copper (*Cu*)-based, and iron (*Fe*)-based SMAs.

NiTi SMAs initiated the commercial applications of alloys exhibiting SME owing to their high percentage shape recovery, among other mechanical properties [63]. These are binary system alloys containing almost equal amounts of nickel and titanium. Adding more nickel above 50 atomic percentage (at.%) can lower the transformation temperatures. Thus, by altering the composition, the extent of phase transformation temperatures can be adjusted. *NiTi* SMAs possess high ductility, excellent self-centering capability, good fatigue resistance, and superior corrosion resistance. As a result, these alloys have been extensively investigated and employed in different engineering applications. Several factors generally influence their mechanical behavior, including cyclic loading, loading rate, and ambient temperature [64–70]. The alloys can be hot, or cold rolled but tended to harden quickly; hence frequent annealing is needed. In addition, machining and welding parts from the *NiTi* alloy require special tools and expertise [71,72].

Other alternative compositions of *NiTi* SMAs, such as *NiTiNb* and *NiTiHfPd*, have been developed to improve some target material properties. For instance, adding *Nb* ternary element to *NiTi* alloys widens the thermal hysteresis [73], increases the damping capacity, and yield strength [74,75]. *NiTiNb* in an annealed state has been utilized by many researchers for active confinement and heat-activated prestressing of structural elements [76]. Besides, it is reported that *NiTiHfPd* alloys exhibit significantly larger mechanical hysteresis and damping capacity than many binary and ternary SMAs in a more practical temperature range [75,77,78]. These improvements are useful for applications with high damping demand.

In a search for more cost-effective SMAs, numerous researchers have studied *Cu*-based SMAs of various compositions. These alloys are considered economical because they can be easily manufactured using conventional liquid metallurgy and powder metallurgy routes used for processing traditional *Cu*-based alloys [79]. Also, they do not have high reactivity, which requires special furnace environmental conditions as in the case with the processing of *NiTi* SMAs. The most common *Cu*-based SMAs are the *CuZn* and *CuAl* binary alloys, with a third alloying element often introduced to alter transformation temperature or microstructure. The addition of *Mn* to the *CuAl* system is reported to have enhanced ductility, formability, and shape recovery [80]. *CuAlMn* alloys also exhibit large superelastic strain comparable to *NiTi* alloys and other functional properties such as two-way SME and good damping property. However, they usually have lower strength than NiTi alloys. *CuAlBe* possesses excellent heat resistance and also demonstrates superelastic behavior. Compared with *NiTi* SMAs, *Cu*-based SMAs generally have low recoverable strain, wide transformation temperature range, small hysteresis, and minimal strain rate effects [81,82]. Thus, even though several compositions of *Cu*-based SMAs have been explored, only a few of them have been conceived for earthquake engineering applications [80,83]. One of the setbacks that hinder their use is that they tend to undergo aging resulting in phase stabilization and affecting the transformation temperatures [84].

The *Fe*-based SMAs, also called memory steel, are the third prominent group of SMAs discovered by Sato et al. [85] in 1982. Some types of *Fe*-based SMAs, such as *FePt, FePd*, and *FeNiCo*, exhibit the typical thermoelastic martensitic transformations similar to *NiTi*, with a narrow thermal hysteresis. However, other compositions such as *FeNiC* and *FeMnSi* have a more significant thermal hysteresis in transformation but still exhibit the SME. In particular, *FeMnSi*-based alloys that exhibit the SME effect have been successfully commercialized for civil engineering applications [86,87]. Several researchers have employed thermally activated *Fe*-SMAs for strengthening reinforced concrete structures and steel members [88–90]. There have also been efforts to develop superelastic *Fe*-based SMAs. Tanaka et al. [91] introduced *FeNiCoAlTaB* alloy that shows a recovery strain of over 13% at room temperature and a very high tensile strength of 1200 MPa. Similarly, Omori et al. [92] developed *FeMnAlNi* with a 6% or higher superelastic strain. Although *Fe*-based superelastic SMAs could have cost benefits over *NiTi* SMAs due to relatively cheap alloying constituent and easy fabrication, their development is still in an early stage.

Among the different compositions of SMAs developed to date, *NiTi* SMAs have been the most commonly used alloys for earthquake engineering applications because of their superior mechanical properties and wide availability. Despite their cost and machinability benefits, the Cu- and Fe-based alloys are yet to substitute *NiTi* alloys in numerous applications where they have to compete for selection. Figure 2-4 summarizes the three major SMAs and their comparative advantages. Additional information about the SMAs can be found in references [93,94].

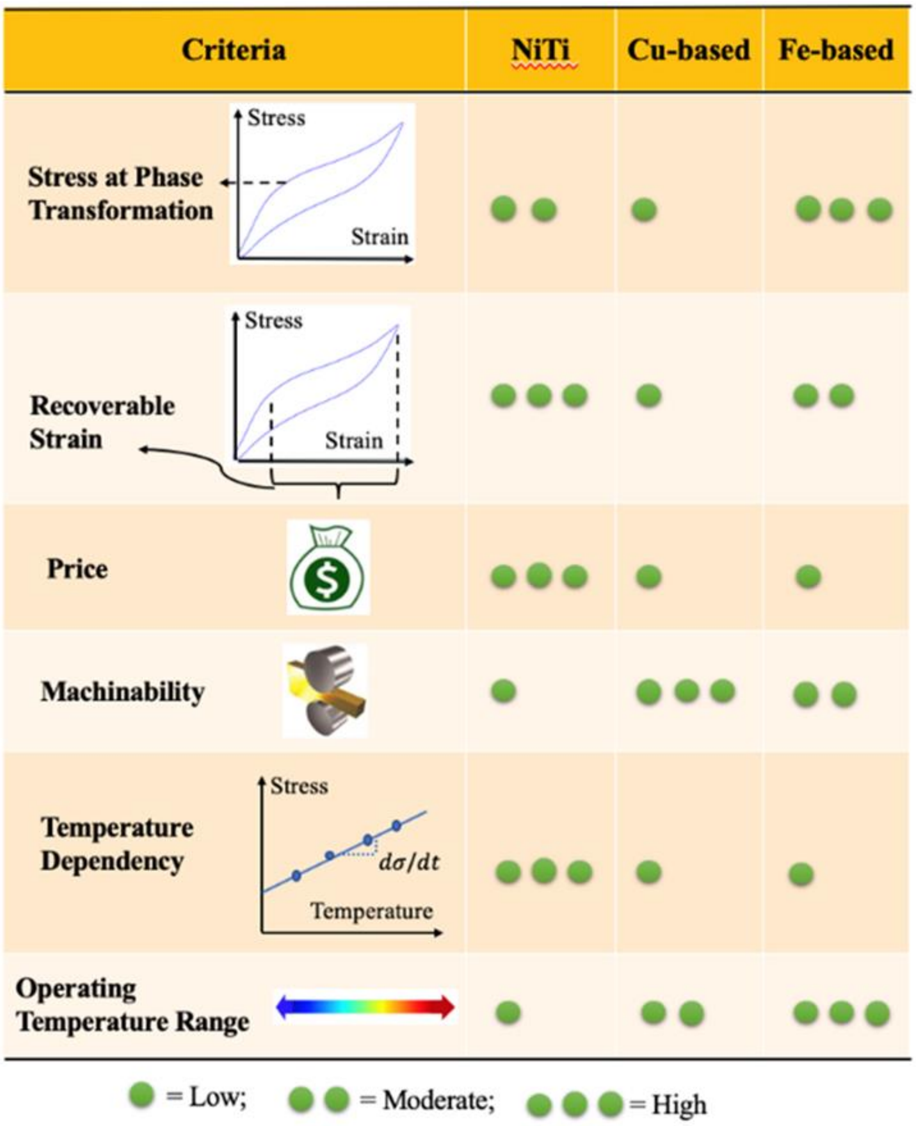

Criteria	NiTi	Cu-based	Fe-based
Stress at Phase Transformation	●●	●	●●●
Recoverable Strain	●●●	●	●●
Price	●●●	●	●
Machinability	●	●●●	●●
Temperature Dependency	●●●	●	●
Operating Temperature Range	●	●●	●●●

● = Low; ●● = Moderate; ●●● = High

Figure 2-4. Relative comparison of the three most commonly used SMAs

2.2.4 Most common forms of SMA products and experimental characterization

Besides being available in different material compositions, SMAs exist in different forms such as wires, cables, bars, or springs. Each type of element has its pros and cons and is suited well to a particular type of application. An SMA element chosen for earthquake engineering application should preferably have (i) high material utilization efficiency from an economic standpoint, (ii) damage tolerance, and (iii) machinability and ease of installation. The most common SMA products are summarized in this section.

2.2.4.1 SMA wires and cables

SMA wires have been the most widely used product in previous studies to develop SMA-based seismic protective systems due to their availability and relatively low cost. Since SMA wires carry only tensile loads, the material is subjected to uniform deformation and thus fully utilized. The mechanical behavior of individual wires has been a major research theme, and it is now well understood [64,95–100]. Available studies in the body of literature concluded that the response of superelastic SMA wires are affected by deformation amplitude, the number of repeated loading cycles, temperature, and loading rate. Some of the practical problems related to the real-life implementation of SMA wires include low force capacity and difficulty in anchoring or end fixing.

SMA cables are relatively new structural elements comprised of multiple strands laid helically in one or more layers around a core. The strands themselves have a center wire around which SMA wires are twined. SMA cables leverage the outstanding mechanical properties of thin wires to carry relatively large axial loads. The cables generally have more considerable tensile stiffness and strength, yet they are compliant in bending and torsion, making them easy to handle. The cables can be manufactured in a large variety of constructions by changing their geometric quantities, such as the diameter of the wires, the number of layers, and the helix angles.

Compared to the extensive characterization of SMA wires, only a few researchers carried out experimental tests to characterize the behavior of SMA cables. Reedlunn et al. [101] tested SMA cables with different layups and confirmed that the SMA cable with 7 x 7 construction could have mechanical responses comparable with that of SMA wires. Ozbulut et al. [102] explored the response of a large diameter SMA cable under different loading amplitudes and rates. Sherif and Ozbulut [103] examined the fatigue behavior of SMA cables. Carboni et al. [104] established a phenomenological model for SMA cables, where the simulations agreed well with the available test result. Biggs and Mas et al. [105] conducted pull-out tests to examine the bond strength between SMA cables and concrete in which the cables are employed as reinforcement. Fang et al. [106] also studied the mechanical behavior of SMA cables with an outer diameter of around 7 mm.

2.2.4.2 SMA bars

Larger size SMA elements such as bars are usually needed to accommodate high force demands in real-world applications. Although SMA bars have not been studied as widely as SMA wires, a number of researchers have examined their mechanical behavior. DesRoches et al. [97] compared the hysteric behavior of SMA bars with different diameters up to 25.4 mm. Fugazza [99] investigated the size effect in SMAs by testing both wires and bars. A common finding obtained from these studies is that both SMA wires and bars can exhibit good SE behavior if properly manufactured and annealed. However, slightly higher residual deformations were observed in bars at high amplitude loadings. Wang et al. [107] studied the tensile performance of SMA bars of original diameters ranging from 8 mm to 30 mm with different heat treatment procedures. Speicher et al. [108] and Fang et al. [109,110] examined the fracture behavior of a series of SMA bars machined into dog-bone shapes with threaded ends.

Other researchers conducted experimental and numerical studies to characterize the torsion or coupled tension-torsion behavior of SMA bars [111–117]. Dolce and Cardone [111] performed torsion tests on bars with round and hexagonal cross-sections. Chung et al. [112] numerically analyzed the responses of circular rods subjected to coupled tension-torsion loading. Mirzaeifar et al. [114] provided the exact closed-form solutions of SMA circular bars under pure torsion. Taheri et al. [115] studied the coupled thermomechanical response of SMA bars and tubes, analytically and experimentally. Reedlunn et al. [116] investigated the isothermal responses of SMA tubes under a series of proportional stretch-twist experiments spanning pure tension to simple torsion to pure compression employing extensive digital image correlation (DIC) measurements.

The bending behavior of SMAs has received increasing scholarly attention more recently. Several researchers have explored the flexural properties of SMAs from the material or mechanical viewpoint [118–122]. Apart from the tension, torsion, and bending properties, there have been also a few studies on the compression and buckling behavior of SMA bars. Rahman et al. [123] explored the characteristics of 2 mm diameter columns made up of SMA under a compression loading-unloading cycle. Pereiro-Barcelo and Bonet [124] experimentally investigated the compression behavior of six 12 mm diameter bars. Watkins et al. [125] performed column buckling tests on SMA bars and tubes with outer diameters of 3.15 mm and 3.18 mm, respectively. Asfaw et al. [126] examined buckling and post-buckling behavior of 12 mm diameter SMA bars by testing a wide range of specimens and considering loading rate effects.

2.2.4.3 SMA springs

SMAs in the form of springs have also been studied for seismic applications. These SMA springs include helical springs, Belleville washer springs, and ring springs. Even though the seismic-tailored application of SMA helical springs is still at its premature stage, a few researchers have utilized them as a component to develop damping devices. Like traditional steel springs, an SMA helical spring can be geometrically described by four key parameters: wire diameter, spring diameter, pitch angle, and the number of active coils indicating the ratio of free length to coil distance. SMA springs can be fabricated from wires or tubes. Annealing, which clearly impacts the mechanical properties of SMA springs, is likely the essential step in the production process [127–131].

Belleville washer springs are another form of SMA springs that are capable of sustaining large loads with a small installation space. Load transfer is relatively even and concentric due to their annular shape, and thus they can have more stable compression behavior than helical springs. Notably, the various combinations (in parallel or series) of the washers can diversify their performance and use. The feasibility of superelastic SMA washers for dampers was first assessed by Speicher et al. [132]. The thermomechanical response of Belleville washers has been studied through experimental and numerical methods [133,134]. Fang et al. [135] performed comprehensive tests on washers with different stack combinations under varying temperature and loading scenarios. SMA ring spring systems have been developed to enhance the “performance-to-cost” ratio of SMA materials. They consist of a number of inner and outer rings assembled to complete a spring. Wang et al.

[136] studied the fundamental load-deformation behavior of individual ring springs. Their test results revealed that the SMA rings exhibited a flag-shaped response with plump hysteretic loops. The rings show reasonable repeatability with an increasing number of cycles, although minor strength degradation accompanied by increasing residual deformation is observed due to transformation-induced fatigue. Figure 2-5 illustrates a schematic representation of the relative material utilization efficiency among the different SMA products.

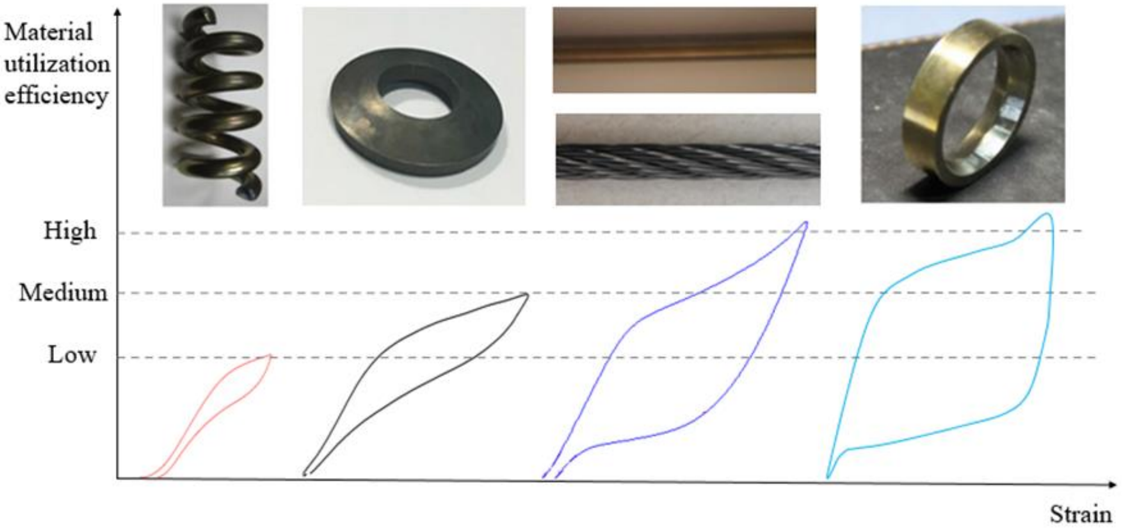

Figure 2-5 Material utilization efficiency SMA helical spring, SMA washer spring, SMA bar/wire, and SMA ring spring [137]

2.3 SMA-based Seismic Dampers

The family of SMA-based dampers and energy dissipators for structural control continues to grow due to increasing interest in self-centering structural systems. Recent advances include new strategies to enhance the energy dissipation capacity of SMAs by coupling them with other supplemental damping elements. Numerous prototypes of SMA dampers have been proposed, numerically studied, experimentally tested, and currently at various development stages. The common constitutive material in all of them is various SMA products: wires/cables, bars, or different springs. In what follows, the literature review on SMA-based dampers is classified according to the form of SMAs (i.e., wires/cables, bars, or springs) used in the device.

2.3.1 Dampers with SMA wires or cables

A number of researchers utilized the inherent damping capacity of SMA wires/cables solely in different dampers. Parulekar et al. [138] designed a device that consists of two concentric pipes that move apart when subjected to load and six SMA wires, each of 1.2 mm diameter, attached between studs connected to the inner and outer pipes. Three of the wires on one side of the device resist tension while the remaining three wires on the other side are slack or vice versa. The device was tested under a sinusoidal cyclic load at different rates and amplitudes to characterize its behavior. Besides, an existing multilinear thermomechanical model was employed to simulate the behavior and validated with the experimental data. In another study [139], the same researchers performed large-scale shake table tests of a 1:3 scaled frame structure model equipped with a similar SMA-based damper installed on a V-bracing configuration. The experimental displacement time histories revealed that the damper reduced the frame response by 40% and 30% for 0.1g PGA and 0.2g PGA excitations, respectively. It was observed that the effectiveness of the damper, as measured by the equivalent damping ratio, decreased as the magnitude of the excitation increased. This was due to the martensitic hardening of the SMAs at higher strains.

Qian et al. [140] developed a re-centering shape memory alloy damper (RSMAD) for the seismic response mitigation of structures. As shown in Figure 2-6, the damper is composed of SMA wires, outer and inner cylinders, a push-pull rod, and other accessories. The SMA wires are the kernel elements that provide both damping and self-centering capabilities. A prototype damper with a stroke of ±9.2 mm was fabricated utilizing Nitinol wires with a diameter of 0.5 mm and length of 115 mm. Different pre-strain levels were applied to the SMA wires, and the damper was tested under various loading frequencies and displacement amplitudes. A modified constitutive model, based on the Graesser and Cozzarelli [141] model that captures the martensitic hardening characteristics of SMA wires was proposed and validated by test data. The efficacy of the RSMAD in controlling the seismic response of building structures was assessed through nonlinear time history analysis. A ten-story steel moment-resisting frame equipped with five or ten SMA dampers in different configurations was analyzed. It was observed that the RSMADs were capable of remarkably reducing structural vibrations, although the location and number of the dampers had considerable influence on the control efficiency.

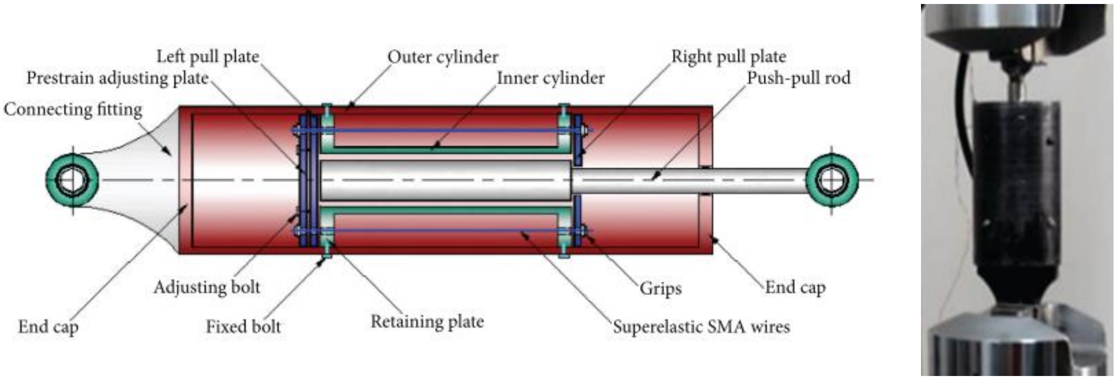

Figure 2-6. Schematics and photograph of RSMAD [140]

Similarly, Soul and Yawny [142] proposed a tension-compression device comprised of coaxial steel tubes transversely crossed by two pins to which and two SMA wires attached, one on each side of tubes. Upon application of external load, a relative displacement between the tubes will occur, and the load is transmitted to the pins at the contact points. The device mechanism is constructed in such a way that regardless of the direction of the applied load, the wires are always subjected to tensile loads. A prototype device was designed using 1.2 mm diameter wires with a nominal member length of 80 mm and tested under different frequencies and incrementally increasing displacement amplitudes. The introduction of pre-straining the wires was shown to be highly beneficial without compromising the self-centering characteristics. Nonlinear time history analysis results showed the effectiveness of the device in limiting maximum and residual displacements by acting as a restrained. In another study [143], the same researchers numerically studied the dynamic response of an idealized structure composed of a mass lying on a PTFE friction layer connected to the ground by the tension-compression device.

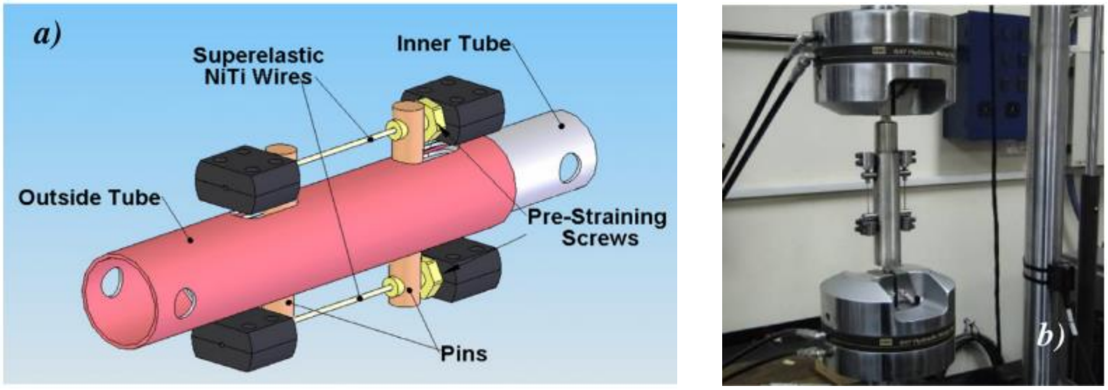

Figure 2-7. Schematics and photograph of a tension-compression device [142]

Since the equivalent viscous damping was obtained only from SMAs, many researchers have explored the development of hybrid dampers with SMA wires/cables. In these dampers, the SMA wires/cables are mainly used for their excellent self-centering characteristics, while a supplemental damping mechanism is used to increase the damping capacity of the device. Several researchers attempted to combine the self-centering capability of SMA wires and the high energy dissipation capacity of metallic yielding dampers. Yang et al. [144] proposed a hybrid device consisting of a set of SMA wires, an energy-absorbing strut made of either mild steel or low strength aluminum, and two freely floating high strength steel tubes, as shown in Figure 2-8. The SMA wires are surrounded by the freely floating high-strength steel tubes, wound by two cylinder-type blocks inside the tubes. An optimal proportion of the SMA wires and energy-absorbing struts was formulated such that the hybrid device exhibits good self-centering capability while maximizing energy dissipation. The performance of the hybrid device was evaluated through numerical analysis of a three-story frame. Results demonstrated that the hybrid braced frame system exhibits comparable energy dissipation capacity to buckling restrained systems while also having excellent re-centering capabilities.

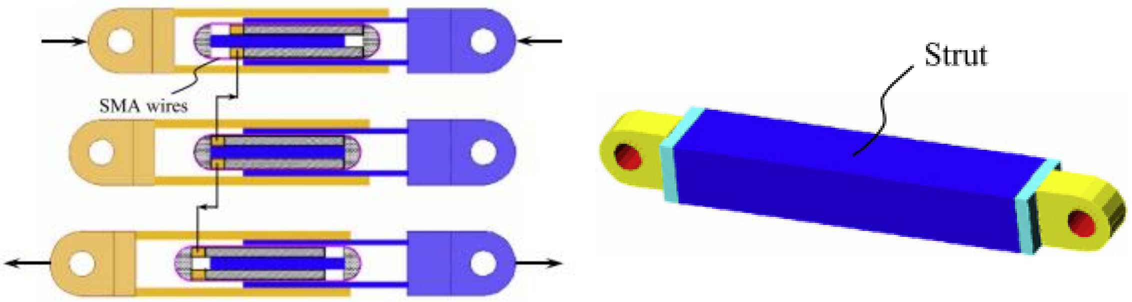

Figure 2-8. A hybrid device proposed by Yang et al. [144]

Jennings et al. [145] explored the effectiveness of a seismic response modification device that combines SMA wires with a mild steel section by hosting it in a scissor-jack brace, which is known for its compact footprint and high displacement magnifications factor. The device was used to develop a seismic retrofit methodology for soft-story wood-frame buildings. Nonlinear time history analysis and full-scale hybrid testing were performed to validate the retrofit design. The study concludes that the proposed retrofit using the SMA-steel device virtually eliminates the soft-story condition and torsional response from the building while meeting inter-story drift criteria set for two limit states: immediate occupancy and life safety. Similarly, Cardone and Sofia [146] investigated the use of SMA-based devices in improving the seismic response of historical buildings equipped with traditional metallic tie-rods.

Viscous or veisco-elastic dampers have also been considered as additional damping components in SMA-based dampers. A few researchers integrated SMA wires with traditional fluid viscous dampers to add self-centering capability and improve their energy dissipation capacity [147–149]. Liu et al.[147] used a typical silicone oil viscous damper as the base component in which several sets of SMA wires were installed on the shell of the damper. Each set is composed of two SMA wires, with one end anchored on the fixed plate and the other on a fixing screw such that the wires can be pre-tensioned by adjusting the fixing screw. The cyclic loading test results indicated that the low damping force produced by the viscous damper alone at low frequency is compensated by the relatively high energy dissipation capacity of the SMA wires at low frequency. Di Cesare et al. [149] proposed a visco-recentring (SMA+VD) device that consists of two viscous fluid energy damping devices and pre-tensioned SMA wires as part of a large research project named

JetPacs (Joint experimental testing on Passive and semi-active control systems). They carried out extensive shaking table tests on a 1:1.5 scaled steel frame equipped either with visco-recentering devices or, for comparison purposes, flexural yielding metallic dampers. A displacement-based design procedure was proposed and validated to evaluate the mechanical characteristics of the SMA+VD. The test results highlighted that the seismic demands on the frame installed with the visco-recentering devices were considerably less than the bare frame.

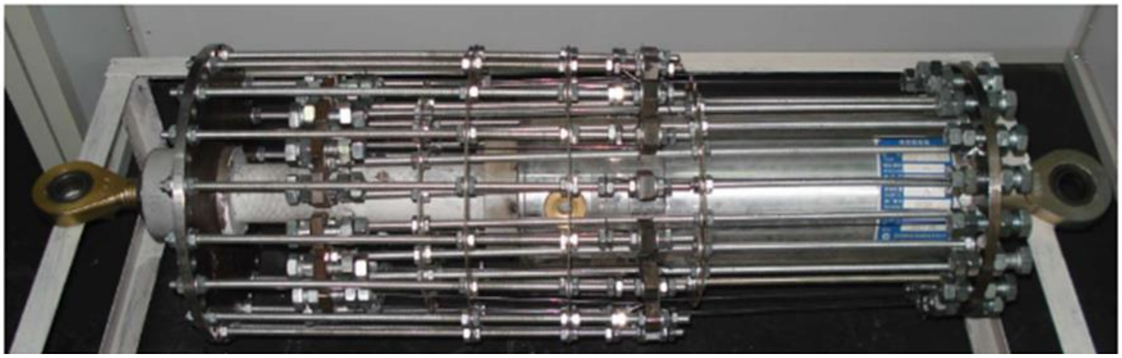

Figure 2-9. SMA-fluid viscous damper [147]

Silwal et al. [150] employed a combination of viscoelastic damper and SMA cables to develop a new energy dissipating device known as the superelastic viscous damper (SVD). This damper consists of two high damped elastomeric compounds sandwiched between and bonded to three identical steel plates and installed SMA cables. Each cable forms a continuous loop; wrapping the loops around the outer two plates improves the compactness and efficiency. Whether the device itself moves left or right, the configuration ensures that the SMA elements will remain under tension. They numerically implemented the SVD to enhance the seismic performance of a six-story steel special moment-resisting frame that exhibits excessive story drifts. The analysis results showed that the hybrid damper is effective in reducing the inter-story drift demands and residual drifts without a considerable increase in peak acceleration demand.

Another mechanism considered for enhancing the energy dissipation capacity of SMA-based dampers has been the friction between two solid bodies sliding to one another. Qian et al. [151] introduced a damper called Superelastic SMA Friction Damper (SSMAFD), which contains pre-tensioned SMA wires and a friction device. The friction device is made of two pairs of steel plates bolted together by high-strength bolts. With a proper design of the friction element and pre-tensioning level of the wires, the device can exhibit simultaneous re-centering and energy dissipation features. The effectiveness of the damper was assessed through shaking table tests of a 1:4 scaled three-story steel frame building with and without SSMAFD under various seismic loading. Their results showed a reduction for major performance indices, such as story displacements, inter-story drifts, and story accelerations of the structural model.

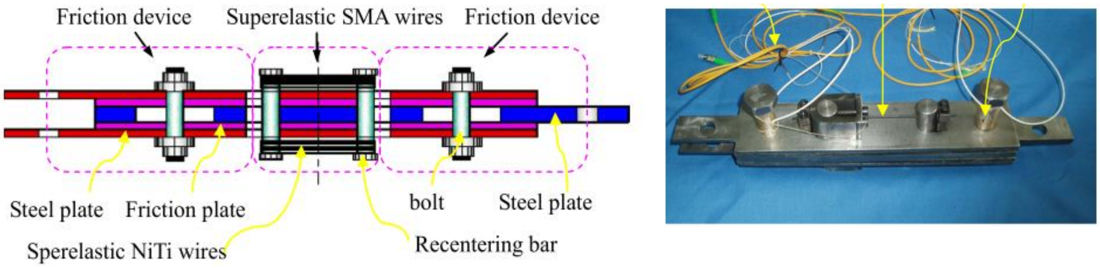

Figure 2-10. Superelastic friction damper (SSMAFD) [151]

Another hybrid device proposed by Li et al. [152] combined the SMA wires with a lead damper. When the proposed Re-centering SMA-Lead Damper (RSLD) is subjected to an external load, there will be a relative movement between the two ends of the RSLD, which will induce shear deformation on the lead and elongates the SMA wire. As a result, the lead under shear and the SMA wire under tension dissipate seismic energy while a compressed spring generates an elastic restoring force. A prototype RSLD consisting of four 0.55 mm diameter SMA wires, each 170 mm long, were fabricated and tested to characterize the hysteretic behavior of the device under different loading rates and displacement amplitude. The test results indicated that the damper revealed adequate energy dissipation capacity and stable hysteresis loops. Numerical analysis of a six-story steel frame building installed with RSLD in five different layouts was conducted to study the influence on structural control. The results from the numerical study concluded that various damper configurations led to different control efficiency.

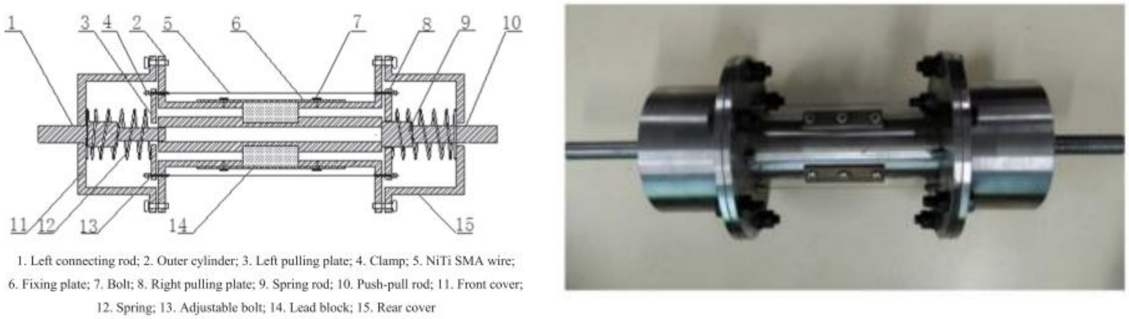

Figure 2-11. Re-centering SMA-lead damper (RSLD) [152]

Alipour et al. [153] proposed an SMA-based damper composed of SMA wires to offer energy dissipation, while a bias spring was incorporated to provide the necessary restoring force. As shown in the figure, the damper employed two damping groups: in which one of them is activated in tension while the other is activated during compression. Each group consists of a pair of SMA wires acting in opposite directions with and without some pre-tensioning. Although SMA wires are tension-only elements, the proposed damper can carry both tension and compression loads. Characterization of individual components and the assembled damper were numerically simulated and validated through monotonic tension-compression tests. The effects of different parameters on the damping ratio of the proposed damper were studied through parametric analysis. It was shown that larger damping values could be achieved if the damper is used at temperatures close to the austenite finish temperature of the wires. Moreover, the damping ratio increases with a decrease in the stiffness of the bias spring.

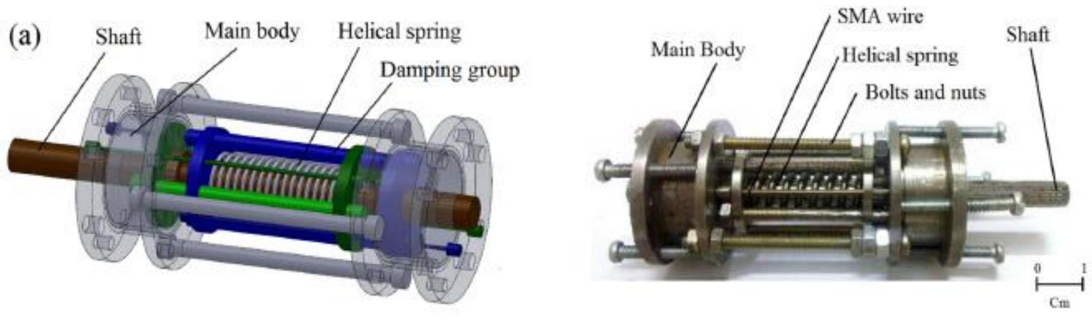

Figure 2-12. Schematic and photograph of the SMA-based damper [153]

Researchers have also employed the concept of deformation amplification to SMA-based devices. Li et al. [154] proposed a Re-centering Deformation Amplified SMA Damper

(RDASD) that can multiply the relative deformation based on actual demands and amply exploit the energy dissipation capacity and re-centering feature of SMA wires. When an external load is applied to the damper, it will cause relative movement between the two ends of the RDASD. A force-transferring lever mechanism amplifies this displacement, and then the end of the lever pulls the SMA wire. During this entire cyclic process, the wires supply both energy dissipation and re-centering capabilities. A prototype RDASD specimen was fabricated and tested under cyclic loading tests. The damper exhibited steady hysteretic behavior with double-flag-shaped hysteretic curves. Moreover, nonlinear time history analysis results revealed that the RDASD could effectively reduce structural dynamic responses.

Zhang et al. [155] proposed a Deformation-Amplified SMA-Friction Damper (DASMAFD), which consists of SMA wires combined with a friction component in parallel. A lever mechanism is implemented to amplify the deformation carried over from the structure to the SMA wires. Besides, a mechanical system is employed to regulate the friction force of the damper. A specimen was fabricated and tested to characterize the behavior of the DASMAFD in two scenarios, i.e., the deformation of the SMA wires was: (1) equal and (2) double the input deformation. Regarding the ratio between the friction force and the martensitic transformation starting force of the SMA wires, five different cases (0,0.25,0.5,0.75, and 1) were considered. Test results indicated that by increasing the deformation amplification ratio, the self-centering and the energy dissipation capabilities of the damper were improved. However, an increase in friction ratio further improved the energy dissipation capacity at the cost of self-centering. The performance of DASMAFD in mitigating the seismic response of a ten-story RC building and the effects of key design parameters (namely deformation amplification ratio and friction ratio) on its performance was evaluated through nonlinear time history analyses. Analysis results revealed the efficacy of DASMAFD when compared with other dampers.

Figure 2-13. 3D rendering and photograph of DASMAFD [155]

An innovative Self-Centering Negative Stiffness Damper (SCNSD) made of SMA wires and prepressed springs arranged in parallel, as shown in Figure 2-14, was invented by Liu et al. [156]. The passive negative stiffness induced by the pre-pressed springs enhances the damping capacity of the damper. When the piston travels upward, the lower part of the SMA wire is pulled to provide a superelastic force while the pre-pressed springs generate a push force that makes the central connector travel upward, which implies a negative stiffness behavior. Similarly, when the piston travels downward, the upper part of the SMA wire provides a self-centering force, and the pre-pressed springs still exhibit negative stiffness. An analytical model of the damping force was instituted, and verification tests were performed. The influence of the negative stiffness was studied by parametric analysis. It was found that an increased equivalent damping ratio can be achieved for a single degree of freedom (SDOF) system with the SCNSD. Moreover, numerical simulation results of the system subjected to earthquake excitations demonstrated that the damper remarkably decreased the peak acceleration and displacement responses.

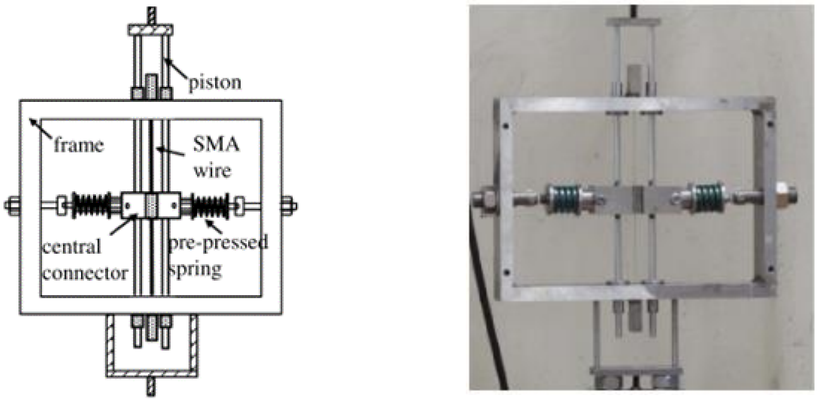

Figure 2-14. Self-centering negative stiffness device (SCNSD) [156]

2.3.2 Dampers with SMA bars

Most of the early efforts to develop SMA-based seismic devices mainly utilized SMA wires due to their better affordability and availability. This led to most of these devices being developed with SMA wires to remain small scale and exploratory. Nevertheless, there have also been several studies where SMA bars were used to develop SMA dampers with a reasonably large force capacity for seismic applications.

Wang and Zhu [157] proposed a device that benefits from the compression behavior of the SMA bar placed between buckling restraining plates. They examined the cyclic tension-compression behavior of a prototype specimen fabricated from a dog-bone shape SMA bar with a reduced segment length of 100 mm and a diameter of 6 mm. An asymmetric stress-strain curve was observed, wherein the compressive stress was higher than the tensile stress at the same strain level. It was concluded that the strain rate had minimal effect on the equivalent viscous damping ratio within a frequency range of 0.1 Hz to 2 Hz.

Qiu et al. [158] employed a group of SMA bars with a buckling restraining plate (BRP) to design a self-centering damper with symmetrical hysteretic behavior for practical applications. The proposed damper implemented two sets of SMA bars that act simultaneously. When one set is subjected to tension, then at the same time, the other set is in compression. Thus, enable symmetric response. First, they tested four individual SMA bars with BRPs in which the original bars, which had a diameter of 12 mm, were milled to two types of cross-sections: 6 mm diameter circular section and 2.4 mm thick flat section. The BRP was constructed by placing a steel plate, one on each side of the SMA bar’s reduced segment with an approximately 1 mm gap, and firmly joined together via high strength bolts. Then, they fabricated two small-scale specimens, one with round bars and the other with flat bars, and tested to validate the design concept. The test results revealed flag-shaped hysteretic responses with satisfactory self-centering capability, moderate energy dissipation, and symmetrical tension-compression responses. While the specimen with flat bars underwent initial bar fracture at the 6% strain cycle, the same failure mode occurred in the specimen with round bars at a 10% strain cycle. A numerical investigation was carried out to examine the efficacy of the proposed damper in seismic response mitigation.

Qiu et al. [159] used combinations of SMA bars and traditional steel yielding energy dissipators in parallel to develop a new SMA-steel damper. It is comprised of three elements: self-centering (SC) element enabled by SMA bars, added damping (AD) element made of bending steel plates, and framing element. Both the SMA bars and the steel plates are connected to the frame element such that they deform concurrently when the damper is subjected to external loads. Furthermore, the components are arranged in such a way that the bars are always in tension when the damper deforms, and the load transferring mechanism induces out-of-plane flexural deformation by which energy is dissipated through the yielding of the steel plates. A prototype SMA-steel damper was assembled utilizing a pair of SMA bars and four steel dissipators. The virgin bars had a diameter of 12 mm and were milled to dog bone-shaped (the reduced section had a diameter of 8 mm) and threaded ends for bolted connection. Each steel dissipator consisted of a bending plate with a diamond hole at the center and base plate. The dissipators were made of 5 mm and 10 mm thick bending steel plates to study the effects of altering the share of the AD element on the overall response of the SMA-steel damper. The test results indicated that the damper showed stable and symmetrical behavior with no strength or stiffness degradation. The authors reported that by adding the steel dissipators made of 5 mm and 10 mm thick bending plates with SMA bars, the equivalent damping ratio has increased by approximately 10% and 20%, respectively. Approximately 90% and 60% of the applied deformation were recovered, respectively. It was observed that the damping is increased at the expense of partially losing the SC capability. A numerical model of the SMA-steel damper was made in finite element software and experimentally validated. The validated model was employed to investigate the influence of some core design parameters, namely the thickness of the bending steel and the diameter of the SMA bars. The parametric study results highlighted that the SC capability would be exhausted by increasing the damping; however, the trend will be stabilized in the end.

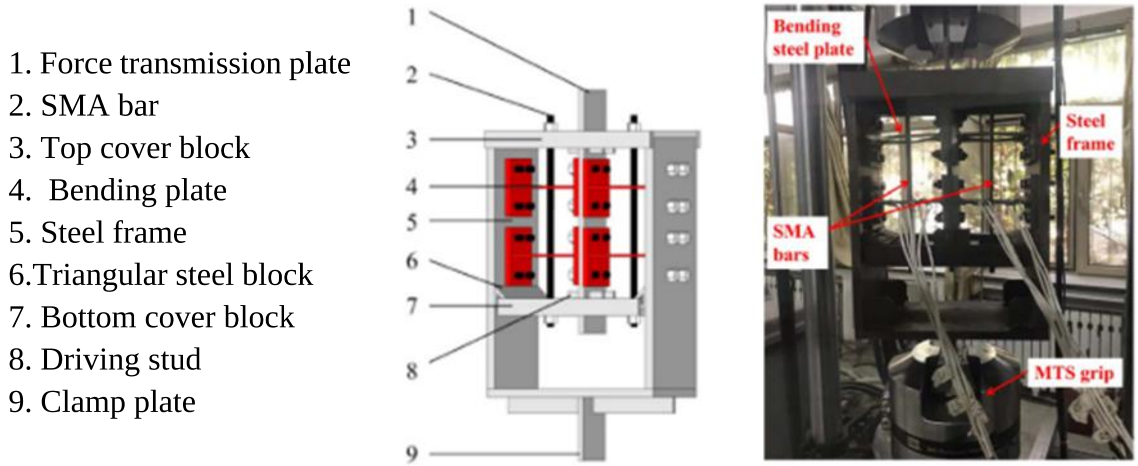

Figure 2-15. SMA-steel damper [159]

Naeem et al. [160] proposed a hybrid energy dissipation device containing conventional steel slit damper and SMA bars. The bars are assumed to resist tension only; hence, two bars were placed in an X shape on each side of the slit damper. The effects of the size of SMA bars on the re-centering behavior of the device were explored through nonlinear time history analyses of a single-story steel moment frame with a hybrid slit-SMA damper. The parametric study results showed that the residual displacement and the base shear decreased as the size of the SMA bar increased. Numerical simulations were also carried out to validate the seismic performance of the hybrid slit damper and compare it with the steel slit damper. They found that the hybrid dampers reduced the maximum inter-story drift and roof displacement by 68% and 48%, respectively, compared to that of the structure equipped with conventional steel slit dampers. Besides, more than 80% reduction was identified in the residual roof deformation. Noureldin et al. [161] investigated the seismic performance of SMA-slit hybrid damper using fragility and life-cycle cost (LCC) analyses of three prototype ordinary moment-resisting frames, i.e., three, five, and eight stories. From the fragility curves, it was observed that the frames retrofitted with the hybrid dampers had the least probability of reaching any limit states (immediate occupancy, life-safety, and collapse prevention) compared to the bare frames and frames installed with the steel slit dampers. Although the initial cost of the frames equipped with hybrid dampers was higher than those with steel slit dampers due to the added SMA cost, it was reported that the LCC of the former was the lowest for a 50-year expected service life. Incorporating SMA bars to the steel slit dampers reduced the LCC of the model structures by 21%-26% for the three, five, and eight-story frames.

Figure 2-16. Configuration and installation scheme of steel slit-SMA hybrid damper [161]

Jalaeefar and Asgarian [162] presented a hybrid device that utilizes an SMA bar and steel bar in parallel to increase the damping capacity of the SMA bar alone while maximizing the recovery of the inelastic steel deformation. The device is made up of two thick rigid plates at each end connected using 8 mm diameter bars as the main loading resisting elements of the device. The space around the bars was filled with high-strength cement grout encased with a steel tube to prevent the bars from buckling. It is necessary to determine the right proportion of SMA to steel to get optimum re-centering and energy dissipation.

Choi et al. [163] studied the hysteretic properties of SMA bars subject to flexure coupled with tension and compression to open a way of incorporating them in damping devices. They considered two types of SMA bars in five different layouts: (1) single superelastic, (2) single martensite, (3) superelastic-superelastic (SS), (4) superelastic-martensite-superelastic (SMS), and (5) martensite-superelastic-martensite (MSM). A typical SMA bar had a dumbbell shape with an overall length of 270 mm, such that the middle segment was

150 mm long with a diameter of 16 mm. Each end of the bar was 50 mm long, with a 20 mm diameter connected to the middle portion through a 10 mm long transition part. The end parts were placed in a custom-designed clamping device by which the bending and axial loads were applied. The test results indicated that the MSM exhibited the most remarkable energy dissipation capacity, while the SMS demonstrated good performance considering both damping and re-centering capabilities.

2.3.3 Dampers with SMA ring springs

The advantages of SMA ring springs such as high-material utilization efficiency and ease of installation, have attracted the attention of several researchers for the development of new seismic devices. Wang et al. [164] introduced a piston-type device that consists of (i) an outer cylinder, (ii) an inner shaft, (iii) an SMA ring spring system, and (iv) two cover plates and a tightening nut. The ring spring system is made up of SMA outer rings and high strength steel inner springs stacked in alternations with mating taper faces. The different components were designed and strategically assembled such that the SMA ring springs are always in compression irrespective of the direction of the damper movement. They conducted quasi-static cyclic tests on individual SMA ring springs to examine their mechanical behavior. Then, a large-scale prototype damper was fabricated using a total of eight SMA outer rings and tested. The results highlighted that the damper exhibited a stable flag-shaped hysteretic response with an equivalent viscous damping ratio that ranges up to 18.5% and no residual displacement.

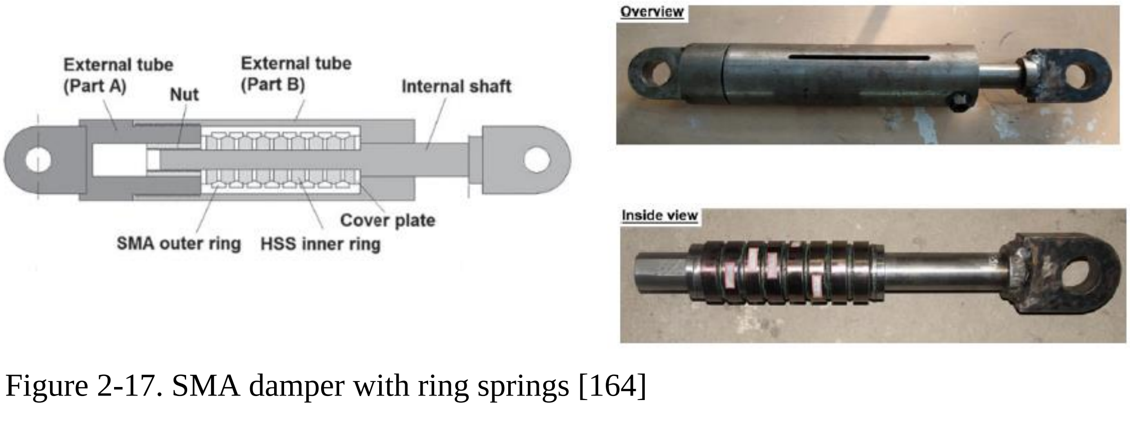

Figure 2-17. SMA damper with ring springs [164]

Choi et al. [165] investigated the use of SMA rings as an energy dissipating device with re-centering capability. They conducted cyclic tests on single and dual SMA rings in five different combinations of martensitic and superelastic rings. A typical ring specimen had a thickness of 10 mm and an outer and inner diameter of 80 mm and 60 mm, respectively. The specimens were cut from an SMA plate using a wire-cutting machine with the designed dimensions. A custom-made T-shaped fixture was fabricated to hold the SMA rings for the application of cyclic loads. The experimental results showed that the dual ring devices exhibited almost perfect symmetric behavior under pulling and pushing actions. They identified that the use of martensitic SMA could increase the damping ratios of the ring systems while the use of superelastic SMA could enhance the self-centering capacity. Numerical models of the SMA ring systems were developed in a finite element framework and validated through experimental test results. The validated models were implemented to examine the effects of the thickness ratio on the symmetric behavior of the SMA ring system.

2.3.4 Dampers with SMA plate

Although most of the proposed SMA-based devices utilized the uniaxial behavior of wires, bars, or springs, a few researchers have explored the potential use of SMAs under other loading conditions such as the flexural for the development of seismic control devices. Wang and Zhu [166] conducted numerical and experimental studies on superelastic SMA U-shaped Damper (SMA-UD), which adopted a similar configuration with conventional steel U-shaped flexural plates. It is made of a Nitinol plate of desired thickness and width bent into a U-shape in which the tails of the two straight parts are bolted to top and bottom cover plates, which in turn can be connected to adjacent structural members. The SMA-UD dissipates energy by converting the shear deformation between the two parallel legs into the damper’s flexural deformation under cyclic loading. A specimen consisting of two groups of SMA-UDs placed symmetrically in a rigid steel frame was fabricated and tested under quasi-static cyclic loading protocol with an incremental displacement amplitude. The test results demonstrated stable and nearly symmetrical flag-shaped hysteresis loops with excellent self-centering capability in several loading cycles. It was found that the strain rate had a negligible effect on the cyclic performance of the SMA-UD. The mechanical behavior of the damper was further examined through finite element simulations.

Hu [167] carried out finite element simulations of SMA slit dampers of various geometric configurations and compared their cyclic behavior with conventional steel slit dampers. Wang et al. [168] examined the feasibility of using superelastic SMA angles as a self-centering device for potential seismic applications. They conducted cyclic loading tests on an L69 mm x 61 mm x 6 mm SMA angles cut from a 15 mm wide Nitinol plate. A total of three specimens, each consisting of two SMA angles installed symmetrically in a stiff steel fixture, were tested under three different loading protocols. The test results highlighted that SMA angles could offer good self-centering and moderate energy dissipation. It was observed that the specimen tested under cyclic tensile loading with incremental amplitude exhibited significant strength degradation in “yield” strength. However, from observation of other specimens, the authors suggested mitigation strategies such as training the SMA angles with a few cycles before being used or inclusion of reversed compressive loading. Thus, the hysteresis loops will stabilize, accompanied by minimal strength degradation and residual deformations. They also conducted finite element analyses to better understand the cyclic response of SMA angles.

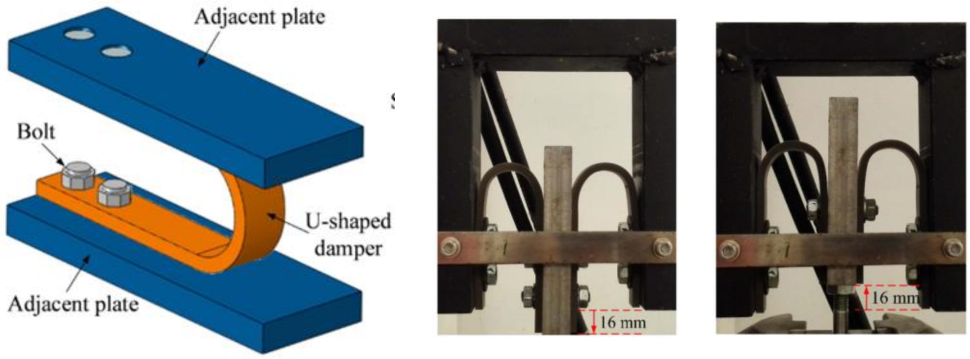

Figure 2-18. SMA U-shaped damper (SMA-UD) [166]

2.4 SMA Bracing Systems

There has been no clear distinction between the definitions of SMA-based dampers and SMA-based bracing systems in the literature. Note that the SMA-based dampers discussed in previous section can be installed into frame buildings using various rigid braces such as chevron or diagonal braces. However, these dampers can also be used in other structural systems without the need for bracing systems. This section reviews previous studies on SMA-based braces developed as lateral load resisting systems in frame structures.

2.4.1 Braces with SMA wires or cables

Several studies have employed groups of SMA wires or SMA cables to develop various types of seismic braces. Qiu and Zhu [169] performed a series of shake table tests on quarter scaled two-story one-bay steel frame equipped with SMA braces (SMAB) under incremental seismic intensity levels. The kernel component of the brace is essentially a device that consists of two sliding steel blocks, two steel rods, and two groups of *NiTi* wires with a diameter of 1 mm. The SMA wires were wrapped around the steel rods at each end that can travel through slots on the steel blocks. When the device is subjected to an external load, the two sliding blocks tend to move away from each other, causing elongation of the SMA wires as one steel rod moves with the outer block while the other rod is constrained by the inner block. The required full length of the brace was achieved by welding a steel tube at each end of the SMA device such that the brace can be connected to the frame via gusset plates. Two SMABs of different force capacities were fabricated and cyclically tested prior to their installation in the braced frame and after completing the shake table tests. The braces exhibited typical flag-shaped hysteresis loops and provided a damping ratio of 5% and a large “post-yield” stiffens ratio of 0.15. However, low initial stiffness was observed due to loose wire loops and the backlash of the assembled SMABs. Their shake table tests and numerical analysis results demonstrated that the SMAB could sustain strong earthquakes without severe damages, performance deterioration, or permanent deformation of the frame. In another study [170], the same researchers proposed a performance-based seismic design method for steel braced frames equipped with the SMAB.

Speicher et al. [171] explored an articulated quadrilateral (AQ) bracing system with the right balance of re-centering and energy dissipation through a combination of SMA wire bundles in parallel with steel C-shaped elements. One of this system’s unique features is that the parts within the AQ can be in tension or compression, while all the parts outside the AQ are tension-only. To determine the contributions of each component and investigate the performance of the bracing systems, they carried out experimental tests on frames braced with three different components of the bracing system, i.e., SMA wire bundle only, C-shaped damper only, and combined SMA wires in parallel with C-shaped damper (PARA). The test results illustrated that the SMA-only bracing system showed excellent self-centering ability, with residual drifts less than 0.1% after the frame was pushed to a 3% story drift. The PARA system exhibited increased damping with an expense of complete re-centering capacity. The frame had residual drifts of 0.5% after being pushed to a 3% story drift. Both SMA-only and the PARA systems had a slight loss in strength and stiffness after multiple cycles. From the analysis of a seven-story building subjected to twenty far-field ground motions, the study found that the SMA and PARA systems performed well in terms of inter-story and residual drifts. Furthermore, the systems effectively reduce the likelihood of forming a soft story by distributing the drifts more evenly over the height of the structure.

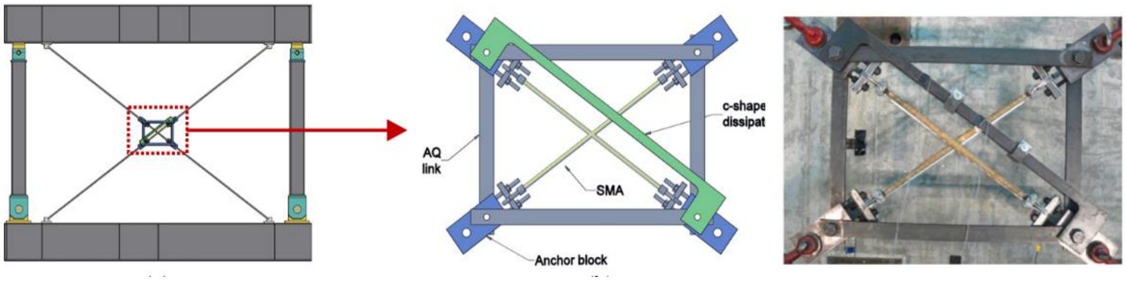

Figure 2-19. AQ bracing system with SMA and C-shape elements [171]

Kari et al. [172] designed and numerically studied a Self-Centering Buckling Restrained Brace (SCBRB) by adding sets of pretensioned SMA wires to conventional buckling restrained brace (BRB). By doing that, the SMA wires overcome the lack of re-centering capability in the BRB while taking advantage of its significant energy dissipation capacity. They carried out a nonlinear time history analysis of four steel moment-resisting frames (two new designs and two retrofits) installed with either SCBRBs or BRBs. Their results demonstrated that frames equipped with SCBRBs exhibited smaller maximum inter-story drifts and considerably smaller residual inter-story drifts than frames incorporating BRBs. Varughese and El-Hacha [173] investigated a tension-only brace that utilizes SMA wires for seismic retrofit applications. They experimentally compared the seismic performance of an SMA braced frame (SMA-BF) with a control frame (CBF) in terms of (i) self-centering, (ii) energy dissipation, and (iii) the ability of the system to reach a target drift of 4%. The SMA-BF was fabricated from forty-four SMA wires with a diameter of 2 mm placed on each face of the steel member and connected to it with a custom-made anchor. The CBF system was made of a mild-steel fuse-type yielding plate. In both cases, the braces were arranged in an X-shaped configuration. The specimens were cyclically tested failure. The test results revealed that the residual strains at 1% drift were 0.41 % and 0.04% in the CBF and SMA-BF systems, respectively, indicating the latter had a significant self-centering capability. It was observed that the SMA wires were not fully utilized due to slippage of the wires inside the anchor; as a result, the amount of energy dissipated in the SMA-BF was very small compared to that of the CBF.

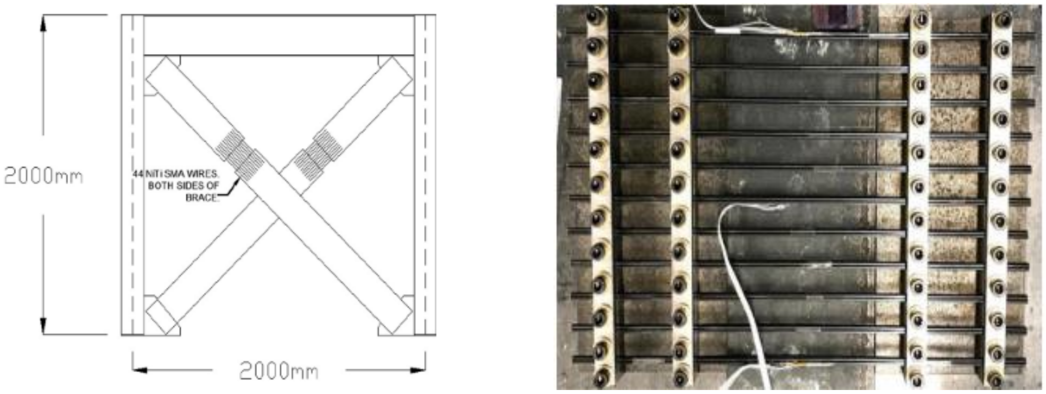

Figure 2-20. Schematic and photograph of SMA-reinforced braced frame (SMA-BF) [173]

SMA cables have been recently implemented in seismic braces to meet the large size demand for practical applications. Shi et al. [174] proposed an SMA-based self-centering bracing system to enhance the seismic performance of steel frame buildings. It consists of: (i) an outer member made of steel box section, (ii) steel I section inner member with an extended web at one end, (iii) SMA cables, (iv) two end plates, (v) a connection plate welded to one end of the outer member, and (vi) two guide members. The inner member is laid concentric to the outer tubular member while the SMA cables are connected to the endplates through a unique anchoring mechanism. The endplates can freely move under the guidance of the inner member. They designed the bracing system in such a way that the SMA cables always work in tension even if the brace itself is subjected to pull or push actions. When it is pushed, the inner member slides to the right and push the right end plate away while the left end plate is kept in place by the outer member. This induces elongation in the SMA cables. Conversely, when the brace is pulled, the reverse will happen. They evaluated the seismic performance of a four-story steel frame building installed with the proposed SMA bracing system through a probabilistic framework. It was found that the SMA bracing system can significantly improve the residual inter-story drift. In a companion study [175], the authors explored the effects of SMA brace design parameters and the ultimate state of SMAs on the seismic and collapse performance of SMA braced steel frame structures. Furthermore, they assessed the seismic collapse performance of steel moment-resisting frames with and without the SMA bracing system under main-shock-after-shocks sequences through a probabilistic hazard framework [176].

Dong et al. [177] presented a Self-Centering Energy Dissipative Brace (SMA-SCEB) that utilizes SMA cables and a friction system. They conducted cyclic loading tests to validate the hysteretic behavior of the SMA-SCEB. Subsequently, the seismic response of steel frame, steel frame braced with SMA-SCEB, BRB, and SCEB with Basalt Fiber Reinforced Polymer (BFRP) cables were compared through numerical analysis. It was highlighted that the SMA-SCEB could significantly reduce the peak drift ratio and residual drift. Chen et al. [178] combined pre-tensioned SMA cables with supplemental Variable Friction Devices (VFDs) to develop a new self-centering brace called as the Variable Friction Self-Centering Energy Dissipation Brace (VF-SCEB). The friction interface of the VFD is designed with certain groove angles, as opposed to flat interfaces in traditional friction devices. The different components of the VF-SCEB, such as inner and outer tubes, are arranged in a way that relative movement between them leads to elongation of the SMA cables and concurrently mobilizes the VFDs. Therefore, a symmetric behavior of the brace was achieved in either tension or compression loading. The shape of the hysteretic curve could be easily adjusted by tuning the design parameters of the SMA cables and the VFDs. A proof-of-concept VF-SCEDB specimen was manufactured and tested under an incremental displacement amplitude of up to 20 mm. The test results showed that the VF-SCEDB exhibited high energy dissipation efficiency without compromising the self-centering capability. They carried out a system-level analysis of three-story concentrically braced steel frames equipped with different types of self-centering braces, including the VF-SCEDBs. The numerical results highlighted that the proposed brace could more effectively reduce the peak deformation and control the residual deformation, and mitigating inter-story drift concentrations.

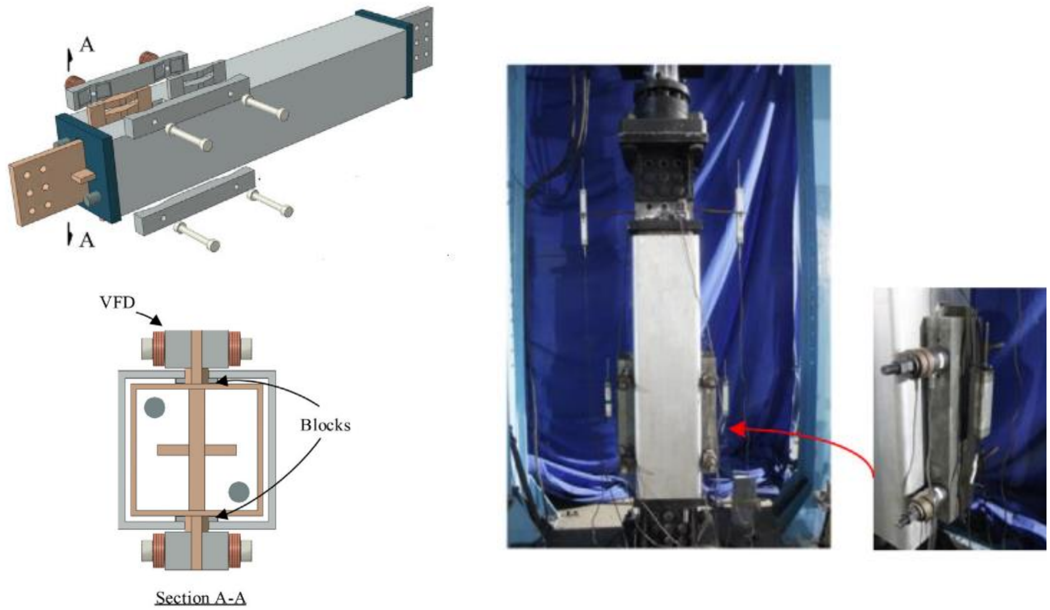

Figure 2-21. Assembly and photograph of VF-SCEDB [178]

2.4.2 Braces with SMA bars

A high-performance Self-Centering Buckling Restrained Brace (SC-BRB) that couples the dependable energy dissipation of a BRB with a self-centering mechanism was developed by Miller et al. [179]. The self-centering mechanism is composed of concentric steel tubes compressed by freely moving anchorage plates secured together with pretensioned SMA bars so that the bars stretch when the brace is either in tension or compression. Two large-scale SC-BRB test specimens with different BRB core dimensions and material properties were designed, fabricated, and tested under standard cyclic loading procedures. The experimental results illustrated that the overall performance of the SC-BRB was promising as quantified by equivalent viscous damping, residual deformation, and cumulative and maximum deformation demands on the BRB core. It was observed that the BRB and SMA systems offer built-in redundancy; as such, the brace holds load-carrying capacity even after one of them failed. The study concluded that the ability of the SC-BRB to fully recover the imposed deformation was related to the ratio of the SMA pre-tension to the BRB core yield strength. Eatherton et al. [180] conducted comprehensive computational studies to propose the SC-BRB design procedure and validate the anticipated performance of buildings equipped with the brace. An analytical model was created and calibrated to reproduce the experimental responses of the SMA and BRB components, including a new material model that captures the accumulation of residual deformation during cyclic loading. The model was proved to simulate the experimental responses of the tested SC-BRB. Then, the validated model was implemented to simulate 147 SC-BRB configurations and conduct an extensive parametric study to examine the effects of key design parameters on the hysteric behavior of the brace. In the second part of the study, the seismic response of fifteen prototype buildings with varying stories (3, 6, and 9) designed with SC-BRB frames was analyzed to provide guidance for the proportioning of SC-BRBs to get suitable seismic performance.

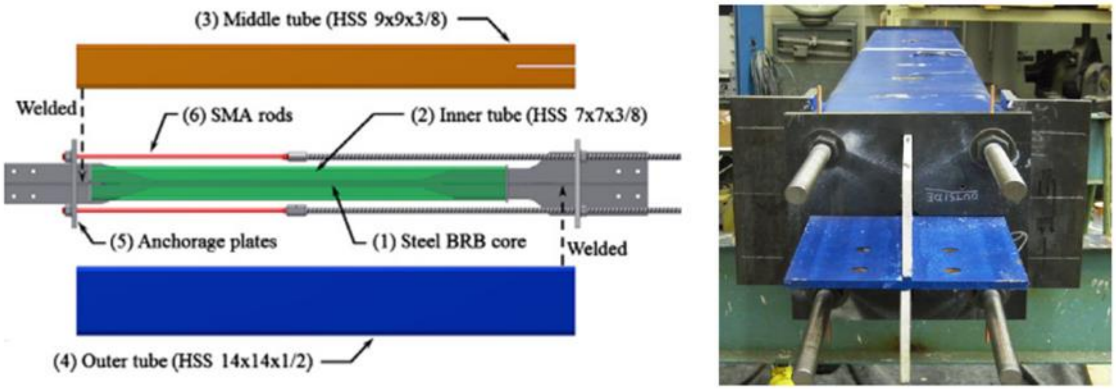

Figure 2-22. Components and photograph of SC-BRB [179]

Cortes-Puenters and Palermo [181] proposed a tension-only SMA brace intended to enhance the seismic performance of sub-standard short RC shear walls by installing externally in an X-shape configuration. It consists of an SMA bar placed at the brace center and connected to rigid hollow structural steel elements. The length of the SMA bars is determined to exploit the range of deformation recovery effectively, and buckling is inhibited in the brace through a mechanism that frees up compressive stresses. Experimental tests were carried out on two SMA braces, one with superelastic effect and the other with shape memory effect, and two companion tension-only steel braces. Finite element analysis results of short RC walls retrofitted with the proposed braces indicated that the walls experienced increases in strength, energy dissipation, and re-centering, as well as a decrease in stiffness and strength degradations. Other researchers have explored similar seismic retrofitting schemes of gravity load designed RC buildings [182].

2.4.3 Braces with SMA ring springs

Building on the bracing system proposed by Speicher et al. [183], Gao et al. [184] investigated the feasibility of ring-shaped SMAs to a bracing system through both experimental and analytical studies. They developed a cross-braced system comprised of an SMA ring at the center and four tension-only cable assemblies anchoring the SMA ring to a frame, which makes it applicable to both new construction as well as upgrading existing structures. A prototype bracing system was designed, fabricated, and tested to evaluate its seismic performance. Compared with two previously developed SMA-based systems, the cross-braced lateral force resisting system performed better as measured by the lateral strength, energy dissipation, damping, and self-centering capability.

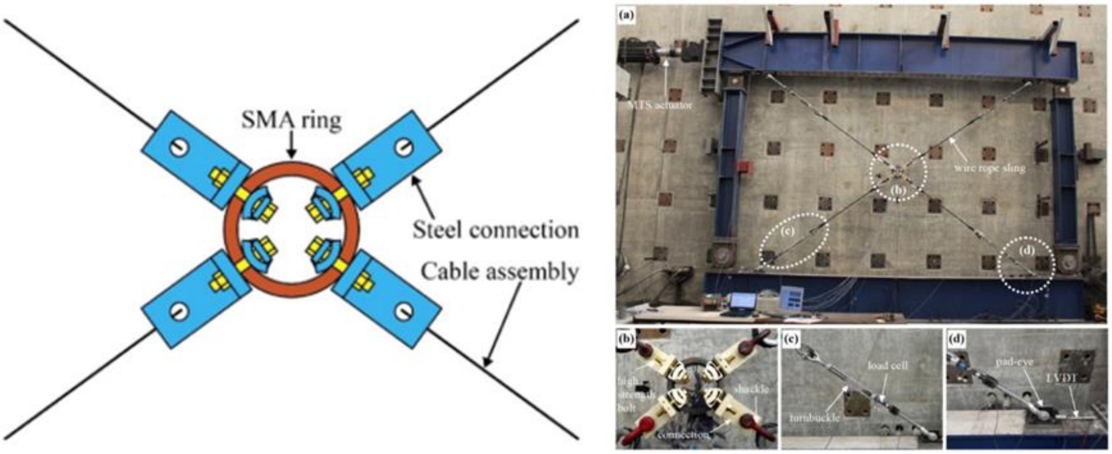

Figure 2-23. A seismic bracing system based on SMA ring [184]

2.5 SMA-based Smart Isolators

During earthquakes, base isolation systems have proven to be effective in mitigating the seismic response of civil structures. SMAs have become essential materials in the field of seismic isolation. SMA-based isolation systems reported in the scientific literature include many types of devices. Analytical, numerical, and experimental studies have been conducted to characterize their seismic performance and the isolated structure subjected to seismic loads. These studies are reviewed in this section. The isolation devices are grouped by the form of SMA product, i.e., wires or cables, bars, plates, and springs. Since more than 90% of SMA-based isolation devices are made of SMA wire/cables, for the sake of discussion, they are further classified into two main categories: elastomeric (based on rubber-like material flexibility and viscous damping) and sliding (based on friction properties).

2.5.1 Seismic isolators with SMA wires/cables

2.5.1.1 SMA-based elastomeric isolation bearings

Ozbulut and Hurlebaus [185] numerically investigated the efficacy of an SMA-Rubber-based (SRB) isolation system to protect highway bridges against near-field earthquakes. The SRB is composed of a laminated rubber bearing and a supplemental device made of several loops of SMA wires wrapped around two wheels. The latter provides extra energy dissipation and self-centering functionality. The sensitivity of the seismic response of a multi-span bridge isolated by an SRB isolation system was examined considering several critical design parameters of the SRB, including ambient temperature changes. A neuro-fuzzy model, developed and experimentally validated by the same researchers in a separate study [186], was implemented to realistically simulate the temperature and loading rate-dependent behavior of the SMA wires. The analysis results indicated a trade-off between displacement and acceleration responses of the deck and the base shear for an increasing value of the forward transformation strength of the SMA wires. The authors suggested that ambient temperature change should be considered during the design of the isolation system as it impacts the response of the isolated bridge considerably.

Bhuiyan and Alam [187] evaluated the seismic performance of a three-span continuous bridge isolated by two types of isolation bearings: High-Damping Rubber Bearing (HDRB) and an SMA-based rubber bearing (SRB). The SRB is made of conventional Natural Rubber Bearing (NRB) wrapped around by SMA wires in the loading direction. Two alternative forms of SMA wires were considered: Nitinol and Cu-based SMAs. The study implemented an advanced strain rate-dependent constitutive model to simulate the mechanical behavior of the HDRB, while simplified analytical models were adopted for the NRB and SMA wires. The numerical results demonstrated that the SRBs satisfactorily control the residual displacement of the deck and the pier displacement for moderate earthquakes; however, the SRBs were not effective under strong earthquakes. Comparative analysis revealed that the model fitted with SRBs experienced significantly higher deck and bearing displacements as well as deck acceleration compared with that of the HDRBs. The study highlighted that the choice of the type and simulation technique of isolation bearings has a noticeable influence on the seismic response of the bridges.

Figure 2-24. Schematics of HDRB and SRB [187]

The efficacy of SMA-based Rubber Bearing (SMARB) in seismic vibration mitigation of buildings subjected to near-fault ground motions having long-period velocity pulses was compared with Lead Rubber Bearing (LRB) by Gur et al. [188]. The SMARB adopted two alternative configurations: SMA wire wrapped around the rubber bearing along the direction of ground motions similar to [187] and SMA cable or bar installed in parallel to the isolator raft and the base on both sides. The isolation efficiency of the SMARB and LRB was assessed by analyzing the change in peak response quantities under different ranges of superstructure-isolator parameters and different earthquake intensities and frequency contents. The analysis results demonstrated that the use of SMARB led to considerable reductions of superstructure accelerations and significant reductions of both the peak and residual displacement of the bearings over the application of LRB. It was noted that the efficiency of the SMARB increased as the earthquake intensities increased (higher PGAs) as well as for ground motions with long-period pulses. Hence, the SMRB was more effective in providing protection for frequency-sensitive equipment by suppressing the transfer of high-frequency components of ground motions. Ghodke and Jangid [189] examined the influence of high austenite stiffness of SMA used in an isolation system that combines SMA and elastomeric bearing. They studied the effects of the isolation period, transformation strength, and the austenite stiffness of SMA on three structural response parameters: top floor acceleration, isolator displacement, and base shear. The results demonstrated that the isolation bearing with high austenite stiffness of SMA amplified the floor accelerations of the base-isolated building while it did not considerably affect the base shear and displacement.

Shinozuka et al. [190] presented optimal performance of SMA-based Lead Rubber Bearing (SMA-LRB) isolated buildings by conducting nonlinear random vibration analysis coupled with stochastic linearization of SMA behavior. They formulated a bi-objective optimization problem that minimizes the isolator displacement and maximizes the isolation efficiency to obtain the optimal combination of the SMA transformation strength and the LRB yield strength. Zhu and Qiu [191] performed an incremental dynamic analysis (IDA) of a prototype bridge installed with an isolation system that consists of elastomeric bearings and SMA cables. They implemented an *ad hoc* displacement-based design (DBD) approach proposed by Liu et al. [192] to design the isolators and the piers based on target pier displacement, isolator displacement, and isolator ductility. The IDA results indicated that the DBD approach estimates fairly well the target displacement under the DBE levels. Moreover, the results demonstrated that the SMA isolators could effectively protect the superstructure by reducing the damage in piers and limiting the total residual displacement of the bridge, especially under the frequent and design basis earthquake levels.

The majority of existing studies on SMA-based isolation systems employ only a single level of SMA element along with either rubber or friction-based bearings. Most recently, Cao et al. [193] introduced a new SMA isolation system that can provide seismic protection for bridge superstructures under multi-level seismic hazards. The proposed system, referred to as Multi-Level SMA/Lead Rubber Bearing (ML-SLRB), consists of LRB and three groups of SMA cables. The cables are adopted to alter the stiffness of the isolation bearing as the magnitude of seismic event increases and provides additional energy dissipation capacity and re-centering capability. During a frequent earthquake, the first group of SMA cables stretched and undergo phase transformation at a pre-determined displacement level, while the second and third groups are inactive due to available slacks. The second and third groups of cables are progressively activated and undergo phase transformation at different design levels of displacements depending on the earthquake magnitude. A design procedure was proposed to determine key parameters such as the cross-sectional area and slack displacements of each group of SMA cables. The effectiveness of the proposed ML-SRB was explored through nonlinear dynamic analyses of a case study bridge subjected to far-fault and near-fault earthquakes scaled to different seismic hazard levels. The performance of the proposed ML-SLRB was evaluated and compared with conventional LRB and SMA-LRBs that consist of only a single group of cables. Their analysis results demonstrated the high isolation efficiency of ML-SLRB at small or moderate earthquakes while effectively bounds the bridge displacements under extreme earthquakes.

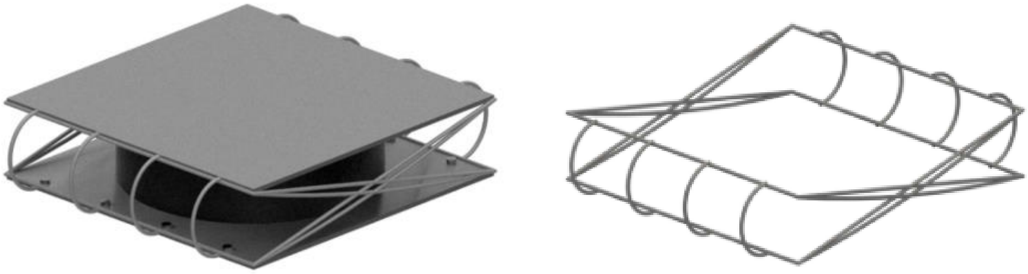

Figure 2-25. Schematics of multi-level SMA/lead rubber bearing [193]

2.5.1.2 SMA-based sliding isolation bearings

Several researchers have exploited the superelasticity and energy dissipation capability of various forms of SMA elements to enhance the performance of traditional sliding-type seismic isolation systems. Ozbulut and Hurlebaus [194] explored the seismic performance of an SMA-based isolation system under variations of environmental temperature. The SMA-based isolation system strategically combined a steel-Teflon sliding bearing, which was employed to dissipate energy through frictional behavior, and SMA wires were used to offer additional energy-dissipating and re-centering capabilities. They predicted the forces of the SMA wires using a neuro-fuzzy model that accounted for the effects of temperature and loading rate. A multi-objective genetic algorithm was employed to find out the length and cross-sectional area of the SMA wires, which were the primary design parameters of the device. Then, a sliding bearing with an SMA device was installed in a multi-span bridge to explore the seismic performance of the isolation system under various outside temperatures. The result demonstrated that temperature changes have a modest influence on the performance of isolated bridge structures. Notably, the results highlighted that the structural responses of the isolated bridge were affected as follows: a maximum of 13% variation on the displacement response and a maximum of 8% change in acceleration response when the temperature change was 20 ^{o}C from the reference temperature of 20 ^{o}C. The result revealed that that SMA-based sliding isolators effectively controlled the structural response of the isolated bridges subjected to earthquake events.

Jalali et al. [195] analyzed the feasibility of incorporating superelastic SMA wires into steel-Teflon flat sliding bearings through nonlinear time history analyses. They reported that the proposed isolation bearings reduced the maximum base shear more than conventional friction pendulum systems. Khodaverdian et al. [196] conducted a numerical study using SMA cables in parallel with steel-PTFE sliding bearings to retrofit an existing railway bridge. Their sensitivity analyses on the influence of environmental temperature suggested that the mechanical behavior of the SMA on the lowest likely temperature should be accounted for during the design of the proposed isolation bearing. Gur and Mishra [197] implemented a multi-objective optimization model to explore the optimal performance of pure friction SMA isolation bearing for protecting buildings against random earthquakes. They conducted nonlinear random vibration analysis through stochastic linearization of the cyclic force-deformation hysteresis of the frictional and SMA parts. A set of optimal characteristics were proposed to ensure the best performances of the isolation. The stochastic response behavior reveals that an optimal combination of the friction coefficient and SMA's transformation strength minimizes the floor acceleration, thereby maximizing the isolation efficiency. However, the isolator displacement reduced monotonically with increasing values of these two parameters. The effect of parameter variations on the robustness of the optimal system is demonstrated under variations in the isolator-superstructure system parameters as well as earthquake loading scenarios. The trends portrayed by the stochastic responses were further verified under a set of real earthquake ground motions.

Zheng et al. [198] presented a methodology to evaluate the seismic resilience and life-cycle loss of traditional and SMA-based isolation bearings. As such, the long-term performance benefits associated with the application of SMAs can be evaluated. To illustrate the significance of the proposed methodology, they considered an isolator that consists of one frictional sliding bearing with and without two SMA cable components. A nonlinear time history analysis was conducted to generate fragility curves of both the sliding and SMA-based bearings. Under the investigated scenarios, life-cycle loss and resilience were formulated considering the direct and indirect losses and hazard recovery trends. The proposed method was then implemented on a reinforced concrete bridge installed with the SMA-based bearings. The applicable performance indices, such as fragility curves, life-cycle loss, and resilience, were investigated and compared with the same bridge isolated by a conventional bearing.

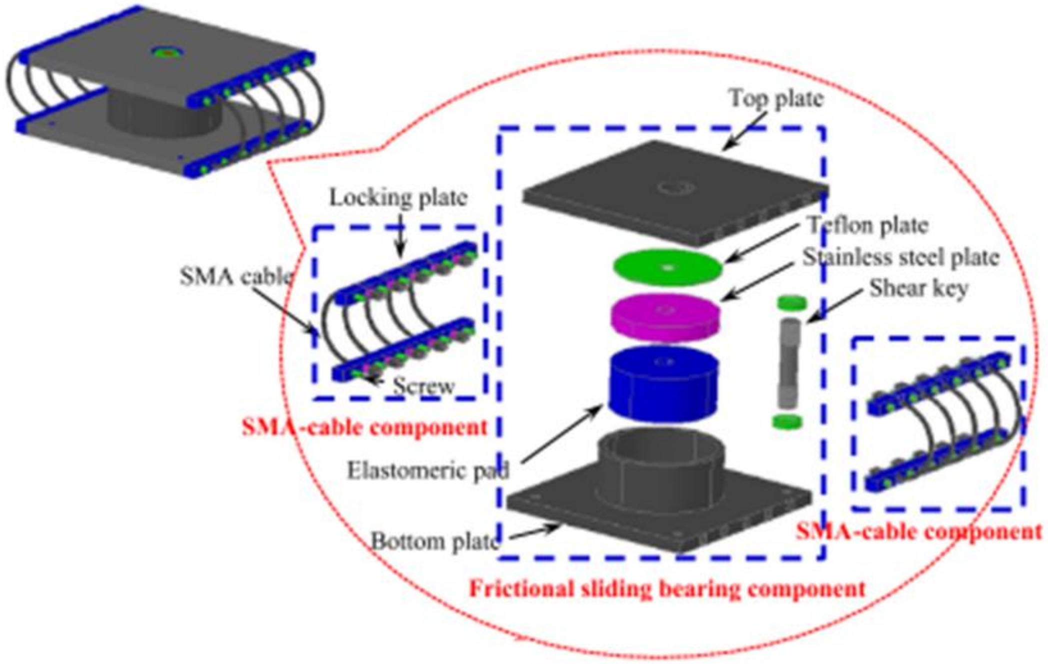

Figure 2-26. Configuration of the modular SMA-cable-based bearing [198]

De Domenico et al. [199] developed an adaptive isolation system that integrates low-friction curved surface sliders (CSSs), alternatively known as friction pendulum system, in parallel with two SMA gap dampers (SMAGDs). The SMAGD is a dissipative element made up of multiple SMA wires grouped together and bounded by a flexible membrane. The SMAGDs furnish supplemental stiffening and energy dissipation only when the isolation system passes a threshold or gap displacement while inactive for displacements less than the threshold. The authors proposed a conceptual model of the system based on a sliding pin and a slotted ring to realize the "gap damper" feature. Since the anchoring system of the left-side SMAGD is symmetrical with the right-side, only one damper is engaged at a time. Depending on the isolation system direction of motion, one acts like a “tension-only” element while the other provides zero compression force. A spring is installed at either anchoring system to generate a restoring force that pushes the sliding pin back to its initial position when the SMAGD no longer pulls it. A linear displacement-based procedure for the preliminary design of structures equipped with CSS + SMAGD system was developed and validated through a series of nonlinear response time-history analyses. They conclude that the proposed adaptive system efficiently integrates the inherent benefits of low-friction and high-friction CSS systems in a single unit.

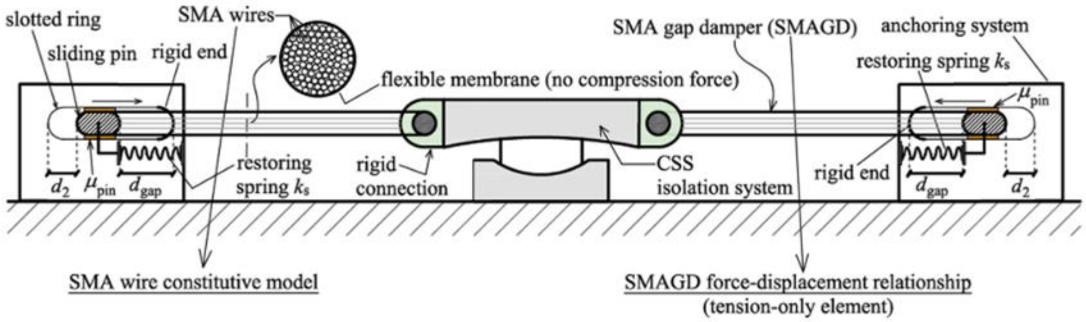

Figure 2-27. Schematics of the SMAGD (adopted from [199]

The work of Dong Liang et al. [200] is one of the few experimental studies on SMA-based isolation devices. They used a traditional friction sliding bearing system as the basic unit and added SMA cables to restrain the bearing when excessive displacement occurs. In addition, the SMA cables provide supplemental damping and self-centering capacity at large displacements. As shown in Figure 2-28, the cables are connected to the top and bottom plates of the friction sliding bearing through spherical hinges. The cables are mobilized and start to provide additional energy dissipation when the relative displacement exceeds a pre-determined target value. Some of the unique features of the proposed bearing compared with other SMA-wire or cable-based bearings are: (1) the cables can work simultaneously when the bearing moves in any horizontal direction due to the unique design of the connection between the SMA cables and bearing plates (2) the cables can control excessive vertical displacements of the bearing under vertical earthquake excitations. The performance of the proposed bearing was assessed by testing two prototype bearings as well as by conducting a numerical case study on a three-span continuous bridge.

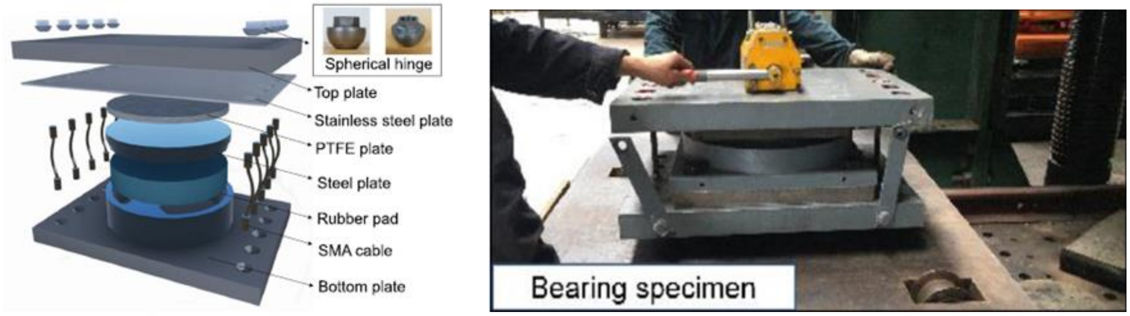

Figure 2-28. Three-dimensional schematic illustration and photograph of SMA-sliding bearing [200]

2.5.2 Seismic isolators with SMA bars

Casciati and Faravelli [201] introduced a new isolation device in which a sliding system is integrated with inclined *Cu*-based SMA bars that provides damping capacity and self-centering capability. Hu [202] proposed an isolation device equipped with large diameter SMA bars arranged radially around traditional LRB. The proposed isolator’s behavior and seismic performance were examined through extensive parametric analyses of single-degree-of-freedom spring models. The responses were compared with those of conventional LRB and LRB with steel bending bars. The study concluded that adding that the SMA bars to the LRB improved the re-centering capability and effectively reduced the lateral displacement even though the bars shortened the fundamental period of the structure. Cardone [203] carried out an extensive parametric study on the self-centering capability of an isolation system that consists of steel-PTFE flat sliding bearing combined with SMA-based auxiliary devices. The results indicated that the self-centering capability is affected by the mechanical behavior of the base isolation system and the characteristics of the ground motion.

2.5.3 Seismic isolators with SMA plates

In an effort to expand the application of SMAs in seismic base isolators, Wang et al. [204] developed new self-centering (SC) seismic base isolators using SMA-U-shaped Dampers (SMA-UDs) proposed by the same researchers [166]. The SC-isolators were designed in two different configurations. In the first type, known as SMA-LRB, a traditional LRB is placed at the center of the isolator, and four pairs of SMA-UDs are symmetrically arranged around it. In the second type, known as SMA-SRB, it has a similar layout with the first one, except the lead core is replaced by energy dissipating steel-UDs arranged in parallel with the SMA-UD. A total of six prototype SC base isolators and two conventional base isolators were fabricated and tested under an incremental displacement loading protocol. According to their test results, the SC base isolators showed flag-shaped hysteresis loops accompanied by significantly reduced residual deformation and sufficient energy dissipation collectively supplied by the lead core (or steel-UDs) and SMA-UDs. It was highlighted that some of the advantages of the SC base isolators are: excellent self-centering capability, adequate energy dissipation, design flexibility, and convenient inspection and replacement.

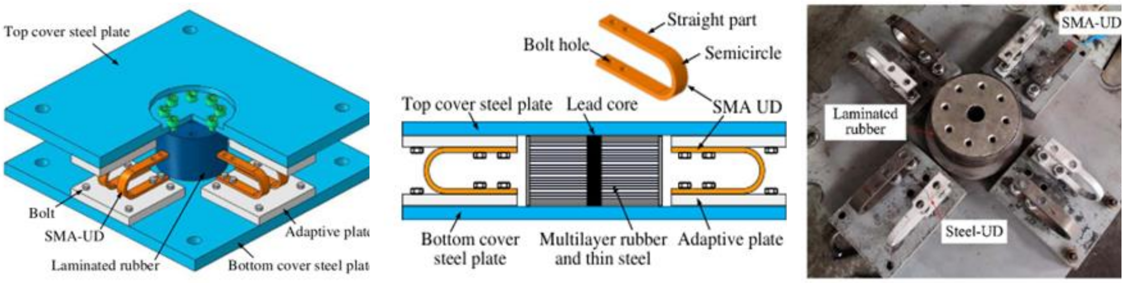

Figure 2-29. Configurations of the SC base isolators and fabricated SMA-SRB [193]

2.5.4 Seismic isolators with SMA springs

Attanasi and Auricchio [205] discussed seismic isolation bearing utilizing eight superelastic SMA springs. Huang et al. [206] experimentally and numerically studied a base isolation system that consists of two SMA helical springs and a linear slider. They implemented a phenomenological model to simulate the complex superelastic behavior of the SMA springs accurately, and a good agreement between the simulated and experimental force-displacement hysteresis curves was observed. They tested an experimental model of a two-story steel frame with two identical SMA helical springs installed at either side of the base in a mini-shake table under different magnitudes of excitations. Tests were repeated with a change of the pre-stroke length of the SMA springs. Besides, the isolated frame with steel springs and fixed base cases were analyzed for comparison. The results demonstrated that the proposed base isolation system can remarkably suppress structural vibrations and has enhanced isolation efficiency compared with a steel spring system.

Liu et al. [207] compared peak response quantities (such as inter-story drift ratio, floor acceleration, residual inter-story drift) of a three-story steel frame isolated with SMA springs against elastic steel springs. Peng and Wenting [208] investigated the feasibility of a new restorable isolator entitled SMA Spring-Friction Bearing (SFB). The SFB consist of a flat sliding bearing that decouples the superstructure from horizontal ground motion and SMA helical springs that provide re-centering mechanism and dissipate energy. A coil specimen made of a 12 mm diameter superelastic SMA bar was tested to characterize and validate the analytical model of the helical spring force-displacement curve. A prototype SFB specimen was fabricated and tested under cyclic loading protocol. Numerical analysis results of a lattice grid structure isolated with SFB illustrated the potential to serve as a structural control device.

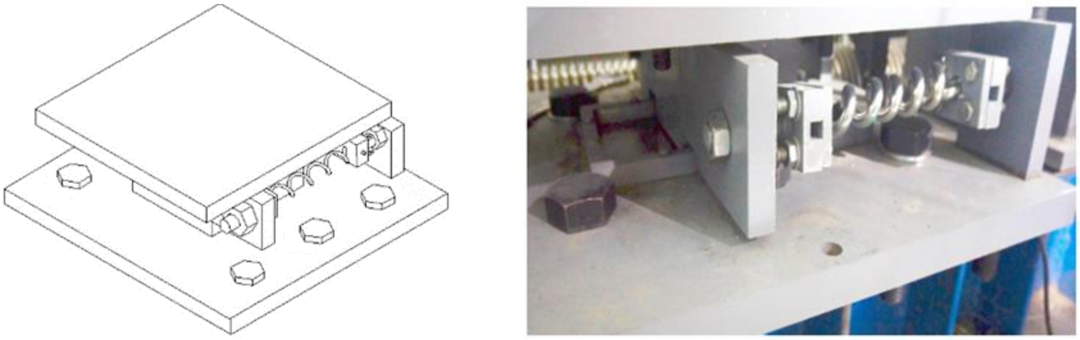

Figure 2-30. Three-dimensional schematic diagram and photograph of the SFB [208])

2.5.5 Comparison of SMA-based and traditional isolation devices

Laminated rubber bearings and sliding bearings are extensively used in building and bridge applications; however, they have some weakness, such as limited shear strain capacity, instability due to large deformations and inadequate self-centering property with unrecovered residual deformations [209]. Generally, requirements for features for the effective performance of isolation devices should include (1) adequate energy dissipation to reduce seismic demand, (2) a good recentering mechanism to avoid excessive bearing deformations and instability, (3) no need for bearing replacement even after a strong earthquake (i.e., no damage on the bearing after excitation), and (4) high durability against cyclic loads. Based on these, SMA-based isolation devices are superior compared with traditional counterparts, such as high damping rubber bearings, lead rubber bearings, friction pendulum bearings. Despite all the advantages that SMA-based isolation bearings offer, their sensitivity to ambient temperature could be considered a potential drawback. For instance, in cold region, the temperature can change from -50 ^{o}C to +40 ^{o}C in some places. Usually, Nitinol's austenite finish temperature ranges from -10 ^{o}C to 44 ^{o}C [210], which clearly demonstrates its potential of losing its superelasticity if the temperature goes below A_f where the system will lose its recentering capability. However, for such applications, SMAs with A_f below -50 ^{o}C, such as *Cu-Al-Be* (A_f of -65 ^{o}C), might be a better choice for outdoor applications [211].

2.6 Summary

Over the past decades, superelastic SMAs have been considered in the development of various seismic protection systems. The appealing properties of SMAs for the seismic application includes, high recoverable strain without any plastic (permanent) deformation, which provides both self-centering ability with large deformation capabilities and allows the reuse of the seismic protection system after repetitive load cycles; non-sacrificial and repeatable energy dissipation capability; and high fatigue resistance. This chapter provides an integrated and holistic review of SMA-based control devices including dampers, braces, and isolation systems. As discussed in this chapter, various compositions (such as NiTi and Cu- or Fe- based alloys) and forms (such as wires, cables, bars, and springs) of SMAs are available and have been explored for use in structural control systems. However, a judicious design that considers performance, cost, and practicality is needed to expedite real-world applications of SMA-based response mitigation systems. The technical review presented in this chapter highlighted important information for the ease of further studies and generated future research directions for researchers working in this field.

Although several SMA-based seismic control devices have been proposed and tested, the SMA elements used in these studies have been mostly small-diameter wires. On the other hand, there have been very limited experimental studies on SMA-based devices with high axial force and deformation capacities. Despite all of the promising features of SMA-based seismic protection systems, the lack of large-scale and practical SMA-based devices has become an impediment to the real-world implementation of such systems. Future research should focus more such realistic devices rather than small-scale laboratory devices to expedite the implementation of SMA-based systems into full-scale structures.

Since the earlier explorations of SMAs for civil engineering applications in the mid-1990s, the cost of SMAs has been cited as one of the major barriers to their adoption. Over the past decades, although the cost of NiTi alloy wires has considerably reduced, high material cost is still a challenge for most of the civil engineering applications of SMAs. One reason for this fact is that the manufacturing cost of large diameter bars compared to wires is still higher as the demand for superlastic NiTi SMAs is driven by medical applications where only small-diameter wires are used. Large-diameter SMA cables made out of individual small diameter wires may bring the cost of large-size SMA elements down – once a high demand for such large size cables is available.

Another possibility for low-cost, commercially available SMAs for large-scale structural applications is *Cu*-based alloys. In particular, superelastic *CuAlMn* SMAs are promising memory materials as they possess advantages such as a large operating temperature range, low temperature- and rate-dependency, and good workability and machinability. However, the strength and energy dissipation capabilities of *CuAlMn* SMAs are limited. Since superelastic behavior in *Fe*-based SMAs reported in 2011 [92], they have been considered as ideal candidates for civil applications as a low-cost SMA material with excellent mechanical properties. However, these *Fe*-SMAs have their own obstacles for industrial applications, such as the need to grow large grains in the microstructure for good recoverability. Given the recent accomplishment in developing *Fe*-based SMAs by several other material science research groups [212–214], it is realistic to expect these ferrous superelastic alloys to be commercialized in the near future.

Despite the concerns on the cost of SMAs, when the SMAs are used in the seismic protection devices such as dampers and isolators, the material cost should not be a deciding factor. Since the SMAs are effectively used in these systems for self-centering and energy dissipation, SMA-based devices could have comparable costs with more commonly used seismic protection systems. In addition, it should be noted that SMA-based devices can be non-sacrificial and can serve effectively even after an earthquake event.

3 BUCKLING AND POST-BUCKLING BEHAVIOR OF SMA BARS

3.1 Overview

Towards the development of SMA-based devices, larger size SMA elements are usually needed to accommodate high force demands in real-world applications. However, lack of more in-depth understanding of SMA's buckling behavior inevitably brings uncertainties when they are used in damping devices and other applications that will be subjected to compression load. To fill this knowledge gap, this chapter discusses the buckling and post-buckling behavior of large diameter superelastic NiTi SMA bars based on information obtained from comprehensive experimental test results. To the best of the author's knowledge, the effects of loading rate on the buckling response of SMAs and their thermomechanical behavior have not been reported in the literature. The tensile and compression responses of NiTi bar characterized under monotonic loading tests up to failure. Digital image correlation (DIC) technique was implemented in all experiments to monitor full-field surface displacements and strains along the specimen length. The temperature field on the surface of the specimens was recorded by an Infrared camera. The load-displacement curves for various slenderness ratios are provided. The interaction between material nonlinearity due to phase transformation and geometric nonlinearity was explored. Data obtained from the DIC measurement system was further analyzed to identify the onset of buckling and to extract experimental critical buckling loads. The effect of loading rate on buckling response of SMAs was investigated by conducting additional testing at higher loading rates on the specimens with three selected slenderness ratios. Furthermore, the thermomechanical behavior of the SMA bars was investigated. At the end of the chapter, comparison of analytical and experimental critical buckling loads is presented.

3.2 Experimental Details

3.2.1 Materials

In this study, commercially available 12 mm diameter superelastic NiTi SMA bars with a chemical composition of 50.7 wt.% Ni and a 49.3 wt.% Ti were used. The as-received bars were heat treated using an electrical furnace at 400˚C for 30 min and then water quenched. The forward and reverse transformation temperatures were determined using a differential scanning calorimetry (DSC). As shown in Figure 3-1, the forward transformation temperatures are -45˚C and -56˚C for martensite start (M_s) and martensite finish (M_f), respectively. The reverse transformation temperatures are -32˚C and -19˚C for austenite start (A_s) and austenite finish (A_f), respectively. The result confirms that the material is superelastic at room temperature.

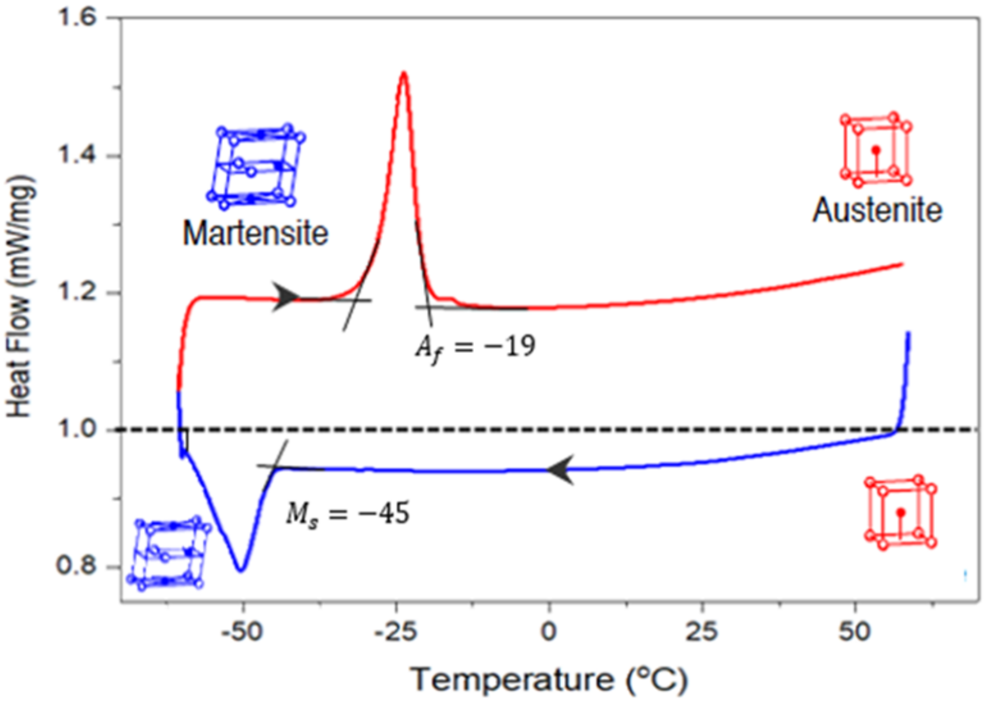

Figure 3-1. Differential scanning calorimetry (DSC) test result

3.2.2 Test matrix

Before the buckling tests, monotonic tensile and compression tests were performed to characterize the material properties of NiTi bar. Two specimens with a total length of 178 mm and 30 mm were prepared for the tensile and compression tests, respectively. The specimens were tested following the ASTM F2516-14 [215] standard. Although the procedure outlined in this standard is for tension test only, it was implemented for the compression test as well as for the sake of comparing the test results under the same loading protocol.

To evaluate the buckling behavior of NiTi SMA bars, a total of 15 specimens with a wide range of unsupported length were tested. The unsupported length of SMA bars ranged from 45 mm to 345 mm, which corresponds to a slenderness ratio of 25 to 115, respectively. The slenderness ratio (λ) is calculated as L_u/r, where L_u is the unsupported length and r is the radius of gyration. A summary of the main test parameters is reported in Table 3-1. The total length of the specimens is designated as L and L_e represents the virtual gauge length used in the computations of strain fields using the DIC technique. The variables are schematically shown in Figure 3-2(a).

The experimental tests were conducted in two stages. First, specimens with slenderness ratio ranging from 25 to 115 were subjected to compressive loads at a quasi-static loading rate of 0.0002 mm/sec per mm and unloaded at the same rate. Then, specimens with three slenderness ratios of 35, 60 and 80, representing short, intermediate, and slender columns, were tested at higher loading rates of 0.005 mm/sec per mm and 0.01 mm/sec per mm, respectively. The goal of these tests was to assess the effect of strain rate on the buckling and post-buckling behavior of NiTi bars. Note that care shall be exercised in selecting the loading frequencies as it can lead to a catastrophic failure at high strain rates.

Table 3-1. Test specimens

Specimen ID	***L* (mm)**	**L_u (mm)**	**λ**	**Crosshead speed (mm/sec per mm)**
SR25a	135	75	25	0.0002
SR35a	165	105	35	
SR40a	180	120	40	
SR45a	195	135	45	
SR60a	240	180	60	
SR80a	300	240	80	
SR95a	345	285	95	
SR105a	375	315	105	
SR115a	405	345	115	
SR35b	165	105	35	0.005
SR60b	240	180	60	
SR80b	300	240	80	
SR35c	165	105	35	0.01
SR60c	240	180	60	
SR80c	300	240	80	

3.2.3 Test setup, procedures, and instrumentations

A test setup that facilitates testing of a broad range of specimens was designed by employing an end condition somewhere in between a true fixed-fixed and pinned-pinned end conditions as this provided a convenient way of specimen mounting operation. Custom fixtures were fabricated from steel plates to hold the specimens in place. They were bolted to the moving and fixed heads of the loading frame. Figure 3-2(a) illustrates the schematic representation of the test setup. The fixtures had a 13.5 mm diameter and a 30 mm deep bottomed holes at the center of the plates, which ensured uniform distribution of the applied load throughout the specimen cross-section at each end. Because the buckling response of a structure is susceptible to geometric imperfections and loading eccentricity, the dimension of the holes was kept to be the same so that all the specimens were precisely inserted into the custom fabricated fixtures at the planned nominal length. This avoided unwanted variation in the specimen's unsupported length, i.e., L_u and hence, variation in critical buckling loads that could happen if the specimens would have been gripped directly to the load frame. Additionally, the fixtures were carefully aligned to plumb, and once set, were remain undisturbed throughout the test. As shown in Figure 3-2(b), the specimen was allowed to freely move in the axial direction while restrained laterally at each end.

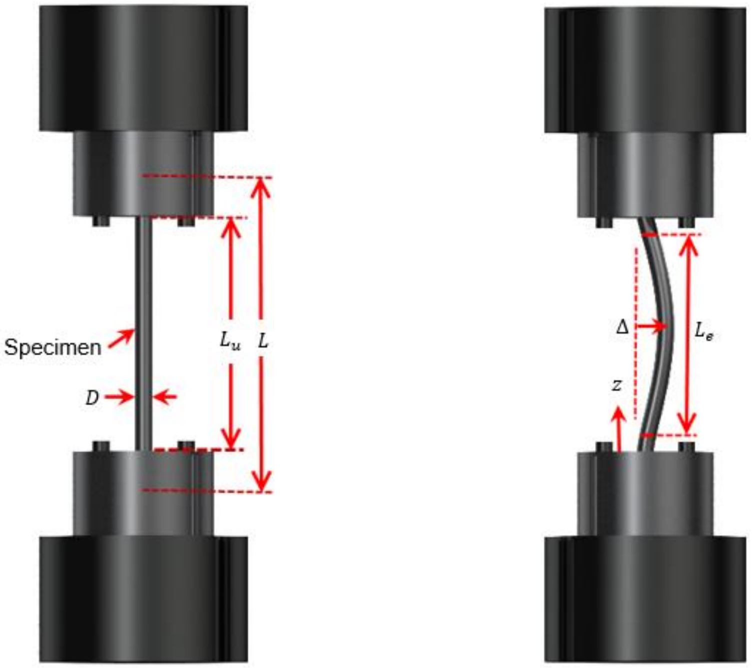

(a) (b)

Figure 3-2. Schematics of the (a) buckling fixture setup and (b) specimen undergoing compressive deformation

All buckling tests were conducted using an MTS 810 servo-hydraulic machine equipped with a 250 kN capacity load cell. In all experiments, displacement-controlled loading and force-controlled unloading procedure were adopted. The displacement of the moving head was commanded at a prescribed rate while the MTS data acquisition system recorded the applied displacement and load.

A digital image correlation (DIC) system was employed to monitor the surface displacement fields throughout the specimen length from which strain fields were computed afterward. Before each test, a base coat of white paint was applied at the gauge section of the specimen succeeded by a dusting of black speckles. A series of images were captured during the test to track the speckle patterns applied to the specimen. Since buckling of the specimen could occur in any plane, two cameras were systematically positioned to capture the deformation of the bar in a three-dimensional space. Standard resolution and high-speed imaging devices were used for the quasi-static and high loading rate tests, respectively. Sequential images were post-processed using a commercial software Vic-3D [216]. In all experiments, the strains are reported using a DIC "virtual" extensometer as a measure of the average strain along the specimen gauge length. A gauge length L_e for the extensometer was chosen along the specimen centerline in the reference configuration as close as possible to the end. The use of DIC extensometer is particularly beneficial for buckling experiments where neither conventional nor laser extensometers would have been practical. In fact, in some of the tests, a laser extensometer was used to measure the axial shortening only up to the onset of buckling. Once the specimen buckled and started to deform out of a plane, the laser infrared signal was lost due to the lateral deformations. The data obtained from the laser extensometer were used only for validating DIC extensometer measurements. A FLIR A655sc (from FLIR system AB Inc., Sweden) infrared camera was employed to record the temperature map on the surface of the specimens. The FLIR A665sc has a high resolution of 460 x 480, which can cover the whole front surface of the specimens. Figure 3-3 shows the buckling test setup with DIC and laser extensometer.

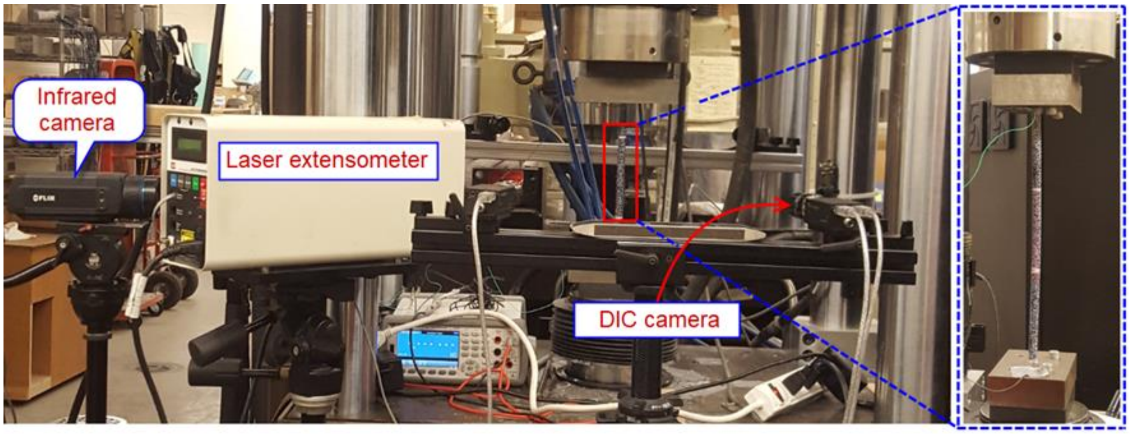

Figure 3-3. Buckling test setup with laser extensometer and DIC system

3.3 Analysis of Experimental Results

3.3.1 Tensile and com pressive behavior under monotonic loading

To illustrate baseline material behavior under pure tensile and compression loading prior to studying second-order effects (i.e., geometric nonlinearity) on material response, Figure 3-4 provides the tensile and compression response of two short specimens loaded up to failure. It can be seen that the stress-strain curve for the tensile behavior depicts a flat stress plateau (i.e., constant stress) due to stress-induced transformations followed by stiff segment. In contrast, the compression stress-strain curve shown in the lower left quadrant of Figure 3-4 did not exhibit flat stress-plateau; instead, it is characterized by a clear-cut slope.

An in-depth understanding of the various forms of deformations linked with the tensile and compressive loading can be achieved through a careful analysis of the DIC surface strain fields presented in the inner plot. In tension, it can be seen from image ③ (just before the stress plateau in the stress-strain curve) that a distinct martensite band was constituted and then disseminated through the gauge length of the specimen (image ④) as the elongation continued the stress plateau. It can be clearly distinguished that the strain field was uniform before stress-induced martensitic transformations (SIMT), i.e. up to ②; and became distinctly heterogeneous between ③ and ④ with a single propagating front as the specimen elongated on the stress plateau. Finally, it turned again to almost uniform at ⑤ after the end of the plateau. On the other hand, under compression, the material did not reveal strain localized propagation, which was confirmed by the absence of clear flat stress-plateau. Rather, the surface strain fields seem to be soundly uniform with only modest wavering, particularly towards the end of the loading. This inhomogeneity might be related to bending of the specimen due to transient buckling.

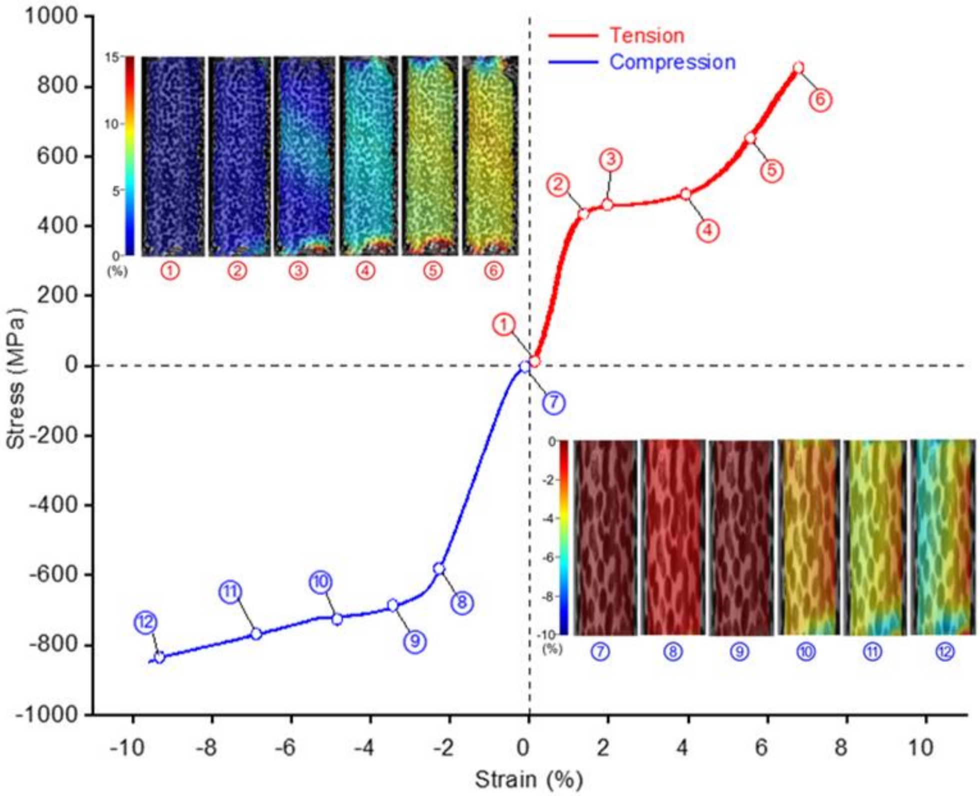

Figure 3-4. Tensile and compression response of NiTi bar: stress-strain curve along with axial strain field contours. Numbers below each image correspond to marks on the stress-strain curve

The NiTi material examined in this study attested the well-established lack of symmetry in tension and compression responses regarding to the stress level at which the martensite transformation begins. The compressive transformation stress and strain values of 600 MPa and 2.1%, respectively, were approximated by reading from the stress-strain curve that corresponds to the end of the linear elastic region. Compared to the tensile transformation stress and strains, it was found that the compressive values are higher by 30% and 50%, respectively. The prime causes of this asymmetric behavior are given as a low crystallographic symmetry of the martensite phase and textures induced during materials processing [217,218]. In general, the observations made in this section are in line with previous investigations on NiTi tubes and coupons [121,217–219]. Therefore, in subsequent discussions, the result shown in the bottom left quadrant of Figure 3-4 is referred to as “pure” compression behavior. Note that this behavior does not represent the true compression response of the material since it is inevitable to completely avoid buckling in a compression test. Although the custom fabricated grips were effective in suppressing the buckling effect, still there might be slight bending of the specimens that could contribute to the total compression response.

3.3.2 Global load-displacement behavior

In this section, an overview of the buckling and post-buckling responses of all specimens ranging from the very short to the slender ones are presented. Owing to the nonuniform local stress and strains in a typical buckling test, in this study results are plotted in terms of the normalized load and normalized axial displacement to differentiate from the macroscopic stress and strain. The applied load (P) was normalized by the cross-section area (A_o), and the DIC axial displacement (δ) was normalized by the virtual extensometer (L_e). The ends of the DIC virtual extensometer (L_e) were strategically selected close to the ends of the specimen as such rotations due to bending of the specimen were small. For the sake of simplicity, the normalized load and normalized axial displacement from now on are referred to as load and displacement, respectively.

Figure 3-5 illustrates the load-displacement curves of NiTi bars with slenderness ratio 25, 35, 40, 45, 60, 80, 95, 105, and 115 tested at a strain rate of 2×10^{-4} s^{-1}. As shown in Figure 3-5(a), the load of the stocky bar, λ=25, increased and experienced phase transformation at 600 MPa. Unlike other conventional elasto-plastic materials such as steel, the sustained load did not decrease with an increase of axial displacement beyond the first instability point. The post-buckling loading response of the bar stiffened to almost a linear response after the 3% displacement and until a peak load of 800 MPa. Upon unloading, an abrupt elastic drop in load parallel to the pre-buckling response was observed.

As can be seen from figure 5b, the short bars (λ=35, λ=40, and λ=45) displayed a peak load and buckled near the onset of phase transformation. In the case of the slenderness ratio of 35, the load undulated during the loading portion of the post-buckling branch. It can be also seen that with increasing slenderness ratio, there were larger decreases in post-buckling load levels. However, upon unloading, all the specimens recovered most of their deformations by exhibiting near typical superelastic behavior. It can be seen that the buckling load for λ=35 is slightly lower than for λ=40. This is contrary to the general trend that buckling load decreases as the slenderness ratio increases. The authors considered the result of λ = 40 as an outlier.

When the buckling response of the long (λ=60 and λ=80) and slender (λ=90, λ=105, and λ=115) bars are examined in Figure 3-5(c) and 5d, it can be seen that the critical buckling load decreases in a steep manner with increasing slenderness ratio. Bending of the specimens due to P-Δ effect caused the load falls off monotonously beyond the peak value up to the final point of loading. During unloading plateau, the load levels remained almost constant up to 0.8% displacement but exhibited a slight increase in all long and slender specimens with the exception of λ=60 specimen. Subsequently, the load decrease along a line parallel to the initial elastic (austenite) branch to a zero load with almost no residual displacement.

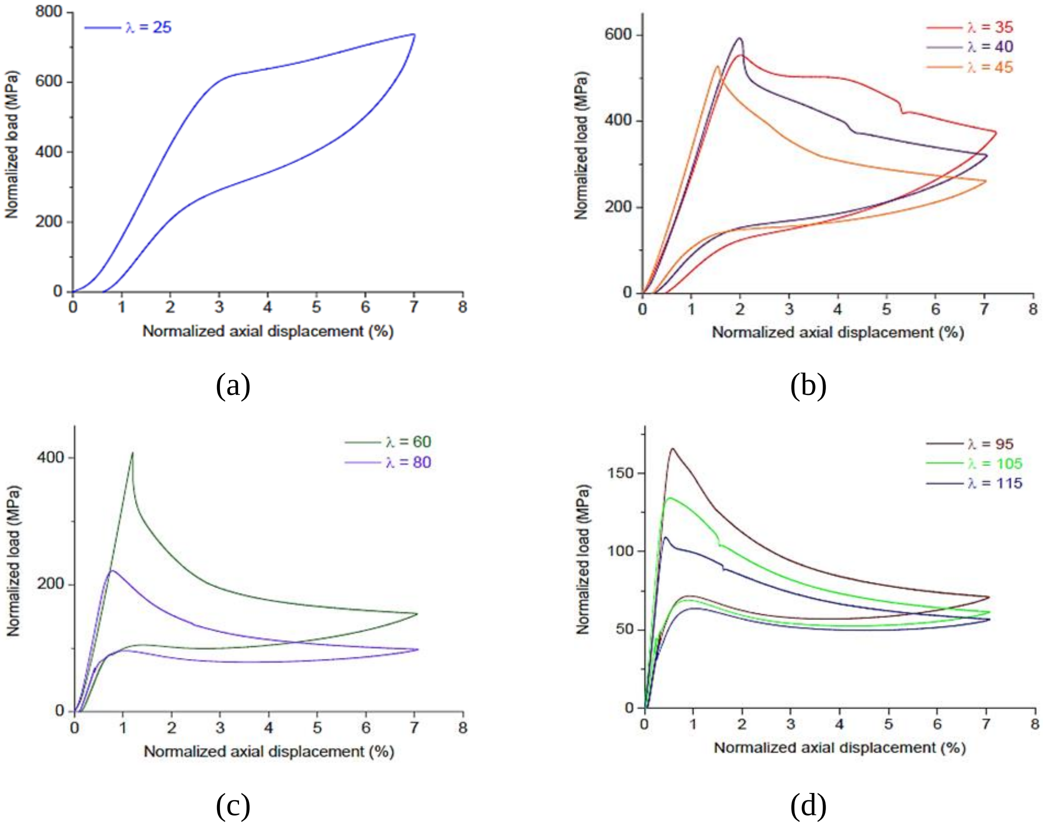

(a) (b)

(c) (d)

Figure 3-5. Normalized load-axial displacement responses for NiTi bars with slenderness ratios of (a) λ=25, (b) λ=35, λ=40 and λ=45, (c) λ=60 and λ=80, and (d) λ=95, λ=105 and λ=115

The buckling responses of all specimens are plotted in Figure 3-6 for better comparison. As can be seen, all specimens exhibited superelastic responses despite being buckled far into the post-buckling regime with a maximum axial displacement of 7%. Most of the specimens returned to almost zero displacement upon the removal of the load. As expected, the critical buckling load decreases as the slenderness ratio increases. The slender specimens buckled considerably below the forward phase transformation stress level of the pure compression response i.e., 600 MPa, while shorter bars buckled near the transformation stress level.

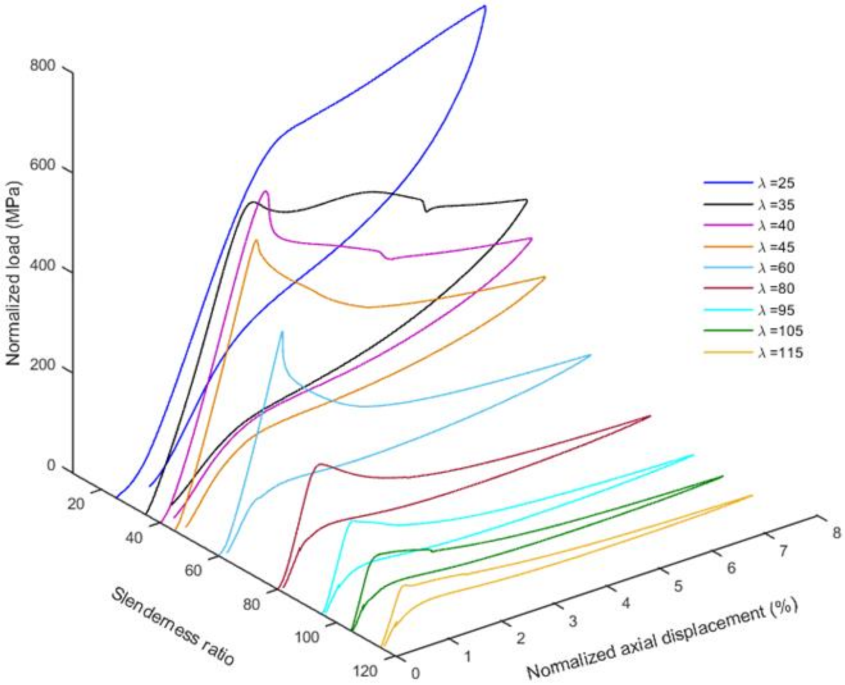

Figure 3-6. Normalized compressive load-axial displacement curves for all slenderness ratios

3.3.3 Axial strain fields

By implementing the DIC technique, axial compression deformation responses of all specimens and the corresponding strain filed contours were obtained and discussed in this section. The axial strain field contours of the specimens with slenderness ratio of 25 are shown in Figure 3-7. Strain field images confirms the fact that there is no strain localization due to transformation. This observation is consistent with the pure compression test result. A close assessment of the mechanical response of λ=25 specimen revealed that there are two peak loads, which are instability points on the equilibrium configuration path (i.e., load-displacement curve) of the bar. At the first peak load, the specimen instability occurred because of the decrease in the tangent modulus of elasticity as the material entered the martensitic transformation phase. However, in contradiction with the general trend that load falls off unvaryingly upon further increase in compression load beyond the first peak load, the bar sustained significantly higher load after the first peak load. When the specimen bent, the innermost fibers of the cross-section were compressed more than the outermost fibers. As a result, the innermost fibers completed their phase transformation into martensite first. The volume fraction of martensite increases as more fibers underwent stress induced phase transformation, this led to a complex movement of the neutral axis of the bar cross-section. Since the modulus of elasticity of martensite is higher than the transformation elasticity modulus as can be deduced from Figure 3-4, the bar stiffened, which in turn increase the resisting moment of the bent bar. Therefore, the bending moment due to the applied load (i.e., the P-Δ moment) was exceeded by the bent bar resisting moment. Thus, because of SMAs unique material properties, the specimen was able to acquire a highly stable post-buckling configuration after the first point of instability. This suggests that the stress-induced martensite transformation coupled with the P-Δ effect may have caused the load to vary non-monotonically with the axial displacement.

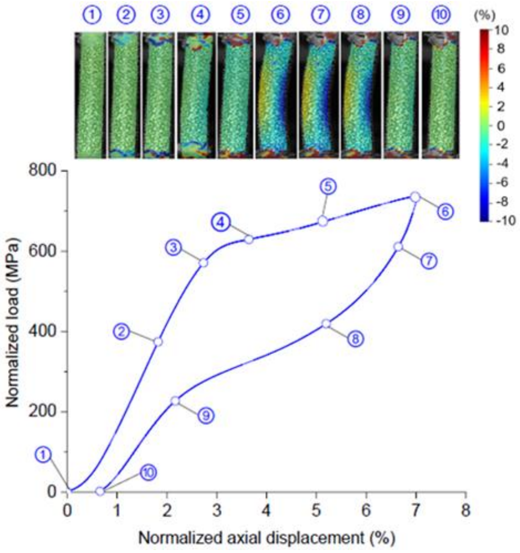

Figure 3-7. Mechanical responses and axial strain fields of λ=25

Figure 3-8 illustrates the axial strain filed contours of specimens with a slenderness ratio of 35 and 45. As can be seen from images ③, ④, and ⑤ higher magnitude concentrated deformation bands were developed at the mid-length of the specimen. Unlike the bar with λ=25, the load after the instability point did not increase even if the material entered into the martensite transformation phase. Since the slenderness was higher, a point on the post-buckling branch of the loading segment was unable to overcome the previously attained maximum load. In other words, the material stiffness after SIMT did not increase enough to resist the bending moment due to P-Δ effect. This might be due to small volume fractions of nucleated martensite that could contribute to the stiffness. It could be speculated that the overall stiffness of the custom fabricated grips contributes to the post buckling stiffness of the specimen. It could be inferred therefore that the influence of the pure compression behavior of NiTi moved away as the slenderness ratio increased.

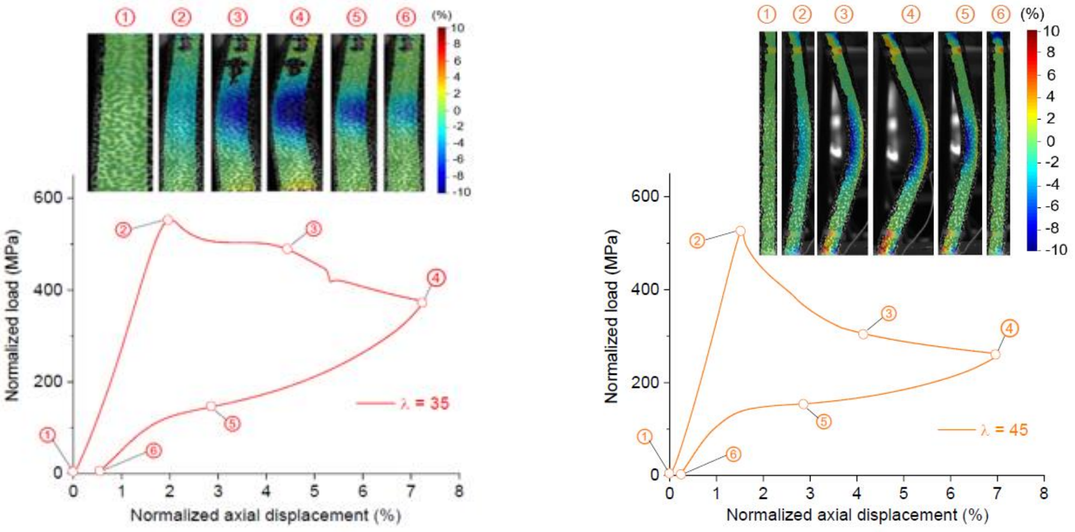

(a) (b)

Figure 3-8. Mechanical responses and axial strain fields for (a) λ=35 and (c) λ=45

Figure 3-9 presents the axial strain field contours of specimens with slenderness ratios of 60, 80, 95, 105, and 115. Note that for the bar with λ=60, the buckling occurred in a plane where the DIC cameras could not capture the buckling shape. The strain field contours have confirmed that formation and growth of distinct martensite bands in a localized manner was less prevailing in NiTi bar buckling tests even though higher magnitude concentrated strain regions arose due to inelastic post-buckling behavior.

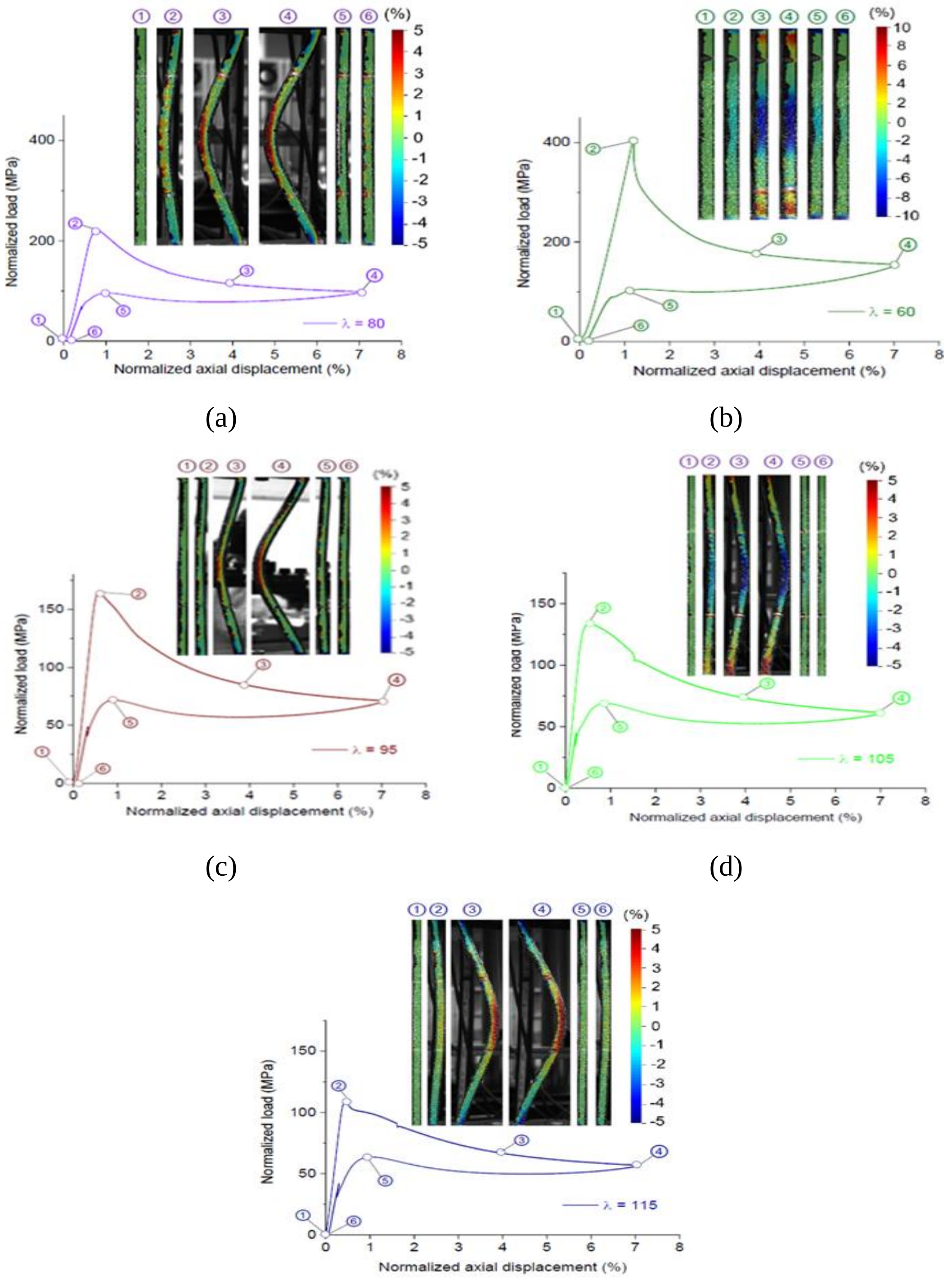

(a)

(b)

(c)

(d)

(e)

Figure 3-9. Normalized full-field axial strains of SMA bars with (a) λ=60, (b) λ=80, (c) λ=95, (d) λ=105, and (e) λ=115 at different loading stages

3.3.4 Lateral deflections

The buckling and post-buckling behavior of superelastic NiTi bars can also be characterized by the lateral deflections of points along the centerline of the specimens under axial load. Figure 3-10 illustrates the lateral deflection profile of each specimen near the end of maximum axial displacement, which is at the end of loading as a function of normalized unsupported length. The normalized unsupported length is computed as the height of the specimen at a given section (*z*) divided by the unsupported length (L_u). In addition, the lateral deflection contours of the specimens with λ=25 and λ=115 are illustrated in Figure 3-11(a) and 3-11(b), respectively. Both the lateral deflection contour and centerline profile were calculated at a single point along the centerline of the specimens.

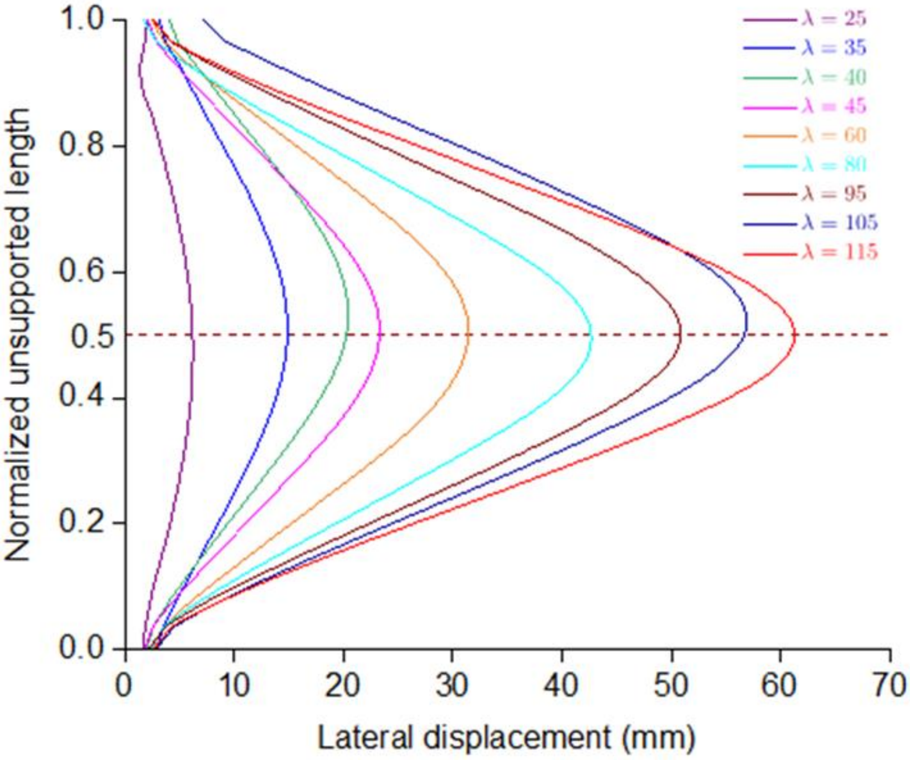

Figure 3-10. Centerline lateral deflection normalized by unsupported length

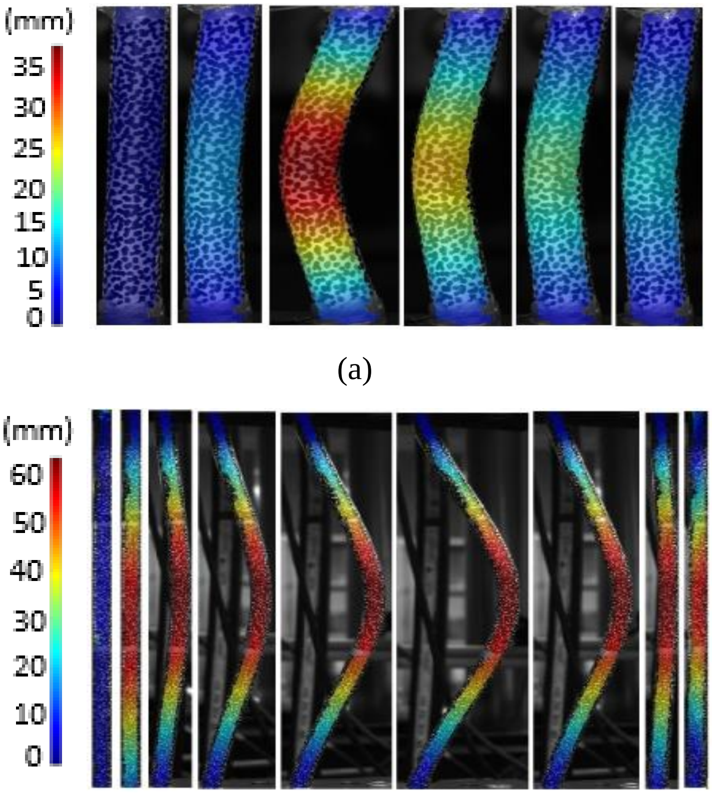

(a)

(b)

Figure 3-11. Representative lateral deflection contours for slenderness ratios of (a) λ=25 and (b) λ=115

As expected, the maximum lateral deflection for all specimens occurred at the mid-length. The shortest specimen experienced displacement primarily in the axial direction with minimal out of plan deformation. All other specimens, initially straight, started to deflect laterally at their respective buckling load. It is apparent that in all cases the post-buckling response had a deformation profile similar to a cosine wave. This concurs well with the end conditions in this experimental set up and expectations for classical column buckling. It can be observed from Figure 3-10 that the abscissa of the normalized profiles at the specimen’s ends were not quite zero. Its noteworthy to mention that the specimens were not completely speckled from one end of the custom fabricated fixture to the other end. A small section of the bars at each end was intentionally left un-speckled. As a result, the lateral deflections were not necessarily zero at the ends of the DIC gauge length. The kink in the lateral deflection of the λ=25 specimen at the ends may be due to this un-speckled region and the custom fabricated grips overshadow the ends of the specimen.

3.3.5 Effects of loading rate on the buckling and post-buckling behavior of SMA bars

To explore strain rate effects on the buckling and post-buckling responses of SMA bars, six additional specimens were tested at loading rates of 5×10^{-3} mm/sec per mm and 1×10^{-2} mm/sec per mm. Figure 3-12 presents the normalized load-displacement curves of the specimens with slenderness ratios of 35, 60, and 80 subjected to loading rates of 2×10^{-4}, 5×10^{-3} and 1×10^{-2} mm/sec per mm. It can be observed that the specimens with a slenderness ratio of 35 and 80 reached higher load values when they were tested at faster rates. On the other hand, the loading rate had no noticeable effect on the critical buckling load of the specimen with λ=60. However, comparing the quasi-static and the faster rate tests, the post-buckling branches of the later showed considerable upward shift for the specimens with all slenderness ratios.

Although majority of the specimens tested in this study buckled at the stress level below the forward transformation stress, the observed higher loads at higher strain rates could be attributed to the nature of phase transformations. In superelastic SMAs, atoms move collaboratively by a shear-like mechanism to initiate a diffusion-less solid to solid transformation. The stress values that correspond to this transformation increase with the increasing loading rate [103].

It can be also seen that the residual deformation response of NiTi bars subjected to buckling is affected by loading rate. For the specimen with λ= 35, the residual deformations increased from 0.47% at quasi-static loading up to 1.15% at faster loading rates. This could be attributed the fact that when the strain rate is high there is limited time for the phase transformations to occur. For the specimens with higher slenderness ratios (i.e., λ=60 and λ=80), a somewhat increase in residual deformations was also observed but the residual deformations were below 0.42% for all considered loading rates.

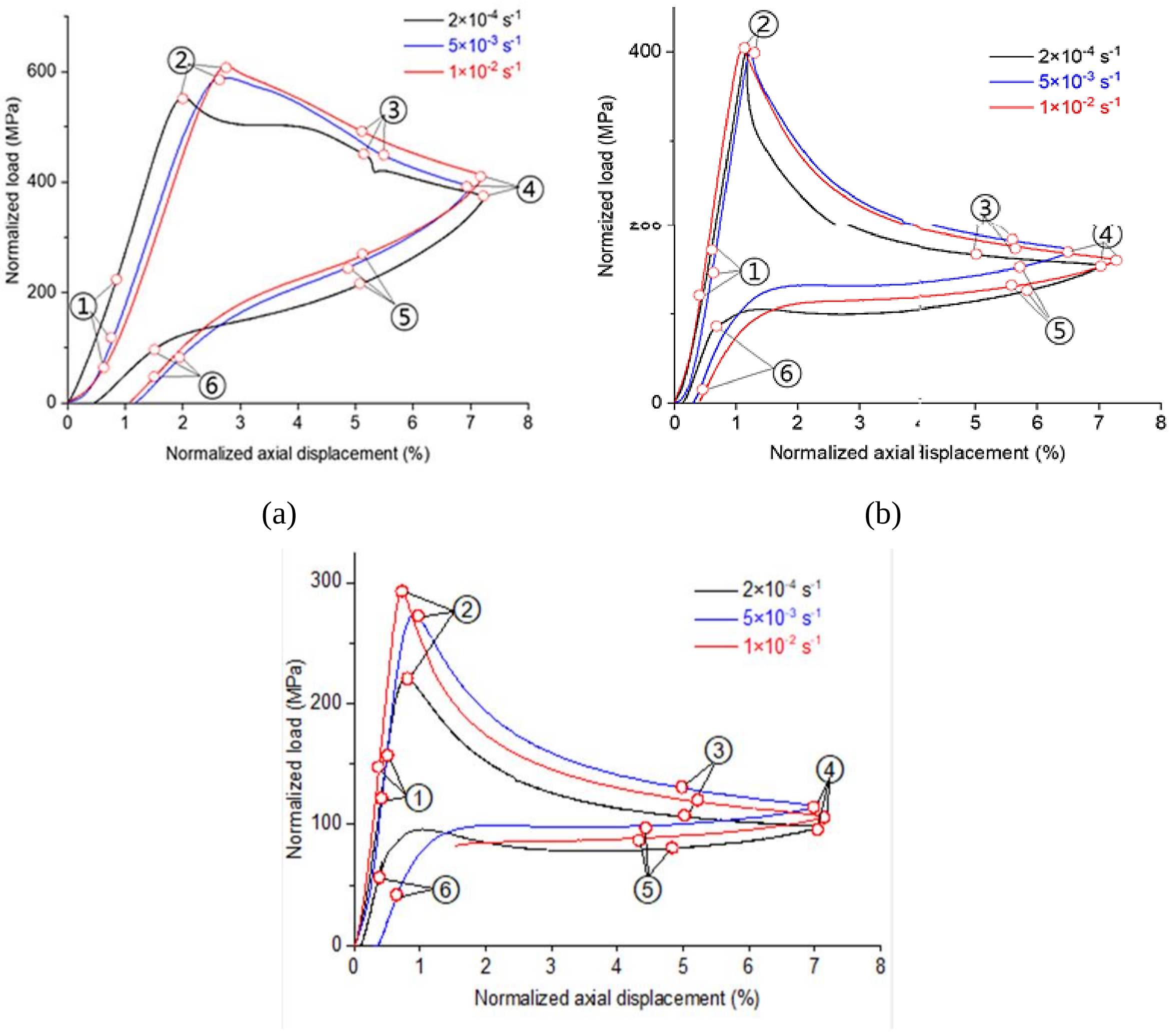

(a)

(b)

(c)

Figure 3-12. Buckling response at different strain rates for specimens with (a) λ=35, (b) λ=60, and (c) λ=80

Figure 3-13 illustrates the evolution of the maximum temperature recorded and temperature contours for the specimens with slenderness ratio of 35, 60 and 80 subjected to loading rates of 2×10^{-4}, 5×10^{-3}, and 1×10^{-2} mm/sec per mm. For the specimens subjected to a loading rate of 2×10^{-4} mm/sec per mm, the maximum temperature increases up to the point of buckling. Once the critical buckling load is reached, the temperature slightly increases or remains constant until the end of the loading protocol. In the unloading phase the temperature decreases as expected however, as the SMA bar returns to the normal position (i.e., recovers the lateral displacements), the temperature decreases below the initial temperature. This might be attributed to the reverse transformation. After the completion of the reverse transformation, an increase in temperature to reach the initial temperature (room temperature) is observed.

Figure 3-13(c) and 3-13(d) display the maximum temperature profile and temperature contours for specimens subjected to a loading rate of 5×10^{-3} mm/sec per mm, respectively. It is observed that with the increased loading rate, the maximum temperature increases up to the end of the loading cycle. The specimen with slenderness ratio of 35 experienced a slight increase in the maximum temperature in the early stages of the unloading protocol. This can be attributed to the inelastic buckling behavior of the specimens with low slenderness ratio, and the sudden change in stress fields at the buckled region as the SMA bar recovers the original shape. During the unloading stage, the maximum recorded temperature decreases for all specimens. However, due to the relatively higher loading frequency, the specimen’s temperature remains above room temperature until the end of the reverse transformation. At the end of the testing protocol, the SMA maximum temperature reaches room temperature.

Figure 3-13(e) and 3-13(f) illustrate the recorded maximum temperature history and temperature contours for the specimens subjected to a loading rate of 1×10^{-2} mm/sec per mm, respectively. It is observed that the temperature increases rapidly up to the critical buckling point and remains constant until the SMA bar returns to its original shape (i.e., up to the completion of the reverse transformation) for slender specimens.

In general, the thermomechanical behavior of SMA bars under compressive loading is highly nonlinear. Multiple factors such as nonlinear strain distributions across the height of the bar and the cross-sectional area at a specific height, forward and reverse transformations and loading frequency contribute to the nonlinearities of the thermal response. Specimens with small slenderness ratio (i.e., λ= 35), experience high strains along the length of the bar, resulting in an increase in temperature in all regions of the bar. For the slender specimens (i.e., λ=60 and λ=80), the temperature increases at the middle-buckled area. This region experiences high strains, however intermediate regions (i.e., between the top grip and buckled area and between the bottom grip and buckled area), experience small strains. It is suspected based on the strain contour plots presented in

Figure 3-13 that intermediate regions do not experience transformations. Further investigations are required to completely understand the thermomechanical behavior of SMA bars subjected to compressive loads.

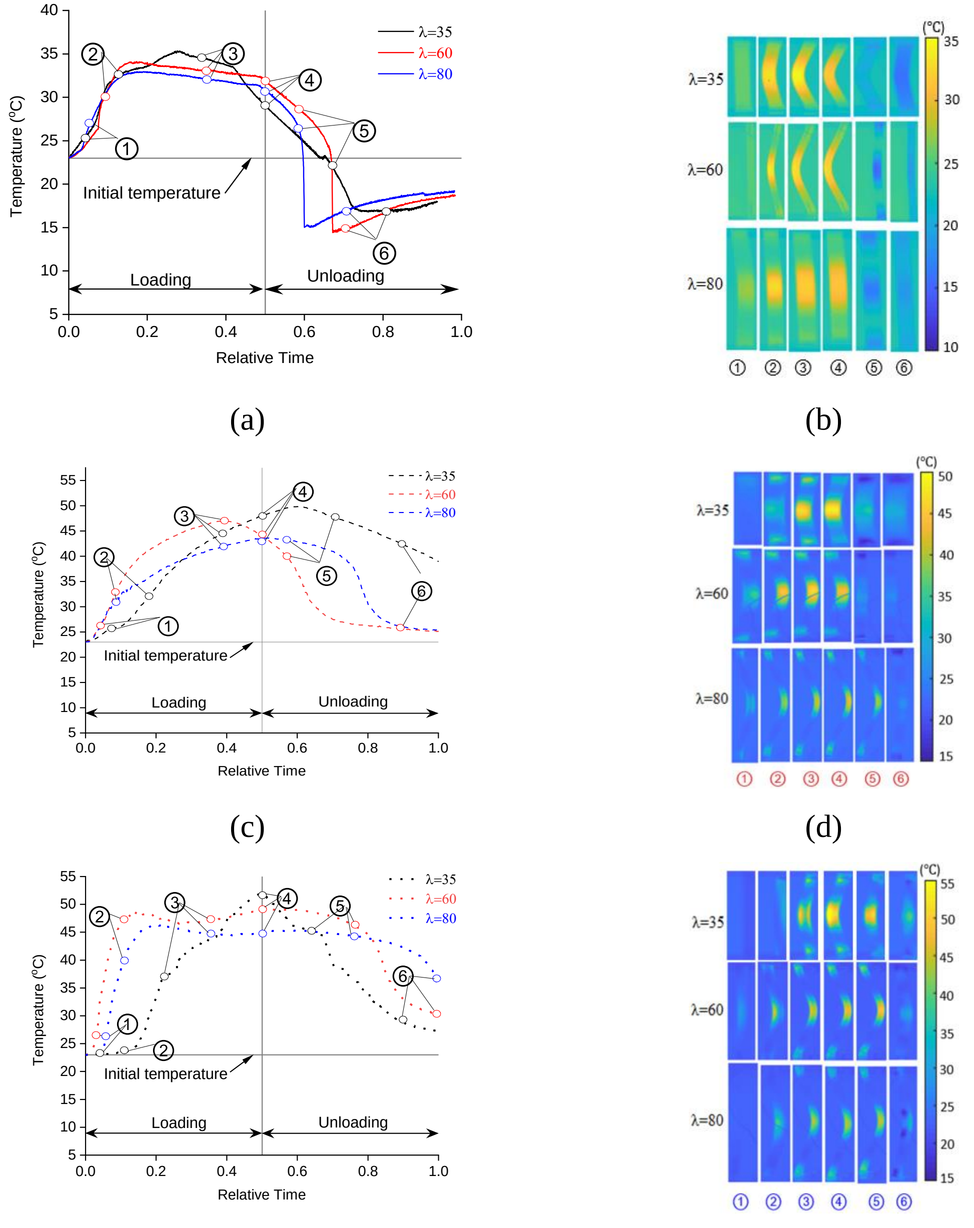

(a) (b)

(c) (d)

(e) (f)

Figure 3-13. The evolution of the maximum temperature with respect to normalized testing time for specimens with λ=35, λ=60, and λ=80 at strain rates of (a) 0.0002/s (c) 0.005/s, and (d) 0.01/s, and temperature field of specimens with λ=35 (first row), λ=60 (second row), and λ=80 (third row) at strain rates of (b) 0.0002/s (d) 0.005/s, and (e) 0.01/s

3.3.6 Buckling onset and determination of experimental critical buckling load

The onset of buckling is an important aspect to characterize since the load at which buckling initiated is an essential design parameter for practical applications of SMA bars. Commonly, the onset of buckling is identified by a substantial increase in the deformation for very small increase in the load parameter. A structure that satisfies conditions such as perfect initial geometry, uniform constitutive properties, rigid boundary conditions, and loaded with perfectly concentric compressive load is considered as ideal structure. In such cases, buckling takes place because of the presence of an inherent bifurcation on the primary equilibrium path to a secondary path [220]. To identify the onset of buckling and determine the critical buckling load, additional response parameters such as normalized lateral displacement and velocity (i.e., 1st time derivative of lateral displacement) were determined from the measured responses. The derivative was calculated by dividing the change in lateral displacement by the time step.

Figure 3-14(a) plots the normalized lateral deflection (Δ/L) against normalized axial displacement (δ/L_e). It can be seen that the normalized lateral deflection gradually changes to a nonzero value close to the onset of buckling. Short and long bars (i.e., $\lambda \leq 80$) buckled at normalized axial displacement of 1-2%, by contrast the slender bars (i.e., $\lambda > 80$) buckled at lower value. The variation of P/A_o and time rate of change of Δ/L (lateral velocity) as functions of δ/L_e are shown in Figure 3-14(b) and 3-14(c), respectively. It is apparent that the maximum velocity tended to lie at the same axial displacement level at which the maximum load occurred. Figure 3-15(a) and 3-15(b) show the velocity heat maps of specimens with slenderness ratio of 60 and 115, respectively. The heat maps reinforce the phenomenon that slender bars buckled instantaneously at lower axial displacements compared with short or long bars.

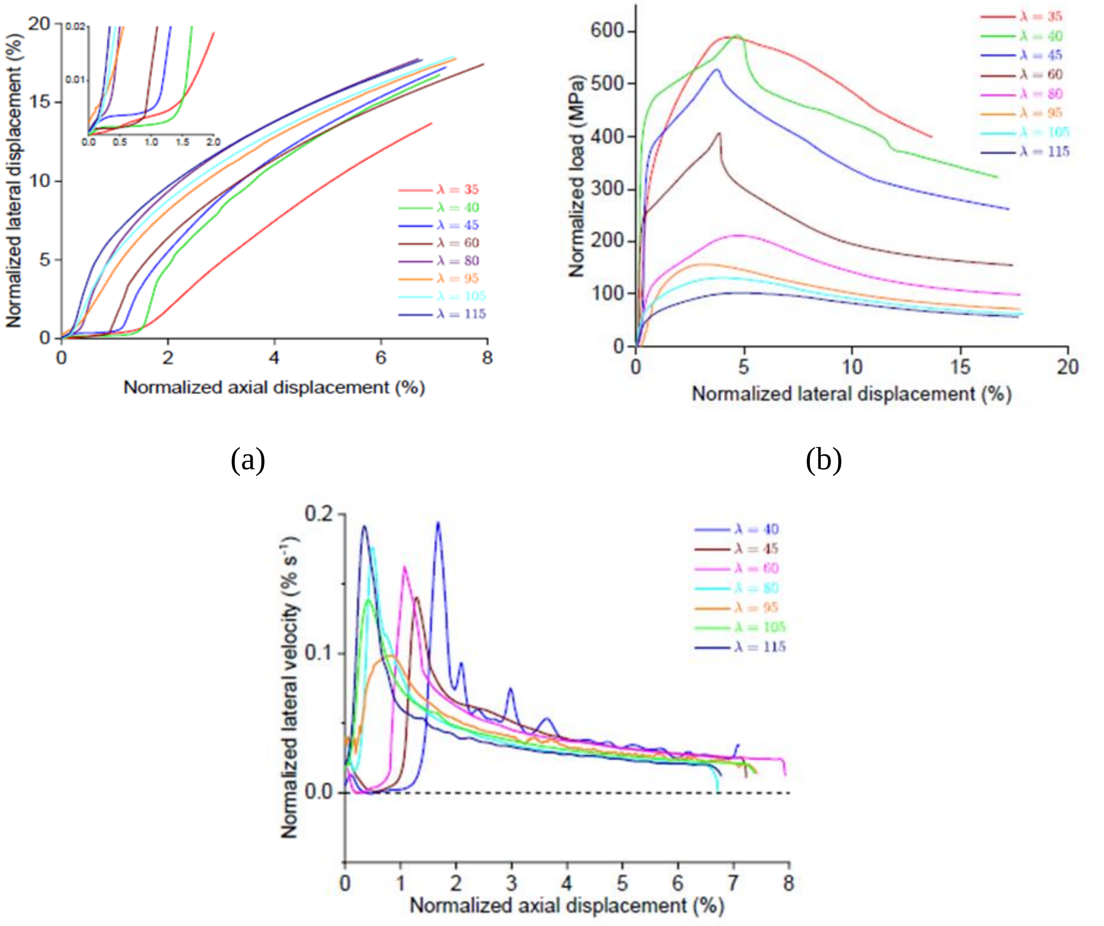

(a) (b)

(c)

Figure 3-14. Bifurcation diagrams: (a) lateral deflection-axial displacement, (b) compressive load-mid-length lateral deflection, and (c) mid-length lateral velocity-axial displacement

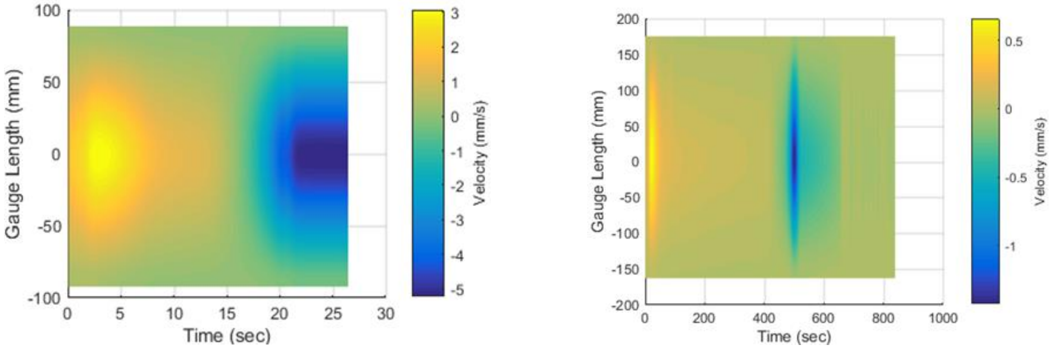

(a) (b)

Figure 3-15. Velocity heat maps for (a) λ= 60, and (b) λ=115

Two methods were considered to determine the experimental buckling loads for each specimen. In the first approach, the normalized load was plotted against normalized axial displacement. In the second approach, the normalized lateral velocity versus the normalized axial displacement was plotted. As illustrated in Figure 3-16(a) for short bars, the peak normalized load occurred at a normalized axial displacement at which the maximum lateral velocity was observed. The good correlation between the peak lateral velocity and the critical load seems plausible because the minimum slope (zero) of the load-deflection curve of a perfect system occurs at the instant of buckling. On the other hand, as shown in Figure 3-16(b), in the case of slender bars, the peak lateral velocity was observed at 85% of the normalized axial displacement at which the peak normalized load occurred. For the sake of uniformity, the experimental buckling loads were determined using the peak normalized load except for the specimen with slenderness ratio of 25 in which the buckling load was reported using peak lateral velocity plot.

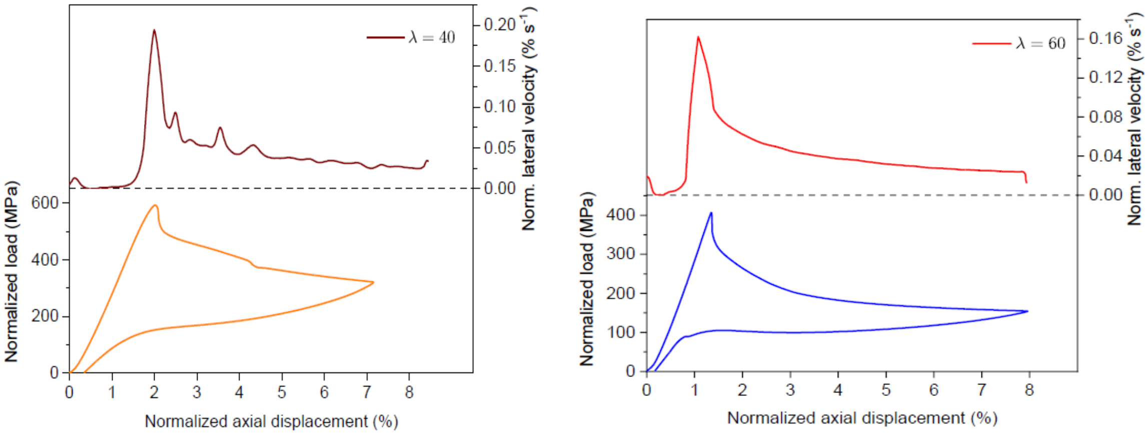

(a) (b)

Figure 3-16. Procedure for extracting experimental critical buckling loads: (a) λ= 40, and (b) λ=60

3.4 Analytical Prediction of Critical Buckling Loads

The theoretical buckling load of an ideal column was analytically predicted for each buckling experiment to assess if experimental errors were introduced in measuring the critical buckling loads. The analytical analysis was carried out using Euler's elastic buckling theory for slender columns and following Shenley's theory of inelastic column buckling for short columns [220]. For Euler's theory, the critical buckling stress is calculated using:

$$\sigma_E = \frac{k\pi^2 E}{\lambda^2} \tag{3.1}$$

where E is the austenite modulus of elasticity, analogous to the Young's modulus in conventional elasto-plastic materials and k is a correction factor that accounts for boundary conditions in the experimental test setup. A k value of 0.6 was used to calibrate flexibilities in the test setup and adjust critical buckling stress calculated based on a true fixed-fixed end condition.

According to the inelastic column buckling theory, the critical buckling stress (σ_c) of a fixed-fixed column is given by:

$$\sigma_c = \frac{4\pi^2 E_c^t}{\lambda^2} \tag{3.2}$$

Where E_c^t is the material uniaxial compressive tangent modulus at the critical buckling stress. The tangent modulus is same as the Young's modulus $E_c^t = E_c$ in the linear elastic region, and the above equation should converge to the classical Euler buckling load within that range. However, in the inelastic range, the tangent modulus ($E^t = {}^{\partial\sigma}\!/_{\partial\varepsilon}$ during loading) varies with the applied load, so equation (3.2) is an inexplicit equation with respect to a loading parameter. Here, $\Lambda = {}^{\delta}\!/_{L_e}$, the axial displacement divided by the DIC gauge length, is chosen as the loading parameter. Thus, it can be inferred from equation (3.2) that buckling resistance of a column depends on the material stiffness (E^t) and the column slenderness ratio (λ). To aid in the determination of σ_c , the following functions are defined as:

$$\sigma(\Lambda) = \frac{P(\Lambda)}{A_o} \tag{3.3}$$

$$\sigma^{'}(\Lambda,\lambda)=\frac{4\pi^2E^t(\Lambda)}{\lambda^2} \tag{3.4}$$

where P is the axial load and. A_o is cross sectional area.

By plotting the experimentally measured pure compression response P/A_o against the function given by equation (3.4), the theoretical critical buckling stress σ_c was determined as the value that corresponds to the intersection of the two lines. This calculation procedure is illustrated in Figure 3-17. Note that the tangent modulus was obtained by taking the derivatives of experimental results after making necessary filtration and curve smoothening to minimize apparent noise effects.

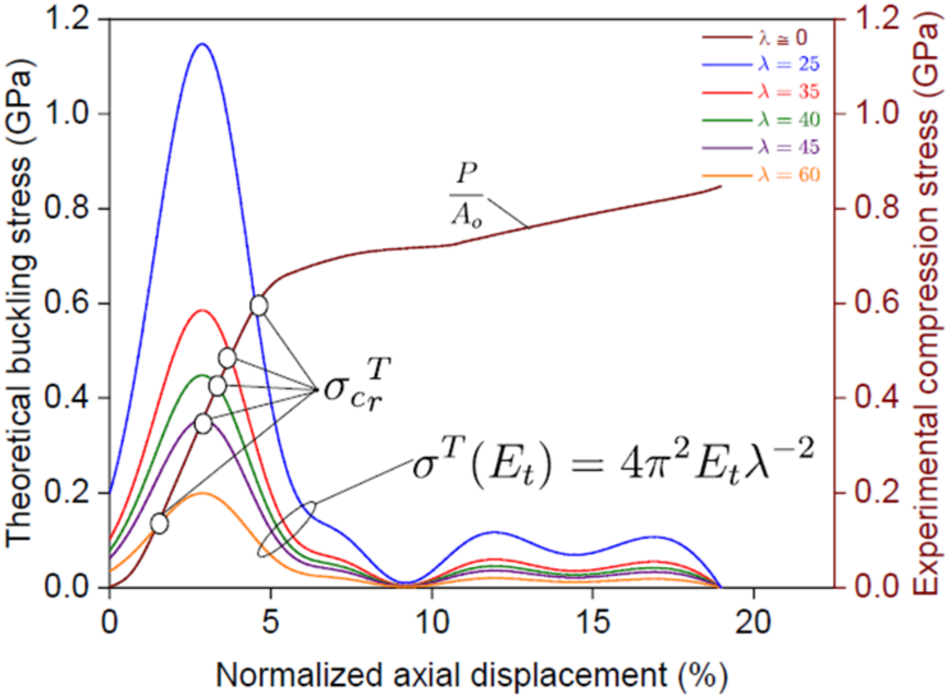

Figure 3-17. Procedure for analytical prediction of critical buckling stresses

The analytically predicted critical buckling loads for all specimens over the range of slenderness ratio examined in this study are shown in Figure 3-18 together with the corresponding experimental values. The compressive forward martensite transformation stress, extracted from the pure compression test, is marked with a red horizontal line. The specimens with slenderness ratios ranging from 60 to 115 buckled elastically in the austenite phase. On the other hand, the specimens with slenderness ratio of 25 and 35 experienced SIMT prior to the onset of buckling. The specimens with slenderness ratio of 45 buckled when the transformation phase began. Therefore, the results suggest that the threshold slenderness ratio for the influence of SIMT on the buckling behavior can be taken as 45. For NiTi SMA bars with $\lambda \leq 45$ (the light gray shaded region in figure 16), the pure compression behavior dominates the buckling and post-buckling behaviors. Whereas, flexural buckling due to secondary moment (i.e., P-Δ effect) governs the buckling and post-buckling responses of slender bars (the unshaded region in Figure 3-18). The theoretical buckling stresses of those specimens that buckled in the elastic region were found to correspond very well with the experimental buckling loads. However, as anticipated, for the specimens with slenderness ratios between 25 and 45, the Euler's elastic buckling model over-predicted the critical buckling loads. For that slenderness ratio range, tangent modulus theory was used to predict the buckling load. For slenderness ratios of 25 and 35, the difference between experimental and analytical buckling loads were 0.1% and 13%, respectively, indicating satisfactory results. However, for the slenderness ratio of 45, the analytical buckling load predicted by tangent modulus theory was 28% lower than the experimental result.

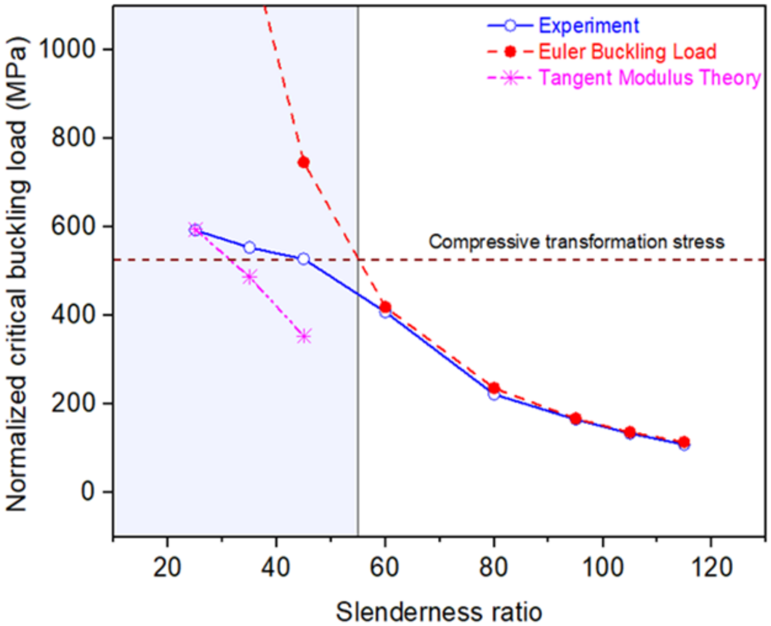

Figure 3-18. Experimentally measured and analytically predicted critical buckling loads for different slenderness ratios

3.5 Summary

In this chapter, the buckling and post-buckling responses of large diameter superelastic NiTi bars were investigated. First, the transformation temperatures were determined using a digital scanning calorimetry. Then, the uniaxial tensile and compression responses were characterized. Next, to explore the effects of material and geometric nonlinearities (i.e., phase transformations and P-Δ effects, respectively) on buckling behavior of SMA bars, fifteen 12 mm diameter bar specimens with slenderness ratios ranging from 25 to 115 were tested under axial compression loading. A digital image correlation system was used to monitor the full field surface displacements. This enabled to observe any interaction between phase transformation and second order effects. The normalized load-axial displacement curves were plotted to illustrate buckling response of superelastic SMA bars. The lateral deflections and rate of change of lateral deflections were analyzed to identify the onset of buckling. Six additional specimens were tested at a strain loading rates of 5×10^{-3} mm/sec per mm, and 1×10^{-2} mm/sec per mm to assess the effect of loading rate on the buckling response of SMA bars. Finally, a comparison between experimental and theoretical buckling loads was presented. The main findings are summarized hereafter:

- Well-known asymmetry in tension and compression response of SMAs were observed in the tested NiTi bars. While stress induced transformation localization was observed in the tensile response, the compression behavior was characterized by homogenous deformation with the absence of flat-stress plateau.
- Slender bars recovered nearly all of the post-buckling deformation upon unloading. This implies that buckling of SMAs may not be considered as failure, which is generally concluded for elastoplastic materials.
- Within the range of slenderness ratio examined in this study, short bars ($\lambda<=45$) were found to buckle inelastically due to the onset of phase transformation induced softening, whereas slender bars ($\lambda=>60$) buckled elastically.
- Geometric nonlinearity due to P-Δ effect has a dominant effect than material nonlinearity on the buckling behavior of slender bars. Therefore, $\lambda=45$ was considered as the threshold slenderness ratio for the transition from inelastic to elastic buckling modes.

- Higher critical buckling loads were observed on specimens with a slenderness ratio of 35 and 80 tested at higher strain loading rates. However, for specimens λ=60, the loading rate does not noticeably affect the critical buckling load, but the post-buckling branches showed a considerably upward shift compared with the quasi-static counterpart. In addition, the residual deformations increased with increasing loading rate.
- Surface temperature variations of specimens tested at various loading rates indicated that that the buckling behavior of NiTi SMA bars is sensitive to the loading rate and slenderness ratio due to the interaction of the heat induced from the phase transformation and the applied load.
- Analytical predictions of the critical buckling loads were performed using the Euler and tangent modulus theories. The Euler's elastic buckling model provided good results for slender specimens buckled elastically at the austenite phase. For inelastically buckled bars, the tangent modulus theory provided reasonable results. However, a more refined analytical model is needed to describe the critical buckling load of these SMA bars.

4 CHARACTERIZATION OF CONFINED SUPERELASTIC DISSIPATORS (CSD)

4.1 Overview

Past studies on seismic applications of SMAs have mainly focused on the utilization of uniaxial tensile behavior of SMAs because of undesirable compression-induced buckling and lack of knowledge on compression behavior. The most commonly adopted solution to this issue is to elaborately design a configuration that converts compression into tension in SMA bars. This obviously discount the SMA contribution under compression and leads to inefficient material utilization in addition to the complex mechanical configuration to realize the function.

Building on the knowledge gained from Chapter 3 on the buckling and post-buckling behavior of SMA bars, this chapter proposes an alternative type of SMA-based damping device named as Confined Superelastic Dissipator (CSD). The proposed dissipator consists of a necked-down superelastic NiTi SMA round bar as the functional kernel component encased in grout filled steel tube. The bar carries tension and compression loads and dissipates energy through axial deformation while the steel tube and infill grout restrain the bar and precludes buckling in compression.

Considering the merits of SMAs, a few studies have been explored the use of SMA bars in buckling restrained energy dissipators [157,158,221]. However, in these earlier efforts, either one or only a few specimens were tested, and the effects of geometric design parameters on the performance of device has not been studied. Furthermore, fuse type dissipators can be fabricated in two ways, “wet” and “dry”, depending on whether an initially liquid filling material is used or not as a part of the buckling restraining mechanism. Each method has its own advantages and disadvantages. For instance, anti-buckling system made of grout filled steel tubes provides continuous lateral support to the SMA bar such that local buckling is inhibited. On the other hand, a dry-type dissipater avoids the need of extra effort for the filling material placement. In the above noted efforts on the SMA-based dissipaters, the buckling restrained mechanism consisted of bolted metal plates.

Firstly, the different components of the CSD and its working principles are discussed, followed by brief summary on the theoretical background on global and local stability criteria for the design of the CSDs. Subsequently, details about fabrication and testing of eight specimens under incrementally increasing cyclic loading are presented. To provide a comprehensive understanding of the dissipators' structural behaviour, several specimens, accounting for different geometric properties, were tested under quasi-static cyclic protocol. The chapter provides detailed discussion on the observed test results of the different specimens interms of overall force-displacement response, the effects of geometric parameters on their failure mechanism and response quantities that are prime interest for earthquake engineering such as energy dissipation, equivalent viscous damping, and self-centering capability. In the final part of the chapter, a numerical case study is conducted to demonstrate one application of the CSDs in seismic retrofitting of non-ductile beam-column connection.

4.2 Description and Potential Applications of CSDs

4.2.1 Description

The CSD is composed of a superelastic NiTi SMA bar placed inside a round steel tube. Figure 4-1displays the component parts and assembled views of the proposed dissipator. It can be seen from Figure 4-1(b) that the SMA bar has a central reduced portion (referred as "fuse") formed by milling down the original rod. By contrast, the ends have a full cross-section and can be threaded to provide a connection of the dissipator to other structural members. The interim space between the SMA bar and steel tube is filled with cement grout. A thin layer of debonding material is employed to prevent shear transfer at the bar-grout interface. The carefully chosen debonding material has the capability of preventing friction between the bar and the restrainer, thus allowing axial independence. It also accommodates lateral expansion of the bar during compression. When the dissipator is loaded in tension or compression, the bar carries the axial load while the steel tube, via the infill grout, restrain it and precludes global buckling in compression. As it moves back and forth inside the steel tube, the axial deformation causes the SMA bar to undergo a phase transformation process. This mechanism allows the dissipation of seismic energy by converting kinetic energy into strain energy. Besides, due to the inherent flag-shaped hysteretic behavior of SMAs, the CSD possesses self-centering capability.

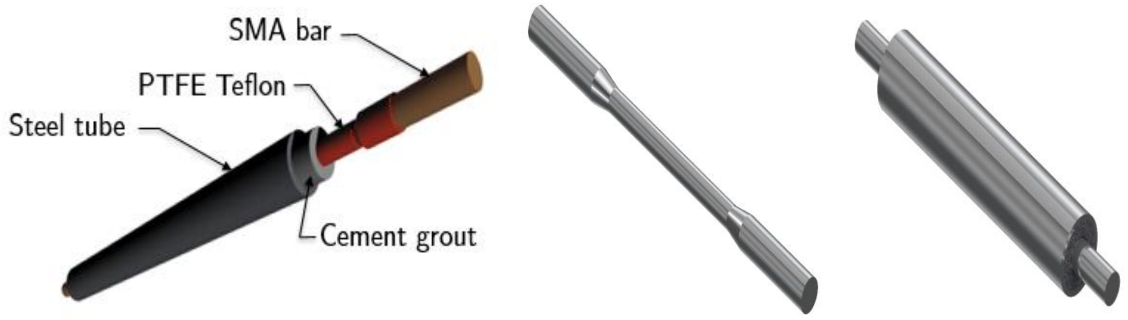

(a) (b) (c)

Figure 4-1. Proposed CSD: (a) component parts; (b) machined NiTi SMA bar; (c) assembled view

Compared with conventional axial dissipators available in the literature, the CSDs have the following additional advantages:

1. Self-centering: Although steel-based buckling-restrained dissipators can provide good energy dissipation and limit deformations, they lack self-centering mechanism and cannot prevent residual displacement following an earthquake. On the other hand, CSDs offer self-centering capability to the structure, which reduces or even eliminates permanent structural deformations.

2. Reusable: Low damage design philosophies [55,222], which more recently have gained increasing attention, commonly employ supplemental energy dissipating devices to limit damages to structural members. Often, these conventional dissipators are left with significant damage aftermath of earthquakes and need to be replaced. However, the use of CSDs in that regard, is advantageous since they are damage tolerant and are reusable dissipators.

3. Corrosion-free: Corrosion significantly degrades the dissipating energy capacity of commonly used conventional metallic dissipators [223]. Typically, the dissipators are installed externally to structural member and are exposed to corrosive environments. Owing to high corrosion resistance of NiTi SMAs, with the use of tubes made up of corrosion resistant materials such as stainless steel and fiber reinforced polymer, CSDs are best suited for applications in harsh environments.

4. Self-sensing: Superleastic SMAs change their crystallographic structures through phase transformation as well as electrical resistance during the loading-unloading process [224]. By studying the relationship between strain and electrical resistance measurements, it is possible to determine the deformation or stress state of an SMA-based dissipators without separate sensors. In that perspective, CSDs have the potential to be implemented for both structural control and health monitoring purposes. This aspect of CSDs is not studied in the current work but can be subject of a future study.

4.2.2 Potential applications

Predictable energy dissipation, inherent self-centering capability, and compact size make CSDs competent candidate for several applications where those features are needed in a single device. As illustrated in Figure 4-2, the CSDs the mini plug and play type CSDs offer a wide range of applications. They can be leveraged for earthquake protection of structural components such as beam-column joints, walls or columns, and non-structural components such as computer servers, merchandizing pallet racks, standby power generators, transformers, and other expensive medical equipment. Given the simple installation of the device in a variety of structures, they can be referred to as “plug and play” devices. It is envisioned that the CSD will find many potential applications in bridges as well. They may be implemented as restrainers to avoid unseating or pounding, as a component of ductile end cross frames (or diaphragms) to resist transverse earthquake loading, or as external energy dissipators in rocking piers and bents.

It is also worth noting that CSDs could have great potential to be part of connections between precast bridge elements, thus promoting accelerated bridge construction (ABC) in moderate to high seismic zones. ABC has been embraced worldwide as a way of reducing on-site construction time, traffic disruptions, environmental impacts, and improving work-zone safety and construction quality. Although many ABC techniques have been successfully implemented in low seismic areas, the application is very limited in regions of moderate-to-high seismic activity. Connection details are the most critical issue facing the use of precast elements in seismic regions, especially if they are located where inelastic deformations occur. They must not only be easy to construct but also must be robust enough to maintain the integrity of component elements under seismic loading. In this regard, as shown in Figure 4-2(b), the CSDs can be installed across the column-footing or column-bent cap interfaces of precast concrete piers to form dissipative controlled rocking (DCR) system. The bridge can rock and re-center to plumb after an earthquake while the input seismic energy is dissipated through the CSDs.

4.2.3 Design considerations

The design steps of the CSD are inspired by the BRB design procedure [225]. It primarily involves an examination of the potential global and local instabilities of the dissipator when it is subjected to compressive forces. Figure 4-2 illustrates the deformation behavior of the CSD when subjected to elongation and shortening. For reference, the undeformed configuration and nomenclature of various parameters are shown in Figure 4-2(a).

Knee-braced steel frame

Dissipated controlled rocking (DCR)
Multi-column bent

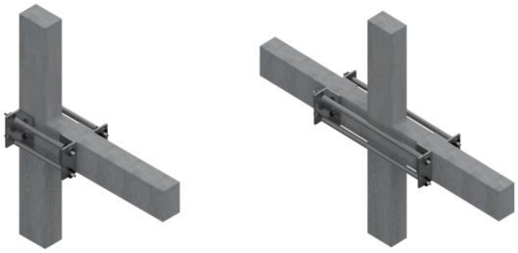

Self-centering RC beam-column

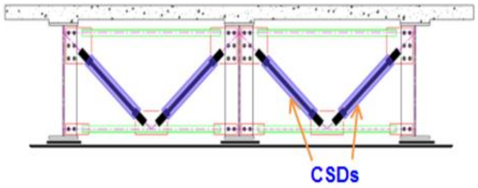

Ductile end cross frame

Cross laminated timber (CLT) beam-column

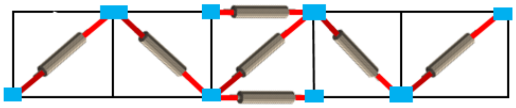

Steel or timber trusses

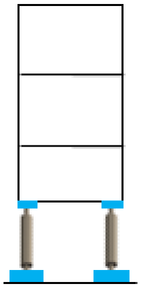

Servers

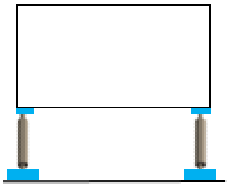

Transformer/
fragile medical equipment or
other expensive equipment

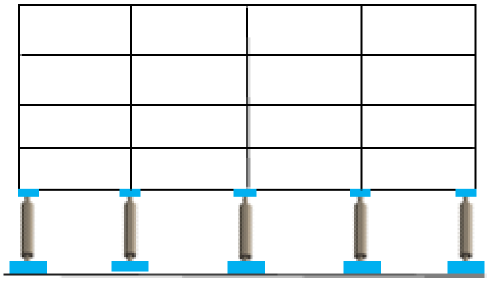

Merchandize pallet racks

Figure 4-2. Potential applications of CSDs for seismic protection of various structural and non-structural components

For the sake of simplicity, the load applied to the dissipator, P is assumed to be known from structural analysis. The CSD factored design strength, φP_n must satisfy the relationship given in equation (4.1).

$$\varphi P_n \geq P \tag{4.1}$$

The factored design strength can be determined based on equation (4.2).

$$\varphi P_n = \varphi(A_{SMA}\sigma_s^{AM}) \tag{4.2}$$

where A_{SMA} is the area of the SMA bar at the reduced section, $\varphi = 0.9$ is a strength reduction factor, and σ_s^{AM} is forward transformation start stress of SMA bar, and P_n is the CSD nominal strength. The superelastic strain amplitude (maximum recoverable strain), ε_L is another key parameter in the seismic design of SMAs. In this study, a value of 6% is conservatively taken. Given the cross-sectional area (A_{SMA}) calculated from equation (4.2), the reduced diameter of the SMA bar, d_R can be easily determined.

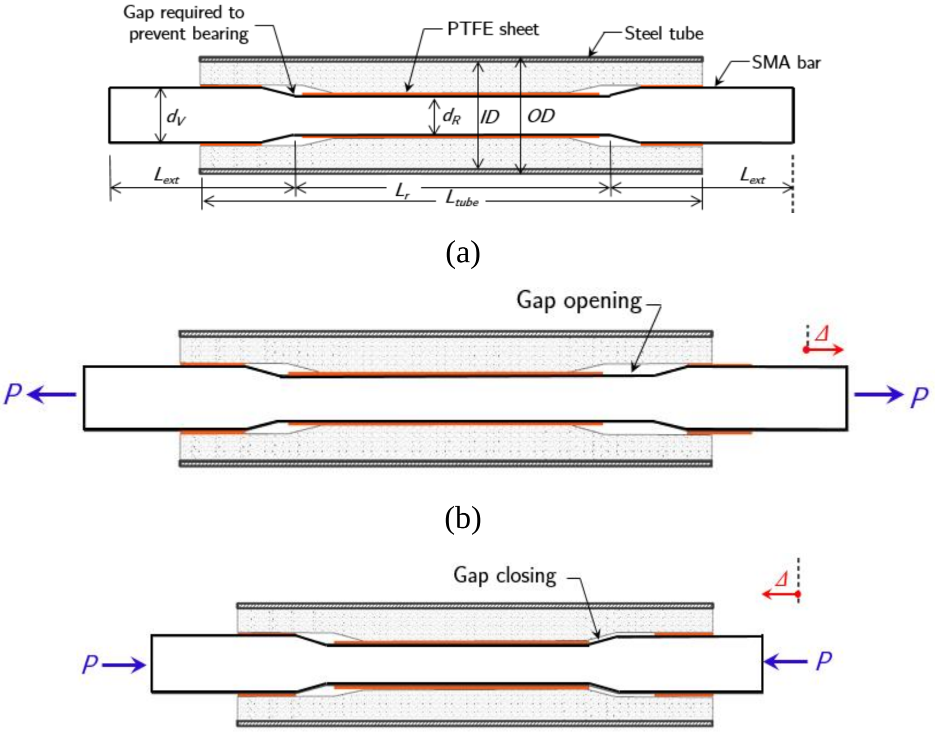

(a)

(b)

(c)

Figure 4-3. Working principle of the CSD: (a) equilibrium; (b) tension; (c) compression

As stated before, the cross-section of the SMA bar gradually increases at the ends to ensure that the phase transformation occurs over a specified length of the fuse. The transformation could be forced to occur within the fused portion by ensuring that when the fuse reaches the forward transformation finish stress, the stress on the virgin bar ends should be below the transformation start stress. This is mathematically expressed in equation (3) as follows:

$$d_R \leq d_V \times \sqrt{\frac{\sigma_s^{AM}}{\sigma_f^{AM}}} \tag{4.3}$$

where σ_f^{AM} is austenite to martensite forward transformation finish stress, d_R and d_V are the SMA bar diameters at the fuse and unreduced sections, respectively. Two possible details are recommended to transition from the full section of the bar to the fuse portion. As shown in Figure 4-4(a), both a circular tapered transition from d_V to d_R with a taper radius of $r_t = d_R$ and a 4:1 slopped transition will inhibit stress concentrations. A gap between the taper and the grout fill shall be provided to prevent direct bearing and undesirable overstrength when the dissipator is in compression. The required gap bearing may be estimated by equation (4.4) as:

$$\Delta_b = 1.25(L_r \times \varepsilon_L) \tag{4.4}$$

where Δ_b is gap bearing, ε_L is maximum recoverable strain, and L_r is length of fuse portion. As illustrated in Figure 4-4(b), an Ethylene vinyl polystyrene foam could be employed to form the gap.

Depending on the intended application of the SMA-based dissipator, the required stroke and/or stiffness can be obtained from structural analysis. Then, the required fuse length of SMA bars can be determined from either equation (4.5) or (4.6) as follows:

$$L_r = \frac{E_{SMA} A_{SMA}}{K} \tag{4.5}$$

$$L_r = \frac{\Delta_D}{\varepsilon_r} \tag{4.6}$$

where K and Δ_D are given stiffness and stroke, respectively, E_{SMA} is the modulus of elasticity of SMA at the full austenite state.

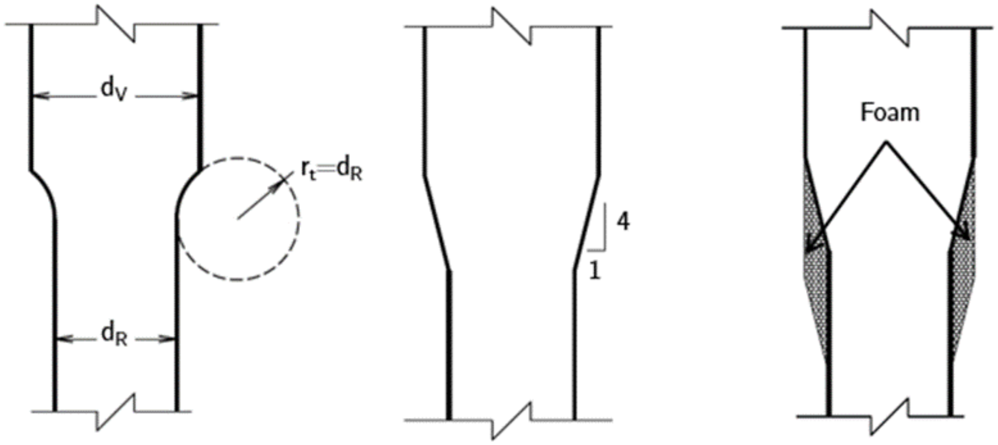

(a) (b)

Figure 4-4. CSD details: (a) recommended taper details to transition from virgin SMA bar. end to dog-bone milled section; (b) dissipator transition area with gap bearing

Once the necessary geometric parameters of the SMA bar are proportioned, the next step is the design of the buckling restraining system. It should be designed such that it ensures the global and local stability of the SMA bar. The global stability of the CSD may be estimated directly from the Euler theory of buckling. Figure 4-5(a) shows the schematic of the CSD in compression, while Figure 4-5(b) and 4-5(c) show the distributed load on the SMA bar and the encasing grout/steel tube in the deformed configuration. The unknown distributed load $w(x)$ shown in Figure 4-5(b), is the transverse reaction of the confining tube/encasing grout along the SMA bar. The equilibrium of the SMA bar in its deformed configuration is given by equation (4.7) using the system of axes shown in Figure 4-5(a) as:

$$E_{SMA}I_{SMA}\frac{d^4y(x)}{dx^4}+P\frac{d^2y(x)}{dx^2}=-w(x) \tag{4.7}$$

where $y(x)$ is the transverse deflection, P is the axial load, and I_{SMA} is the moment of inertia of the SMA bar. The negative sign on the right-hand side of equation (4.7) results from the fact that $w(x)$ acts in the direction opposite to the deflection $y(x)$. The equal and opposite distributed load $w(x)$ is loading the encasing grout/steel tube, as shown in Figure 4-5(c). The equilibrium equation of the tube when it is bend is given as:

$$E_s I_s \frac{d^4 y(x)}{dx^4} = w(x) \tag{4.8}$$

where $y(x)$ is the same transverse deflection appearing in equation (4.7), and $E_s I_s$ is the flexural rigidity of the encasing grout/steel tube. Eliminating the unknown $w(x)$ in equations (4.7) and (4.8) and rearranging the terms gives the following equation:

$$\frac{d^4 y(x)}{dx^4} + \frac{P}{\left(E_{SMA} I_{SMA} + E_s I_s\right)} = 0 \tag{4.9}$$

For a CSD with an unsupported length of L_{un}, the following equation yields the critical buckling load of the dissipator:

$$P_{cr} = P_e = \frac{\pi^2}{(KL)^2}\left(E_{SMA} I_{SMA} + E_s I_s\right) \tag{4.10}$$

where KL is the effective (equivalent) length ($K = 1$ for a pinned end condition and $K = 2$ for a fixed end condition).

Note that those K values are for theoretical cases. However, the actual boundary conditions for a real-world implementation or a laboratory test setup are somewhere in between pinned and fixed. Hence, it is important to adjust the K value accordingly. Neglecting the bending rigidity of the SMA bar, $E_{SMA} I_{SMA}$, which is two or three orders of magnitude smaller than the bending rigidity of the encasing grout/steel tube $E_s I_s$, equation (4.10) simplifies to:

$$P_{cr} = P_e \approx \frac{\pi^2 E_s I_s}{(KL)^2} \tag{4.11}$$

Therefore, equation (4.11) indicates that the critical buckling load of the CSD is merely the Euler buckling load of the steel tube. Accordingly, the global stability of the dissipator is ensured when the Euler buckling load of the tube exceeds the austenite to martensite transformation finish load of the SMA bar, i.e., $A_{SMA}\sigma_f^{AM}$.

The effectiveness of the dissipator can be increased when the local buckling of the SMA bar along the restrained length does not occur. Assuming that the reaction of the confining grout can be approximated by an elastic foundation, the distributed load $q(x)$ exerted along the SMA bar, as depicted in Figure 4-5(c), can be expressed as $q(x)=\beta y(x)$, where β is a distributed spring constant with dimension of $[F]/[L^2]$ and $y(x)$ is the transverse deflection of the SMA bar. With this assumption, equation (4.7) is rewritten as:

$$E_{SMA}I_{SMA}\frac{d^4y(x)}{dx^4}+P\frac{d^2y(x)}{dx^2}+\beta y(x) \tag{4.12}$$

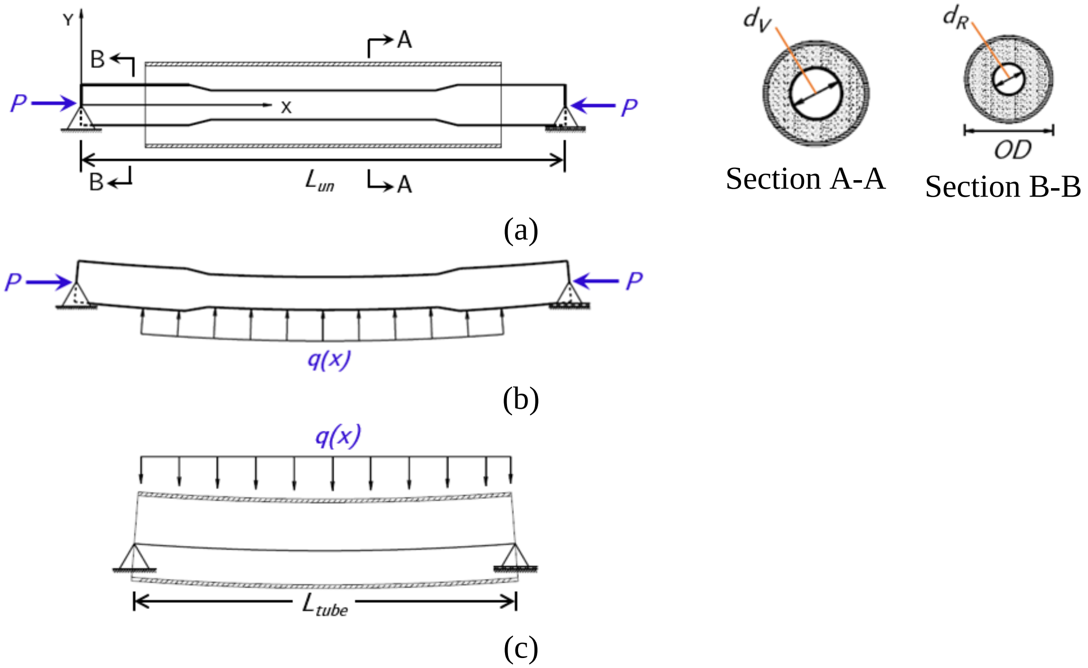

(a)

(b)

(c)

Figure 4-5. (a) The CSD under axial compression load; (b) distributed load along SMA bar in the deformed configuration; (c) distributed load along the encasing grout/steel tube

The solution of the homogeneous equation (4.12) can be obtained by following either an energy method approach or direct integration. Thus, the critical load due to buckling of the SMA bar in higher modes is given by:

$$P_{cr} = 2\sqrt{\beta E_t I_{SMA}} \tag{4.13}$$

where E_t is tangent elongation modulus. The equation (4.13) has a format similar to the equation developed for the steel core unbonded BRBs as provided in Wada *et al.* [226], among others. Therefore, to avoid high order local buckling of the SMA bar, the following criterion must be satisfied:

$$P_{cr} = 2\sqrt{\beta E_t I_{SMA}} \geq A_{SMA}\sigma_f^{AM} \Rightarrow \beta \geq \frac{\left(\sigma_f^{AM} A_{SMA}\right)^2}{4E_t I_{SMA}} = \frac{\pi(\sigma_f^{AM})^2}{E_t} \tag{4.14}$$

$$\beta = E_g \frac{1-\nu}{(1+\nu)(1-2\nu)} \tag{4.15}$$

where E_g is the Young’s modulus and ν is the Poisson’s ratio of the encasing grout. As given in equation (4.15), the value of the distributed spring constant β can be estimated by computing the one-dimensional compression modulus of grout confined by the steel tube and longitudinally by its neighbouring grout assuming plain strain conditions. It is crucial to ensure that adequate grout exists between the SMA bar and the inner wall of the restraining tube. There may be a possibility of local buckling where the grout cover is thin. In general, care should be exercised in sizing the different components of the dissipator.

4.3 Experimental Testing

4.3.1 Materials

In this work, 12 mm diameter superelastic NiTi SMA bars with a chemical composition of 50.7 wt.% Ni and a 49.3 wt.% Ti were procured from Baoji Seabird Metal Material CO. LTD. The as-received bars were heat-treated using an electrical furnace at 400°C for 30 min, and then water quenched. The forward and reverse transformation temperatures were determined using a differential scanning calorimetry (DSC). As can be seen in Figure 4-6, after the heat treatment, the forward transformation temperatures are -45°C and -56°C for martensite start (M_s) and martensite finish (M_f), respectively. The reverse transformation temperatures are -32°C and -19°C for austenite start (A_s) and austenite finish (A_f), respectively. The result implies that the material is superelastic at room temperature.

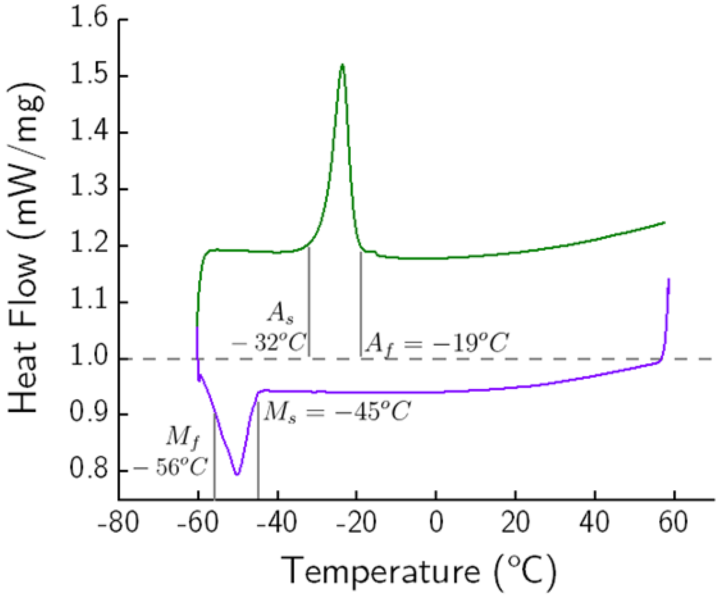

Figure 4-6. Differential scanning calorimetry (DSC) test result

For the confining tubes, 4130 Alloy steel circular hollow sections were used as readily available materials. A general-purpose non-shrink cementitious grout SikaGrout®-212 was employed to fill the gap between the SMA bar and steel tube. Table 4-1presents the mechanical properties of the grout as provided by the manufacturer.

Table 4-1 Mechanical properties of SikaGrout®-212 grout.

	Plastic	**Flowable**	**Fluid**
Compressive strength (MPa)	51.7	42.7	40
Flexural strength (MPa)	9.6	8.2	6.8
Splitting tensile strength (MPa)	4.1	3.9	3.4
Tensile adhesion strength (MPa)	13.7	13.1	13.1

4.3.2 Test matrix

The experiments were designed in a way that important geometric parameters that could influence the failure mechanism of dissipator were strategically evaluated. Among the parameters to be considered were the fuse diameter, length, and the strength and stiffness of the buckling restraining system. The variations in fuse diameter (d_R) and length (L_r) were collectively accounted for by a slenderness ratio, defined as $\lambda = {}^{4L_r}\!/_{d_R}$. These were accomplished by testing a total of eight specimens. Four different specimens were fabricated for a fuse slenderness ratio of 60. The fuse lengths for those specimens were 20 mm, 135 mm, 150 mm, and 180 mm, while the diameters were 8 mm, 9 mm, 10 mm, and 12 mm, respectively. A variation in fuse slenderness ratio (60, 75, and 90) was considered for the largest fuse diameter of 15 mm. Thus, the fuse lengths of last three specimens were 225 mm, 281 mm, and 338 mm, respectively. Two specimens having the same slenderness ratio of 75 but different diameters of 12 mm and 14 mm were tested to identify the effect of the fuse diameter on the hysteretic behavior of the dissipator. Overall, a constant difference between fuse and external diameter that ranges from 2 mm to 5 mm was taken into account. The summary of the testing schedule is reported in

Table 4-2. In the table, *OD*, *ID*, and L_{tube} refer to the outer diameter, inner diameter and length of the steel tube as depicted on Figure 4-3(a)The nomenclature of specimens is based on fuse diameter and length; for instance, D8L120 refers to a specimen with a fuse diameter of 8 mm and length 120 mm.

Table 4-2. Test parameters.

Specimen ID	d_V **(mm)**	d_R **(mm)**	L_{ext} **(mm)**	L_r **(mm)**	L_{total} **(mm)**	**λ**	***OD*** **(mm)**	***ID*** **(mm)**	L_{tube} **(mm)**
D8L120	12	8	90	120	300	60	28.6	19.1	250
D9L135	12	9	107.5	135	350	60	28.6	19.1	298
D10L150	12	10	112.5	150	375	60	28.6	19.1	322
D12L225	16	12	102.5	225	430	75	22.2	31.8	369
D14L262	16	14	118.8	262.5	500	75	22.2	31.8	436
D15L225	20	15	72.5	225	370	60	28.6	38.1	309
D15L281	20	15	78.4	281.3	438	75	28.6	38.1	372
D15L337	20	15	83.75	337.5	505	90	28.6	38.1	433

4.3.3 Specimen fabrication

Figure 4-7 illustrates the steps in the CSD fabrication. First, the SMA bars were machined to dog-bone shape and then heat-treated. Small pieces of ethylene vinyl polystyrene foam were attached at both ends of the tapered sections to form a pocket that will allow the shortening of the SMA bar without compressing the grout. Wrapping the polystyrene with tape will ensure that the gap gearing will be located at the correct place after the grout is set. The SMA bar was then covered with a 0.8 mm thick adhesive-backed polytetrafluoroethylene (PTFE) sheet followed by a layer of 0.09 mm thick adhesive PTFE tape. The PTFE tape was used to cover over the seams and edges of the PTFE sheet such that the grout will not get under the sheet. The tape and the sheet act as a debonding layer between the grout and the SMA bar. This enables the bar to slide relatively free inside the restraining tube while also allowing (through the compressibility of the tape/sheet layer) a small amount of transverse expansion of the bar associated with Poisson’s effect. The debonding layer thickness was estimated by correlating the axial deformation and change in diameter of the fuse section using a Poisson ratio of 0.2. The space between the restraining tube and the SMA bar was filled with SikaGrout®-212 grout. The grout was mixed by adding a necessary amount of water to get a flowable consistency. Pouring was performed by sealing or covering one end of the tube, holding the other end in an upright position. As such, gravity ensured an even distribution of the grout through the inner tube. The SMA bars must be centered as accurately as possible within the confining steel tube when the grout is poured. Finally, the specimens were left for a couple of days for the grout to harden.

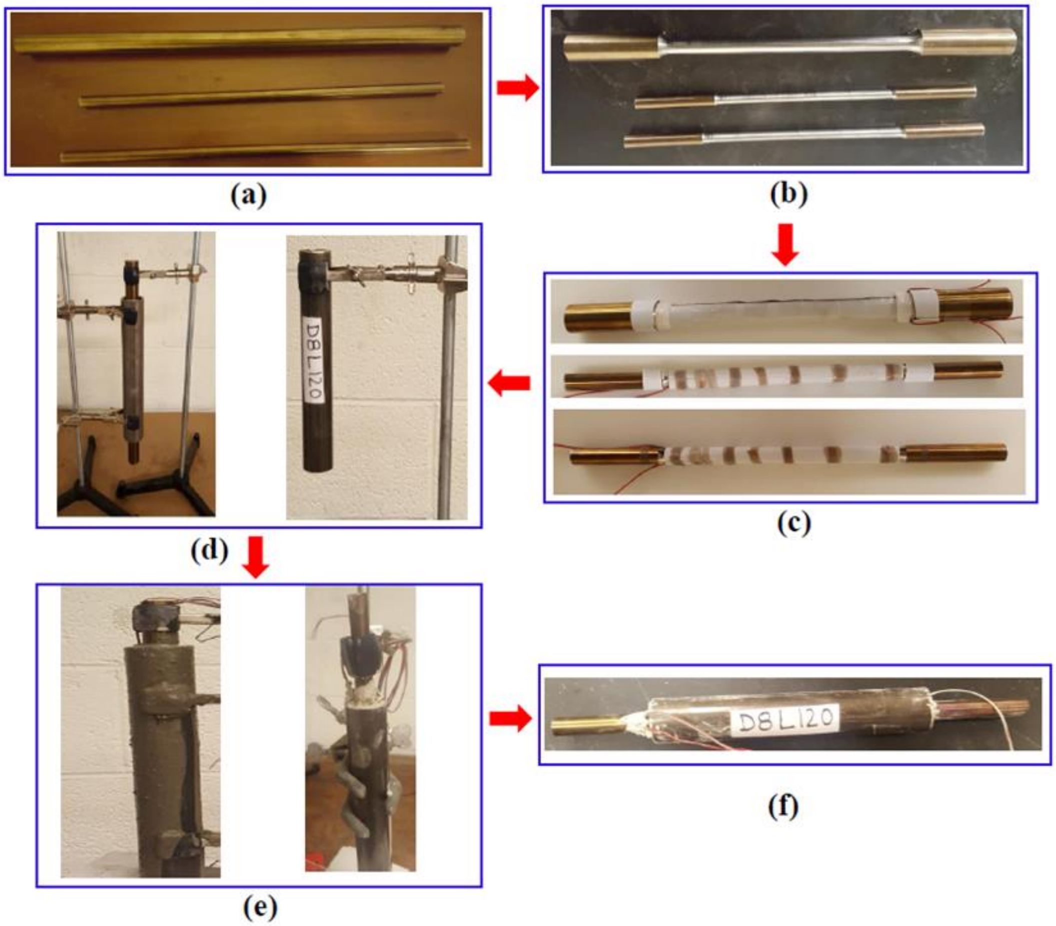

Figure 4-7. A general fabrication process for the CSDs: (a) as-received SMA bars; (b) bars machined to dong-bone shape and heat-treated afterward; (b) adhesive-backed Teflon tape used as the debonding material; (c) SMA bars inserted into the restraining tubes and one end of the CSDs completely blocked with stopper to prevent the grout from pouring out; (d) SikaGrout® poured from the top end of the CSDs; (e) final view of a CSD.

4.3.4 Test setup and loading protocol

All tests were performed using an MTS 810 servo-hydraulic universal testing machine equipped with a 250 kN capacity load cell. The specimens were gripped by MTS 647 hydraulic wedge grips with semi-circular grooves at the center. Figure 4-8 shows a photograph of the test setup.

During a typical test, an incrementally increasing deformation loading pattern was applied to each specimen. In particular, the deformations corresponding to 1% strain in SMA bar up to failure with a 1% increment were applied. The specimens were subjected to two cycles of each loading amplitude. The loading pattern was controlled by the cross-head displacement, which was derived from the nominal axial strain of the central fuse section multiplied by the fuse length, L_r. This was commanded at a prescribed rate while the MTS built-in data acquisition system recorded the axial deformation and applied load. Since a slip between the specimen and the grips was inevitable, a laser extensometer was utilized to quantify the slip value. All tests were conducted at room temperature with a constant rate of 0.05%/s in the loading and unloading paths.

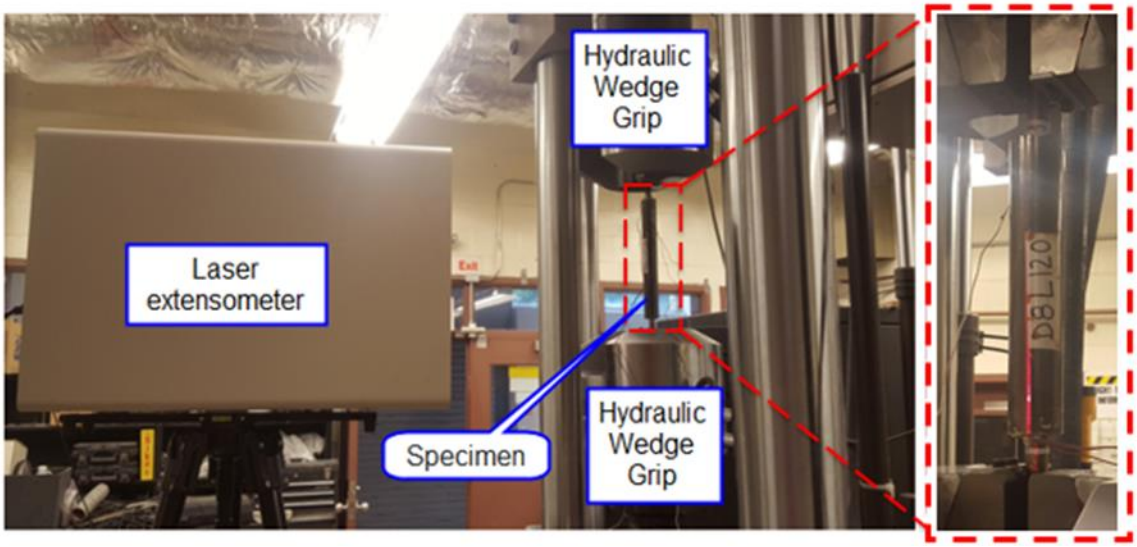

Figure 4-8. Photograph of test setup

4.4 Test Results and Discussions

4.4.1 Force-displacement hysteresis behavior

The axial force-displacement hysteretic loops are presented in Figure 4-9 and 4-10. The tensile state of the specimens is plotted in the positive direction. The nominal axial strains, defined as the axial deformation divided by the SMA bar fuse length, are shown in the second abscissa. Importantly, all specimens exhibit stable flag-shaped hysteretic behavior with and excellent self-centering characteristics. As evident in the figures, they reveal an asymmetric tension-compression force-displacement relationships. The lack of symmetry can be attributed to the well-established asymmetric NiTi material behavior, which is caused by the low crystallographic symmetry of the martensite phase [227] and textures induced during the material processing [218]. Aside from the inherent asymmetric material behavior, it would be reasonable to suppose that the grout-tube confining system took part in resisting some part of the compression load. The larger forces observed in compression, especially in more slender specimens, are likely due to increased friction forces between the SMA bar and the surrounding restraining apparatus resulting from Poisson's effect.

Comparison of Figure 4-9(a), 4-9(b), and 4-9(c) indicates that the ratio of SMA bar diameter at the ends (d_V) to that of the reduced section (d_R) has marked influence on the behavior of the CSDs. Specimens D8L120, D9L135, and D10L150 have the same slenderness ratio, which is 60, and the same outer diameter of 12 mm. Since one of the main objectives of this work was to investigate the behavior and failure mechanisms of CSDs, d_R was varied from 8 mm to 10 mm keeping constant slenderness ratio. Specimen D8L120 failed relatively earlier than the other two. It is conceivable that the reduction of the original SMA bar cross-section by 33% (i.e. from 12 mm to 8 mm) caused the early failure. This suggests that there should be an upper threshold on the d_V to d_R ratio to avoid low cycle fatigue failure. The force-displacement diagram of specimen D9L135 displayed slight fluctuation in the loading portion of the compression phase. This may have been related to the presence of localized voids during the grouting process. Since clearance between the SMA bar and the steel tube was tight, the grout must be flowable to fill the space around without an external vibrator. As illustrated in Figure 4-9(c), specimen D10L150 experienced strength degradation during the last three cycles of compression loading while the tension excursion exhibits a typical SMA behavior. The strength degradation is likely attributed to grout crushing. Although there was no visible external damage on the CSD, based on subsequent visual inspection of the failed specimen, it was concluded that this degradation in compressive strength likely occurred as the grout started to crush in a localized region adjacent to the neck zone. As a result, the local buckling of the SMA bar occurred, and subsequently, fracture ensued.

When the responses of the specimens with a slenderness ratio of 75 and the same SMA bar outer diameter of 16 mm are examined in Figure 4-9(d) and 4-9(e), the specimens revealed fairly similar behavior. Both specimens D12L225 and D14L262 failed at a compression deformation of about 13.5 mm. Three specimens with the same diameter (both d_V and d_R) were tested and compared to evaluate the effects of the different lengths of the SMA bar fuse portion. It can be observed from Figure 4-10(f), 4-10(g), and Figure 4-10(h) that the displacement capacities of specimens D15L225, D15L281, and D15L337 increased with an increase in the fuse length. The specimens with a slenderness ratio of 60, 75, and 90 experienced failures during the tensile cycles at loading amplitudes of 6% (13.5 mm), 6.5% (19 mm), and 7% (23.6 mm), respectively.

It is worth noting that no global instability was observed in any of the test specimens. This suggests that the stability criteria used in the design of the buckling restraining system successfully inhibit buckling. Furthermore, the comparison of the buckling responses of unrestrained SMA bars presented in Chapter 3 with Figure 4-10 of similar slenderness ratios also reinforces this observation.

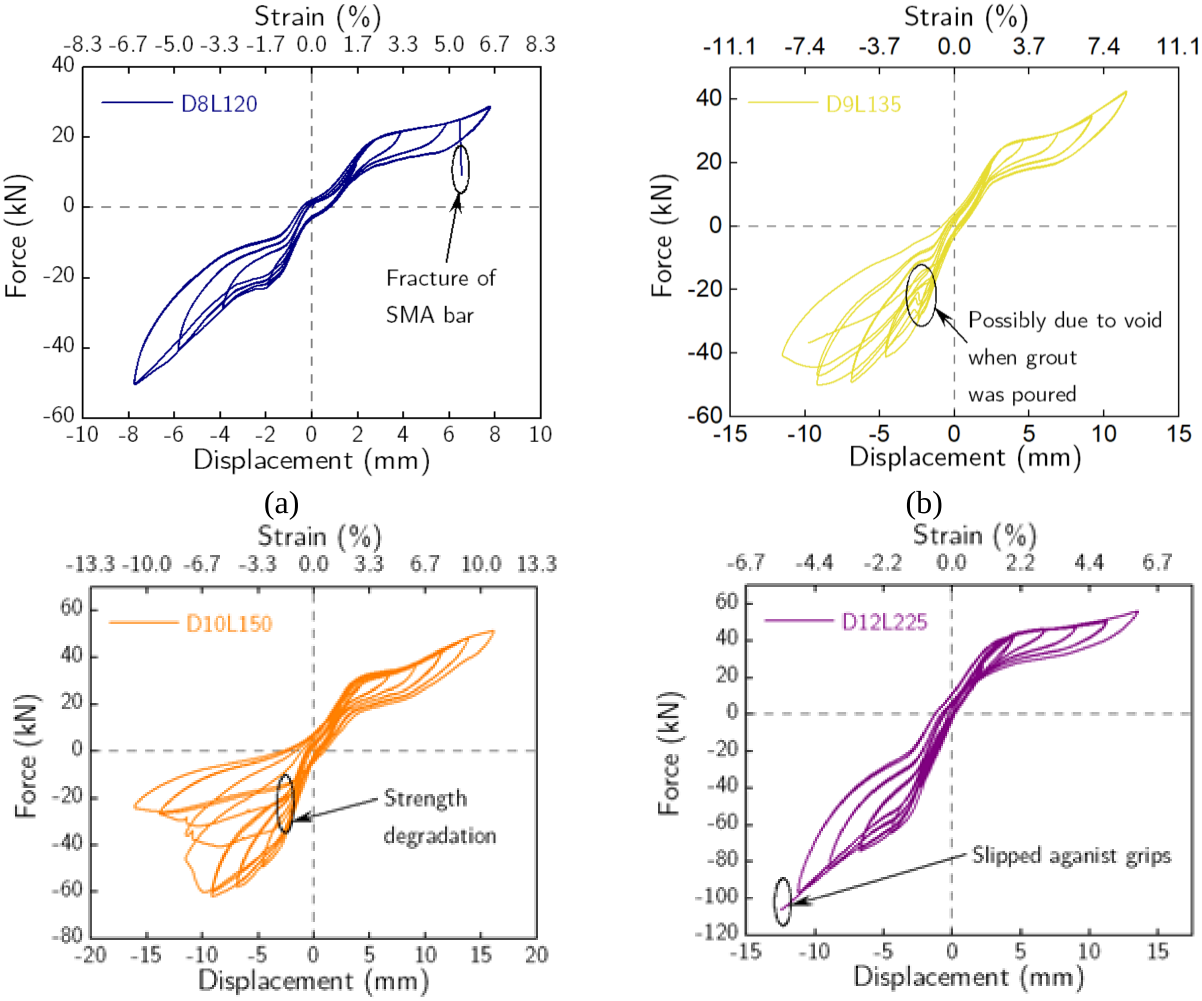

(a) (b)

(c) (d)

Figure 4-9. Experimental force-displacement cyclic response for specimens: (a) D8L120; (b) D9L135; (c) D10L150; (d) D12L225

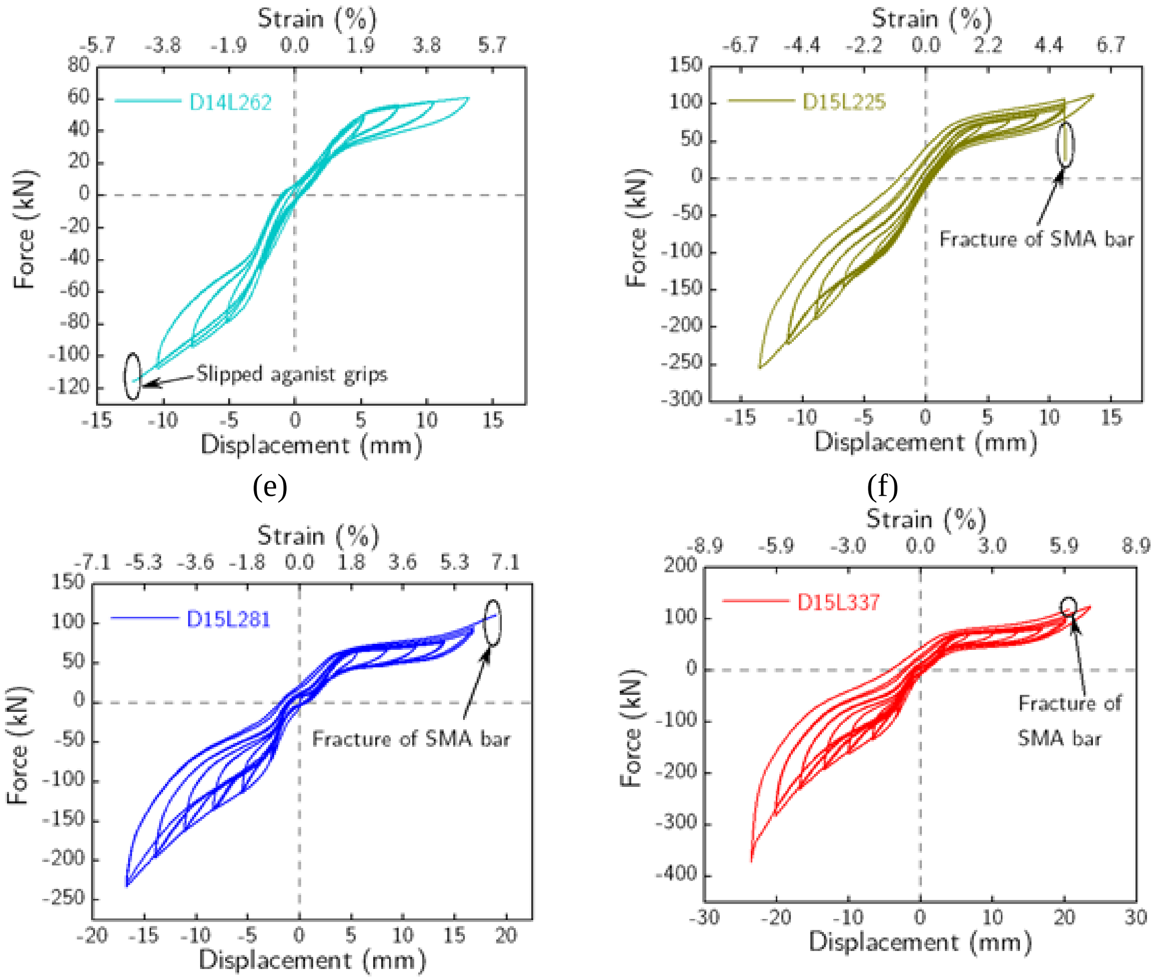

(e) (f)

(g) (h)

Figure 4-10. Experimental force-displacement cyclic response for specimens: (e) D14L262; (f) D15L225; (g) D15L282; (h) D15L337

Figure 4-11 shows the variation of peak tension and compression forces with loading amplitudes. For all specimens except D10L150 in compression, the maximum axial tension and compression forces increase with increased loading amplitude. The peak compression load of specimen D10L150 decreased after the 4% loading cycle due to local buckling. Comparing the changes in the maximum tension load between specimens having the same original SMA bar diameter but different fuse diameter, one can observe that the fuse diameter controls the CSD force capacity as expected. In the majority of the cases, the peak tension load increased moderately with increasing loading amplitude with the exception of some cases in which it remained almost constant. On the other hand, the peak compression force kept increasing consistently, especially for the D15 series specimens. It is also worth noting that the ratio of the first cycle force to the last cycle ranged from 1.87 to 2.68 in tension whereas in compression it varied from 1.60 to 4.29. In addition, the ratio of the peak compressive force to the peak tension force was calculated for each specimen for each cycle. The specimens produced maximum values of the ratio of the peak compressive force to the peak tension force between 1.11 and 2.98. These observations highlight the asymmetric response of the CSDs in tension and compression. It should be noted that for practical applications where asymmetric hysteretic behavior are not suitable, combining two or more CSDs can provide a symmetrical hysteretic behavior. For instance, a pair of CSDs can be installed in an X-shape configuration such that while one of them is in tension and the other is concurrently in compression in compression, resulting in the combined tension-compression response to be symmetrical.

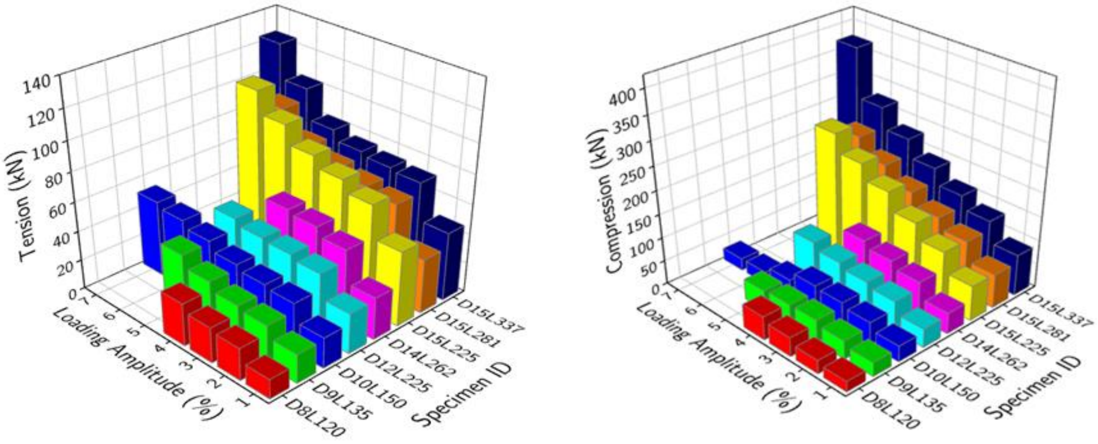

(a) (b)

Figure 4-11. Variation of peak force with strain amplitude; (a) tension and (b) compression

4.4.2 Energy dissipation and equivalent viscous damping

Since the CSDs are designed as supplemental energy dissipating elements to prevent damage to the primary structure and provide self-centering capability, the energy dissipation capacity and residual deformation of these devices are an essential benchmark of their performance. The energy dissipated per cycle (E_D) and the cumulative energy dissipated are analyzed in this subsection. The dissipated energy is calculated by computing the area between the loading and unloading force-displacement curves of both tension and compression loops. Figure 4-12 shows the energy dissipated per cycle of each loading amplitude for all specimens tested to failure. To enable easier comparison of the results, the specimens with the same external diameter and/or slenderness ratios are grouped together. It can be seen that the energy dissipated by the specimens increases rapidly with the increasing loading amplitude. Note that for specimen D10L150, the energy dissipated at the 5%, and 6% strains were about the same and increased only slightly at the 7% strain cycle. This can be attributed to strength degradation due to local buckling. The cumulative energy dissipated at each strain cycle for all specimens can be seen in Figure 4-13. It can be also seen that at lower loading cycles, each specimen exhibits similar rate of increase in cumulative energy dissipation. However, at higher loading amplitudes, specimens D15L337, D15L281, and D15L225 exhibited an exponential increase in energy dissipation, while the rest of the specimens did not show such performance.

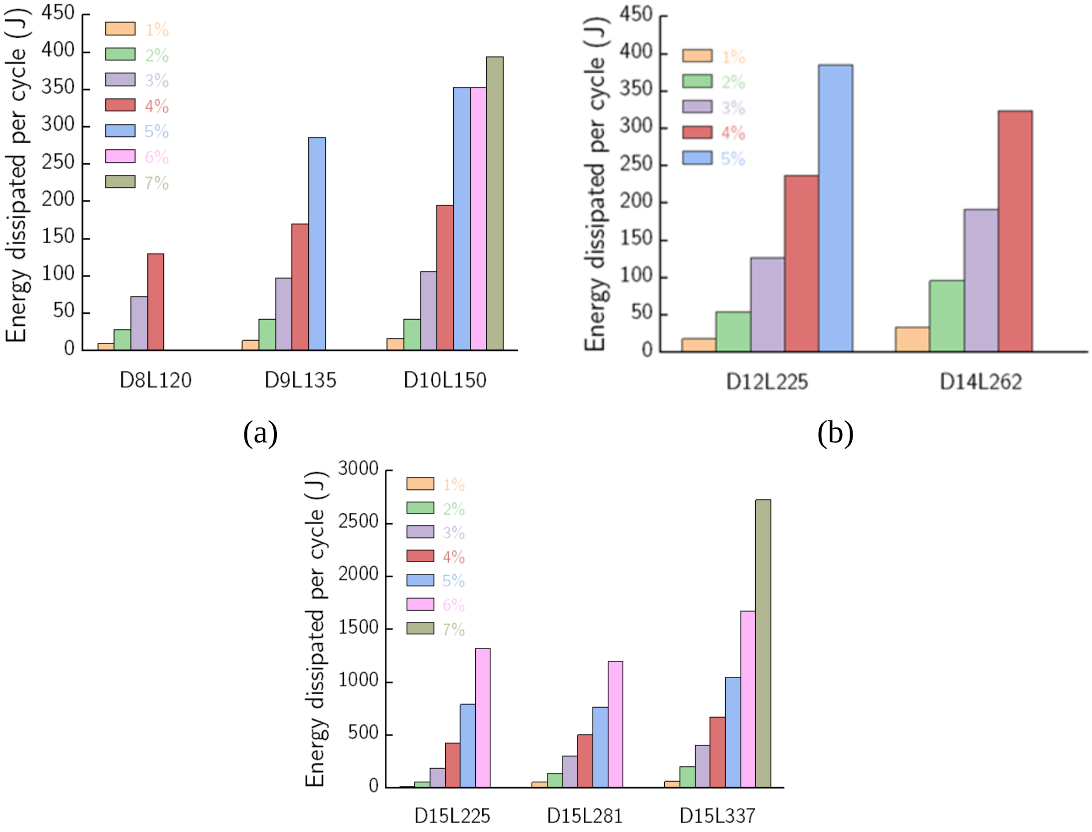

(a) (b)

(c)

Figure 4-12. Energy dissipation plot for specimens with slenderness ratio of: (a) 60; (b) 75; (c) 60, 75, and 90

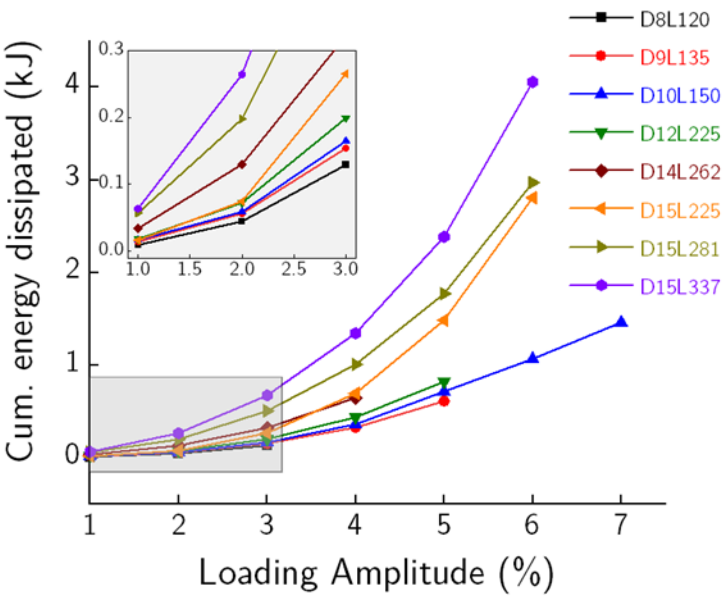

Figure 4-13. Cumulative energy dissipated for all specimens

For each specimen, the equivalent viscous damping ratio ζ_{eq} is computed using the equation provided below:

$$\zeta_{eq} = \frac{E_D}{2\pi(E_{so}^{+} + E_{so}^{-})} \tag{4.16}$$

where E_D energy dissipated per cycle (hysteresis area), E_{so}^{+} and E_{so}^{-} are elastic strain energies for the same cycle calculated as the energy absorbed in a linear system as illustrated in Figure 4-14. Given the stable hysteresis loops under the same loading amplitude, the variation between the first and second cycle was minimal. The average hysteresis area of both cycles at each amplitude was employed in the E_D calculation.

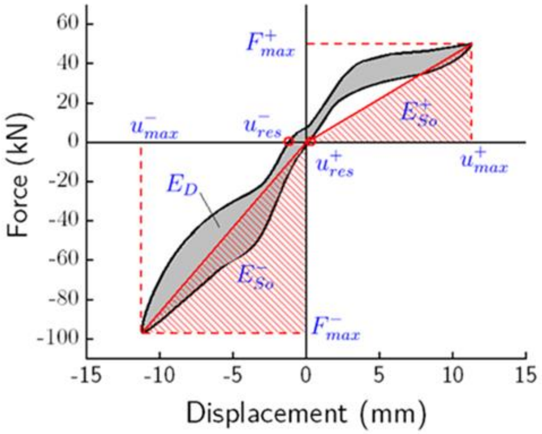

Figure 4-14. Illustration of equivalent viscous damping (EVD) calculation

Figure 4-15 shows the variation of equivalent viscous damping ratio with loading amplitude. It can be observed that the equivalent viscous damping ratio ranges up to 11.6%, which indicates that the CSDs can be good source of supplemental energy dissipation for seismic protection of structural systems. Note that the equivalent viscous damping ratio (and residual strain, and relative self-centering efficiency in the next subsection) of specimen D10L150 for 6% and 7% loading amplitudes are considered as outliers and are omitted from Figure 4-15 and Figure 4-16 since the local buckling was observed in this specimen.

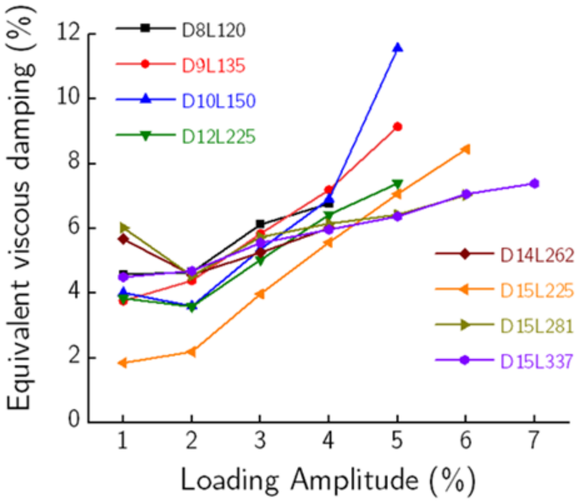

Figure 4-15. Equivalent viscous damping ratio versus loading amplitude

4.4.3 Self-centering capability

To evaluate the self-centering behavior of the CSDs, the residual strains, computed as the displacement of the loading point at the zero-force per loading cycle divided by the length of the reduced section of each specimen, at the end of each loading cycle are analyzed. Figure 4-16(a) shows the variation of the residual strain with the maximum strain amplitude in each cycle for all specimens. It is evident that the residual strain for all specimens at the 5% loading cycle is less than 0.8%. It is worth noting that maximum residual strain exhibited by the longest specimen, i.e., D15L337 for the last 7% strain cycle, is 1.3%, which is still very small.

To more quantitatively assess the self-centering capability of the tested specimens, a parameter called relative self-centering efficiency (RSE) and given by the equation below [228] is computed:

$$RSE = 1 - \frac{u_{res}^{+} - u_{res}^{-}}{u_{res}^{+} + u_{res}^{-}} \tag{4.17}$$

where u_{res}^{+} and u_{res}^{-} are the tension and compression residual displacements, respectively, as illustrated in Figure 4-14.

RSE can be employed to evaluate the capacity of the CSDs to self-center after cyclic loading as well as to assess the percentage of the recoverable peak displacement. An RSE value corresponding to a perfectly self-centering device with zero residual deformation is equal to one, while an RSE value of zero corresponds to a device without any re-centering capacity. The relationship between the relative self-centering efficiency versus the strain amplitude for all of the tested specimens is provided in Figure 4-16(b). For all specimens, the RSE values were above 92% when the loading amplitude was 2% or above, indicating a very good self-centering capability. There was a decrease in RSE value when the loading amplitude increased beyond 4% due to increased residual deformations as shown in Figure 4-16(a).

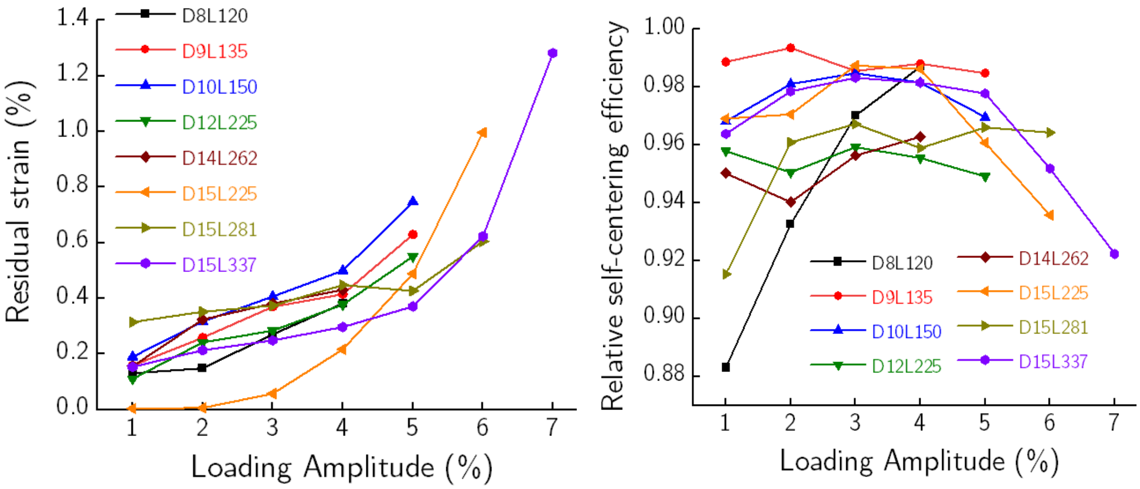

(a) (b)

Figure 4-16. (a) Residual strain; (b) relative self-centering efficiency of the CSDs

4.4.4 Failure modes

Figure 4-17 shows photographs of selected failed specimens. In general, all specimens failed in three modes: (1) the SMA bar ruptured at the transition (neck) region from the full section to the reduced portion, (2) the SMA bar fractured near the ends where it was gripped, and (3) specimens slipped against the hydraulic wedge grips. Based on these classifications, specimens D8L120, and D15L225 can be categorized under failure mode 1, whereas specimens D9L135, D10L150, D15L281, and D15L337 failed in mode 2. The other two specimens, D12L225 and D14L262, experienced the third failure mode. In all cases, no out of plane bending or sway of the restraining tube was observed. The failure mode 1 observed here was very similar to the results obtained in [157,158,221,229]. It was also consistent with other related studies [110,230] where dog-bone shape SMA bars with threads at both ends were employed in beam-column or column base connections. Although in the later studies the rupture occurred over the threaded area and was caused by insufficient ratios of the net threaded-to-shank cross section diameter, in general, SMA bars are more susceptible to fracture when they are machined. In view of this point, special attention should be given to the neck region which is potentially a vulnerable zone. A closer inspection of Figure 4-17(b) indicates that it is essential to provide sufficient insertion length i.e., distance from the beginning of the transition zone to the end of the restraining tube. Although the test matrix in this work did not consider the insertion length as a separate test parameter, it was between 10% to 42% of the SMA bar length at the reduced section for the tested specimens.

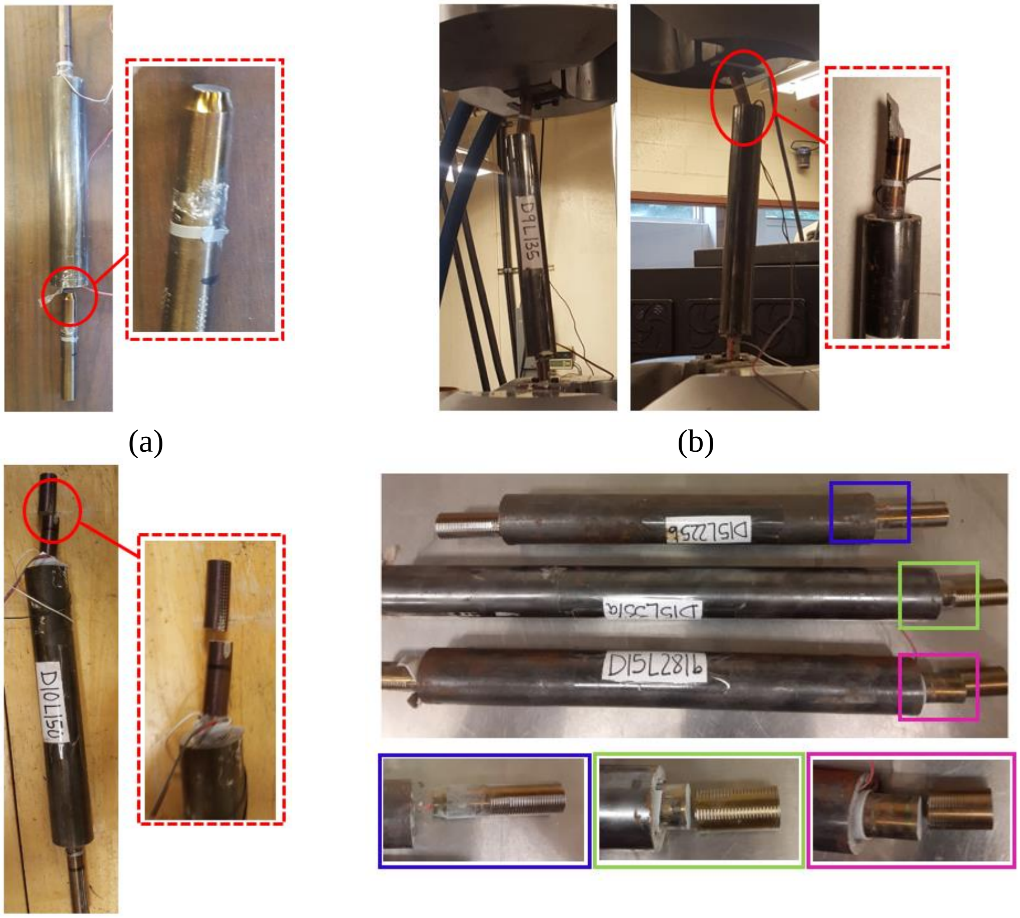

(a) (b)

(c) (d)

Figure 4-17. Photographs of selected failed specimens: (a) D8L120; (b) D10L150; (c) D9L135; (d) D15L225, D15L281 & D15L337

While all the specimens exhibited satisfactory results, it is believed that the performance of the CSDs can be effectively enhanced by suppressing failure modes 2 and 3 as these are test setup related issues. Future work should therefore consider custom-made grips.

4.5 A Case Study on Application of CSD for Seismic Retrofitting of Substandard RC Beam-Column Joints

Seismic vulnerability of non-ductile reinforced concrete (RC) buildings constructed prior to the1970s is a major concern worldwide. Past earthquake reconnaissance showed that strong earthquakes could significantly damage non-ductile RC buildings, particularly to their beam-column joints [231,232]. These structures were designed to carry gravity and wind loads and may have critical structural deficiencies. Therefore, they are not modern-code compliant and can be considered as substandard. Non-seismically designed structures are mainly characterized by inadequate reinforcement details, such as lack of joint transverse reinforcement, insufficient transverse reinforcement in columns, column lap splice located in potential plastic hinge regions, and inadequate anchorage detailing [233]. Several retrofitting techniques for beam-column joints such as increasing section areas, wrapping with FRP, installing steel haunches, post-tensioned SMA bars, etc have been studied and some of them implemented in practical applications [234,235]. Given the considerably high number of existing substandard RC buildings in the inventory [236,237], this section proposes practically viable seismic retrofit strategy using the CSDs. A numerical case study on representative substandard RC beam-column subassemblies was conducted to assess the effectiveness of the proposed retrofit solution.

4.5.1 Numerical modeling and validation

Numerical models of substandard RC interior and exterior joint assemblages were created in the OpenSees finite element program. As illustrated in Figure 4-18, the beams and columns in the joint assemblage are modeled using the force-based *BeamColumn* element with fiber sections, divided into the unconfined and confined concrete zones to incorporate the effect of hoops. The uniaxial *Concrete02* material model in OpenSees is used as the constitutive model for the confined and unconfined concretes. The corresponding stress and strain values at the peak and the crushing points of confined concrete are calculated using the Chang and Mander model [238]. Longitudinal reinforcement is represented using the *steel02* material model while a zero-length slip spring is adopted to model the bar-slip effect at the interface of the beam-column joint. The joint rotation spring is modeled using *pinching4* material. The joint size is represented by the rigid links, as shown in Figure 4-18. To describe the nonlinear shear behavior in the joint, model proposed by Altah and Kunnath [239] was employed.

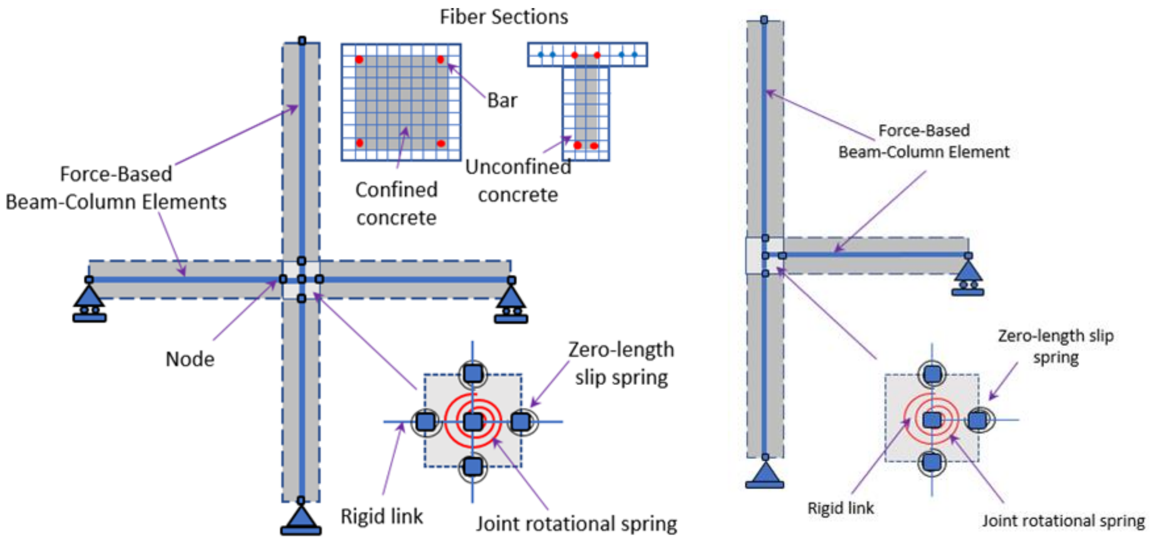

Figure 4-18. Modelling details of substandard reinforced concrete beam-column joint assemblage

The effectiveness of the numerical model is validated by comparing with experimental results described in Lehman et al. [240] and Kuang and Wong [241]. Figure 4-19 shows the geometric properties and reinforcement details of exterior and interior joints. Comparisons of the force-displacement hysteric relationship reported in Lehman et al. and Kuang and Wong versus the numerical results in this study are presented in Figure 4-20. As can be seen, a reasonable match of between the experimental and numerical predictions was achieved. The numerical model satisfactorily captures the measured global cyclic response, including the stiffness and pinch hysteretic behavior.

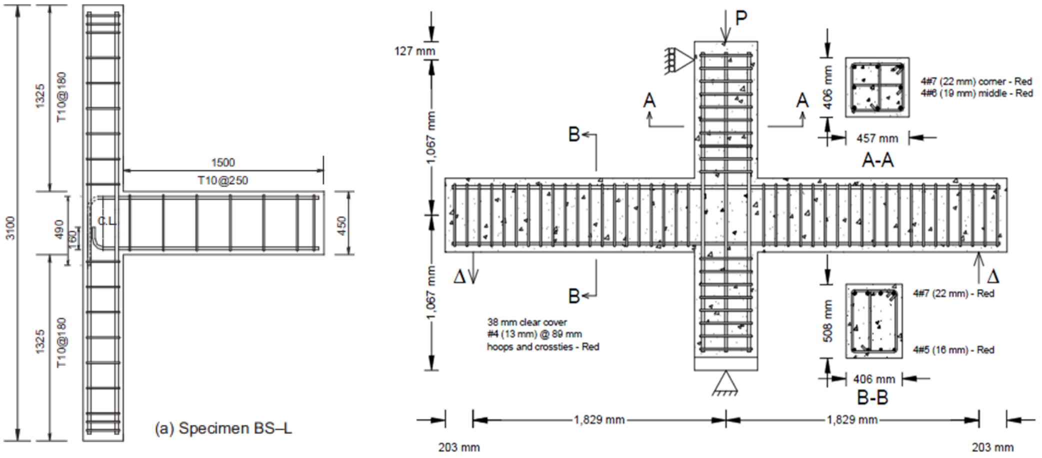

(a) (b)

Figure 4-19. Geometric properties and reinforcement details of (a) exterior [241] and (b) interior [240] RC beam-column joints

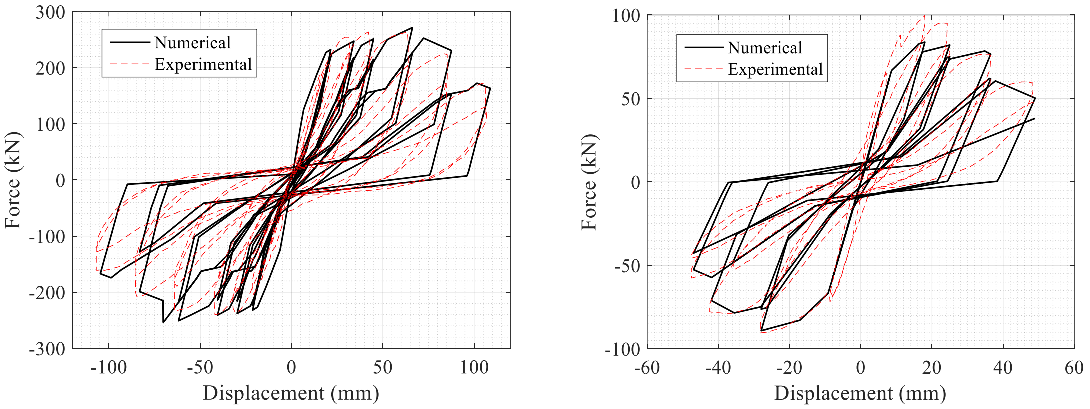

(a) (b)

Figure 4-20. Comparison of the force-displacement relationships between the experimental and numerical results of substandard RC beam-column joints: (a) exterior and (b) interior

4.5.2 CSD retrofit schemes and mechanics of joints

Figure 4-21 shows the proposed retrofit schemes for different joint typologies in which CSDs are installed in the vicinity of the beam-column joints. The underlying principle of adding the CSDs is to protect the vulnerable panel zone from excessive damage by redirecting the stress flow around the joint area and forcing the development of a plastic hinge in the beam. As such, the damage could be eliminated or minimized to spalling of cover in columns or minor cracks in joints while enhancing the global response. The CSDs can be considered as stiffening elements and also sources of supplemental damping to the system.

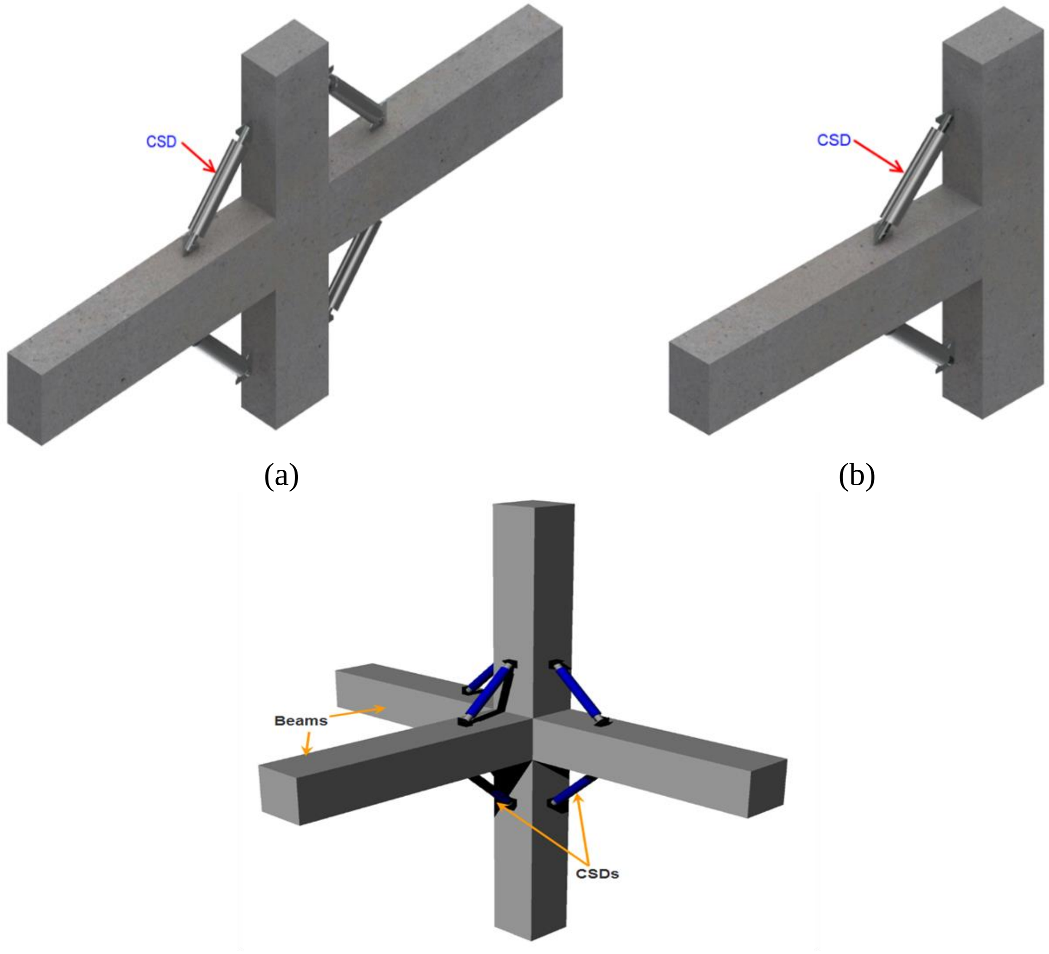

(a) (b)

(c)

Figure 4-21. Proposed CSD retrofit configurations for (a) interior, (b) exterior, and (c) corner beam-column joints

In order to achieve the above performance goal, it is important to understand the behavior of the beam-column joints retrofitted with CSDs and identify the effect of adding CSDs in redistributing the shear forces and moments in the joints. First, consider an as-built beam-column joint subassembly formed by the assumed points of inflection at mid height of columns and midspan of beams. Figure 4-22 shows the mechanics of the joint when subjected to an interstory shear force applied at the top of the column, i.e., V_c which leads to bending moments M_{cb} and M_{bc} in the column and beam at the faces of the joint, respectively. Based on equilibrium of the joint and applying simple statics, the horizontal joint shear force induced by the applied load V_c is given by:

$$V_{jh} = \frac{M_{bc}}{jd_b} - V_c = V_b\left(\frac{L_b}{jd_b} - \frac{L_b + {}^{d_c}\!/_{2}}{L_c}\right) \tag{4.18}$$

where jd_b is the lever arm of internal forces in the beam at the column face, d_b and d_c are the depths of the beam and column, respectively. Other symbols are shown in Figure 4-22. This shear force is the major cause of failure in the joint panel zone. Now, consider the same joint sub-assembly retrofitted with two CSDs as shown in Figure 4-23. As seen, under the applied beam end load, V_b, the maximum bending moment in the beam occurs at a point of connectivity of the CSDs, $M_{b,\max}$, given by:

$$M_{b,\max} = V_b(L_b - L') \tag{4.19}$$

where L' is the horizontal projected length of the CSD. Beyond the point of connectivity of the CSD, the bending moment in the beam gradually reduces. The rate of reduction depends on the relative stiffness of the CSD and the beam. Thus, at the face of the column, the moment in the beam M'_{bc} is less than the moment $M_{b,\max}$. Similarly, the bending moment was reduced in the column at the face of the beam M'_{cb} and the reduced shear forces in the beam V'_b and column V'_c beyond the CSD. The reduced joint horizontal shear force for the CSD retrofitted joint V'_j can now be obtained as:

$$V'_{jh} = \frac{M'_{bc}}{jd'_b} - V'_c \tag{4.20}$$

where jd'_b is the lever arm of the internal forces in the beam at the face of the column.

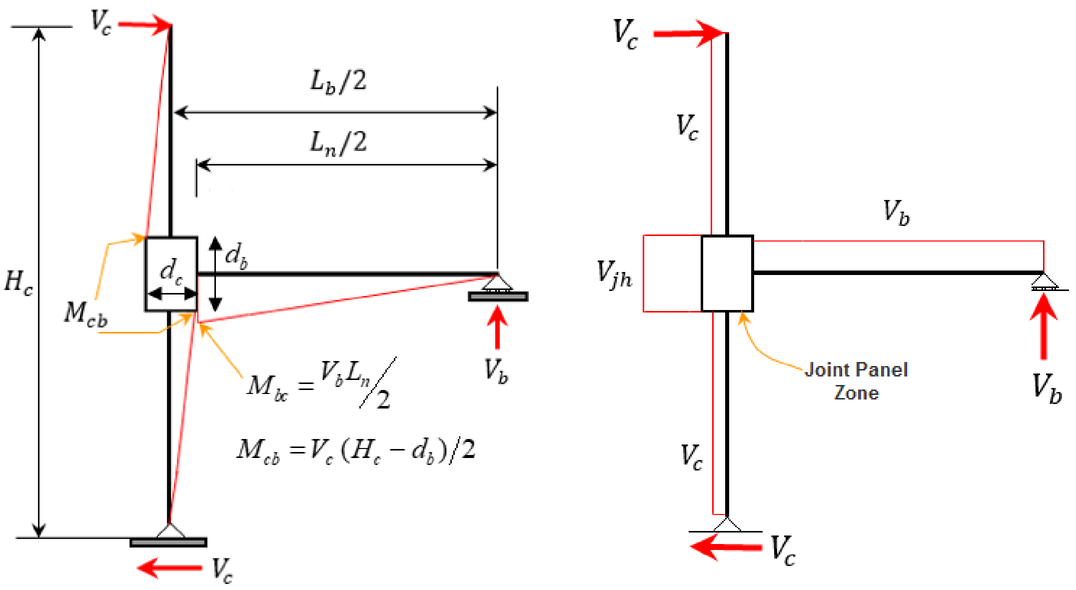

(a) Bending moment diagram (b) Shear force diagram

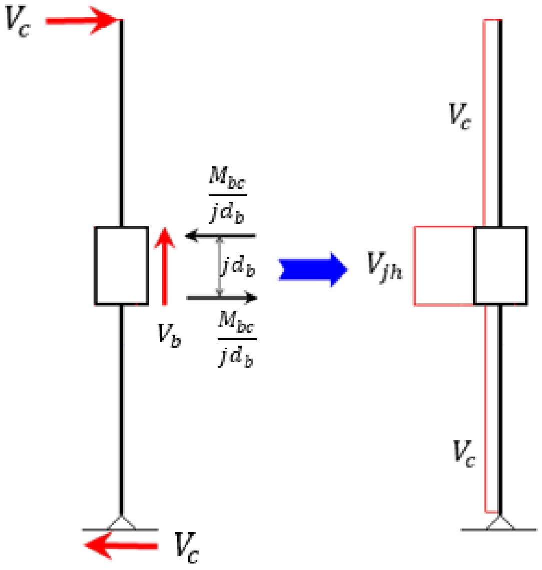

(c) Induced nominal horizotal shear force in the joint

Figure 4-22. Mechanics of an as-built exterior joint

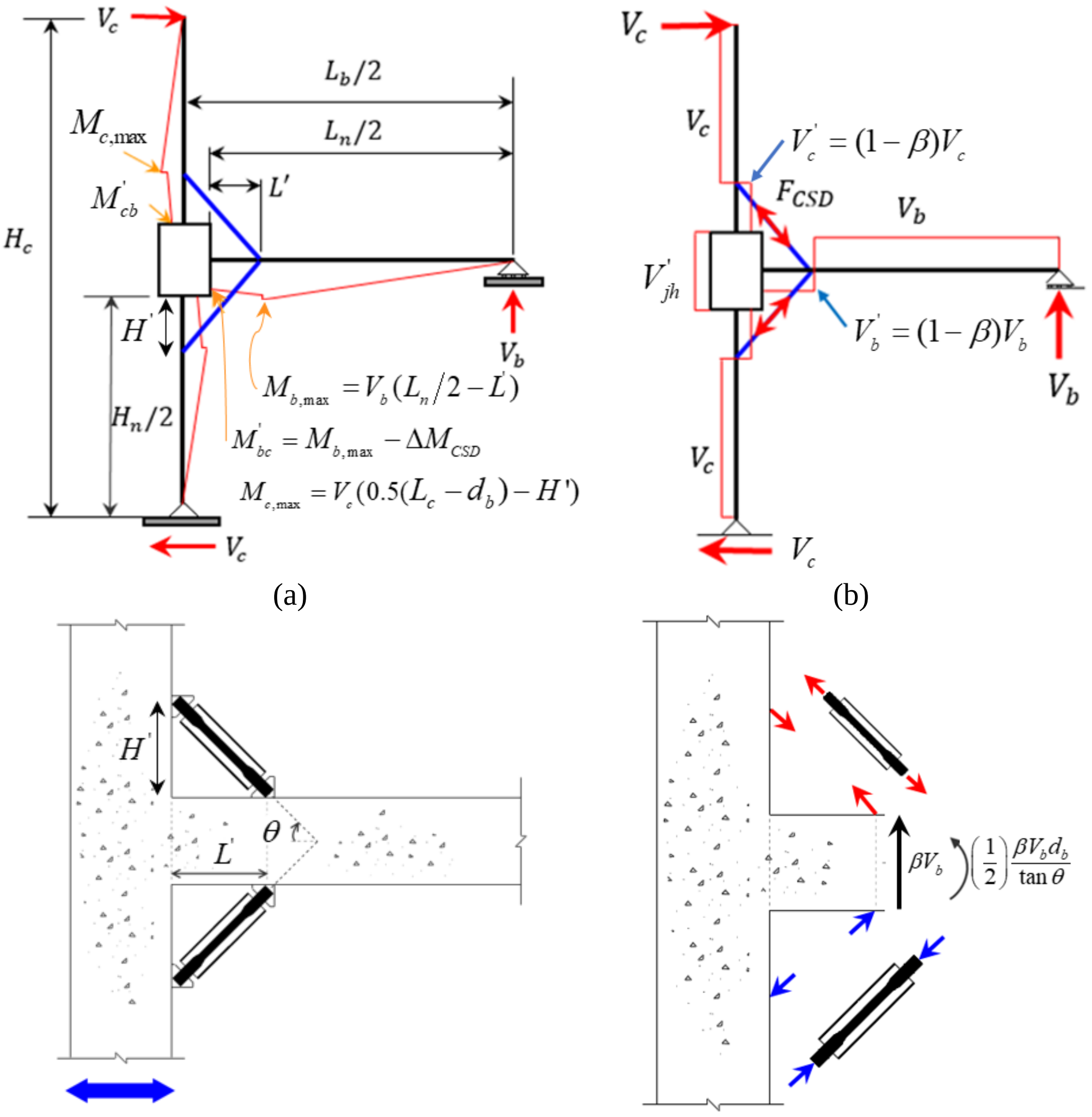

(a) (b)

(c)

Figure 4-23. Mechanics of joint retrofitted with CSDs

Based on the aforementioned mechanics, it can be observed that the effect of the CSD in reducing the joint horizontal shear force is essentially two-fold: 1) modifying the critical section for flexure and thereby reducing the maximum bending moment in the beam for a given applied load (effects of geometry); and (2) further reducing the bending moment at the face of the column due to redistribution of forces (effects of stiffness). Therefore, by designing the CSD appropriately, the horizontal joint shear stress can be significantly reduced compared with the as-built joint. However, it should be noted that at the point of connectivity of the CSDs with the beam and column, the shear force suddenly rises.

Therefore, for cases where the members are or may become shear critical due to the addition of the CSDs, the proposed retrofit solution should be combined with other shear strengthening techniques such as wrapping with FRPs.

The design of CSD retrofit includes proper selection of key design parameters such as the distance from the column interface L, inclination angle θ, and force capacity of the CSD F_{CSD}. These parameters should be carefully selected such that undesirable brittle failure mechanisms within the joint panel zone can be inhibited. Furthermore, the reversal of the strength hierarchy must be assured during the design process by forcing the flexural plastic hinge in the beam close to the damper connection points.

Based on acceptable performance target, the three parameters can be selected using the following procedure:

- The joint shear stress should not exceed the allowable shear stress defined by ACI318 [242]

$$\tau'_{jh} = \frac{V'_{jh}}{A_j} \le \tau_{\max} \tag{4.21}$$

- For the plastic hinges to form in beams, the maximum moment $M_{b,\max}$ at the intersection of the CSD with the beam should reach the yielding moment $M_{b-yield}$ while the corresponding shear force V'_b should not exceed the shear strength of the beam based on ACI 318

$$V'_b = \frac{M_{b-yield}}{\frac{L_b}{2} - \frac{h_c}{2} - L} \le V_n^b \tag{4.22}$$

- To avoid plastic hinge and shear failure in columns, the maximum moment $M'_{c,\max}$ at the intersection of the CSD with the column should not reach the yielding moment $M_{c-yield}$. The corresponding shear force, $V_c^{'}$ or $V_b^{'}$, should not exceed the shear strength of column based on ASCE/SEI 41-06 [243]

$$V_c^{'};V_b^{'}=\frac{M_{c-yield}}{{L_c}/{2}-{h_b}/{2}-L\tan\theta}\le V_n^c \tag{4.23}$$

$$M_c^{'};M_b^{'}=M_{b-yield}\,\frac{L_b\left({L_c}/{2}-{h_b}/{2}-L\tan\theta\right)}{L_c\left({L_b}/{2}-{h_c}/{2}-L\right)}\le M_{c-yield} \tag{4.24}$$

Following the above design procedure, the CSDs were designed with the intention of protecting the joint region from excessive damage while forcing a plastic hinge in the beam outside from the column interface. Beam and column members must also be protected against excessive shear demand and brittle failure by controlling the damper's design parameters. Previously validated numerical models of the two joints were used with the addition of the CSDs. The CSDs were modeled as pin-connected truss elements using a self-centering material model in which the parameters were calibrated with experimental results presented in section 4.4. The three parameters (i.e., L , θ , and F_{CSD}) were adjusted iteratively until equations 4.21 to 4.24 are satisfied. Table 4-3 summarizes the final design iteration output and SMA properties used for simulation.

Table 4-3: Parameters used for CSD modelling

	Exterior Joint	Interior Joint	SMA mechanical properties		
L	140 mm	180 mm	E_{SMA}	27579	Mpa
α	50°	45°	σ_s^{AS}	414	MPa
L_{SMA}	466.46 mm	565.69 mm	σ_f^{AS}	550	MPa
A_{SMA}	798 mm^2	548 mm^2	σ_s^{SA}	390	Mpa
			σ_f^{SA}	200	Mpa
			ε_L	3.5	%

The hysteretic behavior of the original and CSD retrofitted joints are shown in Figure 4-24. It can be seen that the CSDs exhibited promising behavior for relocating the plastic hinge in the beam and protecting the joint panel zone from brittle shear failure. It is also observed that dampers provide re-centering capacity to the joint and increase the energy dissipation capacity of the joint.

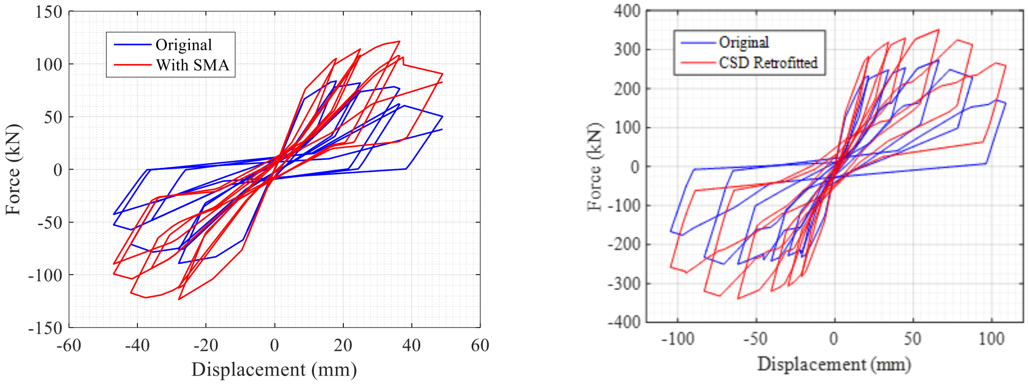

(a) (b)

Figure 4-24. Force-displacement hysteretic responses of RC beam joints with CSDs: (a) exterior and (b) interior

4.6 Summary

This chapter explored mechanical response of a shape memory alloy-based energy dissipator, fabricated from a machined superelastic NiTi SMA bar and steel tube filled with grout. The SMA bar dissipates the energy through superelastic deformation both in tension and compression, while the grout-filled steel tube serves as a buckling restraining system and prevents the SMA bar from buckling in compression. The theoretical derivations for the design of the buckling restraining system were described. An experimental program was conducted where eight CSD specimens with varying fuse diameter (8 mm to 15 mm) and fuse length (120 mm to 337.5 mm) were tested under cyclic loading. The main findings can be summarized as follows:

- Most of CSD specimens sustained peak deformation corresponding to at least 5% strain of SMA bars. Only one specimen, which had an original and fuse diameter of 12 mm and 8 mm, respectively, failed at 4% strain. This specimen was intentionally designed with a higher ratio of original to reduced cross-section diameter.
- Although the specimen with a fuse diameter and length of 9 mm and 135 mm, respectively, showed the typical SMA behavior up to 6% strain in tension, it

experienced strength degradation after the 3% strain cycle in compression. This was due to the local crushing of the grout followed by the SMA bar fracture towards the end.

- In the design of the buckling restraining system, the stability criteria used to ensure stable behavior of the CSDs mainly depends on the design parameters such as the reduced cross-section and neck zone cross-section of SMA bar, restraining tube properties, and insertion length. It was shown that the proposed criteria successfully prevent premature failure due to global and local buckling of the SMA bars. However, sufficient grout should be present between the SMA bar and the inner wall of the restraining tube to avoid local buckling, which may occur in regions where the grout cover is thin due to poor workmanship.
- All specimens showed good energy dissipation capacity with an equivalent viscous damping ratio of up to 11.6%. The specimens with a fuse diameter of 15 mm performed better compared to the other specimens. The maximum force in these specimens reached up to 125 kN in tension and 372 kN in compression.
- An excellent self-centering capability was observed in all devices. The maximum residual deformation exhibited by the specimen with a fuse length of 337 mm (the longest of all specimens) was 1.3% of the applied peak displacement of 23.6 mm.
- It was found that the ratio of fuse diameter to original SMA bar diameter has a considerable influence on the failure modes of the CSD. It was concluded that the CSD designs with smaller ratios performed better and sustained higher levels of deformation before failure.
- Numerical analyses of two CSD retrofitted substandard RC beam-column joints were conducted and the responses of the joints with, and without CSDs were examined. The results indicate that CSDs can effectively improve the response of RC joints.

5 DEVELOPMENT AND TESTING OF SUPERELASTIC FRICTION DAMPER (SFD)

5.1 Overview

SMAs can be produced in different forms such as wires, cables, bars, or springs. However, as noted in Chapter 2, most of existing SMA-based seismic devices available in the literature have employed the SMA wires as they are more widely available. This led to development of devices with low force capacity. Other forms of SMA such as helical springs, Bellville washers [164], and plates [166,168] have been shown promising results to increase the capacity of dampers or braces. However, these products are not readily available in the market and usually their cost is considerably higher. Moreover, the fabrication process of devices equipped with helical springs or Bellville washers is more complicated and sensitive on construction precisions.

SMA cables have recently been suggested as a more convenient form of SMAs that can accommodate high force demands of structural applications [102,105] An SMA cable is composed of multiple strands. Each strand has a core wire around which other SMA wires are twined. The strands can be laid in various configurations to form a cable. SMA cables leverage the outstanding mechanical properties of wires to carry relatively high tensile loads. Previous experimental studies have shown that SMA cables possess large levels of recoverable strain and high fatigue life [23-25]. They are less sensitive to initial imperfections and exhibit redundant failure mode. Given these advantages, there is a growing interest in using SMA cables for seismic applications, specifically in braces/dampers [150,175,177,178] and isolation bearings [193,200]. In addition, more recently, Shi et al. [244] developed and experimentally validated the performance of an anchorage system for end connections of SMA cables, which is critical to foster their practical applications.

Another challenge for SMA-based seismic control systems is the limited damping capacity of SMAs. The inherent energy dissipation capacity of SMAs is usually inadequate to render their use as the sole damping source in seismic applications. When SMA-only dampers are used in a building, it can effectively control peak and residual displacement response. However, they could lead to an increase in floor acceleration response, consequently, damage to acceleration sensitive non-structural components. Note that damage to non-structural components often accounts for the majority of economic losses in an earthquake [6]. In addition, a detrimental high-mode effect could be induced due to limited damping [245]. Several hybrid devices have been proposed by combining different forms of SMAs with other supplemental energy dissipating elements such as metallic yielding elements, viscoelastic material, lead block or friction between two solid sliding bodies to augment their damping capacity. Despite their simplicity, metallic yielding dampers are susceptible for low cycle fatigue failure and, hence, require replacements after an earthquake event. The studies reviewed in Chapter 2 revealed the enhanced seismic performance of SMA-based hybrid dampers compared to SMA only dampers. However, some of those studies have only considered conceptual development and assessment of the damper response through numerical simulations without actual fabrication and testing, while some others have tested small-scale dampers with SMA wires. In addition, there is a lack of experimental test data on the temperature sensitivity of SMA-based dampers, which is an important consideration for the real-world implementation of such systems [246].

The main objective of this chapter is to address the above two issues, i.e., limited force capacity and inadequate damping, by proposing a new damper called Superelastic Friction Damper (SFD). The proposed damper leverages the high tensile resistance and superior SC capability of SMA cables and the prominent damping capacity of a friction device. A detailed description of the fundamental working principle of the SFD is first presented, followed by a theoretical analysis of its hysteretic behavior. The chapter then focuses on the fabrication process and extensive experimental testing of a large-scale prototype damper. The effects of loading rate and ambient temperature on the damper characteristics such as hysteretic curves, energy dissipation, self-centering capability, and stiffness are evaluated. Lastly, a parametric study that investigates the influence of key design parameters on the hysteretic behavior of the proposed SFD is presented.

5.2 Superelastic Friction Damper

5.2.1 Damper description

Figure 5-1 shows an isometric view of the SFD. The damper comprises SMA cables, inner and outer steel members, friction pads, slotted end plates, and connection plates. The outer member consists of a pair of steel channels with bonded friction pads on the outside face of the web. The inner member is made up of I-shaped steel, in which the web serves as a sliding interface for the friction pads. The selection of appropriate friction interface material is vital to achieve long-term stable sliding behavior. Several types of friction interfaces have been tested by different researchers [247,248]. Past studies showed that mild steel against mild steel interface is susceptible to severe stick-slip behavior and exhibited significant hardening behavior and abrupt softening [249,250]. In this study, friction pads made out of metal-free brake and clutch lining (also termed non-metallic melded strip) were used. The use of a brake lining pad against stainless steel (BL-SS) makes the sliding interface self-lubricate. As a result, the stick-slip phenomenon decreases, and a constant coefficient of friction is obtained independent of the loading rate. Furthermore, the sliding interface is resistant to rust and can provide long-term stable behavior. Also, non-metallic pads have high-temperature resistance, high friction coefficient, and generally excellent wear resistance [251].

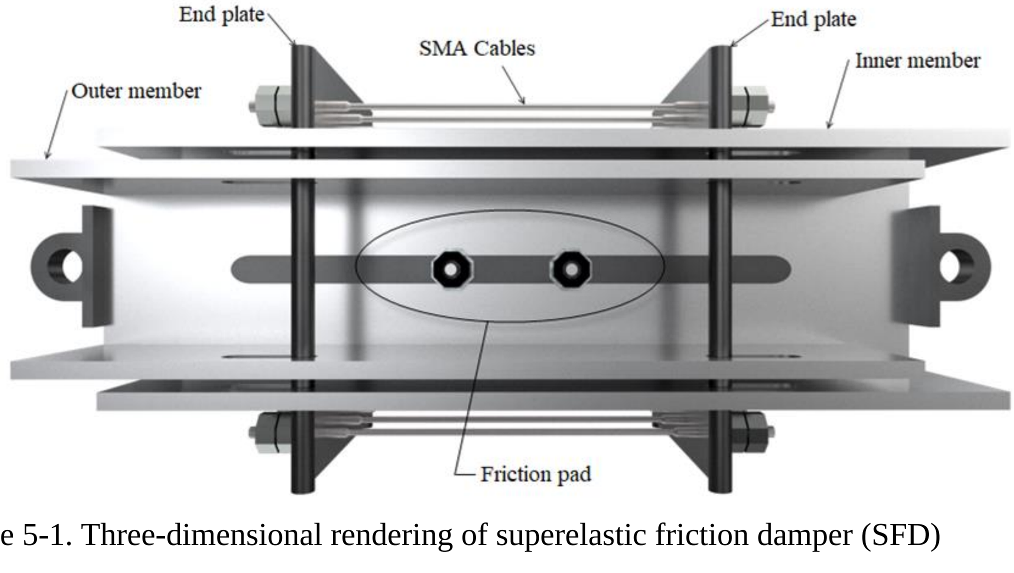

Figure 5-1. Three-dimensional rendering of superelastic friction damper (SFD)

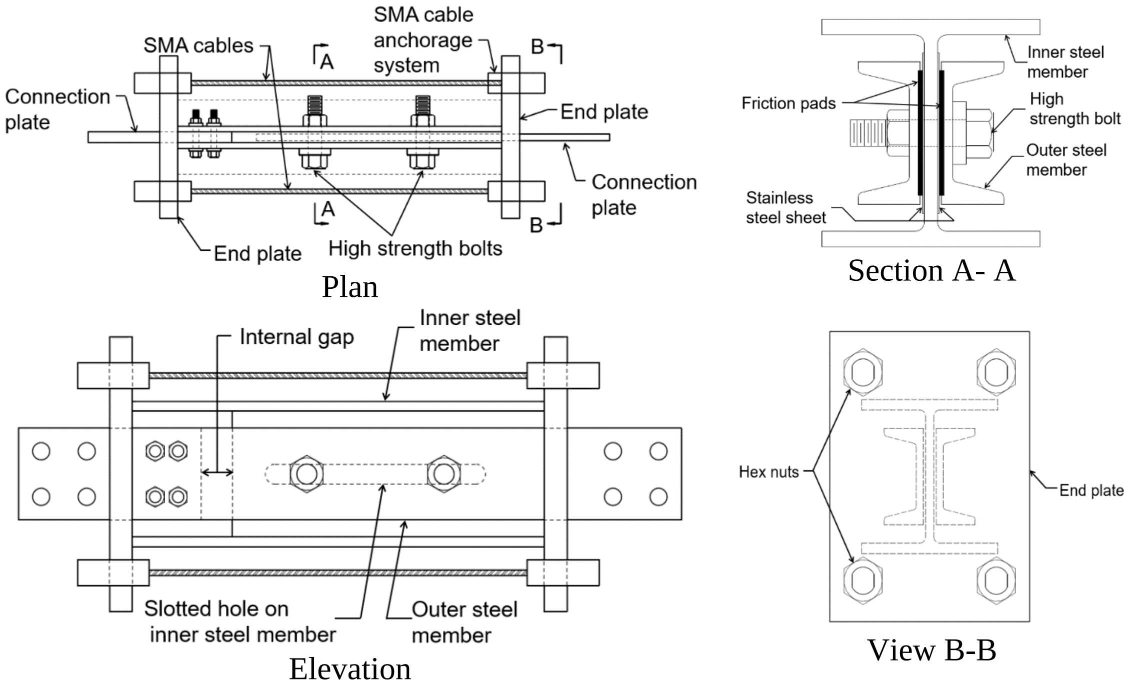

Figure 5-2. Superelastic friction damper: plan, elevation, and section views

Highly polished (mirror finish) stainless-steel sheets are welded to both sides of the I-shaped web, which is realized with a slotted hole that allows sliding of the outer members. The inner and outer members are connected by high-strength bolts, which are used to provide a normal pressure that generates pre-determined friction force between the members. The top and bottom flanges of the I-section are copped at one end, while a portion of the web is cut out at the opposite end. The end plates have vertical slotted holes that allow the connection plates to pass through and bolted to the inner member at one end and the outer members on the opposite end. The SMA cables are anchored to the end plates such that they axially clamp both the inner and outer members at both ends.

5.2.2 Advantages of proposed SFD

Compared with many of the existing seismic protective technologies, the SFD offers the following advantages:

1. Adaptable hysteretic response: The proposed damper integrates both self-centering and energy absorption capabilities into one compact device. By adjusting the proportions of SMA cables and friction, the device can meet various desired performance targets in terms of self-centering and energy dissipation. The self-centering capability of the device helps minimize residual drifts and hence make post-event recovery more rapid, while additional damping provided by the frictional component can minimize acceleration response.

2. Scalability for real-world application: The force and stroke capacity of the device can easily be adjusted by changing the length and cross-sectional area of SMA cables. Compared to limited deformability of self-centering devices that rely on post-tensioning of steel or FRP strands, the proposed damper can easily achieve large deformations due to considerably higher tensile strain capacity of SMA cables.

3. Reusability: As both the energy dissipation offered by both SMA cables and frictional component of the SFD is non-sacrificial, there is no need to replace any component after a design level event. The SFD can provide reliable and repeatable hysteretic response after several earthquakes. As confirmed by many tests, the friction dampers can offer damage-free performance after series of large excitations, which suggests that the post-earthquake inspection and repair work may not be needed at all in the proposed SFD system. Some of the merits of the use of friction devices as supplemental energy dissipation systems for seismic protection of structures are: (i) reliable and repeatable hysteretic behavior of damper which is almost independent of velocity and displacement amplitude; (ii) close-to-rectangle force-displacement hysteresis loops that provide significant energy dissipation capacity; (iii) high initial stiffness that causes the damper slip in early loading and, as a result, the energy dissipation begins in small lateral displacements.

4. Multifunctionality: given the self-sensing potential of SMAs, the SFD can be leveraged to develop simultaneous control and condition assessment device. The data collected from the damper can be used to assess the remaining capacity of a structure subjected to a major earthquake event to make decisions related to post-earthquake serviceability and repairability. Note that this behavior is not studied in the research reported herein.

5. Easy of fabrication and installation: the proposed damper is characterized by a straightforward structural layout and a clear working mechanism (described below). It can be easily assembled in the factory or on-site without requiring unique fabrication process or equipment. The only tool needed during assembling the different components is a torque wrench to tighten the friction bolts, making the SFD outperform other self-centering devices based on post-tensioned tendons or springs. The latter has some drawbacks associated with post-tensioning. For instance, the re-centering materials need to be pretensioned in advance, pretension loss is inevitable, and it further decreases the elongation capacity of the re-centering material.

6. *Versatility:* the SFD is suited not only for new construction but also for retrofitting existing buildings. It can be utilized in different ways; just like any other type of damper, it can be mounted on chevron braces. Alternatively, for framed buildings, it can also be placed in the brace to the gusset plate connection illustrated in Figure 5-3. Moreover, the SFD can be combined with isolating devices to reach higher energy dissipation capacity in the case of base-isolated buildings. From the designer's point of view, the friction force can be readily tuned to achieve different hysteretic shapes and meet design requirements.

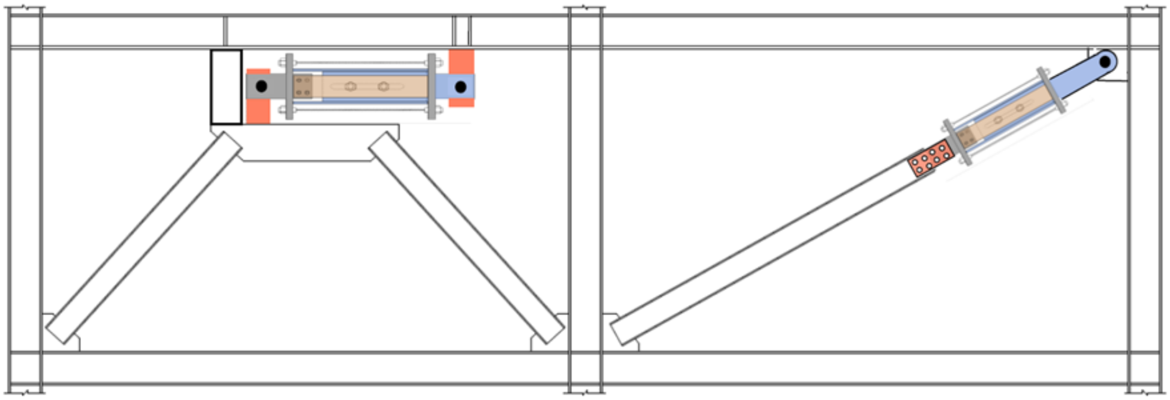

Figure 5-3. Sample SFD installation schemes

The above advantages of the SFD are qualitatively compared with other existing seismic protective systems in Table 5-1.

Table 5-1 Qualitative comparison of existing seismic protection technologies with SFD.

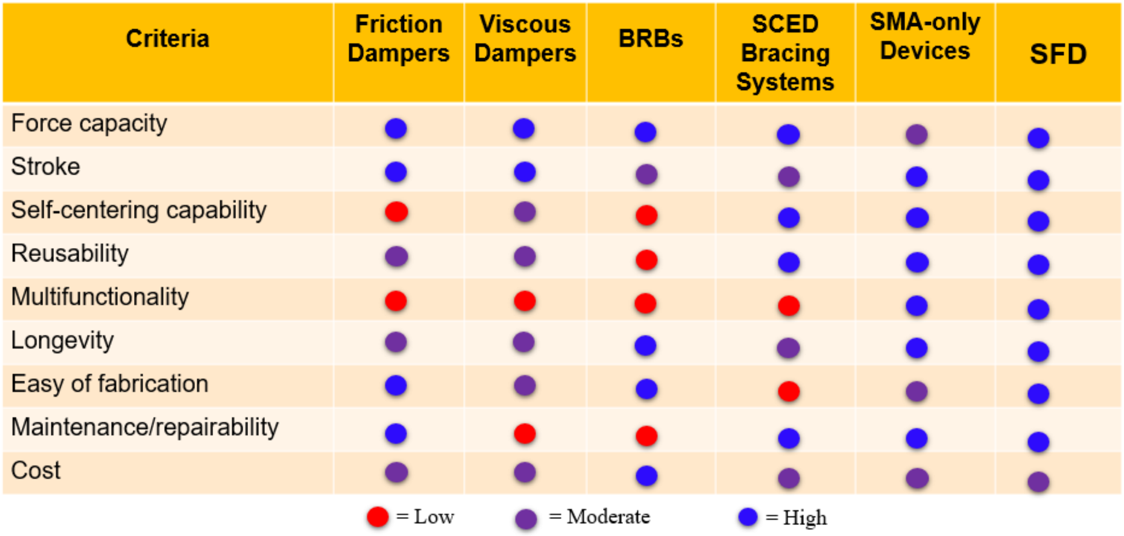

Criteria	Friction Dampers	Viscous Dampers	BRBs	SCED Bracing Systems	SMA-only Devices	SFD
Force capacity	🔵	🔵	🔵	🔵	🟣	🔵
Stroke	🔵	🔵	🟣	🟣	🔵	🔵
Self-centering capability	🔴	🟣	🔴	🔵	🔵	🔵
Reusability	🟣	🟣	🔴	🔵	🔵	🔵
Multifunctionality	🔴	🔴	🔴	🔴	🔵	🔵
Longevity	🟣	🟣	🔵	🟣	🔵	🔵
Easy of fabrication	🔵	🟣	🔵	🔴	🟣	🔵
Maintenance/repairability	🔵	🔴	🔴	🔵	🔵	🔵
Cost	🟣	🟣	🔵	🟣	🟣	🟣

🔴 = Low 🟣 = Moderate 🔵 = High

5.2.3 Working mechanism

Figure 5-4 illustrates the operating principle of the damper. The left connection plate (based on the orientation of the figure) is bolted to the outer members while the web of the inner member is extended out for attachment with structural elements. For the sake of discussion, assume the left end of the damper is fixed while the right end is connected to a loading apparatus. However, it should be noted that for real-world application, either end of the damper can move. First, consider that the damper is under axial tension load. No relative movement between the inner and outer members occurs when the applied load (F) is less than the static friction force. Under this condition, the axial deformation of the SFD is caused by the elastic deformation of the members. When the tension load exceeds the slip load, the inner member pulls the right end plate and move together; however, the left end plate remains stationary because it is constrained by the outer member. Hence, the separation of the two end plates stretches the SMA cables. An external gap opens between the right end of the outer member and the right end plate. Internally, a gap of nominally the same magnitude opens on the left-hand side.

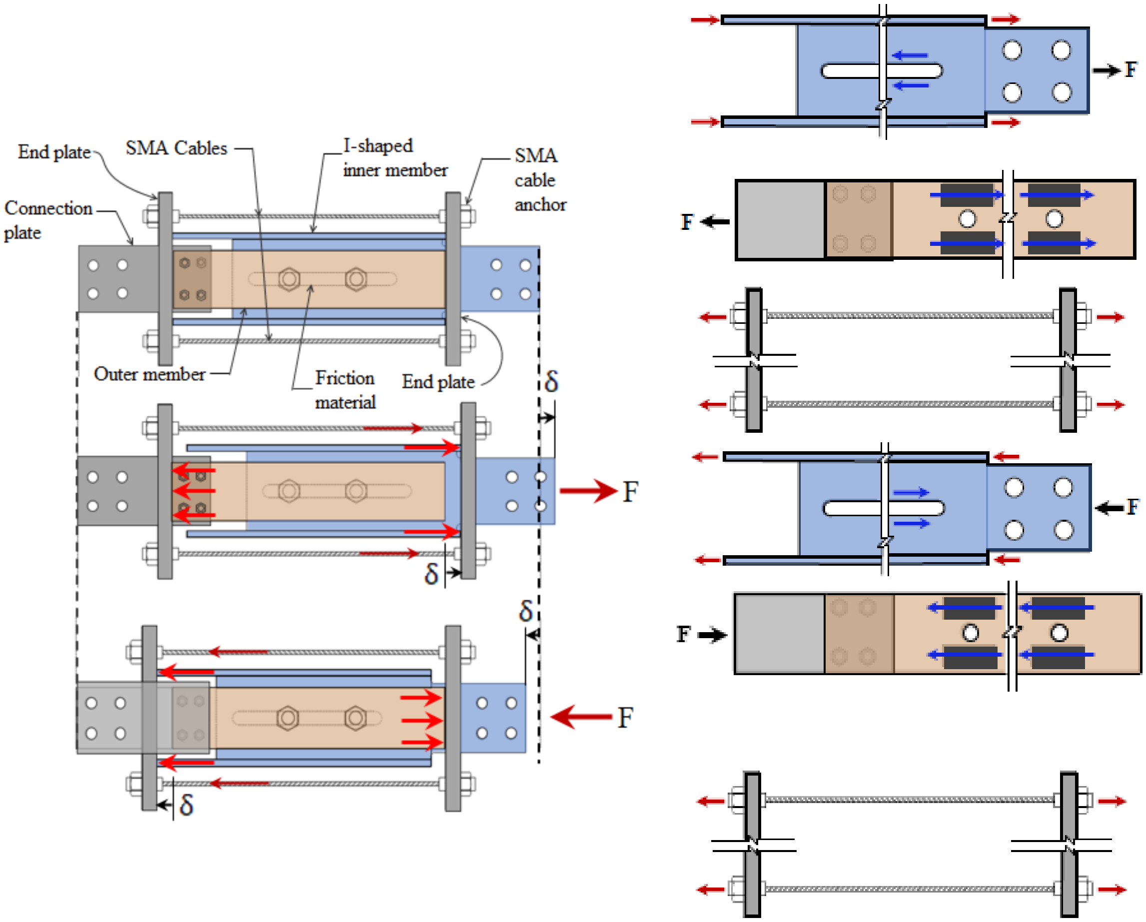

(a) (b)

Figure 5-4. Working principle of the proposed damper, and (b) free body diagrams

When the damper is subjected to compression load, the opposite case occurs: this time, the left endplate moves leftwards as it is pushed by the inner member. The right endplate is constrained by the outer member and, therefore, cannot be moved. An external gap opens between the left end of the outer member and the left endplate. Thus, both compression and tension loads cause the endplates to move apart, resulting in elongation in the SMA cables. In other words, the cables are always in tension regardless of the direction of movement of the damper. Consequently, due to the inherent SC capability of SMAs, the cables provide a restoring force that continually pulls all of the elements back to their initial positions upon the removal of the load. As a result, a bi-directionally functioned damper is realized.

5.2.4 Theoretical analysis of the SFD hysteretic behavior

5.2.4.1 *Mechanical properties of superelastic SMAs*

The unique strain recovery property of an SMA material is due to reversible phase transformations between its austenite and martensite phases. For superelastic SMAs, these phase transformations are stress induced. The stress-strain relationship of superelastic SMAs can be represented by a simplified piecewise-linear model as shown in Figure 5-5 [252,253]. In the figure, σ and ε denote the stress and strain, respectively, wherein the subscripts *M* and *A* denote the martensite and austenite phases, while *s* and *f* denote the starting and ending points of the phase transformation, respectively. The model is characterized by the following parameters: (1) four transformation stresses $\sigma_{Ms}, \sigma_{Mf}, \sigma_{As}, \sigma_{Af}$; (2) the corresponding transformation strains $\varepsilon_{Ms}, \varepsilon_{Mf}, \varepsilon_{As}, \varepsilon_{Af}$; (3) moduli of elasticity for austenite state $E_A / E_M^{'}$; forward and reverse transformation states E_{AM} / E_{MA} , and martensite state $E_M / E_M^{'}$; (4) maximum stress $\sigma_{\max}$ and strain $\varepsilon_{\max}$; (5) residual strain ε_{res}

When a superelastic SMA is subjected to a load, it initially exhibits linear elastic behavior, with the slope of the stress-strain curve being equal to the elastic modulus of the austenite phase (E_A) as shown in Figure 5-5. The forward phase transformation from austenite to martensite begins when the stress reaches at a stress level σ_{Ms} (similar to “yield” stress). During the phase transformations, the slope of stress-strain curve decreases to E_{AM} and material transforms from austenite to martensite The subsequent strain hardening represents the elastic loading behavior of martensite. Upon unloading, the stress decreases linearly, and the onset of reverse transformation is marked by an evident change of the unloading slope on the stress-strain curve. An unloading phase transformation plateau with a slope of E_{MA} and nearly the same length as the loading phase transformation plateau is observed during the reverse phase transformations. Once the material completely transforms austenite, the slope of unloading path changes to $E_A^{'}$ and the stresses decreases to zero with negligible residual strain upon the removal of the load. In particular, if ε_{max} is less than 6-8% (depending on the composition of the material), then there would be almost no residual strains upon unloading, while larger residual strains would be present if the material is loaded for higher values of ε_{max}.

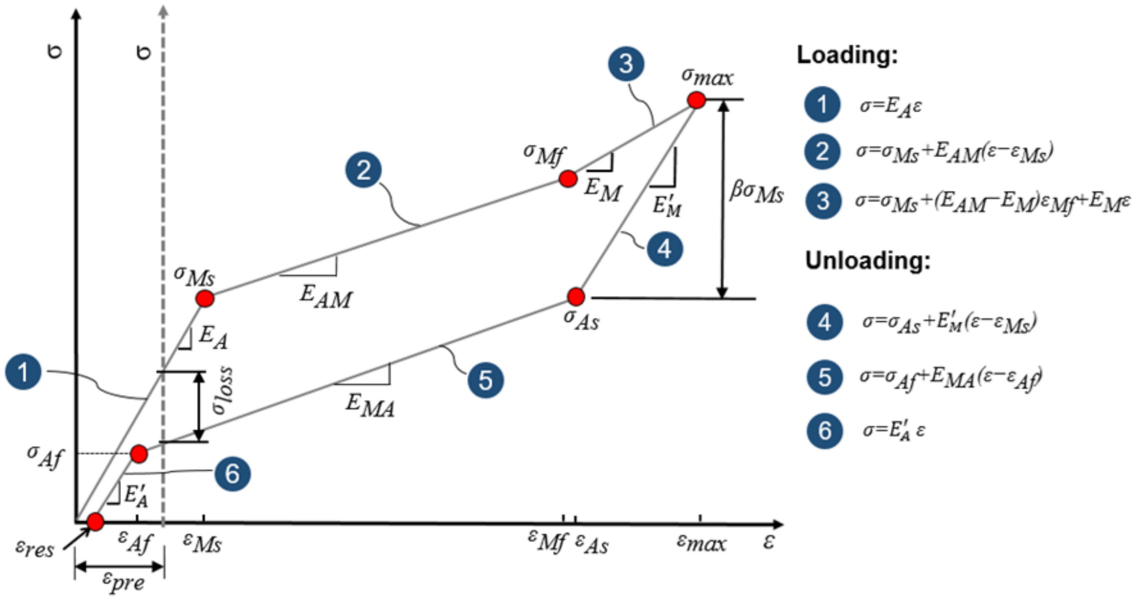

Figure 5-5. Simplified piecewise-linear model of superelastic SMA

During the whole loading-unloading process, SMA exhibits a flag-shaped hysteresis loop accompanied by moderate energy dissipation. Moreover, unlike the yielding behavior of steel, the stress plateau of SMA is due to the phase transformation by shear lattice distortion and is not associated with any induced damage in the SMA. Finally, note that pre-straining of SMAs could eliminate potential residual strains. The applied prestrain (ε_{pre}) will lead to a rightward shift of the abscissa in Figure 5-5. Note that after a loading and unloading cycle, the actual prestress level may decrease by a magnitude that can be represented by the distance between the intersection points of the abscissa and the loading and unloading branches as indicated with σ_{loss} in Figure 5-5.

5.2.4.2 Prediction of damper response through analytical expressions

Since the SFD combines SMA cables and a friction device in parallel, the hysteretic behavior of the damper can be obtained by linear superposition of the two response mechanisms as illustrated in Figure 5-6. As discussed above, superelastic behavior of SMA cables can be idealized using a piece-wise self-centering model. The work done internally by the frictional forces on the displacement at the interface between the sliding friction pads and the inner member provides additional energy dissipation to the damper. The frictional forces depend on dry Coulomb friction between materials and the magnitude of the normal force at the sliding interface and can be simulated by a rectangular hysteresis loop.

The force-deformation constitutive relation of the damper can be characterized by defining eight critical points as labelled in Figure 5-6. Owing to the symmetrical response of the damper, only the first quadrant response is labelled in the figure and described below.

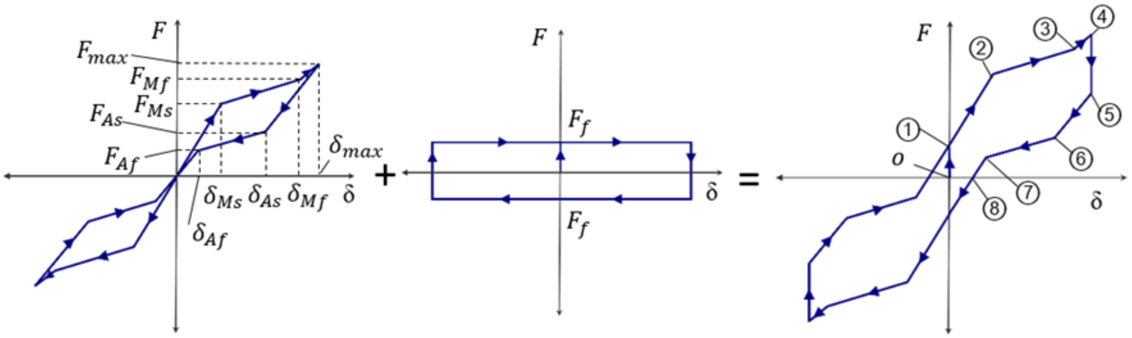

Figure 5-6. Idealized force-deformation response of the proposed damper (not to scale)

In the initial stage of loading, i.e., from the origin point O to ①, the axial load is less than the activation force F_1, which is the sum of the pre-tension force of SMA cables (if applicable) and the static friction force. When the applied load exceeds F_1, the relative movement of the inner and outer members occurs and the stiffness of the damper changes to the stiffness of the SMA cables. Since SMA cables are still in austenite phase during stage ①-②, the stiffness of the damper can be expressed as:

$$K_{1-2} = \frac{E_A A}{L} \tag{5.1}$$

where A and L are the area and length of SMA cables, respectively. As the applied load increases, the SMA cables reach to a “yield-like” state as signified by point ② in Figure 5-6 and begin experiencing the austenite-to-martensite phase transformation. The stiffness is controlled by the SMA cables and they are within the austenite-to-martensite phase transformation stage. The damper "yield" strength F_2 and damper deformation δ_2 at point ② as well as damper stiffness K_{2-3} between points ② and ③ are given as:

$$F_2 = F_{Ms} + F_f + F_{ini} = (\sigma_{Ms} + E_A \varepsilon_{pre})A + F_f \tag{5.2}$$

$$\delta_2 = \left(\varepsilon_{Ms} - \varepsilon_{pre}\right)L \tag{5.3}$$

$$K_{2-3} = \frac{E_{AM} A}{L} \tag{5.4}$$

where F_{ini} is the initial pretension force induced by the prestrain ε_{pre} and F_f is the friction force.

As the loading increases, the SMAs complete the martensite transformation at point ③ and the corresponding force, deformation and stiffness of the damper is given as:

$$F_3 = F_{Mf} + F_f + F_{ini} = \left(\sigma_{Mf} + E_A \varepsilon_{pre}\right)A + F_f \tag{5.5}$$

$$\delta_3 = \left(\varepsilon_{Mf} - \varepsilon_{pre}\right)L \tag{5.6}$$

$$K_{3-4} = \frac{E_M A}{L} \tag{5.7}$$

Further loading leads to a distinct increase in the slope, which corresponds to the elastic loading of the martensite phase (branch ③-④) and the damper force and displacement is calculated as:

$$F_4 = F_{\max} + F_f + F_{ini} = \left(\sigma_{\max} + E_A \varepsilon_{pre}\right)A + F_f \tag{5.8}$$

$$\delta_4 = \left(\varepsilon_{\max} - \varepsilon_{pre}\right)L \tag{5.9}$$

Once the displacement is reversed after reaching its maximum value, the friction force changes direction, prompting the axial load to immediately drop by twice as much as the friction force plus pretension force $\left(2F_f + F_{ini}\right)$. The instant drop is identified by branch ④-⑤. Here, a parameter β defined as the energy dissipation ratio, is given by equation (5.11).

$$F_5 = F_{\max} - F_f - F_{ini} = \left(\sigma_{\max} - E_A \varepsilon_{pre}\right) A - F_f \tag{5.10}$$

$$\beta = \frac{2F_f + F_{ini}}{F_2} = \frac{2F_f + F_{ini}}{F_{Ms} + F_f + F_{ini}} \tag{5.11}$$

At stage ⑤-⑥, the SMA cables are recovering elastic deformations and the unloading stiffness is assumed to be similar to that of branch ③-④. As unloading continues, the SMA cables start reverting to austenite phase from martensite phase at point ⑥ and completes these transformations at point ⑦. The force continues gradually decrease along branch ⑥ -⑦, whose slope is close to that of branch ②-③. The forces and displacements at points ⑥ and ⑦ are given by equations (5.12) to (5.15).

$$F_6 = F_{As} - F_f - F_{ini} = (\sigma_{As} - E_A \varepsilon_{pre}) A - F_f \tag{5.12}$$

$$\delta_6 = \left(\varepsilon_{As} - \varepsilon_{pre}\right) L \tag{5.13}$$

$$F_7 = F_{Af} - F_f - F_{ini} = \left(\sigma_{Af} - E_A \varepsilon_{pre}\right) A - F_f \tag{5.14}$$

$$\delta_7 = \left(\varepsilon_{Af} - \varepsilon_{pre}\right) L \tag{5.15}$$

Upon complete unloading, although the residual deformations of the SMA cables are expected to be negligible, the added frictional energy dissipation mechanism may lead to a residual deformation. This residual deformation can be estimated as:

$$\delta_8 = \frac{F_f L}{E_A A} - \varepsilon_{pre} L \tag{5.16}$$

Note that if no or very minimum residual displacement is desired, this can be achieved by adjusting the prestrain on the SMA cables in equation (5.16) such that it overcomes the residual deformations due to frictional force. However, the amount of prestrain must be determined carefully. As indicated in Figure 5-5, if ε_{pre} is greater than ε_{Af}, there will be large the prestress loss after a loading-unloading cycle. In contrast, when ε_{pre} is smaller than ε_{Af}, the prestress loss can be ignored because of the minimal difference between the loading and unloading branches of the austenite phase. Therefore, it is recommended to keep the prestrain level of the SMA cables within the range of $0 \le \varepsilon_{pre} \le \varepsilon_{Af}$.

5.3 Experimental Program

5.3.1 Fabrication of prototype SFD

A proof-of-concept damper was designed and fabricated. While the specimen was not scaled from a particular prototype building, it can be considered as approximately half-scale related to a typical mid-rise office building in a high seismic region. Initially, the specimen was designed to have a target ultimate load capacity of 150 kN at a maximum deformation of 30 mm. This was achieved using a total of eight SMA cables, contributing about 120 kN and friction slip force of 30 kN. However, later on the force capacity was reduced to 90 kN by removing four cables and reducing the friction force proportionally due to limitations of the available hydraulic actuator at the testing facility.

The geometric details of the specimen are given in Figure 5-7. The sizes of the main parts were determined according to the following basic rules: (1) the strengths of the inner member, outer member, and other accessories are significantly larger than the maximum possible load resistance of the SMA cables plus the frictional force; (2) the length of the outer and inner members, as well as the distance between the end plates, was dictated by the length of SMA cables, which was determined by the stroke. Thus, for the prototype damper in the present study, the inner member is a *W6×25* I-shaped cross-section, while a couple of *C4×7* channels are used for the outer member. Both members were made up of low carbon steel (nominal yield strength of 248 MPa).

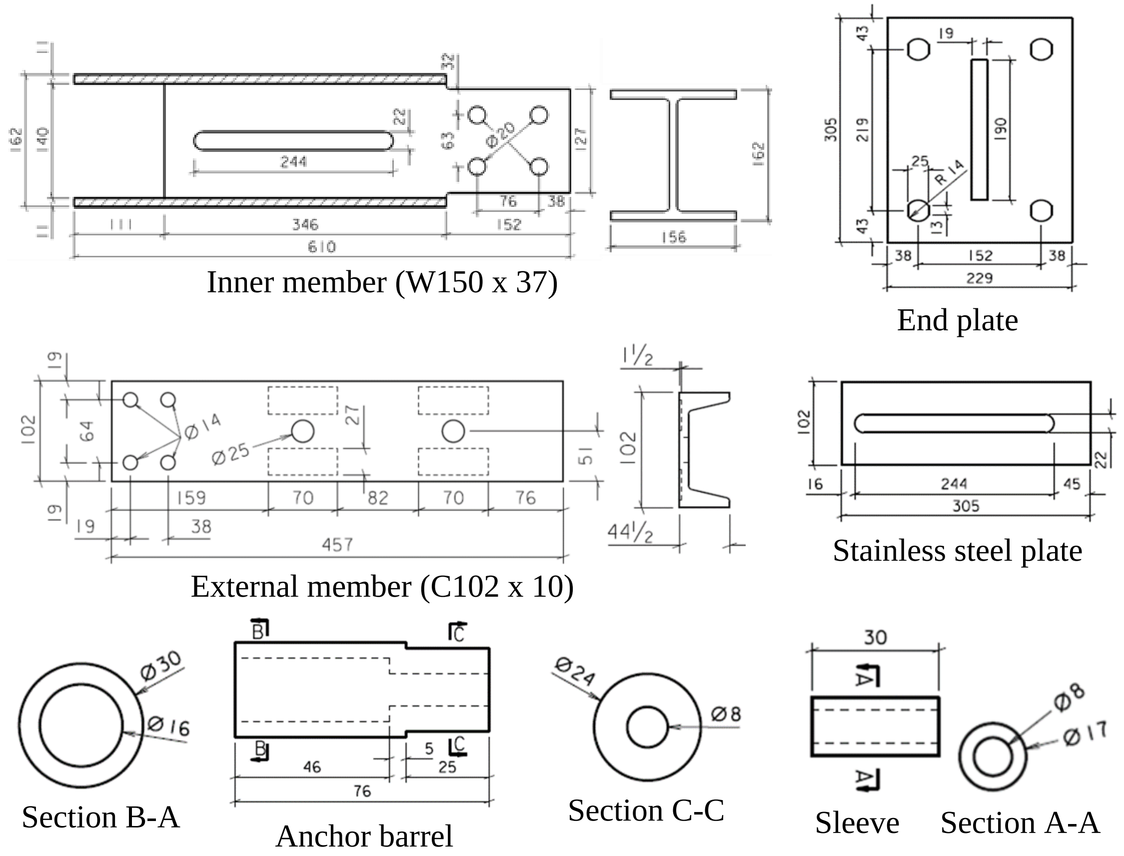

Figure 5-7. Damper specimen geometric details (unit: mm)

The surface between the web of the I-shaped member and the C-channels forms a friction interface activated by the relative motion between the two structural members. These interfaces comprise the energy dissipation mechanism of the system in addition to the inherent contribution of the SMA cables. A 1.5 mm thick sheet of highly polished (mirror-finish) Type 304 stainless steel was welded on either side of the I-shaped member web. Both the stainless-steel plate and the web were detailed with a long-slotted hole whose length was chosen to accommodate a stroke of 30 mm. Four nonmetallic brake and clutch lining friction pads with dimensions of 70 × 30 × 5 mm were attached to each C-channel to form the outer side of the friction interface. The supplier's specification sheet lists a maximum coefficient of friction of 0.47 and an operating temperature up to 480°C. 1.5 mm deep. Recesses of 1.5 mm deep were machined on the outer surface of the C-channels, and the pads were embedded in recesses to avoid potential debonding of the friction pads during cyclic loading. A small amount of epoxy glue was used around the pads to stabilize them in the recess. It is also thought that the recess provides confinement for the friction pads and minimizes distortion in the material during sliding. The inner and outer members were clamped together using two 25.4 mm (1 in.) diameter ASTM A490 [254] high-strength structural bolts. The normal pressure was applied by tightening the bolts using a calibrated torque wrench to the required clamping force, which was controlled by washer load cells. A sufficient number of Belleville washers were placed under the nut to maintain a constant level of normal force on the friction interfaces during sliding and prevent loss of the damper slip load under cyclic loading.

The end plates fitted at each end of the damper are made up of steel plates with dimensions of 229 × 305 × 25.4 mm. Both plates had vertical slots cut using water jet technology. On the right-hand side (based on Figure 5-4 orientation), the flanges of the I-shaped member were copped so that the web extended out and protrude through the end plate slot to be bolted to a clevis. This connection design allowed the axial load to be transferred directly into the flanges and web. On the opposite side, a connection plate was fitted through the slot of the end plate and bolted to the C-channels. It should be noted that a piece of the web was cut out to reserve a gap of 30 mm (equivalent to the stroke) between the left connection plate and the web such that when the damper is subjected to compression load, the inner member will not jam against the connection plate.

5.3.2 SMA cable anchoring system

Superelastic NiTi SMA cables were utilized as the core component of the SFD. According to the material supplier, the chemical composition of the SMA is approximately 50.8% atomic percentage of nickel with the balance contributed by titanium. The austenite finish temperature for the NiTi cables is -22 ^{o}C. Each cable was in a 7×7 configuration, where each cable is made of seven helically wrapped strands and each strand consists of seven monofilament wires laid in left-handed helix. Therefore, the cable is composed of 49 wires with a diameter of 0.885 mm. The nominal outer diameter of the cable is 8 mm and the cross-sectional area is 30.13 mm^2. The cable length was determined based on the objective to limit the SMA strain to 6% at the design deformation capacity of the damper. Hence, the overall length of each cable, including connection hardware, is 500 mm.

Four SMA cables were anchored to the end plates symmetrically at the top and bottom of the damper. It is of paramount importance to ensure that the cables are effectively anchored while fabricating and testing the SFD. Therefore, a custom anchorage system that consists of sleeve, anchor barrel, and hexagonal nut was designed and implemented. The sleeve is a short hollow cylindrical element that houses the SMA cables tightly when it is squeezed by a machine. The anchor barrel is a threaded rod with stepped holes inside which the SMA cable with the sleeve is placed and constrained. The hexagonal nut is used for tightening the anchor barrel. The outer surface of the anchor barrel has two cut-off edges to prevent it from rotating when the nut is tightened. Key dimensions of these hardware are shown in Figure 5-7.

As illustrated in Figure 5-8, the assembly procedure of the anchorage system consists of three steps. The SMA cable is first inserted into the anchor barrel; then the sleeve is placed at the ends of the cable (Step 1). Mechanical pressure is applied using a crimping machine to squeeze the sleeve uniformly and grip the cable tightly (Step 2). It is crucial to monitor the applied pressure to avoid damaging the cable as well as prevent slippage. Compressing the outer diameter of the sleeves from 17 mm to 14 mm was selected as it enabled the anchorage systems to perform well. Finally, the anchor barrel is then pulled up and subsequently passed through the holes on the end plates and the tightening nuts are screwed (step 3). Although the SMA cables were installed snug tight in the current study, pre-tension load can be applied by directly tightening the nuts if needed.

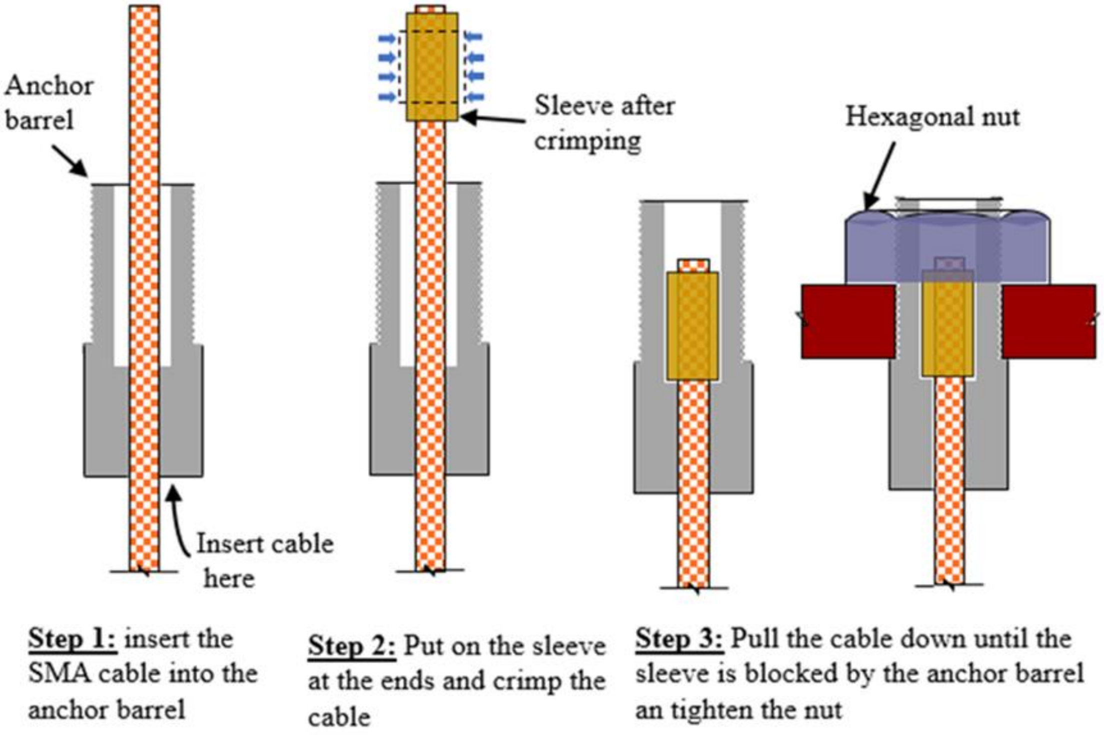

Figure 5-8. SMA cable anchorage system assembly procedure

5.3.3 Test setup, instrumentation, and loading protocol

The cyclic loading tests were conducted in two phases: loading rate characterization tests and temperature sensitivity tests. Photographs of the test setup for each phase are shown in Figure 5-9. The SFD specimen was connected to an MTS 244 hydraulic actuator, which enables a maximum force of 98 kN and a maximum velocity of 381 mm/sec. The damper force and deformation were measured using built-in load cell and LVDT of the actuator. Two LCWD load washer and compression load cells were used to measure the compression force generated from two friction bolts.

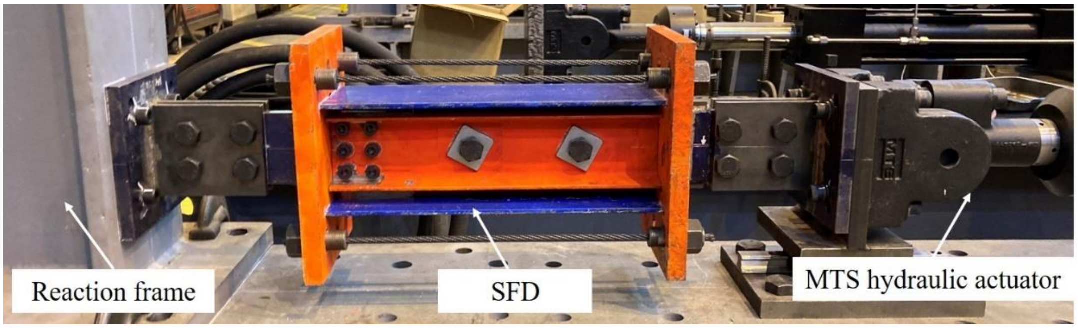

(a)

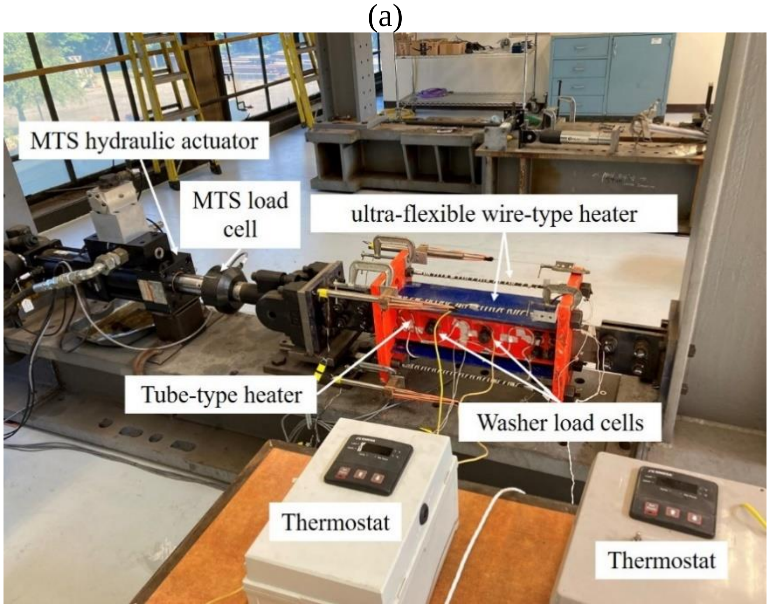

(b)

Figure 5-9. Photographs of test setup: (a) loading rate tests and (b) temperature dependent tests

In the first phase, all the tests were conducted at room temperature of approximately 25°C. The response of the damper with and without SMA cables under different loading frequencies was investigated. In the present study, three different loading patterns illustrated in Figure 5-10 were applied to the SFD. For the friction only tests, a quasi-static loading test at incrementally increasing displacement amplitudes up to 30 mm was performed in the first round. Then, a pre-defined harmonic displacement inputs that includes two ramp-up cycles in the beginning, three full cycles with 25 mm amplitude in the middle and three ramp-down cycles at the end was applied at loading frequencies of 0.05 Hz, 0.1 Hz, 0.5 Hz, and 1 Hz. The complete damper, i.e., SMA cables and frictional component, was also subjected to the same loading protocol but the maximum displacement amplitude was kept at 20 mm instead of 25 mm due to the limitations in force capacity of the actuators. Note that the response of the same SMA cables at different loading rates was reported in Ozbulut et al. [102], and therefore no additional rate-dependency tests were conducted on SMA cables only.

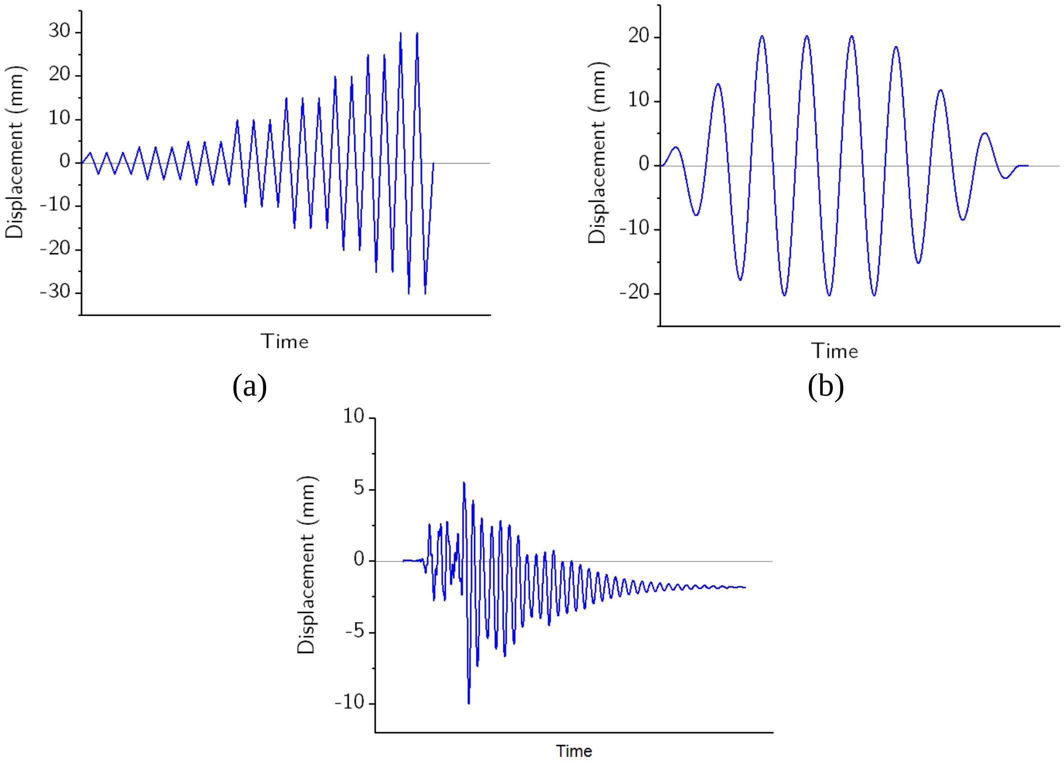

(a) (b)

(c)

Figure 5-10. Loading patterns: (a) quasi-static increasing displacement amplitude; (b) constant amplitude at different loading rates, and (c) response history of SMA-based brace under Northridge earthquake

The second phase of the experimental program consisted of temperature-dependency tests. In particular, the responses of the frictional component, SMA cables, and complete damper at varying temperatures of 25, 30, 40, and 50°C were studied. A shown in Figure 5-9(b), one tube-type heater was uniformly taped on two friction plates and four ultra-flexible wire-type heaters were wrapped on four SMA cables. These heaters could provide a maximum heat output of 65°C. Two programmable thermostats were connected to the tube-type heater and ultra-flexible wire-type heaters. Temperatures of friction plates and SMA cables were regulated by two thermostats individually. Due to difficulties in modifying the test set up for tests at temperatures below room temperature, the response of the damper at temperatures lower than 25°C was not pursued in this study. The harmonic tests during the second phase were conducted at a loading frequency of 0.1 Hz and consisted of three loading cycles. The testing for the sub-components of the damper was carried out at 10 mm and 20 mm displacement amplitudes, whereas the combined damper was tested only at 10 mm displacement amplitude due to limitations in force capacity of the actuator. In addition, a displacement response history of a self-centering brace obtained from numerical simulation of a four-story building subjected to the 1994 Northridge earthquake was also applied to the SFD. The purpose of this test was to characterize the behavior of the SFD under a realistic earthquake loading condition. The displacement history is shown in Figure 5-10(c) and was applied to the SFD during the tests under various temperatures.

5.4 Test Results and Discussions

5.4.1 Responses of frictional component

Figure 5-11 shows the force-displacement response of the damper in the absence of the SMA cables, i.e., frictional component only. In Figure 5-11(a), the response of the frictional component is shown under a quasi-static loading with a displacement amplitude incrementally increasing up to 30 mm. In Figure 5-11(b) through 5-11(f), the hysteresis curves are plotted separately for four loading frequencies, namely, 0.05, 0.1, 0.5, and 1 Hz, at a constant amplitude of 25 mm. In general, the damper displayed a completely stable, repeatable, and reliable behavior with insignificant dependence on the frequency for the range considered in this study. The relative movement between the external member (together with the friction pads) and the internal member led to the friction action and hence absorbed kinetic energy. It is evident from the results that the force-displacement behavior of the damper is elastic perfectly plastic without hardening and the hysteresis curves are close to rectangle. It is also noticed that the hysteretic curves are not perfectly symmetrical in terms of load resistance, especially at the 0.05 Hz frequency. In particular, when the damper is loaded in the push direction, the load resistance was slightly smaller than when it is loaded in the pull direction. This can be attributed to unexpected friction between the connection plate and the inner member, in which the latter was supposed to move freely within the slot at the end plate. Nevertheless, the difference in the peak force when the damper was loaded in the push or pull directions was less than 2%. The maximum static friction force is virtually identical to the sliding friction force. It is noted that loading frequency had very little influence on the sliding friction force. The frictional resistance was kept almost constant with no noticeable fading under repetitive sliding motions throughout the experiment. The slipping motion was uniformly smooth, chatter-free, and without any stick-slip behavior based on test observations. At the end of the tests, the damper was dismantled, and the friction pads were inspected. The pads were all kept in one piece; no signs of damage or breakage were observed.

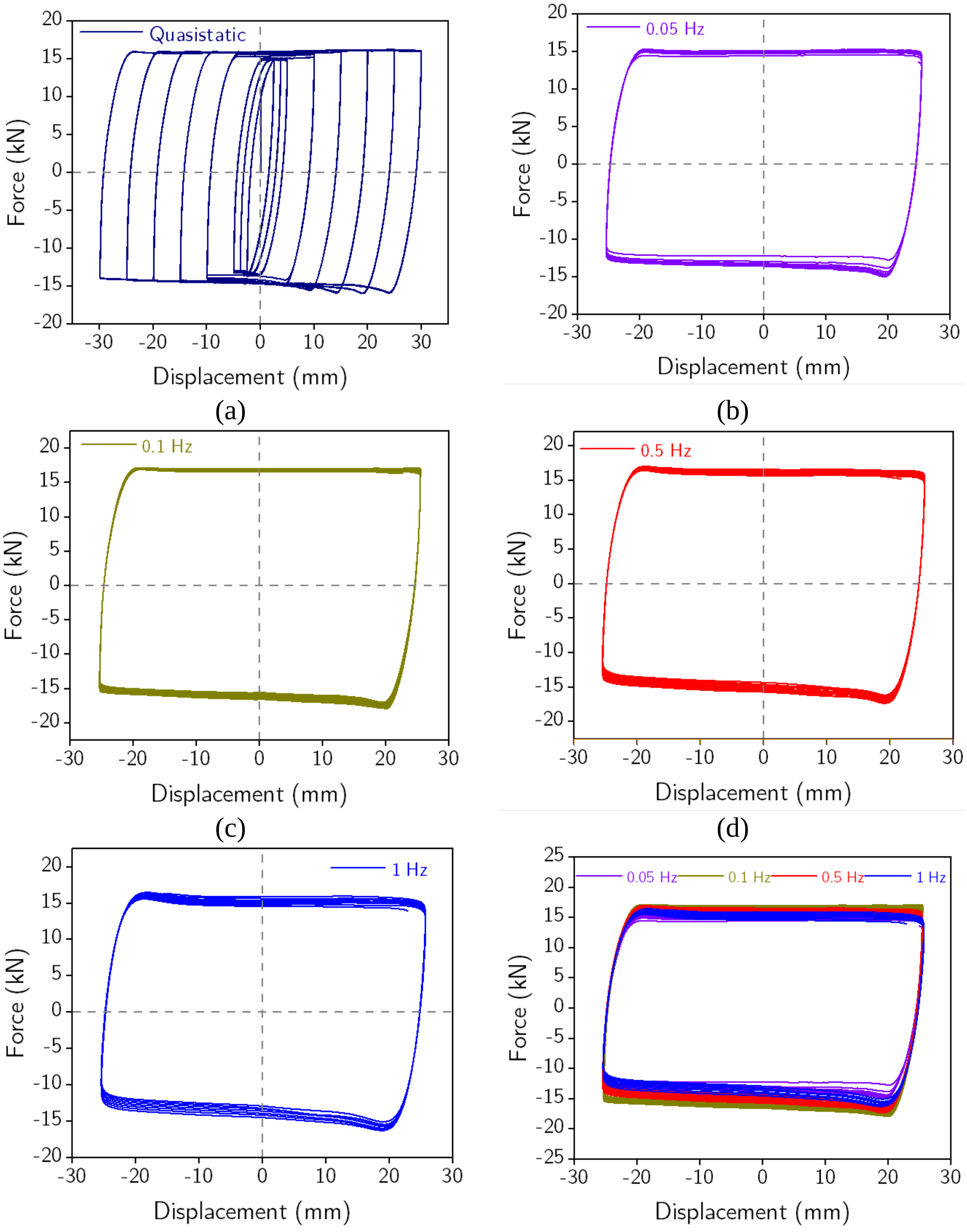

(a) (b) (c) (d) (e) (f)

Figure 5-11. Friction only damper force-displacement hysteresis curves under different loading frequencies: (a) quasistatic, (b) 0.05 Hz, (c) 0.1 Hz, (d) 0.5 Hz, (e) 1 Hz, and (f) dynamic test results combined together

Even though the force-displacement relationships displayed highly repeatable frictional behavior, the bolt clamping forces were somewhat fluctuating during the sliding motions. Figure 5-12 illustrates the time history of clamping force ratio (CFR) for the quasistatic loading case, in which CFR is defined as the ratio of the real-time clamping force to the initial clamping force. It can be seen that CFR of the right bolt (based on Figure 5-9 orientation) ranged from 0.91 to 1.09, while for the left bolt, it ranged from 0.97 to 1.02. However, this minor fluctuation seems to have insignificant influence on the overall frictional force. The inconsistent bolt force, particularly the right bolt, might be attributed to the slightly bending behavior of the high-strength bolts when subjected to load reversal, and/or extra friction was unexpectedly induced between the left connection plate and the inner member when the specimen was in compression. It is believed that the extra friction and asymmetric behavior can be eliminated if the void between the connection plate and inner member is appropriately enlarged.

The variation in the slip load was within a permissible tolerance of $\pm 10\%$. This indicates that the Belleville washers played an essential role in maintaining the clamping force of bolts. A typical Belleville washer is a high resistance cone-shaped annular disc spring that flattens when compressed and returns to its original shape when the load is released. In this way, if the bolt had to lose the preloading level due to the wearing of the friction material, the disc spring would restore the force by keeping the bolt shaft in tension. As such, the use of Belleville washers is suggested to prevent partial loss of bolt preloading and, therefore, the degradation of the slip force during the lifetime of the damper.

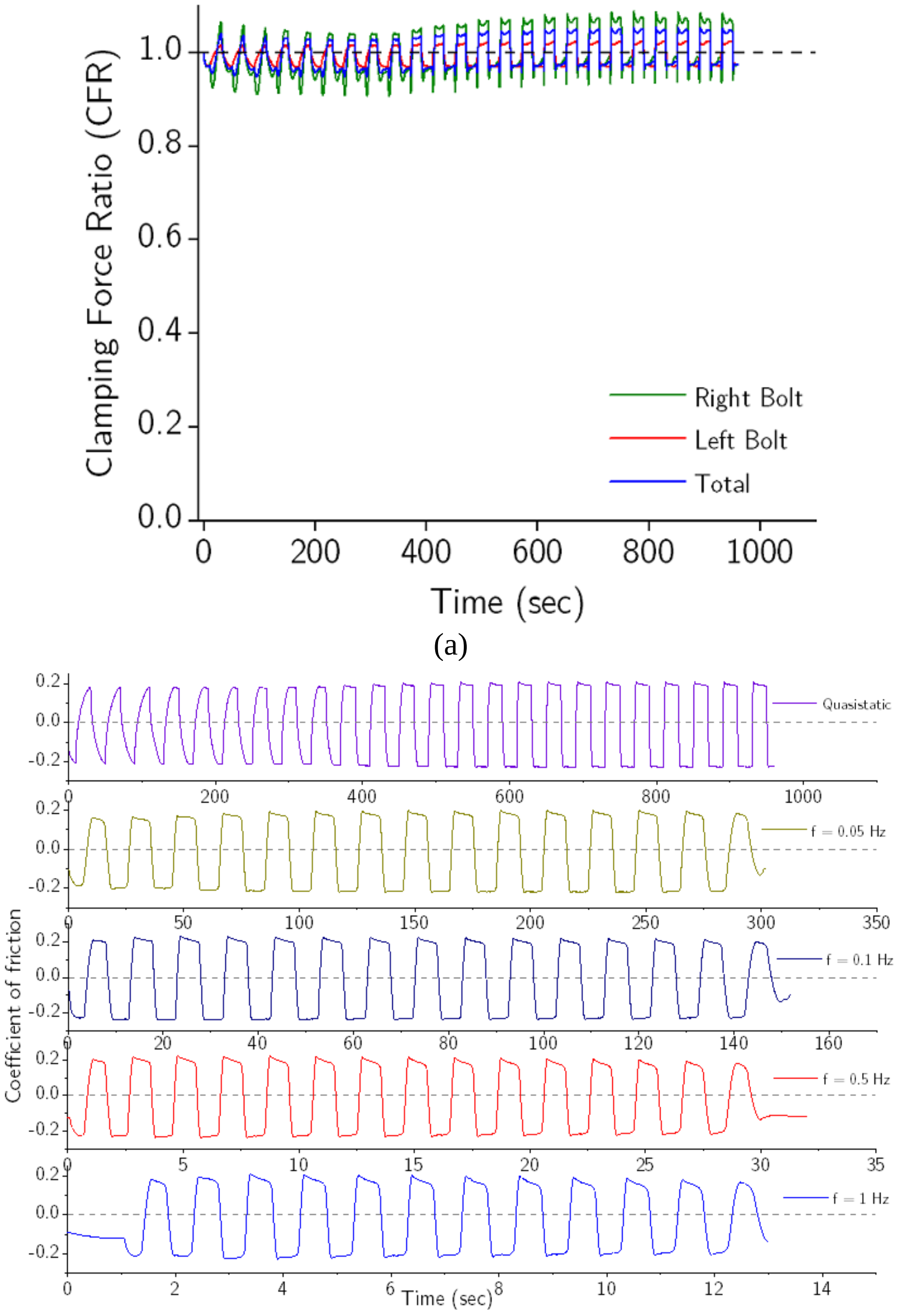

(a)

(b)

Figure 5-12. Time history of (a) clamping force ratio and (b) coefficient of friction

Figure 5-12(b) shows the variation of the friction coefficient of the sliding interfaces, derived by dividing the frictional force (considering double shear) by the clamping force. In this study, the average coefficient of friction associated with the quasi-static loading rate was considered as the static coefficient of friction, while the one obtained from a high loading rate (i.e., f = 1Hz) was considered as the kinetic coefficient of friction. Based on the experimental results, the static and kinetic friction coefficients were calculated to be about 0.22 and 0.21, respectively.

5.4.2 SFD cyclic force-displacement responses

In this section, the results of the experimental tests on the overall damper, i.e., SMA cables and frictional component, are discussed. Figure 5-13 shows the force-displacement response of the SFD under different loading frequencies. The overall response of the damper was consistent with the intended working principle. The behavior of the damper in the two loading directions look symmetrical. As can be inferred from Figure 5-13, the damper first exhibited considerably high initial stiffness before the relative motion of the friction interface is triggered. The forward phase transformation of the SMA material was initiated at approximately 8 mm deformation, leading to the “yield”-like behavior followed by a transformation loading plateau with a particular hardening slope beyond the “yield” point. The observed hardening slope is essentially the stiffness of the SMA cables during phase transformations. A larger hysteresis was observed in the SFD compared to a typical SMA behavior due to the frictional contributions in the SFD. Note that the tests at quasi-static loading and at different loading frequencies consisted of three loading cycles at given loading amplitude. There was no visible difference in the damper response under different loading cycles, indicating a stable response for the damper. As can be seen from Figure 5-13(f), there was also no significant effect of loading frequency on the damper response. This will be evaluated more quantitatively in the next subsection. Finally, the damper response at higher displacement amplitudes could not be characterized as the maximum force of the damper would be above the capacity of the load cell of the actuator used in the tests. The strain on the SMA cables is estimated to be approximately 4.2% strain considering the 480 mm anchor-to-anchor length of SMA cables.

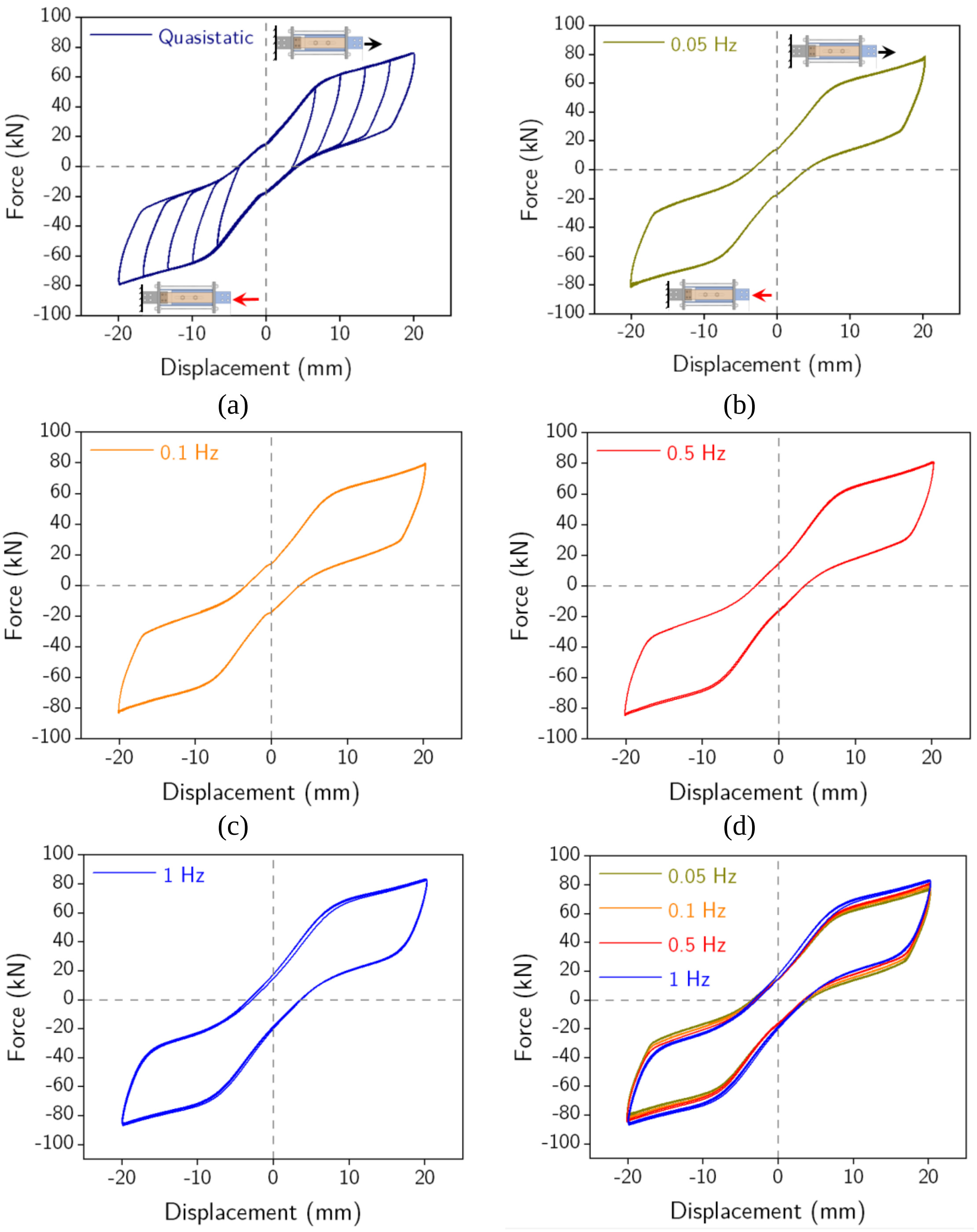

(a) (b)

(c) (d)

(e) (f)

Figure 5-13**.** Force-displacement hysteresis responses of the SFD under different loading frequencies: (a) quasi-static, (b) 0.05 Hz, (c) 0.1 Hz, (d) 0.5 Hz, (e) 1 Hz, and (f) all combined

5.4.3 Energy dissipation capacity, self-centering capability, and secant stiffness

To further assess the cyclic performance of the SFD, the hysteretic parameters of prime interest for earthquake engineering applications such as dissipated energy, equivalent viscous damping ratio, recentering capability, and effective stiffness were evaluated for the tests conducted at different loading frequencies. The dissipated energy was calculated as the area under the hysteretic response of the SFD. The equivalent viscous damping (EVD), is calculated based on the following equation:

$$\xi_{eq} = \frac{E_D}{4\pi\left(E_{so}^{+} + E_{so}^{-}\right)} \tag{5.17}$$

where E_D is the total energy dissipated per cycle and E_{So}^{+} and E_{So}^{-} are the elastic strain energy embodied by an equivalent linear system at the same peak displacement and force as illustrated in Figure 5-14(a).

Self-centering capability is one of the most important properties for the damper, which is expected to control the residual deformation of the structures after earthquakes effectively. The damper is also supposed to have tolerable residual deformation during the service life such that it is reusable. The self-centering capability of the damper is provided by the restoring force of the SMA cables, while it is also largely influenced by the frictional force. To quantitatively evaluate self-centering capability of the SFDs, a parameter called relative self-centering efficiency (RSE) is computed as follows [255]:

$$RSE = 1 - \frac{u_{res}^{+} - u_{res}^{-}}{u_{\max}^{+} - u_{\max}^{-}} \tag{5.18}$$

where $\mathrm{u}_{\mathrm{res}}^{+}$ and $\mathrm{u}_{\mathrm{res}}^{-}$ are the residual displacements along pull and push loading directions, respectively. The RSE quantifies the percentage of the recoverable peak displacement. An RSE value corresponding to a perfectly self-centering device with zero residual deformation is equal to one, while a value of zero corresponds to a device without any recentering capacity. Finally, the secant stiffness is computed using the equation below:

$$K_s = \frac{F_{\max}^{+} - F_{\max}^{-}}{u_{\max}^{+} - u_{\max}^{-}} \tag{5.19}$$

where F_{max}^{+}, u_{max}^{+} , F_{max}^{-} , and u_{max}^{-} are the maximum force and displacement along pull and push loading directions, respectively, as illustrated in Figure 5-14(a).

The energy dissipation properties of the damper are shown in Figure 5-14(a) and 5-14(b) in terms of dissipated energy and EVD, respectively. The energy dissipation per cycle was about 1.6 kJ and remained almost constant as the loading rate increased. The SFD provided a minimum of 14% EVD throughout the tests. It can be seen from Figure 5-14(b) that the EVD slightly decreased as the loading frequency increased except at 1 Hz. This tendency can be attributed to the fact that the SMA cables exhibits slightly higher force levels at increasing loading frequencies as shown in an earlier study [102] . Therefore, the secant stiffness of the overall damper increases with increasing loading frequencies as shown in Figure 5-14(c). This, in return, increases the elastic strain energy, and decreases the EVD.

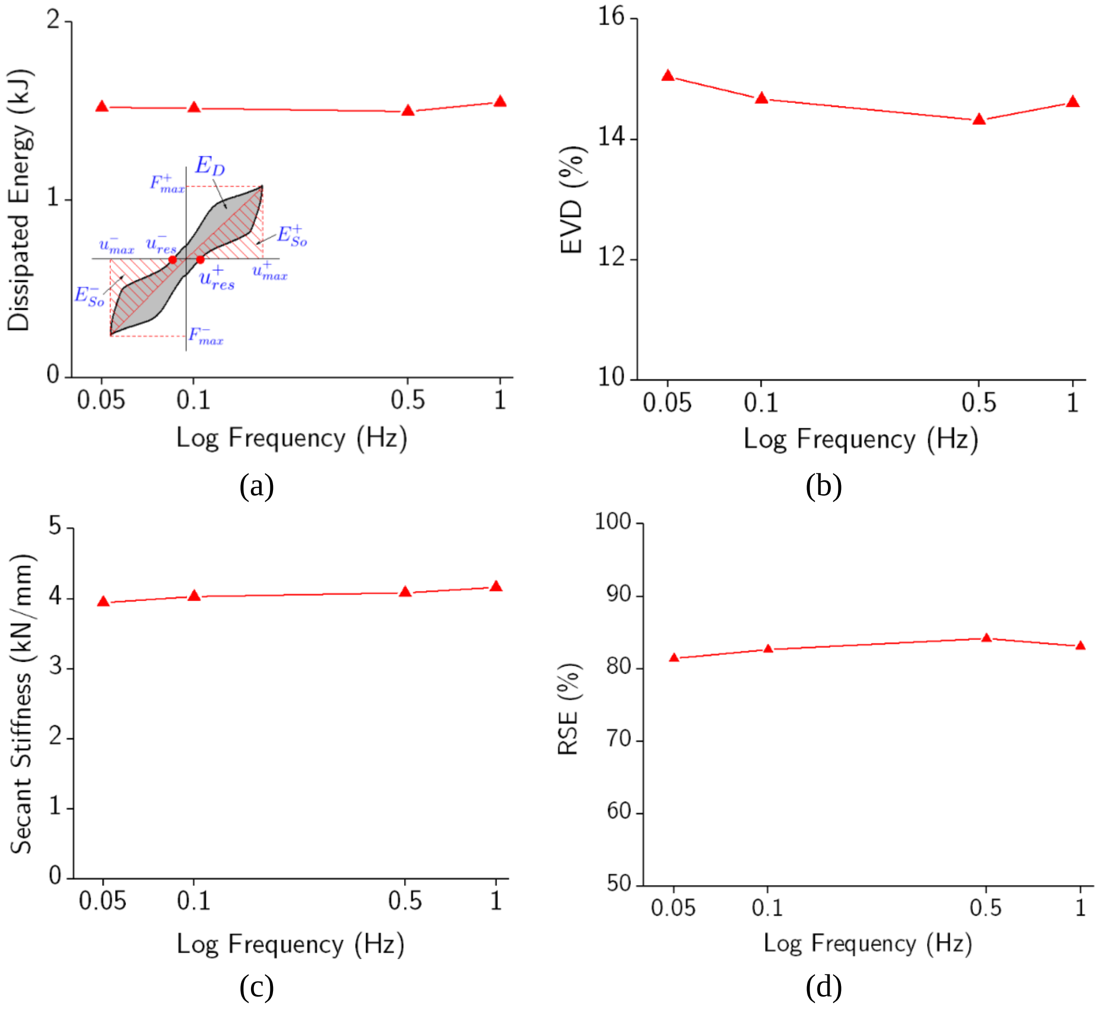

(a) (b) (c) (d)

Figure 5-14. Variation of cyclic properties of the SFD with loading frequency: (a) dissipated energy, (b) EVD, (c) RSE, (d) secant stiffness

Self-centering capability of a damper is an important parameter to effectively control the residual drifts in a structure after an earthquake. In the developed SFD, the self-centering capability is provided by the restoring force of the SMA cables, while it is negatively influenced by almost perfectly plastic behavior of the frictional component after the slip. As shown in Figure 5-14(d), the RSE values ranges from 82% to 84% for the tests conducted at different loading, frequencies which indicates a very good self-centering capability for the developed damper. In other words, for an applied displacement of 20 mm, the maximum residual deformation was just 3.6 mm. As can be seen from Figure 5-13(a), the residual deformations did not increase with increasing displacement amplitude since they were mainly due to frictional force that remained constant. No further residual deformations would occur in the device if the tests could continue up to about 30 mm since the SMA cables can fully recover their strains up to 6-7%. Overall, the results presented in Figure 5-14 clearly show that the loading frequency has a negligible effect on the hysteretic properties of the damper.

5.4.4 Effects of temperature

The response of both SMA cables and friction devices is sensitive to changes in environmental temperature. The force-displacement response of each subcomponent of the SFD, i.e., friction and SMA cables, at four different temperatures are presented in Figure 5-15(a)-(d) for displacement loading amplitudes of 10 mm and 20 mm. Note that there was a problem in data acquisition during the SMA cables only test at 10 mm amplitude and 50°C and no results presented for this case in Figure 5-15(c). Also, during the SFD test at the 50°C, the test was terminated at 18 mm since it reached the force capacity of the actuator. It can be seen that the hysteresis loops (force levels) of the SMA cables slightly shifted upward with increasing temperature. This is because temperature affects the stress-induced phase transformations in SMAs. In particular, the stress levels that initiate phase transformations increase with increasing temperature. Note that in the developed hybrid damper, the force contribution of the SMA cables was six times larger than the friction force. Therefore, as evident in Figure 5-15(e), the temperature dependency of the damper response was dominated by the SMA cables.

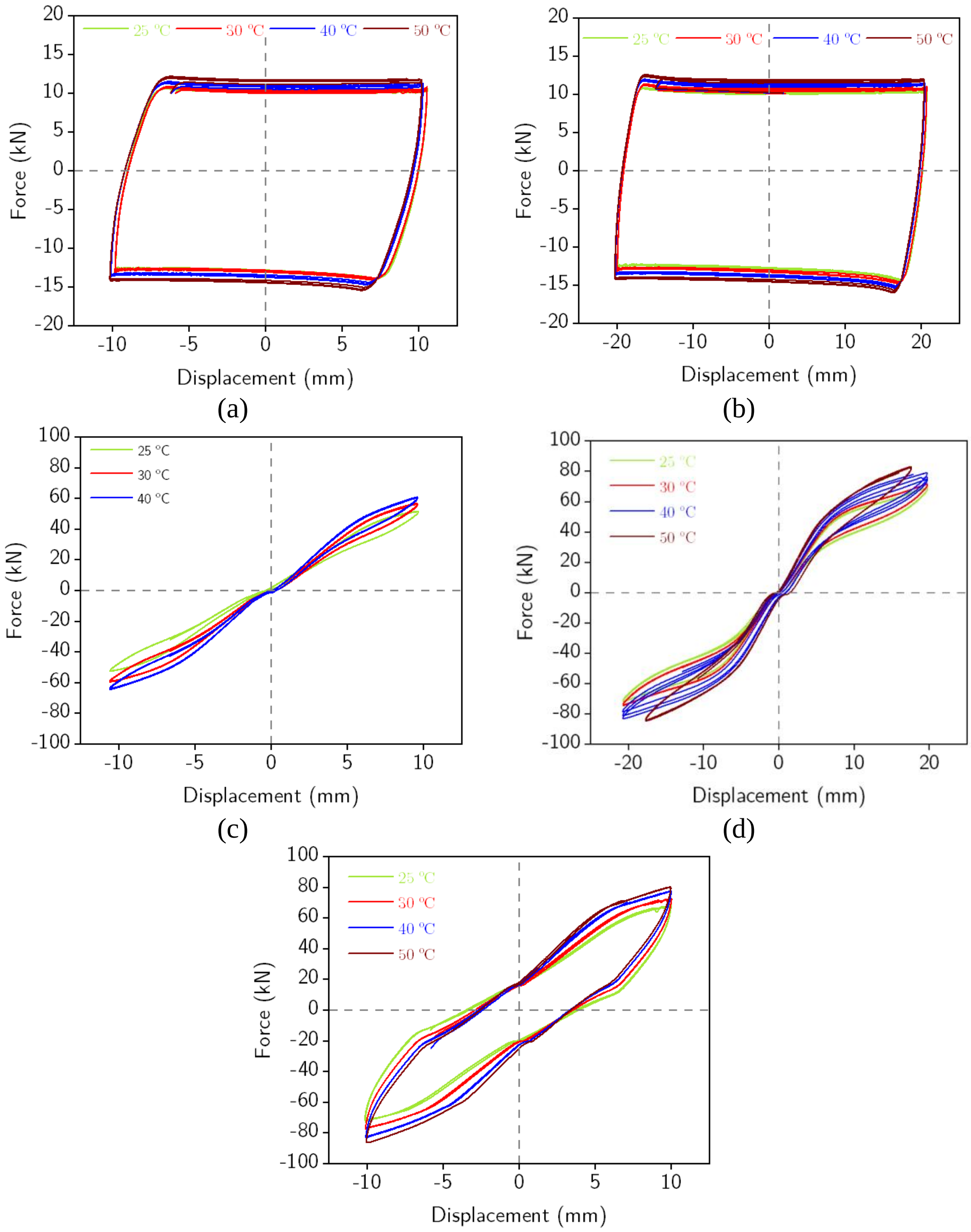

(a) (b)

(c) (d)

(e)

Figure 5-15. Effects of temperature on the hysteresis loops for friction only (a) at 10 mm and (b) 20 mm loading amplitude; SMA cables only (c) at 10 mm and (d) 20 mm loading amplitude; and (e) SFD at 10 mm loading amplitude

The variation of dissipated energy, EVD, secant stiffness, and RSE with temperature is shown in Figure 5-16. As the damper reached at higher force levels at higher temperatures, both the dissipated energy and secant stiffness increased slightly with increasing temperature. As a result, the EVD has remained almost constant at increasing temperatures. On the other hand, the RSE is increased from 63% to 70% when the temperature is increased from 25°C to 50°C. This is due to the fact that the frictional force remains almost constant while the forces in the SMA cables increases with the temperature as shown in Figure 5-15.

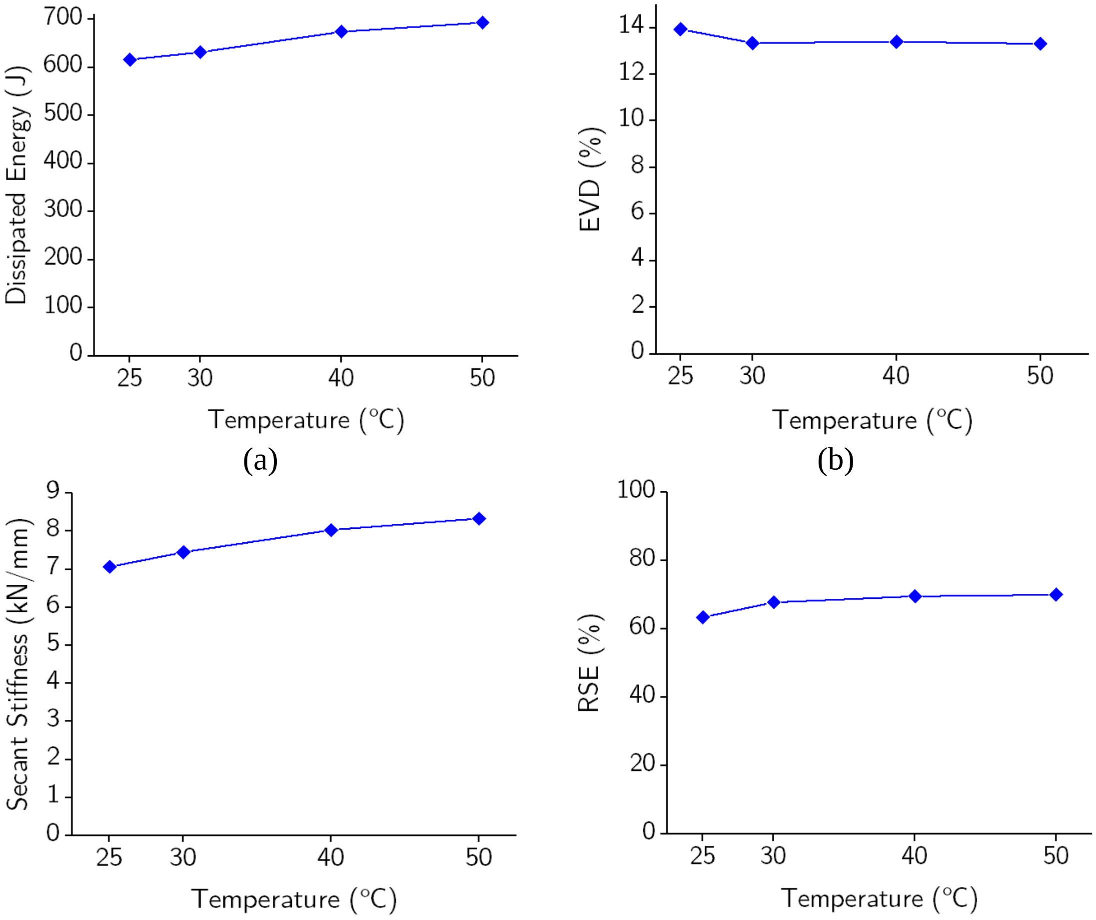

(a) (b) (c) (d)

Figure 5-16. Variation of cyclic properties of the SFD with temperature for (a) dissipated energy, (b) EVD, (c) secant stiffness, and (d) RSE

Finally, the response of the SFD under a displacement history obtained from earthquake loading at different temperatures is shown in Figure 5-17. The damper exhibited its characteristic behavior without any problem under this random dynamic loading. The response of the damper was consistent for the tests conducted at different temperatures, while the damper reached at a higher force level at higher temperatures.

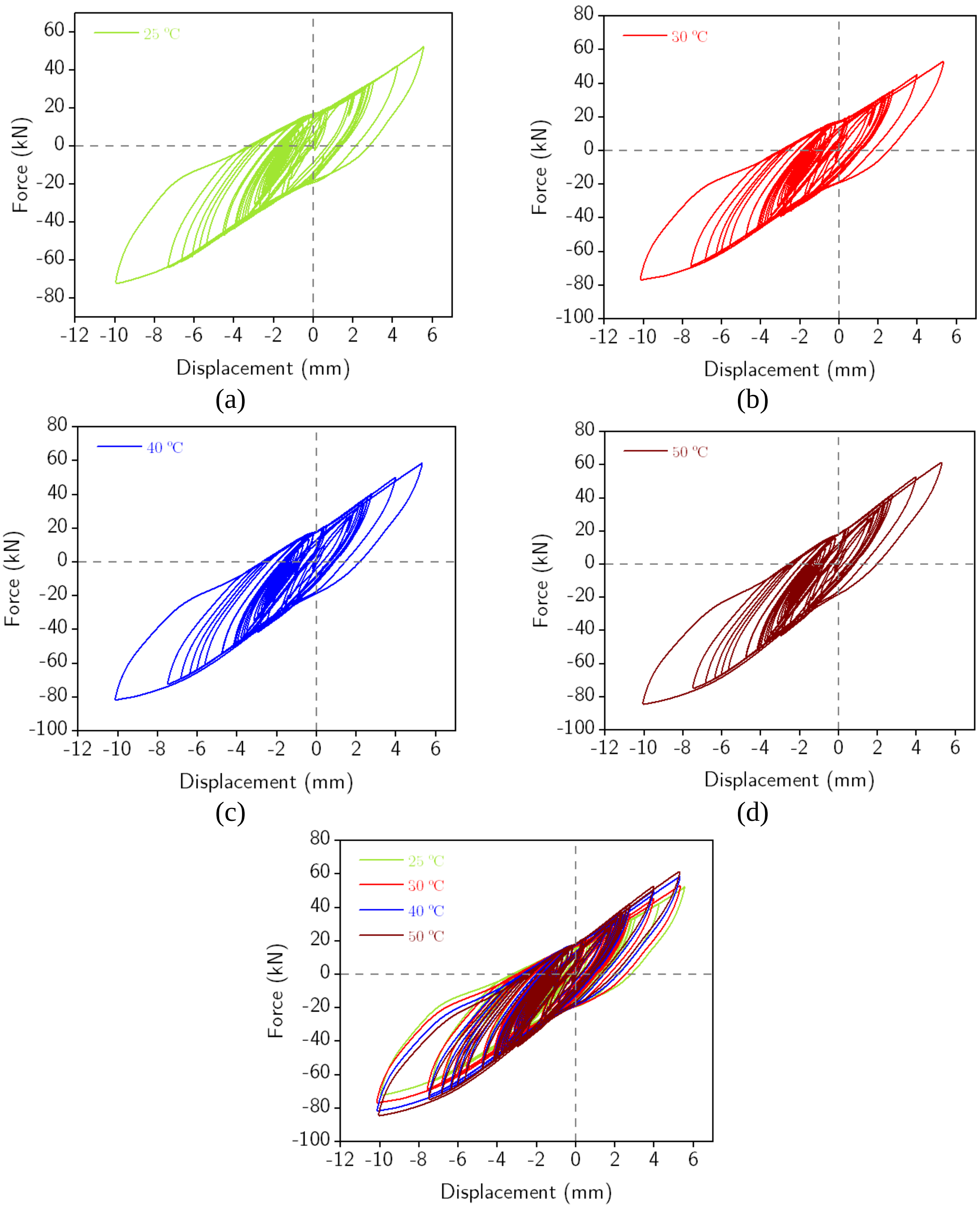

(a)

(b)

(c)

(d)

(e)

Figure 5-17. Force-displacement hysteresis responses of the SFD under pre-defined displacement loading protocol at different ambient temperatures

5.5 Parametric Study

5.5.1 Modeling of damper and validation

To enable further understanding of the cyclic behavior of the proposed damper, a simple yet effective numerical model was developed in the nonlinear finite element program OpenSees software [256]. The damper is represented by a parallel combination of five springs, as illustrated in Figure 5-18(a). The model implements three *SelfCentering* and an *ElasticMultiLinear* material behaviors to capture the flag-shape hysteretic curve of the SMA cable. Although the stress-strain relationship of SMAs can be simulated by a single *SelfCentering* material, which is a multi-linear constitutive model, it is evident that experimental stress-strain curves exhibit round corners. Thus, certain discrepancies between the experimental curves and a multi-linear model are unavoidable at those corners. Therefore, to minimize the discrepancies and enable a smooth transition, combination of three *SelfCentering*, and one *elasticmultilinear* material behaviors was adopted in this study. The hysteretic response of the friction subcomponent of the SFD was simulated using the *Steel01* material with very high initial elastic stiffness and zero hardening properties. The parameters selected for each material model are summarized in Table 5-2. The model was calibrated to reflect the actual test results through proper tuning of the parameters. Figure 5-18(b) compares the experimental results of the quasi-static loading test at room temperature with model prediction. It can be seen that the numerical model can successfully reproduce the experimental response of the SFD. Note that the effect of temperature change is not considered in this model but the model parameters can be adjusted for simulating the response of the damper at different temperatures as needed.

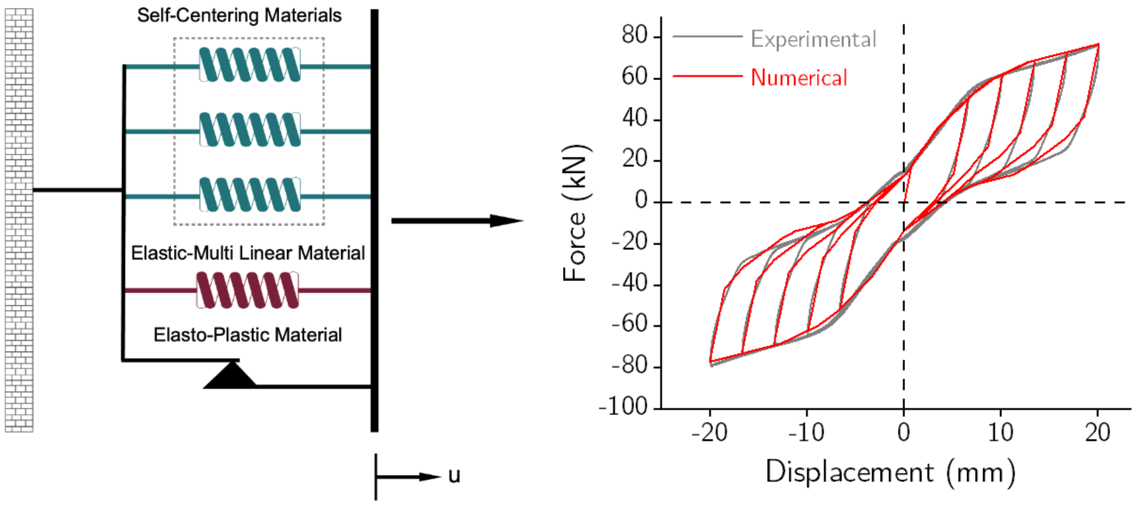

(a) (b)

Figure 5-18. (a) Schematic representation for SFD model; and (b) comparison between experimental result and proposed model prediction.

Table 5-2. Parameters for proposed SFD model.

Parameters			
Self-Centering Material	Spring 1	Spring 2	Spring 3
Initial stiffness (*k1*) (kN/mm)	2.63	1.75	1.23
Post-transformation stiffness (*k2*) (kN/mm	0.53	0.53	0.18
Forward transformation force (kN)	8.90	0.61	0.61
Ratio of forward to reverse activation force (β)	1	1	0.6
Elastic-Multi Linear Material			
Displacement (mm) and force (kN) at different points of the envelope	[-45.72 -7.12], [-7.11 -8.01], [0 0], [7.11 8.01], [45.72 7.12]		
Elastic Perfectly Plastic Material			
Yield strength (*Fy*) (kN	13.34		
Initial elastic tangent (*Eo*) (kN)	1000		
Strain hardening ratio (α)	0		

5.5.2 Selected design parameters and analysis results

A parametric study was conducted to examine the influences of some key design parameters on the hysteretic response of the developed SFD by employing the validated numerical model. In particular, the design parameters varied in the parametric study include the cross-sectional area (A), length (L), and prestrain (ε_{pre}) of SMA cables as well as frictional force (F_f). The prototype damper that was physically tested in the laboratory served as a baseline, and the identified parameters were systematically varied. The values for the design parameters in the experimental tests were A = 120.56 mm^2, L = 500 mm,

$\varepsilon_{pre} = 0\ \%$ and F_f = 13 kN. In the parametric study, the length and area of the SMA cables are increased 50% and 100% compared to their experimental values. The frictional force was varied to be zero,1 × F_f or 2 × F_f. The prestrain was selected as 0%, 0.5% and 1%. The considered parameters are summarized in Table 5-3. In all cases, one parameter varied while the others remained constant.

Table 5-3. Range of parameters selected in the parametric study.

Parameter	**Range of values**
Friction force, F_f (kN)	0, **13***, 26
Area of SMA cables A, mm^2	**120.56**, 180.84, 241.12
Length of SMA cables, L (mm)	**500**, 750, 1000
Prestrain of SMA cables, ε_{pre} (%)	**0**, 0.5, 1

***Bold** values refer to the baseline (reference case).

Figure 5-19 compares the hysteretic response of the SFD with different design parameters. As can be seen from the figure, with an increase in friction force, the hysteresis loops become considerably wider, and energy dissipation and maximum damper force increases. However, this comes with a penalty of increased residual displacements. When the cross-sectional area of the SMA cables is increased, the force capacity of the damper together with its initial stiffness increases considerably as shown in Figure 5-19(b). On the other hand, an increase in the SMA cable length leads to a decrease in the initial stiffness. However, the deformability of the damper increases significantly as shown in Figure 5-19(c). Finally, applying modest amounts of prestrain into SMA cables can limit or completely eliminate the residual deformations as shown in Figure 5-19(d). The initial stiffness of the damper also increases with the applied prestrain.

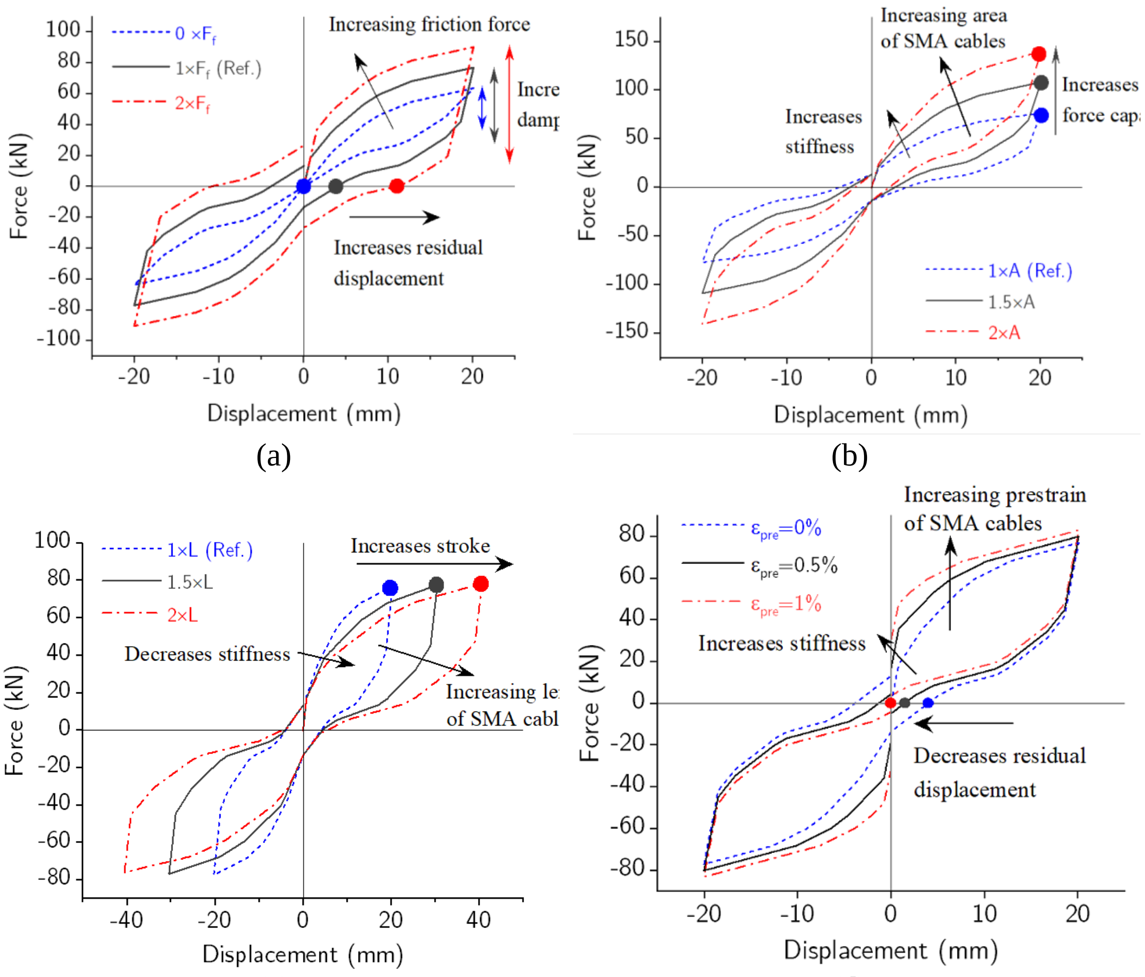

(a) (b)

(c) (d)

Figure 5-19. Parametric study results: influence of (a) friction force, (b) area of SMA cables, (c) length of SMA cables, and (d) pretensioning of SMA cables

For the SFDs with different design parameters, the amount of energy dissipated per unit deformation by individual subcomponents and the entire damper is computed and the results are shown in Figure 5-20. The energy dissipation efficiency of an SFD increases with increasing friction force (due to higher frictional energy dissipation) and the area of SMA cables (due to higher energy dissipation in SMA cables). On the other hand, the length of SMA cables and prestrain on SMA cables have minimal effect on energy dissipated per unit deformation. Nevertheless, applying a prestrain of 1% on SMA cables leads to 11% increase in energy dissipation. Also, despite the frictional component provides higher energy dissipation than SMA cables for most design cases, the contribution of SMA cables to the total energy dissipation is considerable. For example, for the reference design case, the SMA cables provides 37% of total energy dissipation.

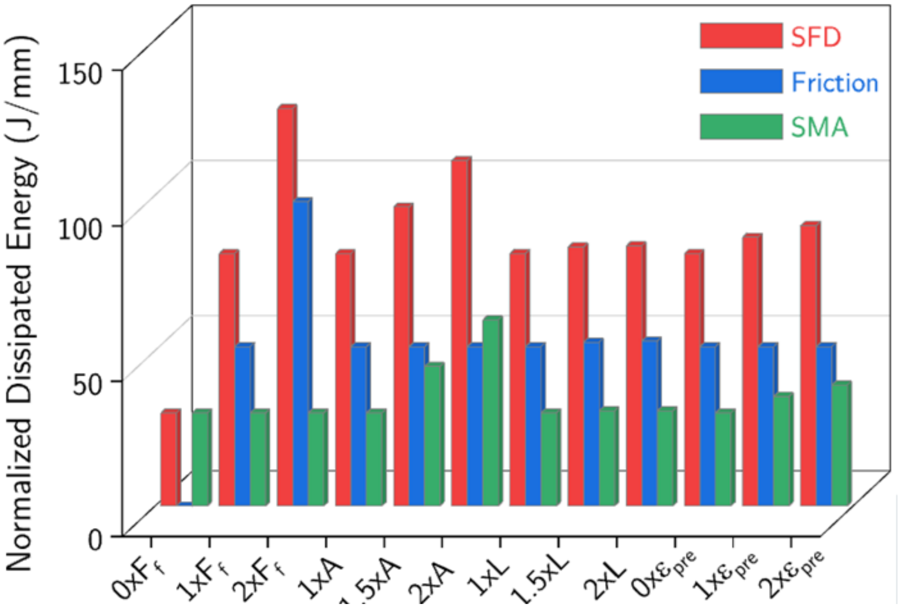

Figure 5-20. Variation in energy dissipated by the SFD, friction, and SMA as the friction force, area, length, and prestrain of SMA cables varies.

Figure 5-21 illustrates the variation of the EVD, secant stiffness, and RSE of the SFD with different design parameters. Although the dissipated energy per unit displacement increases with both frictional forces and area of SMA cables, increasing the frictional forces leads to higher EVD values while an increase in the area of the SMA cables somewhat decreases the EVD. This can be attributed to the fact that the secant stiffness, i.e., elastic strain energy, increases at a higher rate for increasing values of SMA cable area. Note that a change in SMA cable length does not have any effect on the EVD, while the presence of prestrain on SMA cables slightly improves the EVD. In addition, the parameters that significantly affect the RSE are the frictional force and prestrain of SMA cables. Note that increasing frictional force rapidly deteriorates the RSE, while increasing prestrain improves the self-centering capability of the damper.

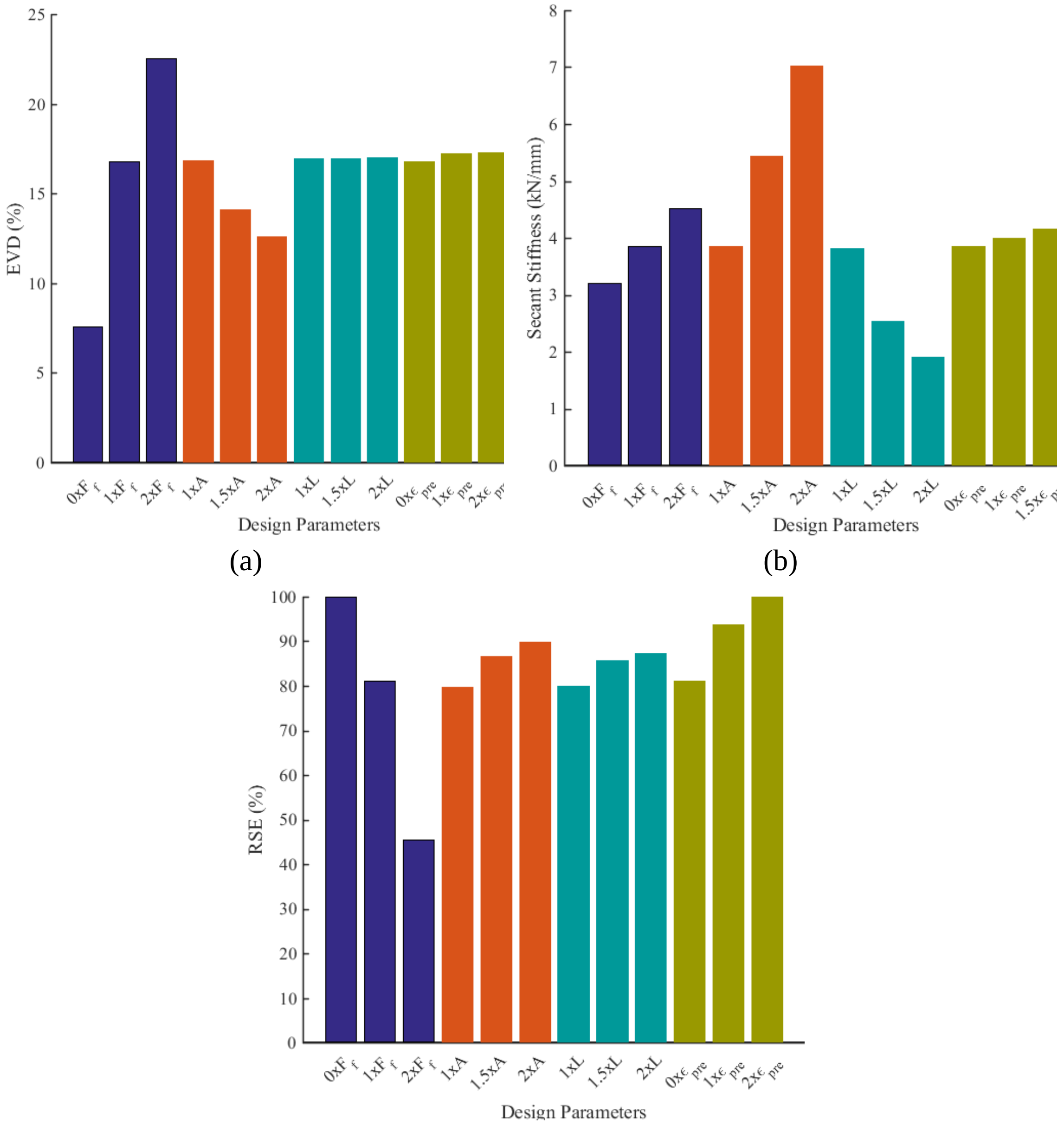

(c)

Figure 5-21. Influence of friction, area, length, and prestrain of SMA cables on hysteretic parameters: (a) EVD, (b) secant stiffness, and (c) RSE

In the second part of the parametric study, the influence of force distribution between the SMA cables and friction force was investigated since it determines the energy dissipation capacity and self-centering capability of the SFD. To quantify the proportion of SMA cables and friction, it is convenient to define a relationship between the friction force F_f and the damper “yield” resistance F_y as given by equation 12.

$$F_f = \gamma F_y \tag{5.20}$$

where γ denotes the ratio between F_f and F_y, which can be termed as friction ratio. As given in equation 2(a), the "yield" resistance of the SFD is the summation of F_{Ms} and F_f when there is no prestrain on the SMA cables. Thus, the contribution of the SMA cables to the damper "yield" resistance is $(1-\gamma)F_y$. That means if γ equals 0, the damper utilizes entirely SMA cables to resist the force demand and it exhibits a complete self-centering behavior with no additional energy dissipation from friction. If γ equals 1, the SFD will be a pure friction damper with elastic perfectly plastic behavior and no re-centering capability. In the parametric study, γ is varied from 0 to 0.5 while the other parameters are kept constant, i.e., L=500 mm and $\varepsilon_{pre} = 0$ %. Note that for the prototype damper, the γ value was 0.23.

As can be seen in Figure 5-22, the hysteretic loop is significantly widened as γ increases, and the energy dissipation increases about 150% when γ changes from 0 to 0.5. However, the increase in energy dissipation is realized at the cost of reduced self-centering capability. It can be clearly seen that a larger γ results in a larger residual displacement. Therefore, it recommended to select a γ within the range of $0.20 < \gamma < 0.33$ to have good balance between energy dissipation and self-centering capacities.

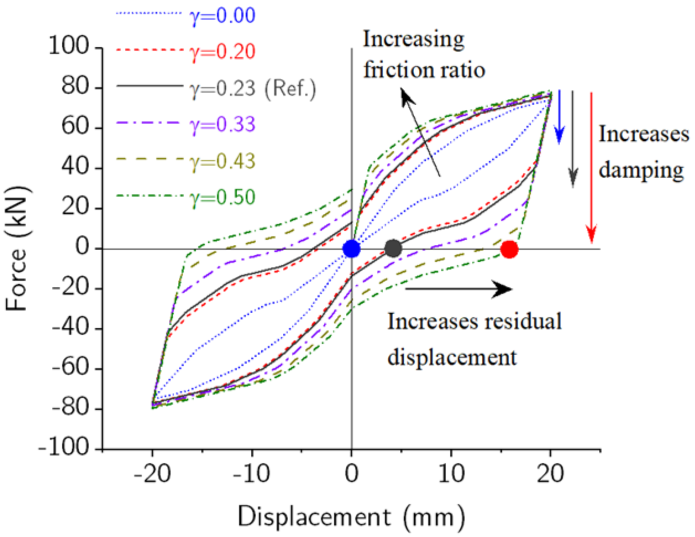

Figure 5-22. Effects of proportion of SMA cables and friction force on the response of the SFD

5.5.3 Optimal proportion of the SMA cables and friction force

As increasing energy dissipation and self-centering capability are contradictory objectives, the performance of the SFD depends on the participation ratio of the SMA cables and friction device. Indeed, as the participation of the friction force increases, the energy dissipation increases with an expense of increased residual displacement. A trade-off between energy dissipation and self-centering capability should be made when designing the SFD and achieve a resilient structure, one that has the performance with the possible highest energy dissipation, lowest cost, and small residual drift. For the current prototype damper, an optimal design of the damper may be obtained through parametric analysis. To quantitatively assess the friction contribution, an energy dissipation ratio (EDR) parameter is introduced. It is the ratio of energy dissipated by the friction mechanism to the total energy dissipation of the SFD.

Figure 5-23 plots the solution space to determine optimal design between self-centering and energy dissipation for various combinations of SMA and friction. The plot exhibits that as soon as the friction force contribution exceeds 33.3%, the RES degrades rapidly while the EDR continues to be steady without a fast upward tendency. The paths of these two ratios interest at approximately γ =0.46. This implies that a damper designed with 31.5% contribution from friction force and the remaining 68.5% by SMA cables makes the best use of physical correlation characteristics between recentering and energy dissipation. Compared to pure SMA cables case, the total damping significantly increased to over 68% when a 31.5% friction was added to the damper. The self-centering capability was lost by less than 36%. Therefore, based on these observations, an optimal design of the SFD can be achieved if the friction contribution is kept within in $\pm 20\%$ from the ideal point (shaded region in Figure 5-23).

In practice, the design of a lateral load resisting system equipped with the proposed damper should begin with determining the required load resistance and deformation demand of the damper. Based on desired performance target, an initial energy dissipation factor (γ) can be set, and then the area of SMA cables and the magnitude of friction can be calculated. Appropriate friction should be determined to provide the necessary friction force. Different combinations of the friction material, bolt torque, number, and diameter of bolts can be adopted as long as the reliability of the friction device is ascertained by either field test or other quality control procedures. Subsequently, the length of the cables can be determined based on allowable residual drifts for different structural damage levels.

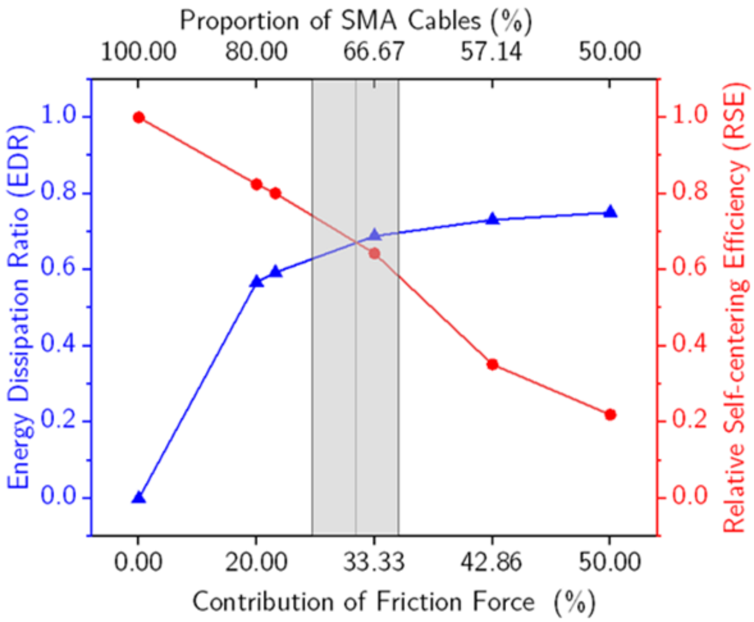

Figure 5-23. Solution space for the determination of optimal design between self-centering capability and energy dissipation

For instance, according to FEMA P-58 suggestions, the residual drift has to be limited to 0.5% to ensure economical repair of a structure [257]. If the drift is limited to 0.2%, the repair will be further narrowed to non-structural members. With less SMA material consumption in the SFD than the solely SMA-based lateral load resisting system, the flag-shaped hysteresis curve of a system equipped with the SFD could substantially become fatter by maintaining a small target residual displacement. Therefore, reaching the residual drift thresholds corresponding to repairability could be easily achieved. Once the arrangement of the SMA cables and friction pads are determined, the seismic performance of the designed structure should be checked. If the response fails to satisfy the performance target, the shape of the damper hysteresis curve could be readily tuned by changing the proportions of the SMA cables and the preload of the high-strength bolts in the friction device. Finally, all other capacity-protected components such as the internal and external members, connection plates, and end plates should be designed to remain elastic and have negligible bending deformation.

5.6 Summary

This chapter developed a novel shape memory alloy-based hybrid damper consisting of SMA cables and a friction device. The proposed damper offers an improved energy dissipation capacity compared to SMA-only dampers while maintaining good self-centering capability. Additionally, the proposed hybrid damper possesses advantages such as scalability for real-world application, reusability, ease of fabrication, and adaptability of its hysteretic response. The working mechanics and fabrication process of a prototype damper were first introduced, followed by a detailed experimental investigation on a large-scale prototype damper. Moreover, a simple yet effective numerical model was established to replicate the hysteretic response of the experimental specimen and further evaluate its performance through a parametric study. The major findings can be summarized as follows:

- The friction interface of the brake lining pad against stainless steel exhibited an elastic-perfectly plastic slip behavior without hardening, and the hysteresis loop for frictional component were close to rectangle. The slippage motion was smooth, chatter-free, and without any stick-slip behavior. Moreover, the variation in slip load was within permissible tolerance, indicating that the Belleville washers played an essential role in preventing partial loss of bolt preloading and, therefore, the degradation of the slip force during cyclic loading.
- Throughout the entire experimental program, the proposed damper exhibited a completely stable, repeatable, predictable, and reliable flag-shaped behavior without strength and stiffness degradation and negligible dependence on the loading frequency. No damage was observed to any of the damper components, highlighting that a damper installed in a structure and subjected to an earthquake loading would perform well during subsequent earthquakes without the need for the replacement or substantial repair.

- The damper provided a minimum of 14% equivalent viscous and 82% recovery of the peak displacement damping throughout the experimental program. It was found that temperature change from 25ºC to 50ºC has a negligible effect on the damping and self-centering capacity of the damper.
- Since the material models for both SMAs and frictional dampers are already available, a mechanical model to accurately simulate the response of the hybrid damper can easily be developed. The parametric studies conducted using a reliable and validated numerical model of the proposed damper indicates that varying different design parameters such as frictional force, area of SMA cables, or length of SMA cables, the hysteretic response of the hybrid damper including initial stiffness, damping capacity, and self-centering ability can be tuned into a desired target behavior.
- It is possible to eliminate or decrease residual deformations of the damper by applying slight prestrain on SMA cables. Note that this prestrain can be applied by directly tightening the nuts of the SMA cable anchorage system without the need of any external device.
- To maintain a good energy dissipation capacity with robust self-centering capabilities, it is recommended to keep the ratio of slip resistance provided by frictional damper to “yield” resistance provided by SMA-friction hybrid damper to within a range of 0.20 to 0.33.

6 SEISMIC PERFORMANCE ASSESSMENT OF STEEL SPECIAL MOMENT FRAME WITH SFDS

6.1 Overview

In Chapter 5, the test results revealed that the proposed superelastic friction damper (SFD) has excellent self-centering capability accompanied by enhanced energy dissipation capacity. Following the experimental study, the efficacy of the SFD in seismic hazard mitigation of steel frame buildings is further examined through nonlinear response history analysis. First, numerical model of a four-story moment resisting frame building is developed using the OpenSees finite element framework. Next, a nonlinear response history procedure is utilized to design the steel frame equipped with SFDs in accordance with ANSI/AISC 360-16 and ASCE 7-16 design codes. The seismic performance of the frame installed with SFDs is compared with the bare frame concerning response parameters of interest, which include, peak interstory drift, residual interstory drift, and peak absolute floor acceleration. Finally, the analysis is extended to investigate influences of varying the SFD design parameters on the control efficiency of the damper.

6.2 Numerical Modeling

6.2.1 Description and modeling of prototype building

A four-story archetype steel-framed office building used in NIST technical note 2084 [258] for the application of FEMA P-695 methodology is adopted in this study. It is presumed that the building will be constructed in a high seismic area (e.g., somewhere along the west coast of the United States). Building stability and resistance to environmental loads and deformations is provided by special steel moment resisting frame (SMRF) along the East-West (E-W) direction and special steel concentrically braced frame (SCBF) along the North-South (N-S) direction. All lateral force-resisting systems are symmetrically located at the perimeter of the building and orthogonal. The building is rectangular in plan, with five 9.14 m (30 ft) bays in the E-W direction and five 6.14 m (20 ft) bays in the N-S direction. The typical floor framing plan and elevation view are shown in Figure 6-1. The height of the first story is 5.5 m (18 ft) and the remaining story heights are 4.27 m (14 ft). Structural members are designed using ASTM A992 steel ($F_y = 345 MPa$). The dead load is 4.31 kN/m^2 uniformly distributed over each floor. Superimposed dead loads are taken as 0.72 kN/m^2 for floors and 0.48 kN/m^2 for the roof, representing mechanical, electrical, plumbing, and miscellaneous loads. A cladding load was applied as a perimeter load of 3.65 kN/m. Unreduced live load of 2.39 kN/m^2 is applied on all floors and 1.44 kN/m^2 on the roof. Wind loads were not considered in the design of the archetype building members. Additional material and design details can be found in Harris and Speicher [259].

In this dissertation, all the analyses are based on one of the perimeters SMRF that serve as the lateral force resisting system of the building in the E-W direction. The building is located where it is assumed it would be assigned a Seismic Design Category (SDC) at the upper limit of D, i.e., D_{max}. The seismic hazard in ASCE 7-16 is based on a risk-targeted design philosophy and is defined as ground motions having a one percent probability of causing total or partial structural collapse (i.e., “risk”) of properly designed structure in 50 years. This ground motion intensity is denoted in the code as MCE_R. Considering a Risk Category II building, the design spectral acceleration parameters are $S_{DS} = 1.0$ g and $S_{D1} = 0.60$ g, whereas the maximum considered spectral acceleration values are $S_{MS} = 1.5$ g and $S_{M1} = 0.90$ g.

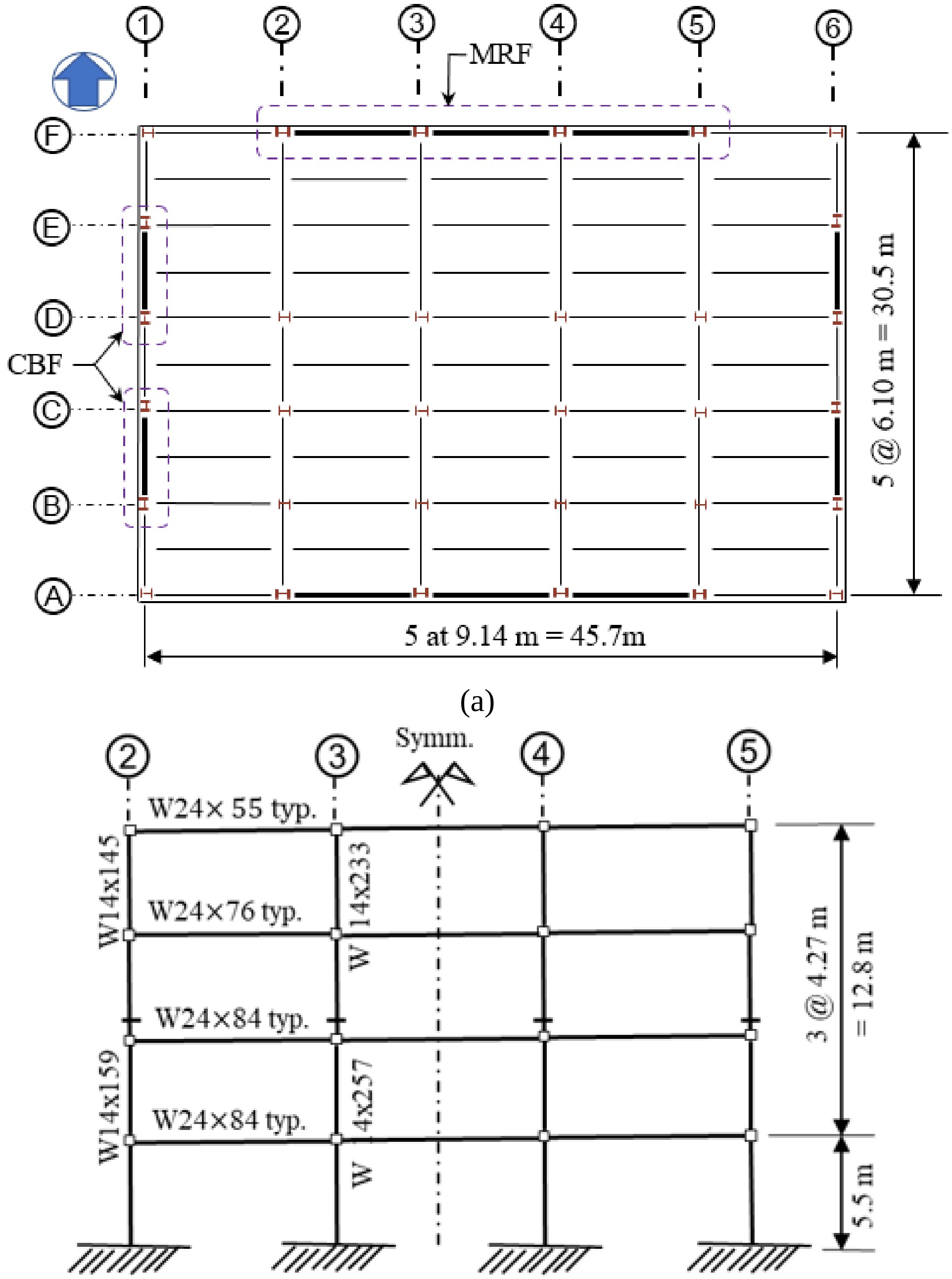

(a)

(b)

Figure 6-1. Four-story steel frame building: (a) Floor plan showing the structural framing layout, and (b) Elevation

A two-dimensional (2D) nonlinear model of the SMRF with panel zone (PZ) and reduced beam section (RBS) was created in the OpenSees structural analysis package. Models for nonlinear analysis can range from uniaxial spring or hinge models, to more fundamental type fiber-based models, to sophisticated continuum finite element models. The choice of model type for a given application requires balance between reliability, practicality, and computational efficiency. The reliability of the model comes from its ability to simulate the critical types of deformation that are of interest to the user and control the response. Concentrated spring modeling approach is implemented in this study since it is computationally efficient by modeling highly nonlinear effects in localized regions of the structure with few degrees of freedom. The plane frame elements of the structure are modeled as elastic beam-column elements with concentrated inelastic rotational springs. A bilinear hysteretic material model based on the modified Ibarra Medina Krawinkler (IMK) deterioration model [260] is used for the plastic hinges to capture cyclic and in-cycle strength and stiffness degradations. The moment-rotation backbone and hysteric curves of the IMK model are shown in Figure 6-2. The key points used as an input to define the model are the yield point, the capping point, the residual point, and ultimate point. The parameters for the different points are determined following recommendations made by Lignos and Krawinkler [261,262], which were derived using multivariate regression analysis of a database of experimental results.

Using RBS, which is an offset from the beam-column joint, ensures that the beam's plastic hinge forms away from the column and thus protects the column's integrity. The RBS connection stiffness was modeled using a prismatic cross-section over the length of the RBS. The width of the RBS was assumed to be equivalent to the actual RBS width at center. The plastic hinge is modeled by a rotational spring placed at the center of the RBS and the spring was assigned a stiffness of 10 times that of the unreduced beam. An elastic beam-column element is used to connect the spring and the PZ. For the columns, nonlinear springs were added at $d_c/2$ away from the face of the beam, where d_c is the depth of the column. These springs followed the same approach as the beams, i.e., the stiffness amplified by 10. A schematic of the OpenSees modeling approach is shown in Figure 6-3.

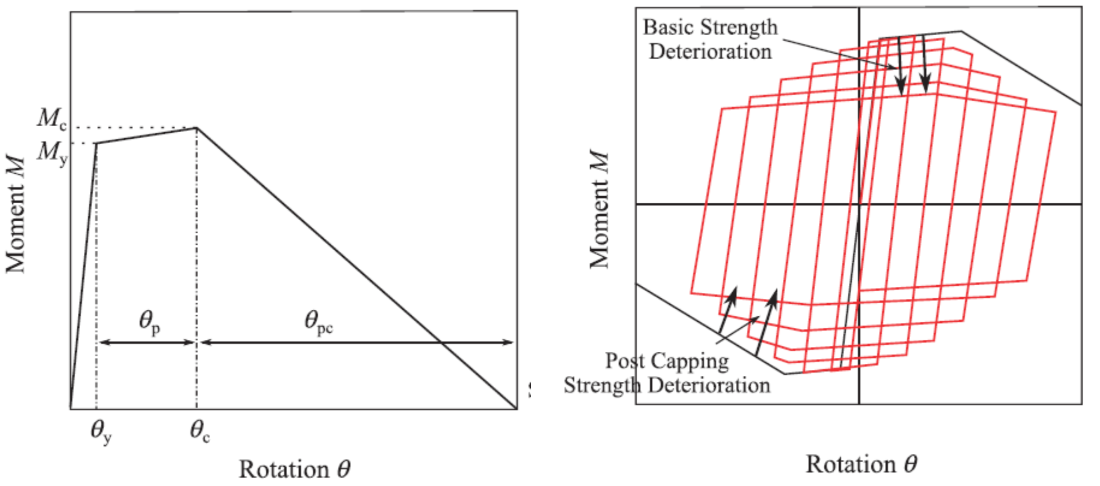

(a) (b)

Figure 6-2. Modified Ibarra-Medina-Krawinkler (IMK) deterioration model (a) monotonic, and (b) cyclic

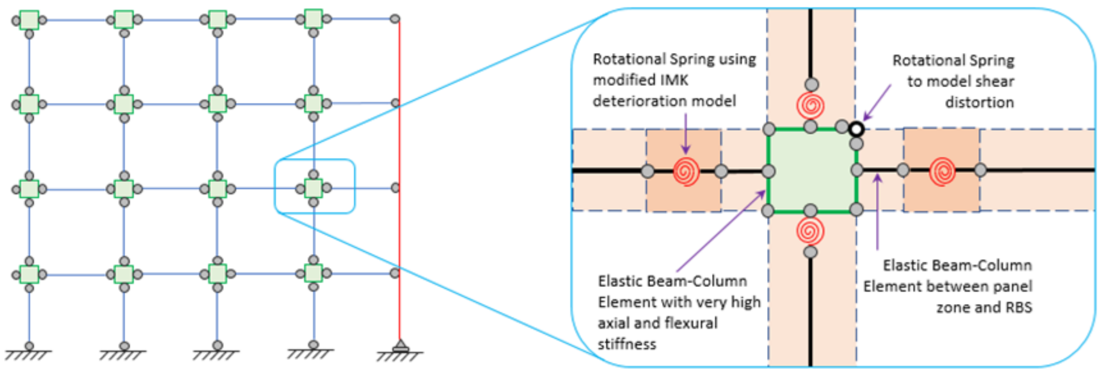

Figure 6-3. Schematics of OpenSees modelling

The panel zone, the joint region where beams and columns intersect, mainly deforms in shear due to the counteracting moments in the beams and columns. To capture these deformations, the panel zones are explicitly modeled using the methodology put forward by Gupta and Krawinkler [263]. Accordingly, the PZ is simulated as a rectangle composed of a set of “rigid” elements connected by simple pin connections at the three corners and a zero-length rotational spring placed at the other corner to simulate the shear distortions in the PZ. Each elastic beam-column elements are assigned with very big area and moment of inertia such that high axial and flexural stiffnesses can be obtained. The rotational spring has a trilinear backbone curve, which is derived using the principle of virtual work applied to the deformed configuration of the PZ.

A leaning column is employed to capture the large $P-\Delta$ and small $P-\delta$ effects arising from the forces acting on the deformed geometry. The leaning column was assigned a moment of inertia equal to the sum of the moment of inertia of the tributary gravity frame columns and the SCBF columns. It is linked with the SMRF by axially rigid truss elements at each floor level as illustrated in Figure 6-3. It is also assumed that the leaning column is elastic along the height of the building; hence, no nonlinear moment hinges were added. Rayleigh damping with a 3% damping ratio for the first and third modes of vibration is assigned to the model to account for the inherent damping of the building.

6.2.2 Design of a steel moment frame with SFDs

Given the fact that SFD is a newly emerged damper, the seismic design procedure of a structure equipped with this damper is not covered in the current design codes. Therefore, the provisions of ASCE 7-16 Chapter 18 that deals with minimum design base shear for structures with added damping devices, in general, is adopted. Thus, a reduced strength version of the fully code-compliant frame is developed first by selecting smaller beam and column member sizes such that the frame has a base shear capacity equal to 75% of the base shear capacity of the original SMRF. The steel members for the beams and columns are selected in accordance with the strength requirements of ANSI/AISC 360-16 [264] under the load combinations provided in the ASCE 7-16. The reduced strength frame satisfies the strength requirements of the design codes but violates the drift limits. The SFDs are then designed with the objective of complying with the story drift requirements and to provide similar strength and stiffness with the original SMRF. The SFDs are installed at each bay of each story level using a chevron configuration. The selected member sizes for the beams and columns as well as a typical installation scheme of the SFD are shown in Figure 6-4. In this more flexible frame, the contributions of the SMRF and SFDs to the lateral load resistance are about 75% and 25%, respectively. The SFDs are primarily responsible to control the story drifts.

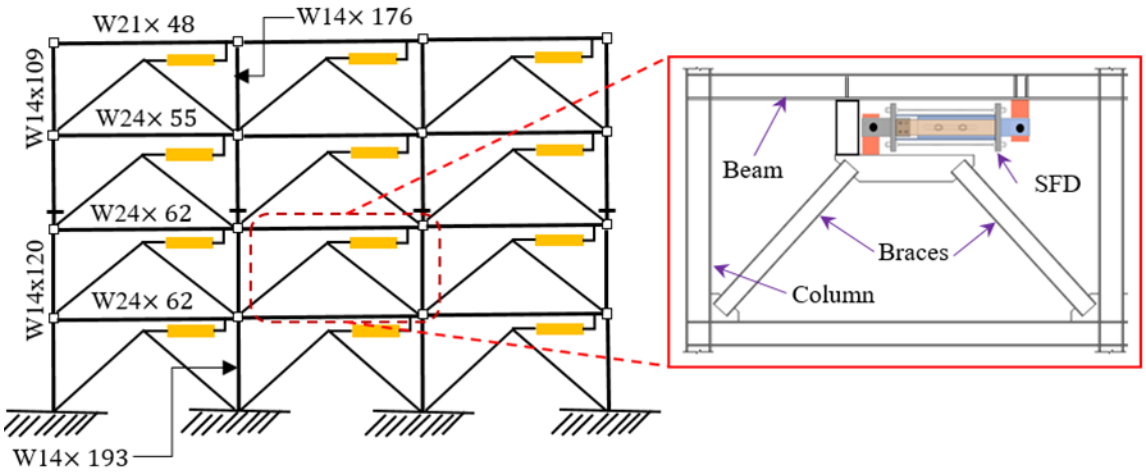

Figure 6-4. A four-story steel moment resisting frame installed with SFDs

The controlled frame, i.e., SMRF with SFDs, is modeled in OpenSees following the same procedure as modeling of the uncontrolled frame summarized in the previous subsection with the addition of elements representing the dampers. The SFDs are modeled using parallel combinations of self-centering springs and a spring assigned with steel02 material as discussed in Section 5.5. In a typical damper, the area of SMA cables is calculated to be 482 mm^2 and the friction force is 52 kN to satisfy the design objectives mentioned above. The selected SFD design parameters can be considered as four times the prototype damper fabricated in Chapter 5. The dampers in all floors are assumed the same.

To check validity of the designed frame fulfilling the code drift requirements, nonlinear response history analyses are performed. A total of 7 ground motions, as summarized in Table 6-1, are selected from the PEER NGA west 2 strong ground motions database [265] and scaled in accordance with the ASE 7-16. In particular, the ground motions are scaled such that the average response spectra for the selected records set is not less than the target response spectrum for periods ranging between 0.2 and 1.5 times the building fundamental period. Since a nonlinear response history is adopted for the design, the code allows to increase the story drift limit by 25%. Thus, for Risk Category II buildings, the allowable story drift at the DBE and MCE levels are 2.5% and 3.75%, respectively. The mean story drift ratios of the controlled frame under seven ground motions are 2.13% at the DBE level and 2.98% at the MCE level. The corresponding values for the uncontrolled frame are 2.16% and 3.70% at the DBE and MCE levels, respectively. Therefore, both frames satisfy the drift requirements at both levels. It should be noted that in this particular case, the controlled frame is designed such that the mean peak interstory drift meets the code drift requirements without aiming to achieve any higher performance objectives.

Table 6-1. Selected ground motions used for the design of frames

EQ ID	**Event Name**	**Station**	**Magnitude (Mw)**	**Distance (km)**	**PGA (g)**
1	Superstition Hills (1987)	El Centro Imp. Co.	6.5	18.2	0.36
2	Imperial Valley (1979)	Delta	6.5	12.6	0.35
3	Loma Prieta (1989)	Gilroy Array #3	6.9	12.2	0.56
4	Kocaeli, Turkey (1999)	Duzce	7.5	15.4	0.36
5	Kobe, Japan (1995)	Shin-Osaka	6.9		0.24
6	Northridge (1994)	Canyon County-WLC	6.7	12.4	0.48
7	San Fernando (1971)	LA-Hollywood Stor	6.6	22.8	0.21

6.3 Performance Assessment

6.3.1 Ground motions

A total of 14 strong motion records are used in the nonlinear response history analyses. The records are selected from the FEMA P-695 far-field record set and are normalized for magnitude, distance, and source conditions as discussed in the report. The ground motion scaling procedure follows the ASCE 7-16 guidance. Figure 6-5 illustrates the set of acceleration response spectra, original and scaled, and the scaled average spectrum. Target spectra for the MCE level developed using the site spectral acceleration values provided in ASCE 7-16 and described in previous section is also shown in the figure. It can be seen that the mean spectrum of the 14 records is not less than the target response spectrum for period ranging from $0.2 \times T_1$ to $1.5 \times T_1$, where T_1 is the fundamental period of vibration for the frame. Therefore, code requirements are satisfied.

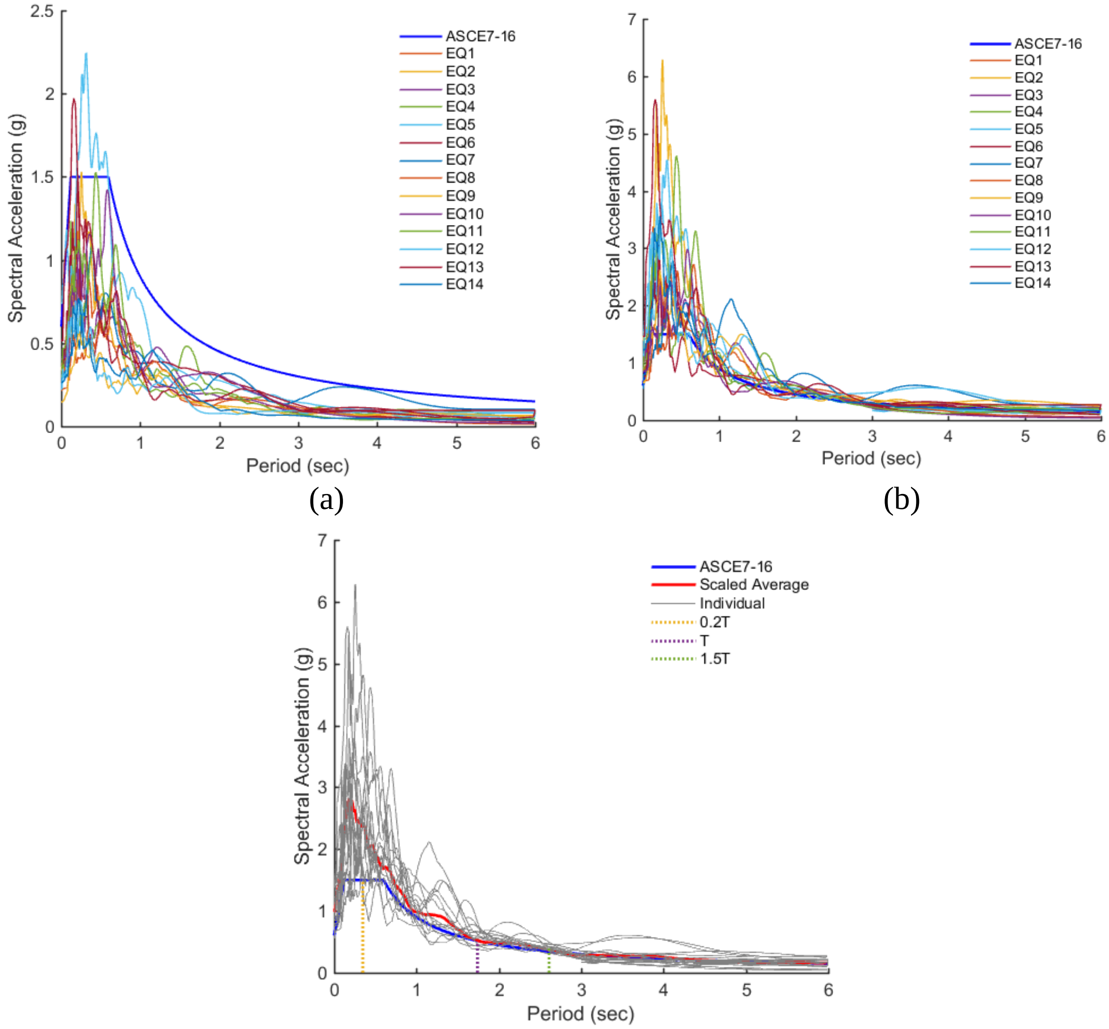

(a)

(b)

(c)

Figure 6-5. Acceleration response spectra: (a) Original, (b) Scaled, and (c) scaled average spectrum

6.3.2 Nonlinear static (pushover) analysis

To obtain an overall understanding on the global behaviors of the uncontrolled and controlled frames, a displacement-driven monotonic pushover analysis is conducted. In this way, it allows a quantitative comparison of the lateral strength and post-yield behavior of each frame under progressive loading process. Figure 6-6 shows the results of the pushover analyses when the frames are subjected to a static lateral force with first-mode pattern based on ASCE 7-16. The pushover process is monitored by a control node at the roof level and is completed when the roof drift ratio reaches to 10%, which is sufficient to capture the progressive development of structural property from initial elasticity to significant nonlinearity. As can be seen, in the elastic ranges, the frames can be regard as two identical frames, but they differ significantly in the inelastic range. After yielding at a roof drift ratio of approximately 1.2%, the controlled frame exhibits a much higher shear resistance than the uncontrolled due to a larger "post-yield" stiffness associated with the SFDs.

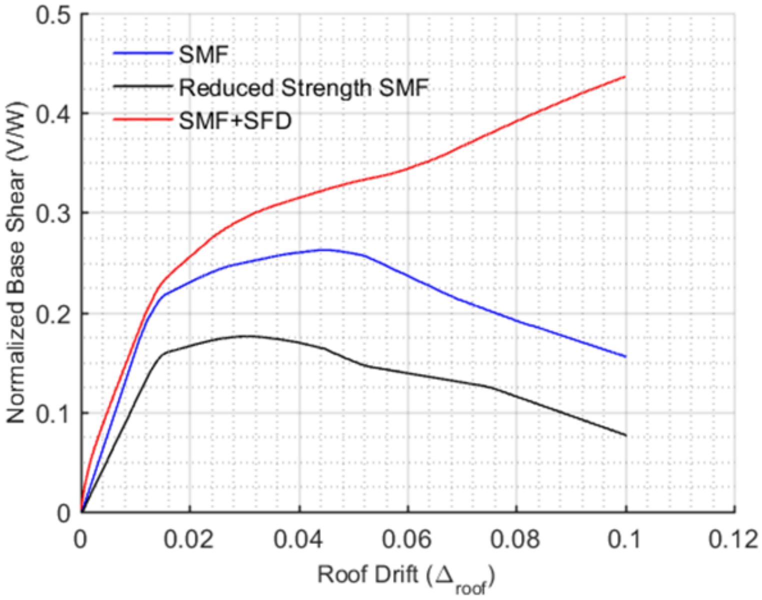

Figure 6-6. Pushover curves of SMF, reduced strength frame, and SMF with SFD

6.3.3 Structural responses and discussions

The seismic responses of the steel frame with and without SFDs are evaluated by subjecting them to realistic earthquake ground motion records. The 14 ground motions mentioned in previous subsection are used to provide a basic performance assessment under two different seismic hazard levels: DBE and MCE. The acceleration time history of each ground motion record is followed by zero values for 10 seconds, with the aim to allow structural vibration to decay and to accurately record the residual deformation. The selected engineering demand parameters for the performance evaluation includes: peak interstory drift ratio (PID), residual interstory drift ratio (RID), and peak floor acceleration (PFA). The PID is selected as an important performance index since it can be correlated with damage in structural elements, while the PFA indicates damage to acceleration sensitive non-structural components. As noted, before, the post-earthquake functionality of buildings is determined based on the RID. These parameters are deemed convenient criteria for measuring the seismic resilience of structures.

Figure 6-7 and Figure 6-8 show the PID, RID, and PFA for the uncontrolled and controlled frames for each ground motions scaled to DBE and MCE levels, respectively. It is evident that the SFDs significantly reduces the drift demand of the controlled frame under both levels. The structure experienced negligible residual drift. From a codified assessment point of view, a set of RID limits are stipulated in FEMA P-58 [8] . Generally, there are four damage state classes: DS1, which restricts the RID to less than 0.2%, such that “no structural realignment is necessary for structural stability, but the building may require adjustment and repairs to non-structural and mechanical components. Amore relaxed second class, DS2, requires RID to be less than 0.5%, such that realignment of structural frame and related structural repairs are economically feasible, and degradation in structural stability is limited. In light of these restrictions, the analysis results show that the controlled frame easily meets class DS1 in almost all earthquake records due to the excellent self-centering capability of the SFDs. On the contrary, the uncontrolled frame exceeds the 0.5% threshold in nine earthquake records. Therefore, expensive repair works are inevitable for the latter case.

The PFA response of the controlled frame increased slightly compared with the uncontrolled frame. The absolute floor acceleration response is directly associated with the difference in interstory shear forces of two adjacent floors [19]. Compared with SMRF, the flag-shaped hysteretic behavior of the SFD has more frequent transitions along the unloading path, and as a result an instantaneous high amplitude PFA pulse is more likely to be produced during an earthquake loading. Nevertheless, the amplification is less than 10% on average, and if needed, it can be effectively controlled by adjusting the SFD design parameters. This will be discussed in more detail in the next subsection.

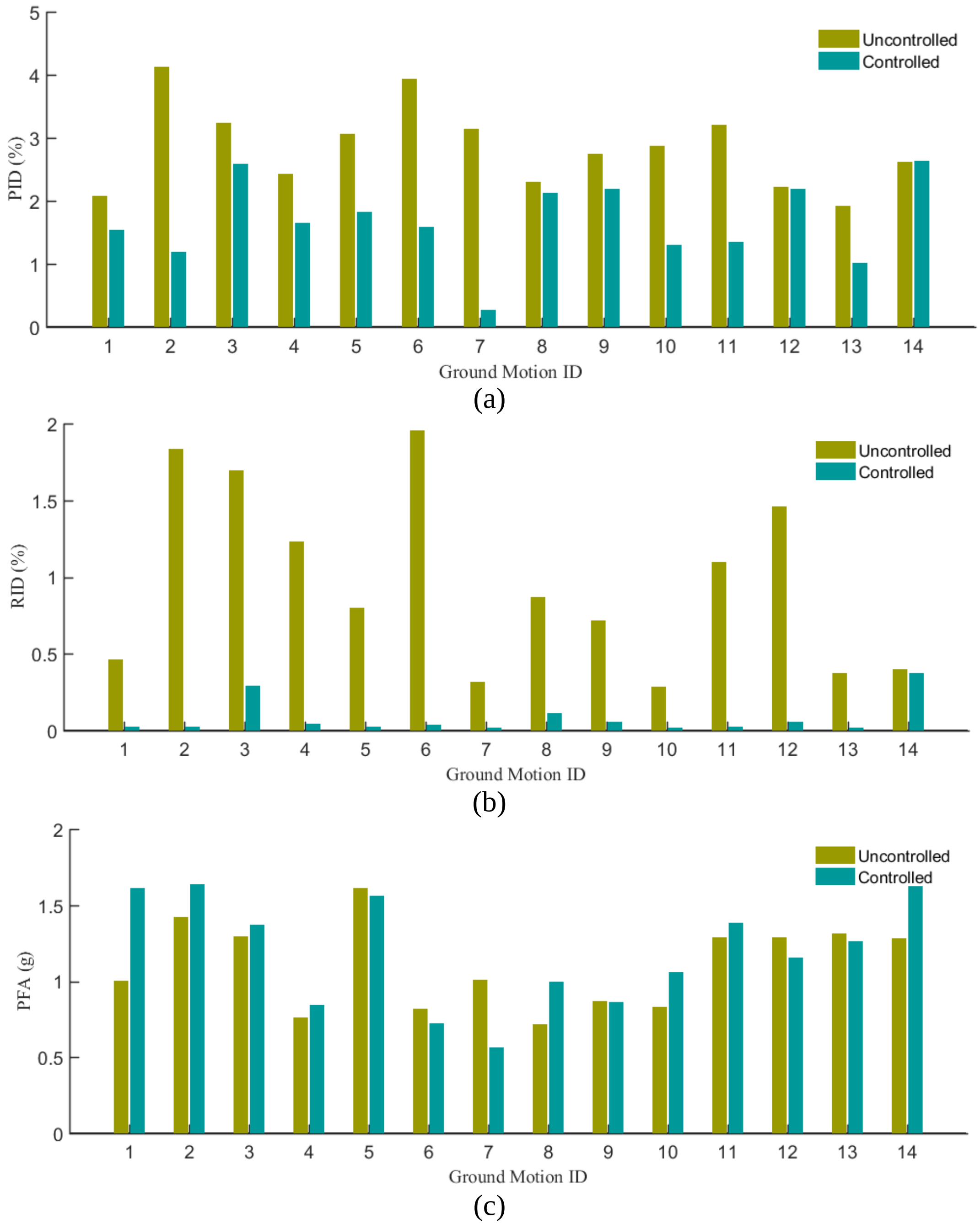

Figure 6-7. Engineering demand parameters: (a) IDR, (b) RDR, and (c) PFA) of controlled and uncontrolled frames subjected to ground motions scaled to DBE level

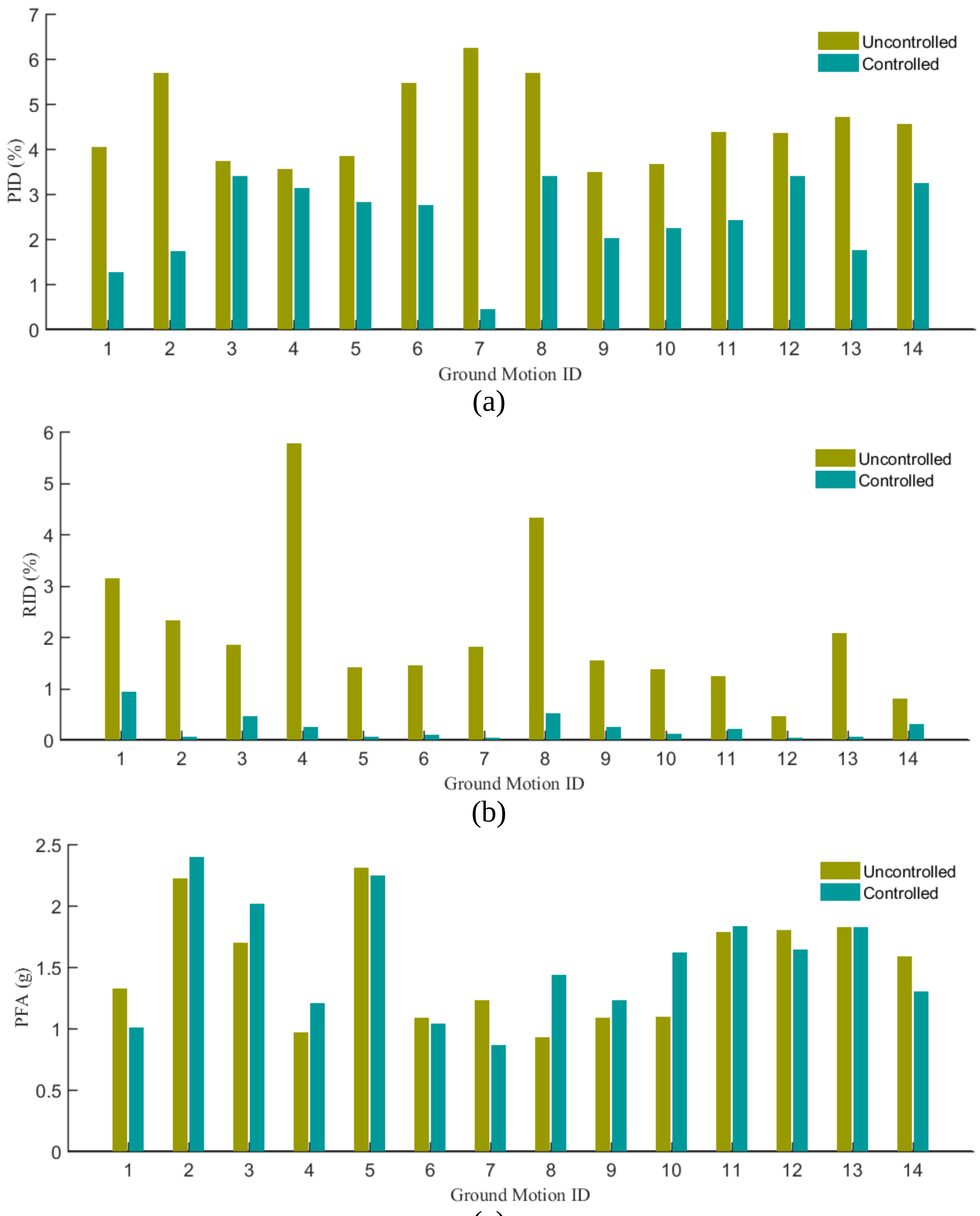

(a)

(b)

(c)

Figure 6-8. Engineering demand parameters: (a) IDR, (b) RDR, and (c) PFA) of controlled and uncontrolled frames subjected to ground motions scaled to MCE level

Figure 6-9 shows the mean height-wise profiles of the PID, RID, and PFA of the uncontrolled and controlled frames under the DBE and MCE seismic hazard levels. These plots not only give the values at each story, but also provide insight into the response deviation among different stories. It can be seen that the PID somehow uniformly distributed along the height of the controlled frame and it is effectively reduced in all stories. Specifically, the mean PID reduced from 2.2% to 1.3% at DBE and from 3.57% to 1.90% at MCE, corresponding to 41% and 47% reductions, respectively. The results clearly demonstrate the efficacy of the SFDs in effectively reducing the displacement demand of the steel frame. It is thought that the nonlinearity of the dampers has been well mobilized and increase the damping of the system, which result in the decrease in PID. Uniform distribution of drifts in structures is of paramount importance which is not generally satisfied in compliance with the state-of-the-art seismic provisions. As such, in order to avoid drift concentrations and soft-story failures, optimum distribution of stiffness and strength should be acquired, which can be realized by installing supplemental damping devices such as the SFD.

Regarding the RID responses, the mean response of the uncontrolled frame violates the DS1 and DS2 requirements at both hazard levels, whereas, the controlled frame meets DS1 requirement with sufficient safety margin at DBE and just meet the limit at MCE. Note that 0.2% and 0.5% limits are generally assessed at the DBE level. However, for the sake of demonstrating the efficiency of the SFD in effectively reducing the RID, the same limits are applied at MCE. The mean maximum residual interstory drift ratio among all the floors under DBE and MCE levels are dramatically decreased by 95% and 90%, respectively, after the dampers are installed. This suggests that the SFDs are more efficient in reducing the residual interstory drift ratio than reducing the peak. It is also observed in Figure 6-9 that the PFA slightly amplified in the upper floors.

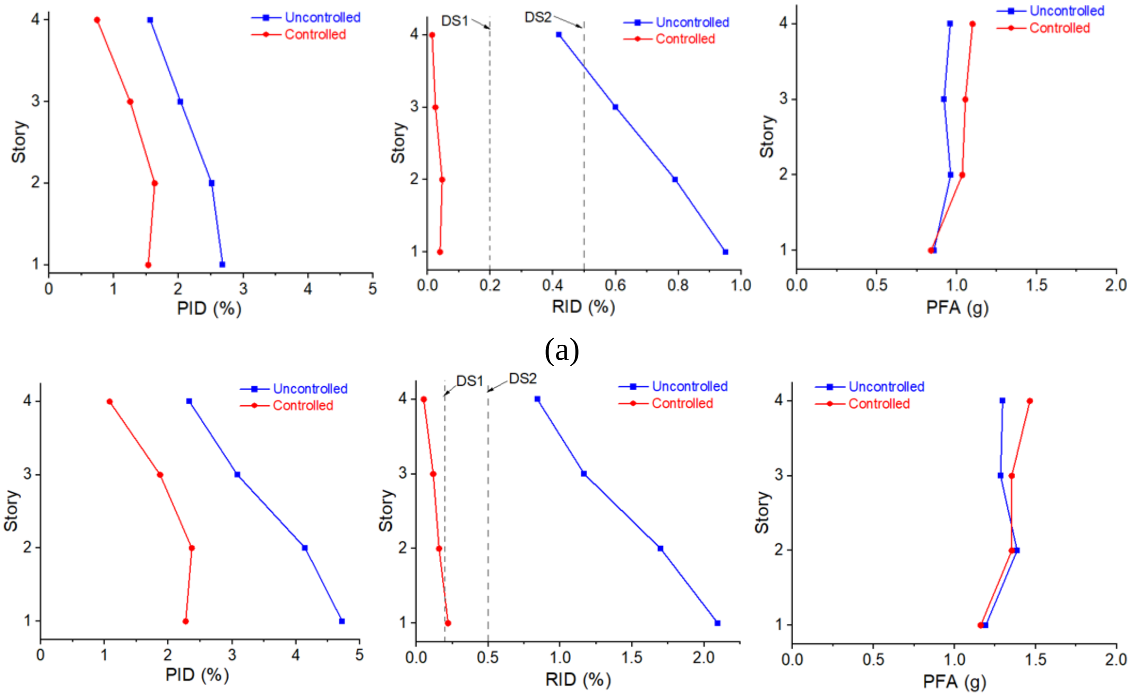

(a)

(b)

Figure 6-9. Comparisons of engineering demand parameters (IDR, RDR, and PFA) between uncontrolled and controlled frames at: (a) DBE and MCE levels

The nonlinear time history analysis results corresponding to representative ground motion records, Imperial Valley earthquake scaled to DBE level and San Fernando earthquake scaled to MCE level are shown in Figure 6-10 and Figure 6-11, respectively. The purpose of these plots is to illustrate the seismic behavior of the frames over time duration. In this case, the roof drift time history clearly shows the uncontrolled frame tends to accumulate nonlinear deformation in a single side as it is deformed into severe inelastic state. This not only causes the peak to occur at a later stage, but also leads to noticeable unrecoverable deformation of about 1%. In contrast, the controlled frame exhibits smaller peak roof drift without incurring residual deformations. The excellent self-centering capability of the SFDs prevents the constant accumulation of plastic deformation toward a single vibration direction. Similar observations can be made when the intensity of the input earthquakes is scaled up to MCE. As expected, the acceleration demand increases with increasing ground motion intensity, but the PFA values for both frames are reasonably consistent for the Imperial Valley and San Fernando earthquakes. The cyclic behavior of the first story damper is also plotted in Figure 6-10(c) and Figure 6-11(c). It is seen that the SFD nearly return to the original shape after experiencing large nonlinear deformation.

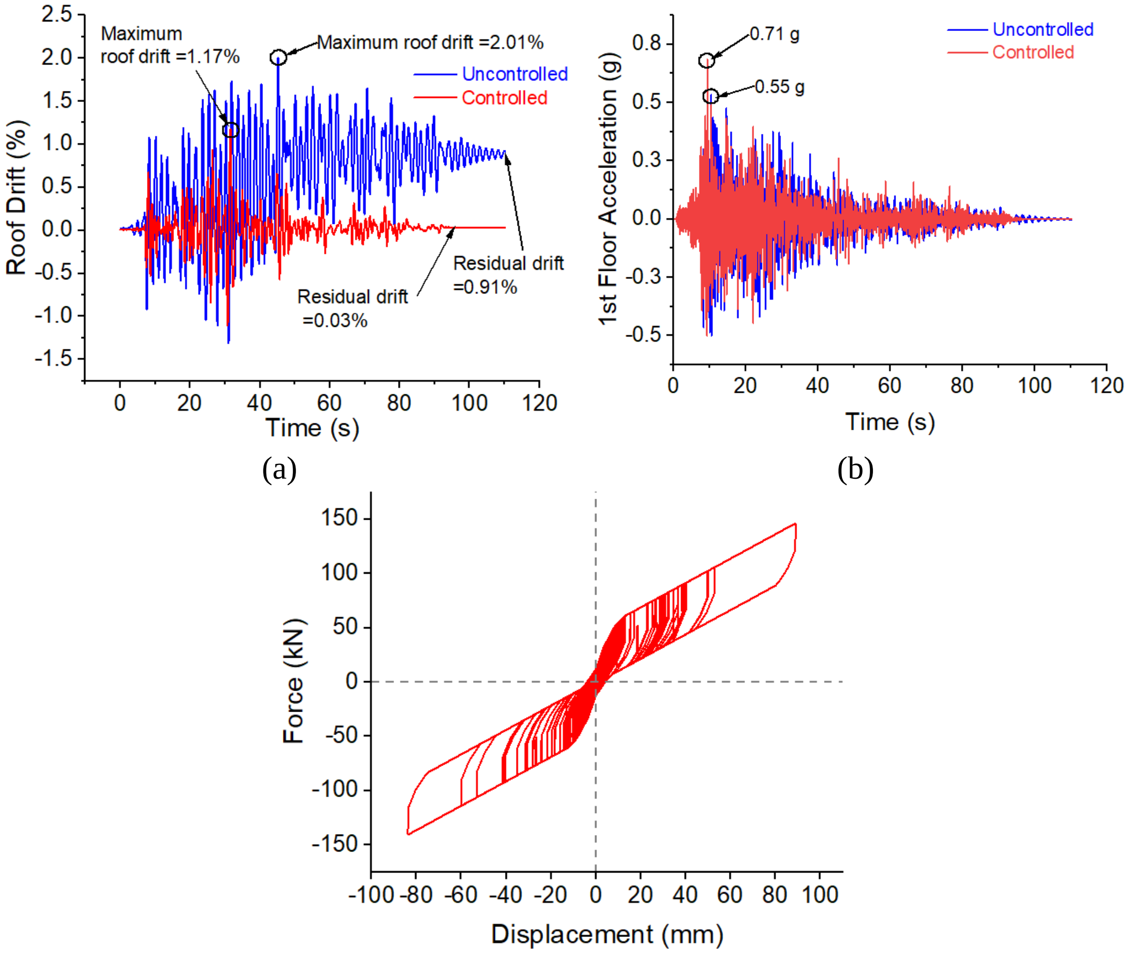

(a)

(b)

(c)

Figure 6-10. Selected response quantities for uncontrolled and controlled frames subjected to Imperial Valley earthquake scaled to the DBE level: (a) Roof drift time history, (b) First floor time history, and (c) the SFD force-displacement hysteresis loop

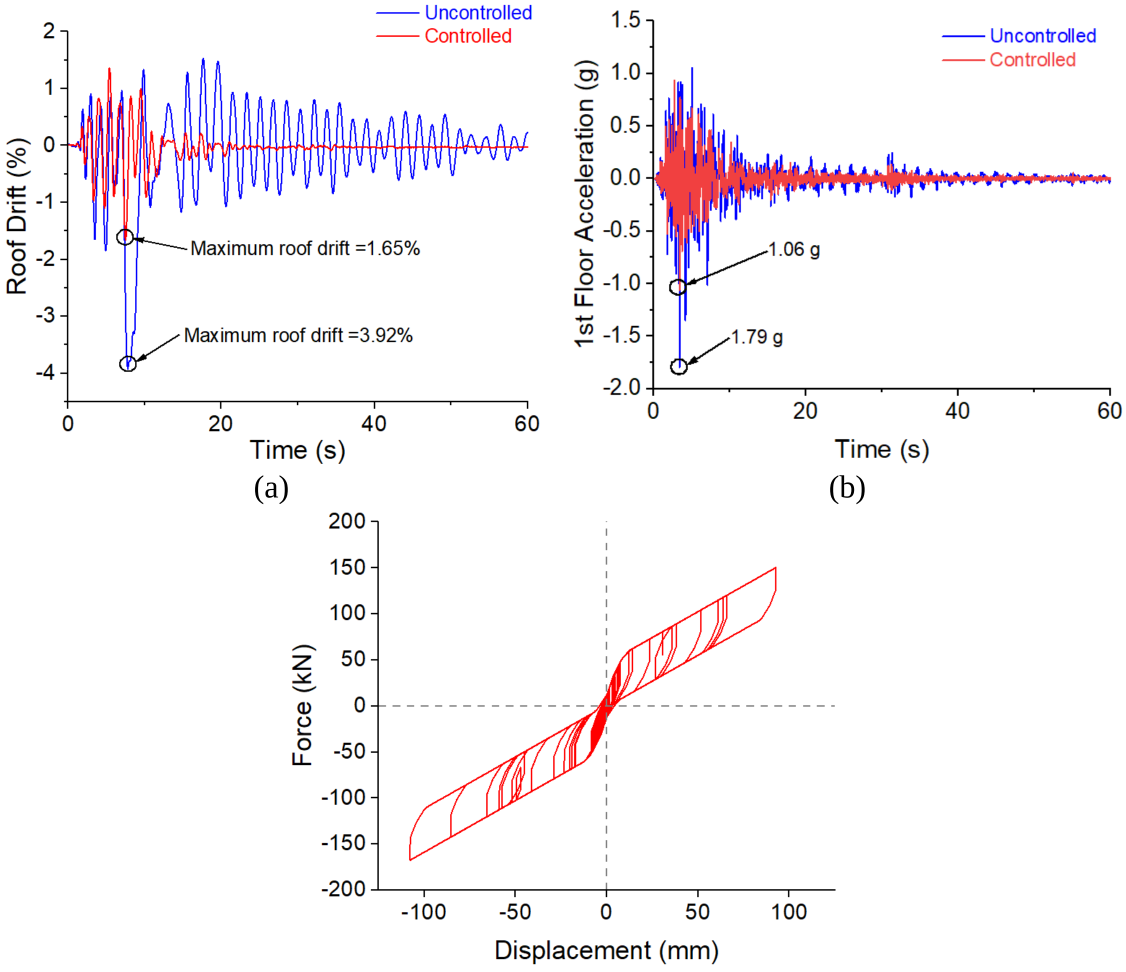

(a)

(b)

(c)

Figure 6-11. Selected response quantities for uncontrolled and controlled frames subjected to San Fernando earthquake scaled to the MCE level: (a) Roof drift time history, (b) First floor time history, and (c) the SFD force-displacement hysteresis loop

6.4 Influence of SFD Design Parameters

To examine the generality of findings obtained in the previous subsection, it is vital to understand the sensitivity of the steel frame responses to the SFD design parameters, particularly, the proportion between SMA cables and frictional force. Thus, a sensitivity analysis is conducted to evaluate the influence of friction ratio and provide guidance for proportioning of SFDs to obtain desirable system-level behavior. As defined in Chapter 5, the friction ratio β is the ratio of the frictional force to the force capacity of the SFD. It varied from 0.1 to 0.5 with an increment of 0.1 and the area of SMA cables are calculated accordingly. Note that the baseline SFD design described in section 6.3 has a β value of 0.23 and for the sake of clarity, the results of this case are not included in this section.

Figure 6-12 and Figure 6-13 show the height-wise distributions of the mean PID, RID, and PFA of the considered cases under DBE and MCE seismic hazard levels. The response parameters of the bare frame are also shown for reference. It can be seen that the PID generally decreases with increasing the friction ratio at both DBE and MCE levels. The mean PID decreases from 1.56% to 1.21% and from 2.38% to 1.99% when the friction ratio β increased from 0.1 to 0.5 at DBE level and MCE level, respectively. However, it should be noted that at one particular case the PID marginally increased when β increased from 0.2 to 0.3. As can be seen in Figure 6-12(c) and Figure 6-13(c), the PFA clearly tends to decrease as the friction ratio of the dampers increases. When β reaches 0.5, the PFA is much closer to that of the SMRF especially, at the DBE level. This can be attributed to increased damping provided by the friction energy dissipation mechanism. Moreover, due to higher forces induced in SMA cables at large seismic excitations, the PFA also increases with the increasing number of SMA cables, which is equivalent to decreasing of β values. Based on this observation, both the controlled and uncontrolled frames are expected to cause a similar degree of damage to acceleration sensitive non-structural components. Nevertheless, depending on the intended use of the building, it seems that the slight amplification of PFA can be effectively controlled by increasing the frictional force without significantly compromising the RID.

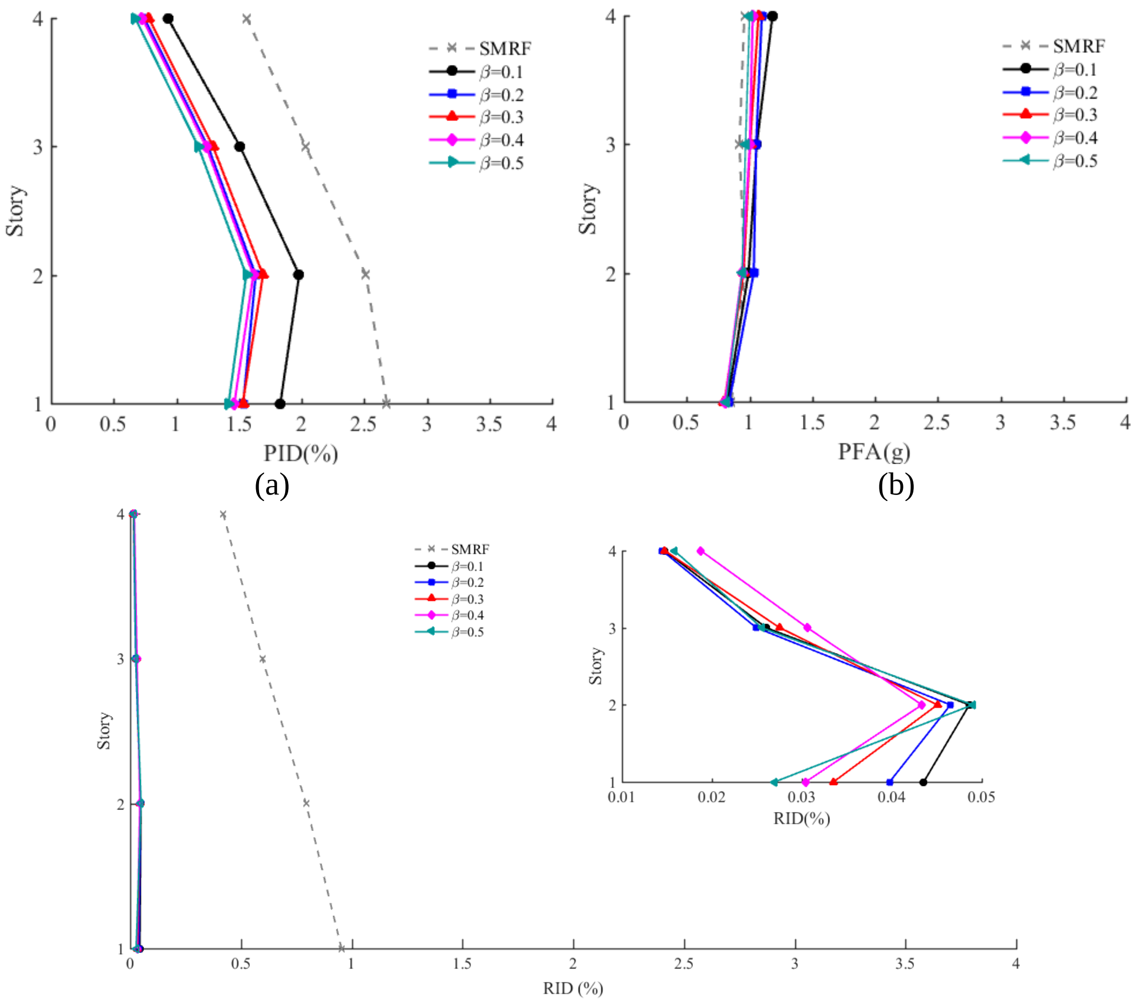

(a) (b)

(c)

Figure 6-12. Mean structural responses at DBE level for different friction ratios: (a) PID, (b) PFA, and (c) RID

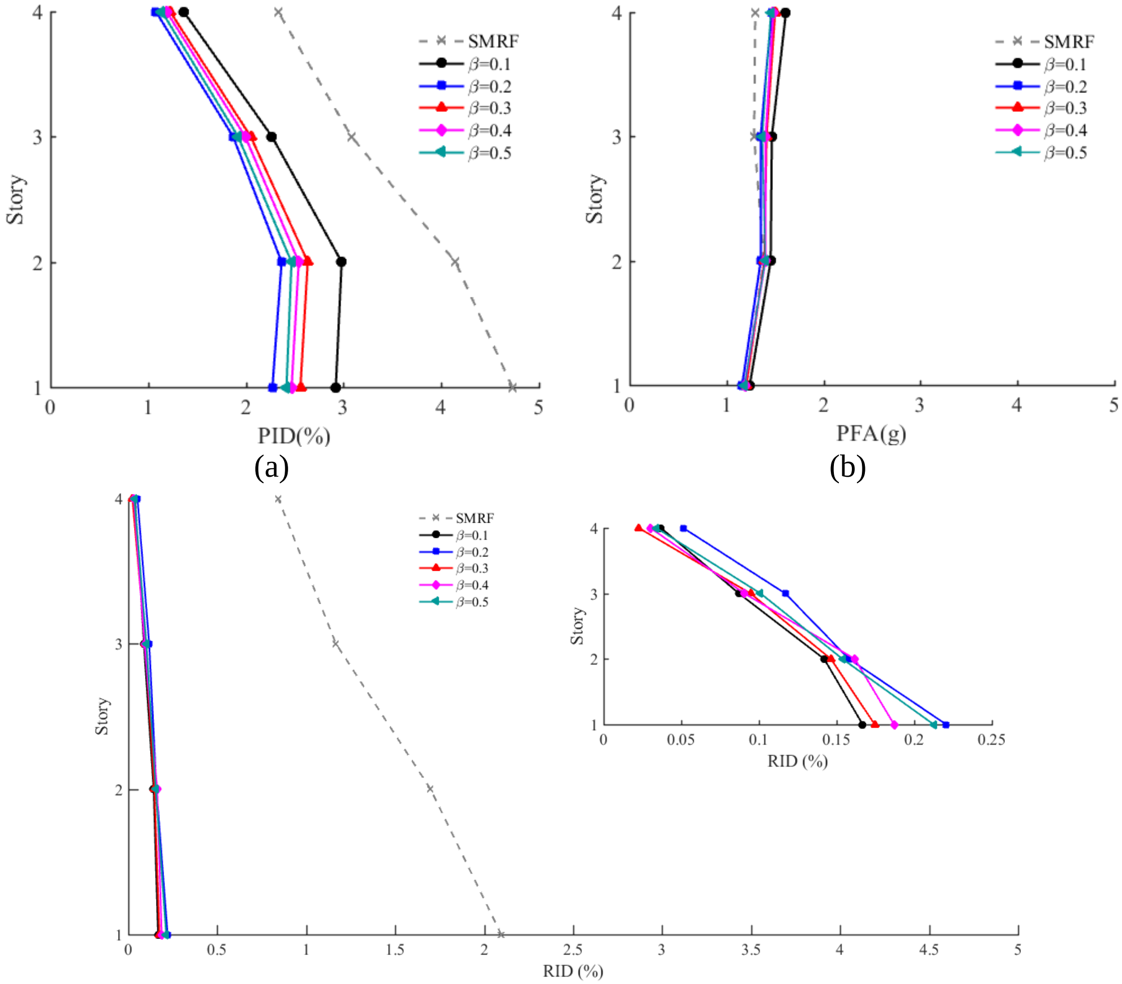

(a) (b)

(c)

Figure 6-13. Mean structural responses at MCE level for different friction ratios: (a) PID, (b) PFA, and (c) RID

The variations of the engineering demand parameters with β are shown in Figure 6-14. Generally speaking, an increase in β effectively decreases the PID, RID, and PFA. Given the increased recognition to RID as a key performance index for seismic resilience assessment, it is important to derive a relationship between the PID and RID. This will enable designers to quickly evaluate the damage state classes (DS1 to DS4) of a building designed based on an estimated PID. The correlation between the two parameters is also useful when one wants to determine the PID limit based on an allowable RID level, for instance 0.2% for DS1.

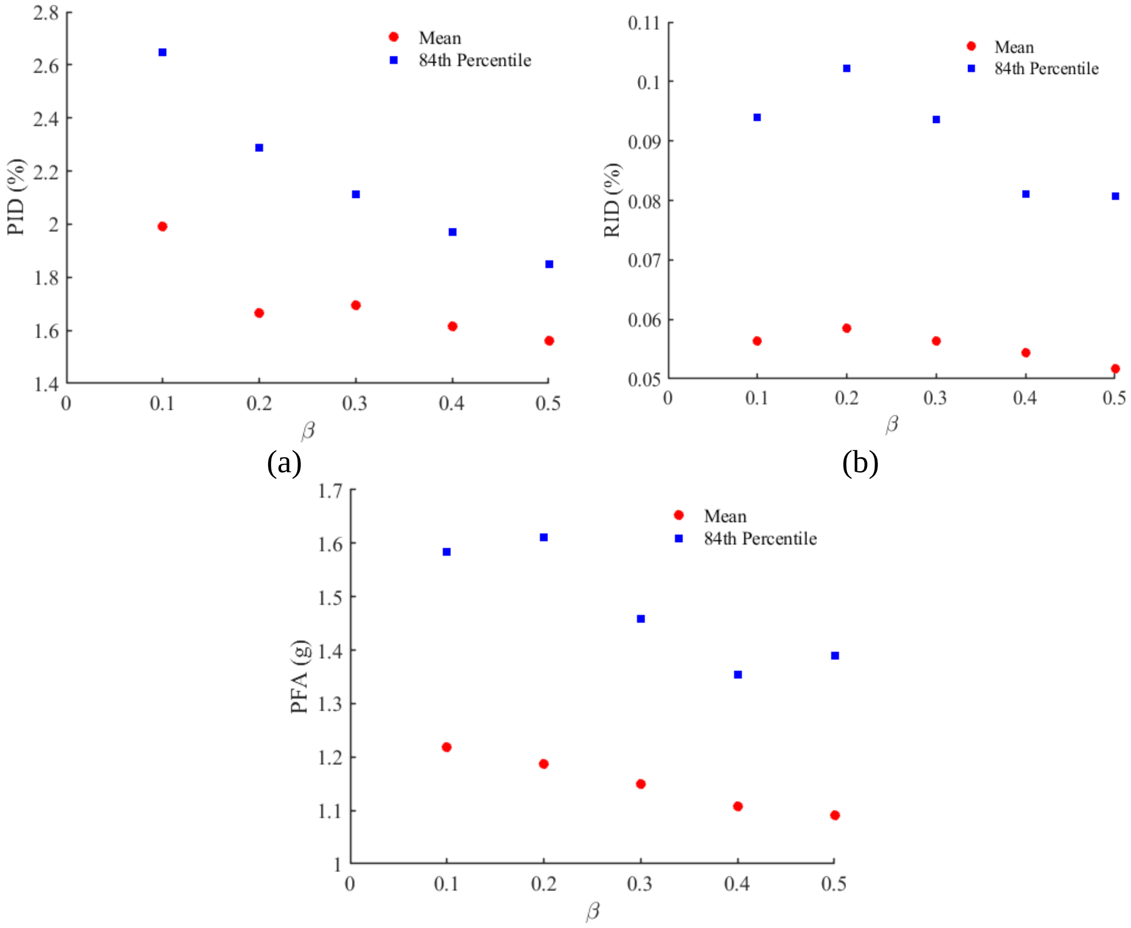

(a)

(b)

(c)

Figure 6-14. Influence of friction ratio on structural responses at DBE: (a) PID, (b) RID, and (c) PFA

7 SUMMARY, CONCLUSIONS, CONTRIBUTIONS, LIMITATIONS, AND RECOMMENDATIONS FOR FUTURE RESEARCH

Recent earthquakes have demonstrated that higher residual deformations can lead to substantial socio-economic losses in building occupation downtime and post-disaster reconstruction. As such, there is a big push for extending rapid re-occupation and functional recovery performance objectives from critical buildings such as hospitals and fire departments to other residential and multipurpose buildings. In light of such needs for resilient cities, there is a need to develop innovative materials and high-performance structural systems that can ensure building integrity and provide higher levels of post-event functionality after disasters such as large earthquakes.

Smart materials such as shape memory alloys (SMAs) have been explored to develop various structural control devices to foster seismic resiliency. SMAs are a class of smart metallic alloys that exhibit multiple unique properties. Their superelastic effect, which is the material's ability to recover large strain upon unloading, has made them appealing materials for earthquake engineering applications. Apart from that, SMAs have good energy dissipation capacity, excellent corrosion resistance, and high fatigue life.

This dissertation focused on developing, characterizing, and evaluating novel SMA-based structural control devices that can withstand strong ground shaking with little or no structural damage and, thus, help to achieve recovery-based design objectives. The study: (1) investigated the buckling, and post-buckling behavior of superelastic NiTi SMA bars to expand their practical implementation; (2) developed a new type of SMA-based energy dissipaters that can be used for various applications, notably for seismic retrofitting of existing substandard RC structures; (3) developed an innovative SMA-based damper that can be implemented to achieve functional recovery performance targets, and (4) evaluated the efficacy of the new SMA-based damper in seismic response control through numerical simulations.

The summary and main conclusions of this dissertation are outlined below, followed by highlighting the major research contributions. In the end, some future research ideas to continue the study of this dissertation are suggested.

7.1 Summary and Conclusions

First, a holistic chronological review of advancement in the field of SMA-based structural control devices was conducted. The critical review presented in Chapter 2 is very comprehensive, and it covered state-of-the-art research from worldwide renowned researchers in the field. The basics of SMAs, including the historical background, material properties, and the different forms of SMAs, are discussed. Analytical, numerical, and experimental studies on the application of SMAs in seismic response control, particularly in passive dampers, braces, and isolation bearings, are critically synthesized. Furthermore, this dissertation summarizes essential aspects of those control devices in terms of their effectiveness and limitations for the ease of further studies and generates future research paths for researchers who will be working in this field. Although effective SMA-based applications lead to convincing potentials for civil engineering, a few challenges such as cost limit their broad implementations. However, remarkable scientific research and technological advancements have been made in using SMAs by material scientists and the civil engineering community. Therefore, substantial achievements can soon be achieved, overcoming some of the challenges.

Second, the buckling and post-buckling behavior of 12 mm diameter superelastic NiTi SMA bars were examined. Initially, the tensile and compression responses of the NiTi bar were characterized under monotonic loading up to failure. Subsequently, a total of 15 specimens with slenderness ratios that range from 25 to 115 were tested to study the critical buckling load and post-buckling behavior of the bars. A digital image correlation (DIC) system was implemented to monitor full-field surface displacements. The interaction between material nonlinearity due to phase transformation and geometric nonlinearity was explored. Data obtained from the DIC measurement system was further analyzed to identify buckling onset and extract experimental critical buckling loads. The effect of loading rate on buckling response of SMAs was investigated by conducting additional testing at higher loading rates on the specimens with three selected slenderness ratios. The temperature field on the surface of the specimens was recorded by an Infrared camera. The analytical critical buckling loads were computed and compared with experimental results. All specimens exhibited a unique buckling behavior characterized with almost a complete shape recovery upon unloading.

Afterward, the studied SMA bars were employed to develop a new SMA damping device named confined superelastic dissipator (CSD). The proposed dissipator consists of a fused superelastic NiTi SMA bar as the functional kernel component encased in grout filled steel tube. The bar carries the axial load and dissipates energy through axial deformation, while the steel tube and infill grout restrain the bar and preclude buckling in compression. Theoretical derivations for the design of the buckling restraining system were presented first. Then, cyclic quasi-static tests were conducted to characterize the hysteretic behavior of CSDs. A total of eight specimens were designed, fabricated, and tested. All specimens exhibited stable and flag-shaped hysteretic behavior with excellent self-centering characteristics. Response quantities of prime interest for earthquake engineering, such as energy dissipation, equivalent viscous damping, and self-centering capability, were evaluated. The effect of geometric parameters such as fuse diameter and bar length on these parameters and failure mechanisms of CSDs were studied. Based on the experimental results and visual observations of failed specimens, specific recommendations were made to improve the performance of the CSDs. These observations and experimental results suggest that the design of CSDs can be tuned to produce the desired deformation and force capacity for different seismic applications.

Next, a large-scale SMA-based friction damper was developed and tested. The proposed damper offers an improved energy dissipation capacity compared to SMA-only dampers while maintaining good self-centering capability. Additionally, it possesses advantages such as scalability for real-world application, reusability, ease of fabrication, and adaptability of its hysteretic response. Analytical equations for predicting the load-displacement relationship of the damper were then derived. A large-scale prototype damper was fabricated, and its mechanical response under repeated cyclic loading at different loading rates and different ambient temperatures was characterized. Following the experimental work, a simple yet effective numerical model of the damper specimen was developed and validated. A parametric analysis was conducted to investigate the influence of key design parameters on the damper performance. Results reveal that the proposed damper exhibits stable hysteretic behavior with negligible loading rate and temperature sensitivity. The damper provides equivalent viscous damping of 14%, accompanied by 82% recovery of the peak damper displacement. The design parameter of the proposed damper can easily be adjusted to meet various levels of performance targets.

Finally, nonlinear response history analyses of a four-story special steel moment-resisting frame installed with the SFD were conducted to evaluate the efficacy of the damper in controlling the response of the frame. First, the four-story frame was designed as a conventional SMRF to meet current seismic design requirements. A numerical model that accounted for strength and stiffness degradation of the frame elements was created using the OpenSees finite element framework. Next, a reduced strength version of the fully code-compliant frame, which satisfied strength requirements but violet story drift limits, was developed. SFDs were designed and installed in all bays of each floor to meet the drift requirements per ASCE 7-16. The SFD is modeled by combining elements assigned with the uniaxial self-centering material properties to simulate the SMA cables and another element with Steel02 material properties to represent the frictional energy dissipating mechanism. The model parameters for these elements were calibrated based on experimental results. Then, the seismic performance of the uncontrolled and controlled frames was evaluated under a suite of 14 far-field strong ground motion records in terms of peak interstory drift (PID), residual interstory drift (RID), and peak floor acceleration (PFA). In the end, a sensitivity analysis study was carried out to evaluate the effect of SFD design parameters, namely the frictional force, on the overall performance of the steel frame with SFDs. It can be concluded that the SFD can significantly reduce or essentially eliminate residual drifts while providing almost the same performance to acceleration-sensitive non-structural components as conventional SMRF. This implies that stringent design objectives such as DS1, which limits the allowable residual drift to 0.2%, can be achieved using SFD. As a result, demolition of damaged structures or expensive repair programs due to excessive residual drift could be averted.

7.2 Originality and Contributions

The main contributions of the presented research in this dissertation, which have not been reported before in the open literature, to the best of the author's knowledge and understanding, are summarized below.

- This study is the first that explore the buckling and post-buckling behavior of large-diameter SMA bars considering rate sensitivity. Most of previous research on SMA bars have been limited to uniaxial tension tests, which hinders the use of SMA bars in situations where they are subjected to compression. This research conducted a series of experimental tests on several specimens with a wide range of slenderness ratios. Furthermore, the implementation of a digital image correlation system and infrared camera enabled careful analysis of the complex thermomechanical behavior of NiTi SMA bars in compression. The comprehensive experimental results presented in Chapter 3 could fill the current knowledge gap and help engineers and researchers expand the practical use of large diameter SMA bars both as structural and energy absorbing elements in various applications.
- This research investigated the effects of geometric parameters on the hysteretic behavior and failure modes of fuse type SMA-based energy dissipater that can be used for seismic protection of structural and non-structural components. Compared with traditional metallic yielding axial dissipaters available in the literature, the proposed device has additional advantages such as self-centering capability, reusability, and high durability. Furthermore, the proposed dissipater takes advantage of the "wet" fabrication procedure in which the anti-buckling system made of grout-filled steel tubes provides continuous lateral support to the SMA bar such that local buckling is inhibited.
- This research developed an innovative superelastic friction damper that leverages the high tensile resistance and excellent self-centering capability of SMA cables and non-sacrificial energy dissipation of a frictional damping mechanism. The proposed damper overcomes two main challenges of SMA-based seismic control devices: (i) insufficient force capacity for real-world application and (ii) relatively low energy dissipation capacity. The temperature sensitivity test results presented

in Chapter 5 are the first that have never been reported before for any SMA-based damping devices.

- Chapter 6 presented an example demonstrating the efficacy of the proposed superelastic friction damper in effectively controlling the structural response of special steel moment resisting frame. Nonlinear response history analyses were carried out, and results revealed that the damper could essentially eliminate system-level residual drifts.
- Given the novelty of the damper presented in Chapters 5 and 6, the University of Virginia has filed for the United States Provisional Patent to protect the invention.

7.3 Limitations and Recommendations for Future Research

The following recommendations are made for future work based upon the limitations of this study and literature review.

- Current SMA material constitutive models are developed based on uniaxial tension tests of SMA wires or small coupons. One of the fundamental assumptions of these models is symmetrical stress-strain relationship in tension and compression. However, as seen in Chapter 3 test results, SMA bars clearly exhibited asymmetric tension-compression behavior. Therefore, a robust constitutive model that captures the asymmetric behavior and accounts for buckling effects needs to be developed and validated.
- Limited parameters that affect the performance of the CSDs were considered during the experimental program. Therefore, parametric studies should be performed by employing a validated numerical model. Also, future work should focus on demonstrating the contributions of the CSDs in the resilient seismic design of different structural systems.
- Additionally, more work needs to be completed to numerically evaluate the system-level performance of non-code conforming RC frames retrofitted with CSDs. Research efforts on SMA-based control devices have mainly focused on mitigating the seismic response of steel structures. In contrast, very few studies on using such devices for the seismic design or upgrading of reinforced concrete structures have

been reported in the literature. Therefore, future research can evaluate the implementation of CSDs in concrete structures.

- In a typical confined superelastic dissipator, the steel tube and the SMA bar are not in direct contact inside the main body of the device. However, the SMA bar could be coupled with carbon steel to connect the CSDs with other structural members. The coupling of two dissimilar metals in a corrosive environment could lead to galvanic corrosion. Therefore, for outdoor applications of the device, additional experiments are required to quantify the effects of chloride-induced corrosion on the hysteric performance of the CSDs.
- To expand the versatility of the CSDs, a brace type dissipater that consists of multiple CSDs arranged in series and/or parallel should be designed, fabricated, and tested. Moreover, additional advantages such as enhanced damping capacity, activation of different parts during various earthquake levels, etc. can be included in the brace type dissipater.
- There have been only *ad hoc* approaches for designing structures installed with SMA-based structural control devices. Earlier efforts utilized current code force-based approaches to design structures with SMA-based devices and compared their performance with other lateral load resisting systems [132,266–268]. Several researchers have recently proposed a displacement-based design procedure for frame buildings with SMA bracing systems [170,269]. Nevertheless, a robust design procedure that can effectively satisfy prescribed performance objectives is still needed to advance the implementations of both the CSD and SFD in various structures.
- In this study, the cyclic response of the SFD was experimentally characterized under different loading conditions. Furthermore, the system-level performance was investigated through numerical simulations. Nonetheless, in this study and also others in the vast body of literature, there is a lack of information on the system-level experimental behavior of structures equipped with large-scale SMA control devices. Future shake table tests or real-time hybrid simulation tests are needed to assess the system-level performance of structures installed with SFDs.

- Further numerical studies are required to assess the mainshock-aftershock collapse performance of steel moment resisting frames with SFDs. In addition, the damper performance in reducing economic losses within a life-cycle context should be studied.
- The challenging problem, which remains open, is to accurately model the behavior of SMAs while assessing the functionality level of structures designed with SMA-based devices after a high-level seismic event. Most of the current SMA models consider a linear hardening behavior with complete shape recovery beyond superelastic strain capacity (red curve shown in Figure 7-1). This modeling assumption results in a reduced residual drift but at the same time increased floor accelerations at high-level seismic excitations of building systems. As can be seen in Figure 7-1, while the re-centering behavior of SMAs deteriorates at high displacement levels, their energy dissipation capacity increases. Therefore, a computational model that can accurately capture the hysteretic behavior of SMAs at high deformation levels is needed.

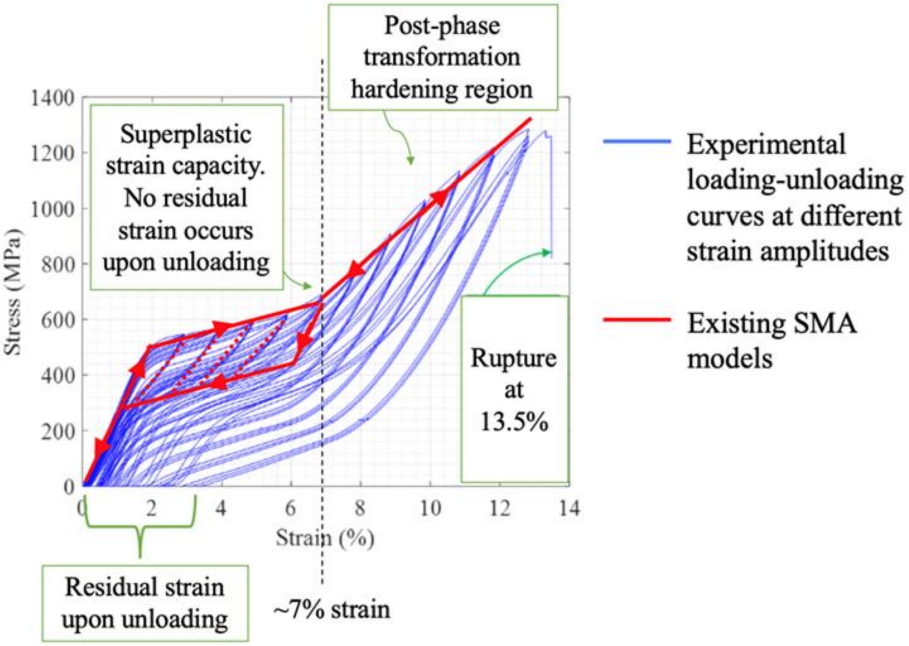

Figure 7-1. Experimental response of an SMA cable under increasing displacement amplitude up to rupture and illustration of existing numerical models.

8 REFERENCES

[1] Kersting R, Arendt L, Bonowitz D, Comerio M, Davis C, Deierlein G and Johnson K J 2021 Recommended Options for Improving the Functional Recovery of the Built Environment *Spec. Publ. FEMA P-2090/NIST SP-1254*

[2] Yu Q S, Wilson J and Wang Y 2014 Overview of the oregon resilience plan for next cascadia earthquake and Tsunami *NCEE 2014 - 10th U.S. Natl. Conf. Earthq. Eng. Front. Earthq. Eng.*

[3] Perry S, Cox D, Jones L, Bernknopf R, Goltz J, Hudnut K, Mileti D, Ponti D, Porter K, Reichle M, Seligson H, Shoaf K, Treiman J and Wein A 2008 The shakeout earthquake scenario-A story that Southern Californians are writing *US Geol. Surv. Circ.* 1–24

[4] Hudnut, K.W., Wein, A.M., Cox, D.A., Porter, K.A., Johnson, L.A., Perry, S.C., Bruce, J.L., and LaPointe D 2018 The HayWired earthquake scenario—We can outsmart disaster:

[5] Kircher C A, Seligson H A, Bouabid J and Morrow G C 2006 When the big one strikes again - Estimated losses due to a repeat of the 1906 San Francisco earthquake *Earthq. Spectra* **22** 297–339

[6] Potter S H, Becker J S, Johnston D M and Rossiter K P 2015 An overview of the impacts of the 2010-2011 Canterbury earthquakes *Int. J. Disaster Risk Reduct.* **14** 6–14

[7] Stevenson J R, Vargo J, Seville E, Kachali H, McNaughton A and Powell F 2012 The recovery of Canterbury's organisations: A comparative analysis of the 4 September 2010, 22 February, and 13 June 2011 earthquakes *Resilient Organ. Res. Rep. 2011/04* 1–54

[8] FEMA 2018 Seismic Performance Assessment of Buildings, Volume 5 - Expected Seismic Performance of Code-Conforming Buildings *Fema P-58-5* **5** 196

[9] Symans M D, Asce A M, Charney F A, Asce F, Whittaker ; A S, Asce M, Constantinou M C, Kircher C A, Johnson ; M W and Mcnamara R J 2008 Energy Dissipation Systems for Seismic Applications: Current Practice and Recent Developments *J. Struct. Eng.* **134** 3–21

[10] Soong T T and Spencer B F 2002 Supplemental energy dissipation: State-of-the-art and state-of-the-practice *Eng. Struct.* **24** 243–59

[11] Chen Y, Chen C, Ma Q, Jiang H and Wan Z 2019 Study on mechanical properties of high damping viscoelastic dampers *Adv. Struct. Eng.* **22** 2925–36

[12] Mehrabi M H, Suhatril M, Ibrahim Z, Ghodsi S S and Khatibi H 2017 Modeling of a viscoelastic damper and its application in structural control *PLoS One* **12** 1–23

[13] Kitayama S and Constantinou M C 2017 Fluidic self-centering devices as elements of seismically resistant structures: Description, testing, modeling, and model validation *J. Struct. Eng. (United States)* **143** 1–10

[14] Yan X, Chen Z, Qi A, Wang X and Shi S 2018 Experimental and theoretical study of a lead extrusion and friction composite damper *Eng. Struct.* **177** 306–17

[15] McCormick J, Aburano H, Ikenaga M and Nakashima M 2008 Permissible Residual Deformation Levels for Building Structures Considering both Safety and Human Elements *14th World Conf. Earthq. Eng.* 8

[16] Miranda C M R and E 2012 Significance of residual drifts in building earthquake loss estimation *Earthq. Eng. Struct. Dyn.* **41** 1477–93

[17] Applied Technology Council 2018 FEMA P-58-6: Guidelines for Performance-Based Seismic Design of Buildings *Fema P-58* **6** 92

[18] Fahnestock L A, Asce M, Sause ; Richard and Ricles J M Seismic Response and Performance of Buckling-Restrained Braced Frames

[19] Tremblay R, Lacerte ; M and Christopoulos C Seismic Response of Multistory Buildings with Self-Centering Energy Dissipative Steel Braces

[20] EERI 2011 The Tohoku, Japan, Tsunami of March 11, 2011: Effects on Structures *Earthq. Eng. Res. Inst. Spec. Earthq. Rep.* 1–14

[21] Moehle J U B, Riddell R U C and Boroschek R U C 2010 8.8 Chile Earthquake of February 27, 2010 *EERI Spec. Earthq. Rep.* **10** 1–20

[22] Chancellor N B, Eatherton M R, Roke D A and Akbas T 2014 Self-centering seismic lateral force resisting systems: High performance structures for the city of tomorrow *Buildings* **4** 520–48

[23] Warn G P, Whittaker A S and Constantinou M C 2007 Vertical stiffness *J. Struct. Eng. ASCE* **133** 484–94

[24] Ricles B J M, Sause R, Garlock M M, Member S and Zhao C 2001 Posttensioned Seismic-Resistant Connections For Steel Frames **127** 113–21

[25] Holden T, Restrepo J and Mander J B 2003 Seismic performance of precast reinforced and prestressed concrete walls *J. Struct. Eng.* **129** 286–96

[26] Christopoulos C and Filiatrault A 2003 Post-Tensioned Energy Dissipating (PTED) steel frames for seismic regions *Proc. Struct. Congr. Expo.* **128** 155–7

[27] Palermo A, Sarti F, Baird A, Bonardi D, Dekker D and Chung S 2012 From theory to practice: Design, analysis and construction of dissipative timber rocking post-tensioning wall system for Carterton Events Centre, New Zealand *Proc. 15th World Conf. Earthq. Eng. Lisbon, Port.* 24–8

[28] Wiebe L and Christopoulos C 2015 Performance-Based Seismic Design of Controlled Rocking Steel Braced Frames. I: Methodological Framework and Design of Base Rocking Joint *J. Struct. Eng.* **141** 04014226

[29] Hajjar M R E and J F 2014 Hybrid simulation testing of a self-centering rocking steel braced frame system *Earthq. Eng. Struct. Dyn.* **43** 1725–42

[30] Ahmadi O, Ricles J M and Sause R 2018 Modeling and seismic collapse resistance study of a steel SC-MRF *Soil Dyn. Earthq. Eng.* **113** 324–38

[31] Xu L, Yao S and Sun Y 2019 Development and validation tests of an assembly self-centering energy dissipation brace *Soil Dyn. Earthq. Eng.* **116** 120–9

[32] Zhang A, Ye Q and Wang Z 2020 Experimental investigation on behavior of re-centering energy dissipative brace *Eng. Struct.* **213** 110606

[33] Chou C C, Hsiao C H, Chen Z B, Chung P T and Pham D H 2019 Seismic loading tests of full-scale two-story steel building frames with self-centering braces and buckling-restrained braces *Thin-Walled Struct.* **140** 168–81

[34] Guo T, Wang J, Song Y, Xuan W and Chen Y 2020 Self-centering cable brace with friction devices for enhancing seismic performance of RC frame structures *Eng. Struct.* **207** 110187

[35] Xiao S J, Xu L H and Li Z X 2020 Development and experimental verification of self-centering shear walls with disc spring devices *Eng. Struct.* **213** 110622

[36] Ding Y and Liu Y 2020 Cyclic tests of assembled self-centering buckling-restrained braces with pre-compressed disc springs *J. Constr. Steel Res.* **172** 106229

[37] Westenenk B, Edwards J J, de la Llera J C and Jünemann R 2019 Self-Centering Frictional Damper (SCFD) *Eng. Struct.* **197** 109425

[38] Wang Y, Zhou Z, Xie Q and Huang L 2020 Theoretical analysis and experimental investigation of hysteretic performance of self-centering variable friction damper braces *Eng. Struct.* **217** 110779

[39] Liu J, Xu L and Li Z 2020 Development and experimental validation of a steel plate shear wall with self-centering energy dissipation braces *Thin-Walled Struct.* **148** 106598

[40] Yousef-beik S M M, Veismoradi S, Zarnani P and Quenneville P 2020 A new self-centering brace with zero secondary stiffness using elastic buckling *J. Constr. Steel Res.* **169** 106035

[41] Ozbulut O E, Hurlebaus S and Desroches R 2011 Seismic response control using shape memory alloys: A review *J. Intell. Mater. Syst. Struct.* **22** 1531–49

[42] Wilson J C and Wesolowsky M J 2005 Shape memory alloys for seismic response modification: A state-of-the-art review *Earthq. Spectra* **21** 569–601

[43] Zareie S, Issa A S, Seethaler R J and Zabihollah A 2020 Recent advances in the applications of shape memory alloys in civil infrastructures: A review *Structures* **27** 1535–50

[44] Chang W S and Araki Y 2016 Use of shape-memory alloys in construction: A critical review *Proc. Inst. Civ. Eng. Civ. Eng.* **169** 87–95

[45] Mohd Jani J, Leary M, Subic A and Gibson M A 2014 A review of shape memory alloy research, applications and opportunities *Mater. Des.* **56** 1078–113

[46] Dong J, Cai C S and Okeil A M 2011 Overview of Potential and Existing Applications of Shape Memory Alloys in Bridges *J. Bridg. Eng.* **16** 305–15

[47] Sattar S, McAllister T, Johnson K, Segura C, McCabe S, Fung J, Levitan M, Harrison K, Harris J, Clavin C, Abrahams L and Sylak-Glassman E 2018 Research Needs to Support Immediate Occupancy Building Performance Objective Following Natural Hazard Events *Nist* 1–95

[48] Cornell A 2004 Hazard, ground motions and probabilistic assessment for PBSD

[49] Deierlein G G, Krawinkler H and Cornell C A 2003 A framework for performance-based earthquake engineering *Proc. 2003 Pacific Conf. Earthq. Eng.* **273** 140–8

[50] Yoshimura M, Takaine Y and Nakamura T 2003 The Fifth U.S.-Japan Workshop on Performance-Based Earthquake Engineering Methodology for Reinforced Concrete Building Structures *Proc. Fifth U.S.-Japan Work. Performance-Based Earthq. Eng. Methodol. Reinf. Concr. Build. Struct.* 239–53

[51] Moehle J and Deierlein G G 2004 a Framework Methodology for Performance-Based Earthquake Engineering *13th World Conf. Earthq. Eng.*

[52] Bruneau M and Reinhorn A 2007 Exploring the concept of seismic resilience for acute care facilities *Earthq. Spectra* **23** 41–62

[53] Almufti I, Willford M, Delucchi M, Davis C, Hanson B, Langdon D, Friedman D, Johnson L, Nielsen G, Riordan N O, Roberts C, Steiner M, Wilson A, Wolski A and

Mote T 2013 REDi ^{TM} Rating System Resilience-based Earthquake Design Initiative for the Next Generation of Buildings 1–133

[54] Mander T J, Rodgers G W, Chase J G, Mander J B, MacRae G A and Dhakal R P 2009 Damage avoidance design steel beam-column moment connection using high-force-to-volume dissipators *J. Struct. Eng.* **135** 1390–7

[55] Mashal M and Palermo A 2019 Low-damage seismic design for accelerated bridge construction *J. Bridg. Eng.* **24** 1–13

[56] Ölander A 1932 An electrochemical investigation of solid cadmium-gold alloys *J. Am. Chem. Soc.* **54** 3819–33

[57] Vernon L B and Vernon H M 1941 Article formed of thermoplastic synthetic resins and process of manufacturing the same

[58] Rachinger W A 1958 A “super-elastic” single crystal calibration bar *Br. J. Appl. Phys.* **9** 250–2

[59] Buehler W J, Gilfrich J V. and Wiley R C 1963 Effect of Low-Temperature Phase Changes on the Mechanical Properties of Alloys near Composition TiNi *J. Appl. Phys.* **34** 1475–7

[60] Wang F E, Buehler W J and Pickart S J 1965 Crystal structure and a unique “martensitic” transition of TiNi *J. Appl. Phys.* **36** 3232–9

[61] Duerig T W and Melton K N 1989 Applications of Shape Memory in the USA Duerig , Melton *New Mater. Process. Futur.* 195–200

[62] Sherif M M, Tanks J and Ozbulut O E 2017 Acoustic emission analysis of cyclically loaded superelastic shape memory alloy fiber reinforced mortar beams *Cem. Concr. Res.* **95** 178–87

[63] Wayman C M 1981 Shape Memory Effect. *Met. forum* **4** 135–41

[64] Malécot P, Lexcellent C, Foltête E and Collet M 2006 Shape memory alloys cyclic behavior: Experimental study and modeling *J. Eng. Mater. Technol. Trans. ASME* **128** 335–45

[65] McCormick J, Tyber J, DesRoches R, Gall K and Maier H J 2007 Structural Engineering with NiTi. II: Mechanical Behavior and Scaling *J. Eng. Mech.* **133** 1019–29

[66] Azadi B, Rajapakse R K N D and Maijer D M 2006 One-dimensional thermomechanical model for dynamic pseudoelastic response of shape memory alloys *Smart Mater. Struct.* **15** 996–1008

[67] Soul H and Yawny A 2013 Thermomechanical model for evaluation of the superelastic response of NiTi shape memory alloys under dynamic conditions *Smart Mater. Struct.* **22**

[68] Soul H, Isalgue A, Yawny A, Torra V and Lovey F C 2010 Pseudoelastic fatigue of NiTi wires: Frequency and size effects on damping capacity *Smart Mater. Struct.* **19**

[69] Xiao Y, Zeng P, Lei L and Du H 2015 Experimental Investigation on Rate Dependence of Thermomechanical Response in Superelastic NiTi Shape Memory Alloy *J. Mater. Eng. Perform.* **24** 3755–60

[70] Sarraj R, Letaief W E, Hassine T and Gamaoun F 2019 Modeling of rate dependency of mechanical behavior of superelastic NiTi alloy under cyclic loading *Int. J. Adv. Manuf. Technol.* **100** 2715–24

[71] Oliveira J P, Miranda R M and Braz Fernandes F M 2017 Welding and Joining of NiTi Shape Memory Alloys: A Review *Prog. Mater. Sci.* **88** 412–66

[72] Kaya E and Kaya İ 2019 A review on machining of NiTi shape memory alloys: the process and post process perspective *Int. J. Adv. Manuf. Technol.* **100** 2045–87

[73] Zhao L C, Duerig T W, Justi S, Melton K N, Proft J L, Yu W and Wayman C M 1990 The study of niobium-rich precipitates in a NiTiNb shape memory alloy *Scr. Metall. Mater.* **24** 221–5

[74] Bao Z Z, Guo S, Xiao F and Zhao X Q 2011 Development of NiTiNb in-situ composite with high damping capacity and high yield strength *Prog. Nat. Sci. Mater. Int.* **21** 293–300

[75] Toker G P, Saedi S, Acar E, Ozbulut O E and Karaca H E 2020 Loading frequency and temperature-dependent damping capacity of NiTiHfPd shape memory alloy *Mech. Mater.* **150** 103565

[76] Suhail R, Amato G and McCrum D 2020 Heat-activated prestressing of NiTiNb shape memory alloy wires *Eng. Struct.* **206** 110128

[77] Karaca H E, Acar E, Basaran B, Noebe R D and Chumlyakov Y I 2012 Superelastic response and damping capacity of ultrahigh-strength [1 1 1]-oriented NiTiHfPd single crystals *Scr. Mater.* **67** 447–50

[78] Karaca H E, Acar E, Tobe H and Saghaian S M 2014 NiTiHf-based shape memory alloys *Mater. Sci. Technol. (United Kingdom)* **30** 1530–44

[79] Dasgupta R 2014 A look into Cu-based shape memory alloys: Present scenario and future prospects *J. Mater. Res.* **29** 1681–98

[80] Y. Araki1, T.Endo1, T.Omori, Y. Sutou, Y.Koetaka R K and 2007 Potential of superelastic Cu–Al–Mn alloy bars for seismic applications *Pacific Conf. Earthq. Eng.* 1–6

[81] Yang S, Zhang F, Wu J, Zhang J, Wang C and Liu X 2017 Microstructure characterization, stress–strain behavior, superelasticity and shape memory effect of Cu–Al–Mn–Cr shape memory alloys *J. Mater. Sci.* **52** 5917–27

[82] Araki Y, Maekawa N, Omori T, Sutou Y, Kainuma R and Ishida K 2012 Rate-dependent response of superelastic Cu-Al-Mn alloy rods to tensile cyclic loads *Smart Mater. Struct.* **21**

[83] Moroni M, Golott P, Sarrazin M and Sepulveda A 2004 Use of Copper-Base Shape Memory Alloys in Seismic Energy Dissipation Devices *13th World Conf. Earthq. Eng.*

[84] Torra V, Isalgue A, Auguet C, Carreras G, Lovey F C, Soul H and Terriault P 2009 Damping in civil engineering using SMA. the fatigue behavior and stability of CuAlBe and NiTi alloys *J. Mater. Eng. Perform.* **18** 738–45

[85] Sato A, Chishima E, Soma K and Mori T 1982 Shape memory effect in $\gamma \rightleftarrows \epsilon$ transformation in Fe-30Mn-1Si alloy single crystals *Acta Metall.* **30** 1177–83

[86] Lee W J, Partovi-Nia R, Suter T and Leinenbach C 2016 Electrochemical characterization and corrosion behavior of an Fe-Mn-Si shape memory alloy in simulated concrete pore solutions *Mater. Corros.* **67** 839–46

[87] Dong Z, Klotz U E, Leinenbach C, Bergamini A, Czaderski C and Motavalli M 2009 A novel Fe-Mn-Si shape memory alloy with improved shape recovery properties by VC precipitation *Adv. Eng. Mater.* **11** 40–4

[88] Shahverdi M, Michels J, Czaderski C and Motavalli M 2018 Iron-based shape memory alloy strips for strengthening RC members: Material behavior and characterization *Constr. Build. Mater.* **173** 586–99

[89] Izadi M, Hosseini A, Michels J, Motavalli M and Ghafoori E 2019 Thermally activated iron-based shape memory alloy for strengthening metallic girders *Thin-Walled Struct.* **141** 389–401

[90] Cladera A, Weber B, Leinenbach C, Czaderski C, Shahverdi M and Motavalli M 2014 Iron-based shape memory alloys for civil engineering structures: An overview *Constr. Build. Mater.* **63** 281–93

[91] Tanaka Y, Himuro Y, Kainuma R, Sutou Y, Omori T and Ishida K 2010 Ferrous polycrystalline shape-memory alloy showing huge superelasticity *Science (80).* **327** 1488–90

[92] Omori T, Ando K, Okano M, Xu X, Tanaka Y, Ohnuma I, Kainuma R and Ishida K 2011 Superelastic effect in polycrystalline ferrous alloys *Science (80).* **333** 68–71

[93] Gangil N, Siddiquee A N and Maheshwari S 2020 Towards applications, processing and advancements in shape memory alloy and its composites *J. Manuf. Process.* **59** 205–22

[94] Alaneme K K and Okotete E A 2016 Reconciling viability and cost-effective shape memory alloy options – A review of copper and iron based shape memory metallic systems *Eng. Sci. Technol. an Int. J.* **19** 1582–92

[95] Dolce M and Cardone D 2001 Mechanical behaviour of shape memory alloys for seismic applications 2. Austenite NiTi wires subjected to tension *Int. J. Mech. Sci.* **43** 2657–77

[96] Tamai H and Kitagawa Y 2002 Pseudoelastic behavior of shape memory alloy wire and its application to seismic resistance member for building *Comput. Mater. Sci.* **25** 218–27

[97] Desroches R, McCormick J and Delemont M 2004 Cyclic properties of superelastic shape memory alloy wires and bars *J. Struct. Eng.* **130** 38–46

[98] Vitiello A, Giorleo G and Morace R E 2005 Analysis of thermomechanical behaviour of Nitinol wires with high strain rates *Smart Mater. Struct.* **14** 215–21

[99] D. Fugazza 2005 Use of shape-memory alloy devices in earthquake engineering: mechanical properties, advanced constitutive modelling and structural applications *PhD Thesis*

[100] Churchill C B, Shaw J A and Iadicola M A 2009 Tips and tricks for characterizing shape memory alloy wire: Part 2 - Fundamental isothermal responses *Exp. Tech.* **33** 51–62

[101] Reedlunn B, Daly S and Shaw J 2013 Superelastic shape memory alloy cables: Part i - Isothermal tension experiments *Int. J. Solids Struct.* **50** 3009–26

[102] Ozbulut O E, Daghash S and Sherif M M 2016 Shape memory alloy cables for structural applications *J. Mater. Civ. Eng.* **28** 1–10

[103] Sherif M M and Ozbulut O E 2018 Tensile and superelastic fatigue characterization of NiTi shape memory cables *Smart Mater. Struct.* **27**

[104] Carboni B, Lacarbonara W and Auricchio F 2015 Hysteresis of Multiconfiguration Assemblies of Nitinol and Steel Strands: Experiments and Phenomenological Identification *J. Eng. Mech.* **141** 04014135

[105] Mas B, Biggs D, Vieito I, Cladera A, Shaw J and Martínez-Abella F 2017 Superelastic shape memory alloy cables for reinforced concrete applications *Constr. Build. Mater.* **148** 307–20

[106] Fang C, Zheng Y, Chen J, Yam M C H and Wang W 2019 Superelastic NiTi SMA cables: Thermal-mechanical behavior, hysteretic modelling and seismic application *Eng. Struct.* **183** 533–49

[107] Wang W, Fang C and Liu J 2016 Large size superelastic SMA bars: Heat treatment strategy, mechanical property and seismic application *Smart Mater. Struct.* **25**

[108] Speicher M S, DesRoches R and Leon R T 2011 Experimental results of a NiTi shape memory alloy (SMA)-based recentering beam-column connection *Eng. Struct.* **33** 2448–57

[109] Fang C, Wang W, He C and Chen Y 2017 Self-centring behaviour of steel and steel-concrete composite connections equipped with NiTi SMA bolts *Eng. Struct.* **150** 390–408

[110] Fang C, Yam M C H, Lam A C C and Xie L 2014 Cyclic performance of extended end-plate connections equipped with shape memory alloy bolts *J. Constr. Steel Res.* **94** 122–36

[111] Dolce M and Cardone D 2001 Mechanical behaviour of shape memory alloys for seismic applications 1. Martensite and austenite NiTi bars subjected to torsion *Int. J. Mech. Sci.* **43** 2631–56

[112] Chung J H, Heo J S and Lee J J 2006 Modeling and numerical simulation of the pseudoelastic behavior of shape memory alloy circular rods under tension-torsion combined loading *Smart Mater. Struct.* **15** 1651–60

[113] Predki W, Klönne M and Knopik A 2006 Cyclic torsional loading of pseudoelastic NiTi shape memory alloys: Damping and fatigue failure *Mater. Sci. Eng. A* **417** 182–9

[114] Mirzaeifar R, Desroches R and Yavari A 2010 Exact solutions for pure torsion of shape memory alloy circular bars *Mech. Mater.* **42** 797–806

[115] Andani M T, Alipour A and Elahinia M 2013 Coupled rate-dependent superelastic behavior of shape memory alloy bars induced by combined axial-torsional loading: A semi-analytic modeling *J. Intell. Mater. Syst. Struct.* **24** 1995–2007

[116] Reedlunn B, LePage W S, Daly S H and Shaw J A 2020 Axial-torsion behavior of superelastic tubes: Part I, proportional isothermal experiments *Int. J. Solids Struct.* **199** 1–35

[117] Safaei K, Nematollahi M, Bayati P, Dabbaghi H, Benafan O and Elahinia M 2021 Torsional behavior and microstructure characterization of additively manufactured NiTi shape memory alloy tubes *Eng. Struct.* **226** 111383

[118] Liew K M, Kitipornchai S, Ng T Y and Zou G P 2002 Multi-dimensional superelastic behavior of shape memory alloys via nonlinear finite element method *Eng. Struct.* **24** 51–7

[119] Hashemi S M T and Khadem S E 2006 Modeling and analysis of the vibration behavior of a shape memory alloy beam *Int. J. Mech. Sci.* **48** 44–52

[120] Mirzaeifar R, Desroches R, Yavari A and Gall K 2013 On superelastic bending of shape memory alloy beams *Int. J. Solids Struct.* **50** 1664–80

[121] Reedlunn B, Churchill C B, Nelson E E, Shaw J A and Daly S H 2014 Tension, compression, and bending of superelastic shape memory alloy tubes *J. Mech. Phys. Solids* **63** 506–37

[122] Mohammad Hashemi Y, Kadkhodaei M and Salehan M 2019 Fully coupled thermomechanical modeling of shape memory alloys under multiaxial loadings and implementation by finite element method *Contin. Mech. Thermodyn.* **31** 1683–98

[123] Rahman M A, Qiu J and Tani J 2005 Buckling and postbuckling characteristics of the superelastic SMA columns - Numerical simulation *J. Intell. Mater. Syst. Struct.* **16** 691–702

[124] Pereiro-Barceló J and Bonet J L 2017 Ni-Ti SMA bars behaviour under compression *Constr. Build. Mater.* **155** 348–62

[125] Watkins R T, Reedlunn B, Daly S and Shaw J A 2018 Uniaxial, pure bending, and column buckling experiments on superelastic NiTi rods and tubes *Int. J. Solids Struct.* **146** 1–28

[126] Asfaw A M, Sherif M M, Xing G and Ozbulut O E 2020 Experimental Investigation on Buckling and Post-buckling Behavior of Superelastic Shape Memory Alloy Bars *J. Mater. Eng. Perform.* **29** 3127–40

[127] Jee K K, Han J H, Kim Y B, Lee D H and Jang W Y 2008 New method for improving properties of SMA coil springs *Eur. Phys. J. Spec. Top.* **158** 261–6

[128] Enemark S, Santos I F and Savi M A 2016 Modelling, characterisation and uncertainties of stabilised pseudoelastic shape memory alloy helical springs *J. Intell. Mater. Syst. Struct.* **27** 2721–43

[129] Savi M A, Pacheco P M C L, Garcia M S, Aguiar R A A, De Souza L F G and Da Hora R B 2015 Nonlinear geometric influence on the mechanical behavior of shape memory alloy helical springs *Smart Mater. Struct.* **24**

[130] Viet N V., Zaki W, Umer R and Xu Y 2020 Mathematical model for superelastic shape memory alloy springs with large spring index *Int. J. Solids Struct.* **185–186** 159–69

[131] Heidari B, Kadkhodaei M, Barati M and Karimzadeh F 2016 Fabrication and modeling of shape memory alloy springs *Smart Mater. Struct.* **25**

[132] Speicher M, Hodgson D E, Desroches R and Leon R T 2009 Shape memory alloy tension/compression device for seismic retrofit of buildings *J. Mater. Eng. Perform.* **18** 746–53

[133] Sgambitterra E, Maletta C and Furgiuele F 2016 Modeling and simulation of the thermo-mechanical response of NiTi-based Belleville springs *J. Intell. Mater. Syst. Struct.* **27** 81–91

[134] Maletta C, Filice L and Furgiuele F 2013 NiTi Belleville washers: Design, manufacturing and testing *J. Intell. Mater. Syst. Struct.* **24** 695–703

[135] Fang C, Zhou X, Osofero A I, Shu Z and Corradi M 2016 Superelastic SMA Belleville washers for seismic resisting applications: Experimental study and modelling strategy *Smart Mater. Struct.* **25**

[136] Wang W, Fang C, Yang X, Chen Y, Ricles J and Sause R 2017 Innovative use of a shape memory alloy ring spring system for self-centering connections *Eng. Struct.* **153** 503–15

[137] Fang, C., & Wang, W. 2019 Economic Seismic Loss Assessment. *Shape Memory Alloys for Seismic Resilience*.

[138] Parulekar Y M, Reddy G R, Vaze K K, Guha S, Gupta C, Muthumani K and Sreekala R 2012 Seismic response attenuation of structures using shape memory alloy dampers *Struct. Control Heal. Monit.* **19** 102–19

[139] Parulekar Y M, Ravi Kiran A, Reddy G R, Singh R K and Vaze K K 2014 Shake table tests and analytical simulations of a steel structure with shape memory alloy dampers *Smart Mater. Struct.* **23**

[140] Qian H, Li H, Song G and Guo W 2013 Recentering shape memory alloy passive damper for structural vibration control *Math. Probl. Eng.* **2013**

[141] Zhang Y and Zhu S 2007 A shape memory alloy-based reusable hysteretic damper for seismic hazard mitigation *Smart Mater. Struct.* **16** 1603–13

[142] Soul H and Yawny A 2015 Self-centering and damping capabilities of a tension-compression device equipped with superelastic NiTi wires *Smart Mater. Struct.* **24** 75005

[143] Soul H and Yawny A 2017 Applicability of superelastic materials in seismic protection systems: A parametric study of performance in isolation of structures *Smart Mater. Struct.* **26**

[144] Walter Yang C S, DesRoches R and Leon R T 2010 Design and analysis of braced frames with shape memory alloy and energy-absorbing hybrid devices *Eng. Struct.* **32** 498–507

[145] Jennings E, van de Lindt J W, Ziaei E, Mochizuki G, Pang W and Shao X 2014 Retrofit of a soft-story woodframe building using SMA devices with full-scale hybrid test verification *Eng. Struct.* **80** 469–85

[146] Cardone D and Sofia S 2012 Experimental evaluation of a device prototype based on shape memory alloys for the retrofit of historical buildings *J. Mater. Eng. Perform.* **21** 2719–28

[147] Liu A, Yu Q, Yao Y and Guo Y 2011 A new type of hybrid-passive-damper *Adv. Mater. Res.* **163**–**167** 4367–72

[148] Yan S, Wang Q and Wang W 2010 Design and experimental investigation on a new type of SMA-fluid viscous damper *Earth and Space 2010: Engineering, Science, Construction, and Operations in Challenging Environments* pp 3198–206

[149] Di Cesare A, Ponzo F C, Nigro D, Dolce M and Moroni C 2012 Experimental and numerical behaviour of hysteretic and visco-recentring energy dissipating bracing systems *Bull. Earthq. Eng.* **10** 1585–607

[150] Silwal B, Michael R J and Ozbulut O E 2015 A superelastic viscous damper for enhanced seismic performance of steel moment frames *Eng. Struct.* **105** 152–64

[151] Qian H, Li H and Song G 2016 Experimental investigations of building structure with a superelastic shape memory alloy friction damper subject to seismic loads *Smart Mater. Struct.* **25**

[152] Li H N, Liu M M and Fu X 2018 An innovative re-centering SMA-lead damper and its application to steel frame structures *Smart Mater. Struct.* **27**

[153] Alipour A, Kadkhodaei M and Safaei M 2017 Design, analysis, and manufacture of a tension–compression self-centering damper based on energy dissipation of pre-stretched superelastic shape memory alloy wires *J. Intell. Mater. Syst. Struct.* **28** 2129–39

[154] Li H N, Huang Z, Fu X and Li G 2018 A re-centering deformation-amplified shape memory alloy damper for mitigating seismic response of building structures *Struct. Control Heal. Monit.* **25** 1–20

[155] Zhang Z, Bi K, Hao H, Sheng P, Feng L and Xiao D 2020 Development of a novel deformation-amplified shape memory alloy-friction damper for mitigating seismic responses of RC frame buildings *Eng. Struct.* **216** 110751

[156] Liu M, Zhou P and Li H 2018 Novel Self-Centering Negative Stiffness Damper Based on Combination of Shape Memory Alloy and Prepressed Springs *J. Aerosp. Eng.* **31** 1–10

[157] Wang B and Zhu S 2018 Cyclic tension–compression behavior of superelastic shape memory alloy bars with buckling-restrained devices *Constr. Build. Mater.* **186** 103–13

[158] Qiu C, Fang C, Liang D, Du X and Yam M C H 2020 Behavior and application of self-centering dampers equipped with buckling-restrained SMA bars *Smart Mater. Struct.* **29**

[159] Qiu C, Wang H, Liu J, Qi J and Wang Y 2020 Experimental tests and finite element simulations of a new SMA-steel damper *Smart Mater. Struct.* **29**

[160] Naeem A, Eldin M N, Kim J and Kim J 2017 Seismic performance evaluation of a structure retrofitted using steel slit dampers with shape memory alloy bars *Int. J. Steel Struct.* **17** 1627–38

[161] NourEldin M, Naeem A and Kim J 2019 Life-cycle cost evaluation of steel structures retrofitted with steel slit damper and shape memory alloy–based hybrid damper *Adv. Struct. Eng.* **22** 3–16

[162] Jalaeefar A and Asgarian B 2013 Experimental investigation of mechanical properties of nitinol, structural steel, and their hybrid component *J. Mater. Civ. Eng.* **25** 1498–505

[163] Choi E, Mohammadzadeh B and Kim H S 2019 SMA bending bars as self-centering and damping devices *Smart Mater. Struct.* **28**

[164] Wang W, Fang C, Zhang A and Liu X 2019 Manufacturing and performance of a novel self-centring damper with shape memory alloy ring springs for seismic resilience *Struct. Control Heal. Monit.* **26** 1–17

[165] Choi E, Nguyen H D, Jeon J S and Kang J W 2019 Self-centering and damping devices using SMA dual rings *Smart Mater. Struct.* **28**

[166] Wang B and Zhu S 2018 Superelastic SMA U-shaped dampers with self-centering functions *Smart Mater. Struct.* **27**

[167] Hu J W 2014 Investigation on the cyclic response of superelastic shape memory alloy (SMA) slit damper devices simulated by quasi-static finite element (FE) analyses *Materials (Basel).* **7** 1122–41

[168] Wang B, Zhu S, Chen K and Huang J 2020 Development of superelastic SMA angles as seismic-resistant self-centering devices *Eng. Struct.* **218** 110836

[169] Qiu C and Zhu S 2017 Shake table test and numerical study of self-centering steel frame with SMA braces *Earthq. Eng. Struct. Dyn.* **46** 117–37

[170] Qiu C X and Zhu S 2017 Performance-based seismic design of self-centering steel frames with SMA-based braces *Eng. Struct.* **130** 67–82

[171] Speicher M S, DesRoches R and Leon R T 2017 Investigation of an articulated quadrilateral bracing system utilizing shape memory alloys *J. Constr. Steel Res.* **130** 65–78

[172] Kari A, Ghassemieh M and Badarloo B 2019 Development and design of a new self-centering energy-dissipative brace for steel structures *J. Intell. Mater. Syst. Struct.* **30** 924–38

[173] Varughese K and El-Hacha R 2020 Design and behaviour of steel braced frame reinforced with NiTi SMA wires *Eng. Struct.* **212** 110502

[174] Shi F, Saygili G and Ozbulut O E 2018 Probabilistic seismic performance evaluation of SMA-braced steel frames considering SMA brace failure *Bull. Earthq. Eng.* **16** 5937–62

[175] Shi F, Ozbulut O E and Zhou Y 2020 Influence of shape memory alloy brace design parameters on seismic performance of self-centering steel frame buildings *Struct. Control Heal. Monit.* **27** 1–18

[176] Shi F, Saygili G, Ozbulut O E and Zhou Y 2020 Risk-based mainshock-aftershock performance assessment of SMA braced steel frames *Eng. Struct.* **212** 110506

[177] Dong H, Du X and Han Q 2019 Seismic responses of steel frame structures with self-centering energy dissipation braced on shape memory alloy cables *Adv. Struct. Eng.* **22** 2136–48

[178] Chen J, Fang C, Wang W and Liu Y 2020 Variable-friction self-centering energy-dissipation braces (VF-SCEDBs) with NiTi SMA cables for seismic resilience *J. Constr. Steel Res.* **175** 106318

[179] Miller D J, Fahnestock L A and Eatherton M R 2012 Development and experimental validation of a nickel-titanium shape memory alloy self-centering buckling-restrained brace *Eng. Struct.* **40** 288–98

[180] Matthew R. Eatherton1, L A F and D J M 2014 Computational study of self-centering buckling-restrained braced frame seismic performance *Earthq. Eng. Struct. Dyn.* **43** 1897–914

[181] Cortés-Puentes W L and Palermo D 2017 SMA tension brace for retrofitting concrete shear walls *Eng. Struct.* **140** 177–88

[182] Sasmal S and Nath D 2017 Seismic performance of non-invasive single brace made of steel and shape memory alloy for retrofit of gravity load designed sub-assemblages *Eng. Struct.* **143** 316–29

[183] Speicher M S, Desroches R and Leon R T 2010 Cyclic Testing of An SMA-Based Articulated Quadrilateral Bracing System Cyclic Testing of a SMA-Based Articulated Quadrilateral Bracing System

[184] Gao N, Jeon J S, Hodgson D E and Desroches R 2016 An innovative seismic bracing system based on a superelastic shape memory alloy ring *Smart Mater. Struct.* **25**

[185] Ozbulut O E and Hurlebaus S 2011 Seismic assessment of bridge structures isolated by a shape memory alloy/rubber-based isolation system *Smart Mater. Struct.* **20**

[186] Van de Lindt J W and Potts A 2008 Shake table testing of a superelastic shape memory alloy response modification device in a wood shearwall *J. Struct. Eng.* **134** 1343–52

[187] Rahman Bhuiyan A and Alam M S 2013 Seismic performance assessment of highway bridges equipped with superelastic shape memory alloy-based laminated rubber isolation bearing *Eng. Struct.* **49** 396–407

[188] Sourav Gur1, Sudib K. Mishra1, and S C 2013 Performance assessment of buildings isolated by shape-memory- alloy rubber bearing: Comparison with elastomeric bearing under near-fault earthquakes Sourav *Struct. Control Heal. Monit.*

[189] Ghodke S and Jangid R S 2017 Influence of high austenite stiffness of shape memory alloy on the response of base-isolated benchmark building *Struct. Control Heal. Monit.* **24** 1–17

[190] Shinozuka M, Chaudhuri S R and Mishra S K 2015 Shape-Memory-Alloy supplemented Lead Rubber Bearing (SMA-LRB) for seismic isolation *Probabilistic Eng. Mech.* **41** 34–45

[191] Zhu S and Qiu C X 2014 Incremental dynamic analysis of highway bridges with novel shape memory alloy isolators *Adv. Struct. Eng.* **17** 429–38

[192] McCormick J, DesRoches R, Fugazza D and Auricchio F 2006 Seismic vibration control using superelastic shape memory alloys *J. Eng. Mater. Technol. Trans. ASME* **128** 294–301

[193] Cao S, Ozbulut O E, Wu S, Sun Z and Deng J 2020 Multi-level SMA/lead rubber bearing isolation system for seismic protection of bridges *Smart Mater. Struct.* **29** 055045

[194] Ozbulut O E and Hurlebaus S 2010 Evaluation of the performance of a sliding-type base isolation system with a NiTi shape memory alloy device considering temperature effects *Eng. Struct.* **32** 238–49

[195] Jalali A, Cardone D and Narjabadifam P 2011 Smart restorable sliding base isolation system *Bull. Earthq. Eng.* **9** 657–73

[196] Khodaverdian A, Ghorbani-Tanha A K and Rahimian M 2012 An innovative base isolation system with Ni-Ti alloy and its application in seismic vibration control of Izadkhast Bridge *J. Intell. Mater. Syst. Struct.* **23** 897–908

[197] Gur S and Mishra S K 2013 Multi-objective stochastic-structural-optimization of shape-memory-alloy assisted pure-friction bearing for isolating building against random earthquakes *Soil Dyn. Earthq. Eng.* **54** 1–16

[198] Zheng Y, Dong Y and Li Y 2018 Resilience and life-cycle performance of smart bridges with shape memory alloy (SMA)-cable-based bearings *Constr. Build. Mater.* **158** 389–400

[199] De Domenico D, Gandelli E and Quaglini V 2020 Adaptive isolation system combining low-friction sliding pendulum bearings and SMA-based gap dampers *Eng. Struct.* **212** 110536

[200] Liang D, Liang D, Zheng Y, Fang C, Fang C, Fang C, Yam M C H and Zhang C 2020 Shape memory alloy (SMA)-cable-controlled sliding bearings: Development, testing, and system behavior *Smart Mater. Struct.* **29**

[201] Dolce M, Cardone D, Ponzo F C and Valente C 2005 Shaking table tests on reinforced concrete frames without and with passive control systems *Earthq. Eng. Struct. Dyn.* **34** 1687–717

[202] Hu J W 2016 Seismic analysis and parametric study of SDOF lead-rubber bearing (LRB) isolation systems with recentering shape memory alloy (SMA) bending bars *J. Mech. Sci. Technol.* **30** 2987–99

[203] Cardone D 2012 Re-centring capability of flag-shaped seismic isolation systems *Bull. Earthq. Eng.* **10** 1267–84

[204] Wang B, Zhu S and Casciati F 2020 Experimental Study of Novel Self-Centering Seismic Base Isolators Incorporating Superelastic Shape Memory Alloys *J. Struct. Eng. (United States)* **146** 1–16

[205] Attanasi G and Auricchio F 2011 Innovative superelastic isolation device *J. Earthq. Eng.* **15** 72–89

[206] Huang B, Zhang H, Wang H and Song G 2014 Passive base isolation with superelastic nitinol SMA helical springs *Smart Mater. Struct.* **23**

[207] Liu Y, Wang H, Qiu C and Zhao X 2019 Seismic behavior of superelastic shape memory alloy spring in base isolation system of multi-story steel frame *Materials (Basel).* **12**

[208] Zhuang P and Wang W 2015 Seismic control effect of lattice grid structure with SMA spring-friction bearings 1543–51

[209] Choi E, Nam T H and Cho B S 2005 A new concept of isolation bearings for highway steel bridges using shape memory alloys *Can. J. Civ. Eng.* **32** 957–67

[210] Strnadel B, Ohashi S, Ohtsuka H, Ishihara T and Miyazaki S 1995 Cyclic stress-strain characteristics of Ti□Ni and Ti□Ni□Cu shape memory alloys *Mater. Sci. Eng. A* **202** 148–56

[211] Yunfeng Zhang X H and S Z 2009 Seismic performance of benchmark base-isolated bridges with superelastic Cu–Al–Be restraining damping device *Struct. Control Heal. Monit.* **16** 668–85

[212] Vollmer M, Arold T, Kriegel M J, Klemm V, Degener S, Freudenberger J and Niendorf T 2019 Promoting abnormal grain growth in Fe-based shape memory alloys through compositional adjustments *Nat. Commun.* **10** 1–10

[213] Ozcan H, Ma J, Wang S J, Karaman I, Chumlyakov Y, Brown J and Noebe R D 2017 Effects of cyclic heat treatment and aging on superelasticity in oligocrystalline Fe-Mn-Al-Ni shape memory alloy wires *Scr. Mater.* **134** 66–70

[214] Ozcan H, Ma J, Karaman I, Chumlyakov Y I, Santamarta R, Brown J and Noebe R D 2018 Microstructural design considerations in Fe-Mn-Al-Ni shape memory alloy wires: Effects of natural aging *Scr. Mater.* **142** 153–7

[215] American Society for Testing and Materials 2015 ASTM F2516−14: Standard Test Method for Tension Testing of Nickel-Titanium Superelastic Materials *ASTM Int.* 6

[216] Correlated Solutions 2018 Vic-3d manuel

[217] Shaw J A and Kyriakides S 1995 Thermomechanical aspects of NiTi *J. Mech. Phys. Solids* **43** 1243–81

[218] Gall K and Sehitoglu H 1999 Role of texture in tension-compression asymmetry in polycrystalline NiTi *Int. J. Plast.* **15** 69–92

[219] Li Z Q and Sun Q P 2002 The initiation and growth of macroscopic martensite band in nano-grained NiTi microtube under tension *Int. J. Plast.* **18** 1481–98

[220] Shanley F R 1947 Inelastic column theory *J. Aeronaut. Sci.* **14** 261–8

[221] Wang B and Zhu S 2018 Seismic behavior of self-centering reinforced concrete wall enabled by superelastic shape memory alloy bars *Bull. Earthq. Eng.* **16** 479–502

[222] Pampanin S 2015 Towards the "Ultimate Earthquake-Proof" Building: Development of an Integrated Low-Damage System *Perspectives on European Earthquake Engineering and Seismology: Volume 2* ed A Ansal (Cham: Springer International Publishing) pp 321–58

[223] Andisheh K, Liu R, Palermo A and Scott A 2018 Cyclic Behavior of Corroded Fuse-Type Dissipaters for Posttensioned Rocking Bridges *J. Bridg. Eng.* **23** 1–14

[224] Shrestha K C, Araki Y, Yamakawa M, Yoshida N, Omori T, Sutou Y and Kainuma R 2015 Feasibility of Cu-Al-Mn superelastic alloy bar as a self-sensor material *J. Intell. Mater. Syst. Struct.* **26** 364–70

[225] Black C, Makris N and Aiken I 2002 Component testing, stability analysis and characterization of buckling-restrained Unbonded Braces

[226] Watanabe A, Fujimoto M, Wada A, Saeki E and Takeuchi T 1990 Development of unbonded brace *Q. Column* **115** 91–6

[227] Orgéas L and Favier D 1998 Stress-induced martensitic transformation of a NiTi alloy in isothermal shear, tension and compression *Acta Mater.* **46** 5579–91

[228] Wang B, Zhu S, Qiu C X and Jin H 2019 High-performance self-centering steel columns with shape memory alloy bolts: Design procedure and experimental evaluation *Eng. Struct.* **182** 446–58

[229] Yoshikazu Araki, Nao Maekawa, Kshitij C. Shrestha, Makoto Yamakawa, Yuji Koetaka T O and R K 2011 Feasibility of tension braces using Cu–Al–Mn superelastic alloy bars *Struct. Control Heal. Monit.*

[230] Fang C, Yam M C H, Ma H and Chung K F 2015 Tests on superelastic Ni–Ti SMA bars under cyclic tension and direct-shear: towards practical recentring connections *Mater. Struct. Constr.* **48** 1013–30

[231] Filiatrault A, Uang C-M, Folz B, Chrstopoulos C and Gatto K 2001 Reconnaissance Report of the February 28, 2001 Nisqually (Seattle-Olympia) Earthquake *Struct. Syst. Res. Proj.*

[232] Hassan, W.M., Park, S., Lopez, R.R., Mosalam, K.M. and Moehle, J.P., 2010. Seismic response of older-type reinforced concrete corner joints. In *Proceedings, 9th US National Conference and 10th Canadian Conference of Earthquake Engineering, Toronto, Canada, paper* (No. 1616).

[233] NIST 2013 Review of Past Performance and Further Development of Modeling Techniques for Collapse Assessment of Existing Reinforced Concrete Buildings (Gaithersburg, Maryland.)

[234] Pampanin S 2006 Controversial aspects in seismic assessment and retrofit of structures in modern times: Understanding and implementing lessons from ancient heritage *Bull. New Zeal. Soc. Earthq. Eng.* **39** 120–34

[235] Kam W Y and Pampanin S 2009 Experimental and numerical validation of selective weakening retrofit for existing non-ductile R.C. frames *Improv. Seism. Perform. Exist. Build. Other Struct. - Proc. 2009 ATC SEI Conf. Improv. Seism. Perform. Exist. Build. Other Struct.* **41084** 706–20

[236] Anagnos T, Comerio M C, Goulet C and Na H 2008 Los Angeles inventory of nonductile concrete buildings for analysis of seismic collapse risk hazards *14th World Conf. Earthq. Eng.* 8

[237] Jaiswal K S and Wald D J 2008 Creating a Global Building Inventory for Earthquake Loss Assessment and Risk Management: U.S. Geological Survey Open-File Report **1160** 113

[238] Chang G. A. and Mander J B 1994 Seismic energy based fatigue damage analysis of bridge columns: Part I - Evaluation of seismic capacity.NCEER Technical Report No. NCEER-94-0006 *State Univ. New York. Buffalo, New York*

[239] By Joseph M. Bracci S K K and A M R 1997 Seismic Performance and Retrofit Evaluation of Reinforced Concrete Structures *J. Struct. Eng. 1JANUARY* **123** 3–10

[240] Lehman D E, Stanton J, Anderson M, Alire D and Walker S 2004 Seismic performance of older beam-column joints *Proc. 13th World Conf. Earthq. Eng.* 1464

[241] Kuang J S and Wong H F 2006 Effects of beam bar anchorage on beam-column joint behaviour *Proc. Inst. Civ. Eng. Struct. Build.* **159** 115–24

[242] ACI Committee 318 2019 318-19 Building Code Requirements for Structural Concrete and Commentary (American Concrete Institute)

[243] American Society of Civil Engineers 2017 *Seismic Evaluation and Retrofit of Existing Buildings* vol 225 (Reston, VA: American Society of Civil Engineers)

[244] Shi F, Zhou Y, Ozbulut O E and Cao S 2021 Development and experimental validation of anchorage systems for shape memory alloy cables *Eng. Struct.* **228** 111611

[245] Qiu C X and Zhu S 2016 High-mode effects on seismic performance of multi-story self-centering braced steel frames *J. Constr. Steel Res.* **119** 133–43

[246] Torra V, Auguet C, Isalgue A, Carreras G, Terriault P and Lovey F C 2013 Built in dampers for stayed cables in bridges via SMA. The SMARTeR-ESF project: A mesoscopic and macroscopic experimental analysis with numerical simulations *Eng. Struct.* **49** 43–57

[247] Ferrante Cavallaro G, Francavilla A B, Latour M, Piluso V and Rizzano G 2018 Cyclic response of low yielding connections using different friction materials *Soil Dyn. Earthq. Eng.* **114** 404–23

[248] Latour M, Piluso V and Rizzano G 2014 Experimental analysis on friction materials for supplemental damping devices *Constr. Build. Mater.* **65** 159–76

[249] Loo W Y, Quenneville P and Chouw N 2017 The influence of surface preparation and the lubricating effect of mill scale on the performance of slip-friction connectors *Constr. Build. Mater.* **155** 1025–38

[250] C. E. Grigorian, T.S. Yang and E P P 1993 Slotted Bolted Connection Energy Dissipators *Earthq. Spectra* **9** 491–504

[251] Xiao X, Yin Y, Bao J, Lu L and Feng X 2016 Review on the friction and wear of brake materials *Adv. Mech. Eng.* **8** 1–10

[252] Lagoudas D C, Mayes J J and Khan M M Simplified Shape Memory Alloy (SMA) Material Model for Vibration Isolation 1–10

[253] Andrawes B and DesRoches R 2007 Effect of hysteretic properties of superelastic shape memory alloys on the seismic performance of structures *Struct. Control Heal. Monit.* **14** 301–20

[254] ASTM 2015 Standard Specification for High Strength Structural Bolts, Steel and Alloy Steel, Heat Treated, 120 ksi (830 MPa) and 150 ksi (1040 MPa) Minimum Tensile Strength , Inch and Metric Dimensions *Astm F3125/F3125M* 1–1

[255] Gilbert C F and Erochko J 2019 Development and testing of hybrid timber-steel braced frames *Eng. Struct.* **198**

[256] Opensees.berkeley.edu. *Open System for Earthquake Engineering Simulation - Home Page*. [online] Available at: <https://opensees.berkeley.edu/> [Accessed 10 September 2021].

[257] FEMA 2018 Seismic performance assessment of buildings, volume 1 - methodology *Fema P-58-1* **1** 340

[258] Speicher M S, Dukes J and Wong K K F 2020 Collapse Risk of Steel Special Moment Frames per FEMA P695 - NIST Technical Note 2084 97

[259] Harris III J L and Speicher M S 2015 Assessment of First Generation Performance-Based Seismic Design Methods for New Steel Buildings, Volume 1: Special Moment Frames (Gaithersburg, MD)

[260] Ibarra L F, Medina R A and Krawinkler H 2005 Hysteretic models that incorporate strength and stiffness deterioration *Earthq. Eng. Struct. Dyn.* **34** 1489–511

[261] Lignos D G and Krawinkler H 2011 Deterioration Modeling of Steel Components in Support of Collapse Prediction of Steel Moment Frames under Earthquake Loading *J. Struct. Eng.* **137** 1291–302

[262] Dimitrios G. Lignos and Helmut Krawinkler 2010 A steel database for component deterioration of tubular hollow square steel columns under varying axial load for collapse assessment of steel structures under earthquakes

[263] Gupta A and Krawinkler H 1999 Seismic Demands for Performance Evaluation of Steel Moment Resisting Frame Structures

[264] AISC 360-16 2016 AISC360/16 Specification for Structural Steel Buildings, an American National Standard 612 pp.

[265] Ancheta T, Darragh R, Stewart J, Seyhan E, Silva W, Chiou B, Wooddell K, Graves R, Kottke A, Boore D, Kishida T and Donahue J 2013 PEER NGA-West2 Database, Technical Report PEER 2013/03

[266] Zhu S and Zhang Y 2008 Seismic Analysis of Concentrically Braced Frame Systems with Self-Centering Friction Damping Braces *J. Struct. Eng.* **134** 121–31

[267] Silwal B, Huang Q, Ozbulut O E and Dyanati M 2018 Comparative seismic fragility estimates of steel moment frame buildings with or without superelastic viscous dampers *J. Intell. Mater. Syst. Struct.* **29** 3598–613

[268] Silwal B, Ozbulut O E and Michael R J 2016 Seismic collapse evaluation of steel moment resisting frames with superelastic viscous damper *J. Constr. Steel Res.* **126** 26–36

[269] Qiu C, Li H, Ji K, Hou H and Tian L 2017 Performance-based plastic design approach for multi-story self-centering concentrically braced frames using SMA braces *Eng. Struct.* **153** 628–38